université PARIS-SACLAY

Habilitation à diriger des recherches

Reactors, reactions, and random numbers

Habilitation à diriger des recherches de l'Université Paris-Saclay

présentée et soutenue à Saclay, le 12 septembre 2023, par

Davide MANCUSI

Composition du jury

José Benlliure Anaya	Rapporteur
Professeur, Université de Saint-Jacques-de-Compostelle (Espagne)	
Forrest Brown	Rapporteur
Professeur, University of New Mexico (États-Unis)	
Tony Lelièvre	Rapporteur
Professeur, École des Ponts ParisTech	
Cheikh Diop	Examinateur
Directeur de Recherche, CEA/DES	
Gaël Poëtte	Examinateur
Ingénieur-Chercheur, CEA/DAM	
Marc Verderi	Examinateur
Directeur de Recherche, Laboratoire Leprince-Ringuet	

Titre : Réacteurs, réactions et nombres aléatoires

Mots clés : Monte-Carlo, transport de particules, modèles de réaction nucléaire, cascade intranucléaire

Résumé : La méthode de Monte-Carlo est un outil omniprésent dans le transport de particules. En physique des réacteurs nucléaires, l'approche Monte-Carlo constitue la méthode de référence pour la résolution de l'équation de transport de Boltzmann linéaire pour les neutrons et les photons. Son utilisation est également très courante dans le transport de particules chargées pour la radioprotection et pour la simulation de détecteurs de particules. Dans de nombreuses applications à haute énergie, les réactions nucléaires élémentaires qui ont lieu pendant le transport sont elles-mêmes simulées à l'aide de modèles de réactions nucléaires basés sur la méthode de Monte-Carlo. Ce document donne un aperçu de la théorie de la méthode de Monte-Carlo dans le transport de particules neutres et chargées. Une attention particulière est consacrée aux principes et aux applications des modèles de réaction nucléaire de la classe des cascades intranucléaires. Quelques sujets de recherche récents sont mis en avant.

Title: Reactors, reactions, and random numbers

Keywords: Monte Carlo, particle transport, nuclear reaction models, intranuclear cascade

Abstract: The Monte Carlo method is a pervasive tool in particle transport. In nuclear reactor physics, the Monte Carlo approach is the "golden standard" for the solution of the linear Boltzmann transport equation for neutrons and photons. Its use is also very common in charged-particle transport for radiation protection and for the simulation of particle detectors. In many high-energy applications, the elementary nuclear reactions that take place during transport are themselves simulated using nuclear reaction models based on the Monte Carlo method. This document provides an overview of the theory of the Monte Carlo method in neutral and charged particle transport. Special focus is devoted to the principles and applications of nuclear-reaction models of the intranuclear-cascade class. A few recent research subjects are highlighted.

Contents

Per Adriano, Arturo e Caterina

1 Introduction

The object of the theory of **radiation transport** is the quantitative description of the propagation of radiation in matter, of the influence of matter on the quality of radiation and of the effect of radiation on the medium it traverses. Radiation can be ionizing or non-ionizing, depending on the possible interactions between the radiation field and the atoms of the medium. Most of the mathematical methods for the solution of radiation transport problems are equally applicable to ionizing and non-ionizing radiation. In this manuscript, however, we will concentrate on ionizing radiation transport.

Radiation transport problems naturally arise in several applications. In **nuclear reactors**, for example, thermal power is generated using a self-sustained chain of neutron-induced fission reactions. The design and analysis of reactors hinges on the description of the interactions between the neutrons in the reactor core and the core itself. Neutrons undergo a variety of **nuclear reactions** with the nuclei of the core. This has two consequences. First, the nuclear reactions determine the characteristics of the neutron field in the reactor core; other types of particles, such as photons, electrons, positrons, protons, etc., may also appear as reaction products. Second, the reactions induced by the radiation field also affect the properties of the core materials. Indeed, nuclear reactions can transfer energy from the radiation field to the material, or from the material to the field. The vast amount of energy released by the fission of the actinides is essential to the existence of nuclear reactors. The energy released by nuclear reactions propagates by several mechanisms (conduction, convection, radiation), heats up the reactor, and is generally extracted[1] to be converted to electrical energy in commercial reactors. Energy deposition also induces thermo-mechanical stresses in the solid materials of the reactor, and affects the flow of any fluid (typically coolant) present in the reactor. Finally, nuclear reactions may result in changes of the isotopic (and possibly chemical) species of the atoms involved, as well as in the appearance of new atoms. Reactions also generally cause transformations in the microscopic structure of the materials. Thus, the structure of the reactor materials is slowly modified by the radiation exposure, and their isotopic composition evolves over time.

The presence of thermo-mechanical, thermohydraulic and isotopic evolution phenomena highlights the fact that a nuclear reactor is a very complex object. Nuclear engineers wish for reliable models for the behavior of nuclear reactors under ordinary, incidental and accidental conditions, but the behavior of the system as a whole is the result of the interplay of several phenomena which need to be well understood in isolation and simultaneously taken into account.

[1] The mechanism of extraction of the energy depends on the type of nuclear reactor considered.

Outside reactor physics, neutrons are less prominent in radiation transport problems. In other applications, an important role is played by charged particles like electrons, positrons, protons, and ions. Cosmic rays, for example, mostly consists of highly energetic hydrogen and helium ions, but all elements up to iron are sensibly represented. In space, cosmic rays represent a major radiological hazard, together with solar flares and other sources of radiation. Space vessels are immersed in the cosmic radiation, which may damage the equipment or (in the case of crewed missions) expose humans to radiation. Determining the type and amount of damage to equipment or the dose received by crews is a radiation-transport problem. Similar shielding problems exist around particle accelerators. Finally, charged-particle transport is important for special classes of nuclear reactors, such as fusion reactors or accelerator-driven subcritical reactors.

A common mathematical model for radiation transport is provided by the **linear Boltzmann transport equation**, which describes the dynamics of the average number of particles in phase space. An analytical solution of the Boltzmann equation is rarely possible, and numerical methods need to be employed. There are essentially two classes of methods:

- **Deterministic methods** rely on the application of discretization techniques to the Boltzmann equation, in order to transform it into a set of linear algebraic equations. Standard numerical linear algebra techniques are then applied, and approximate solutions are obtained. Numerical solvers based on deterministic methods tend to be fast, but the validity of the approximations made in the model must be confirmed by comparing the results with either experimental data or with the results of finer numerical methods.

- **Stochastic methods** rely on a probabilistic interpretation of the Boltzmann equation. They are based on the use of **random numbers** in suitably constructed **Monte Carlo** simulations for the problem to solve. In general, stochastic methods are much less dependent on discretization schemes and approximations than deterministic methods. Monte Carlo simulations for neutron transport problems may even be considered to be essentially approximation-free[2]. Monte Carlo solvers however have two main disadvantages: first, they produce stochastic results, in the sense that each Monte Carlo simulation should be regarded as the result of statistical sampling. Meaningful results can only be obtained by repeating the sampling several times and applying statistical inference methods. Second, for a reasonable sample size, Monte Carlo solvers are generally slower than comparable deterministic solvers. For these reasons, Monte Carlo methods are considered the *golden standard* against which deterministic methods should benchmark the validity of their approximations and discretization schemes.

Any numerical method requires a certain amount of information about the problem to solve. The Boltzmann equation is formulated in terms of double-differential energy-angle **cross sections** and **average multiplicities**. Since deterministic methods are based on the discretization of the Boltzmann equation, they can only be applied if all of these quantities are known. On the other hand, stochastic methods, somewhat unexpectedly, need a different type of information. Indeed, Monte Carlo particle transport is based around the idea of interpreting the double-differential cross sections and the multiplicities as distributions for the average numbers of particles emitted in a certain reaction. The Monte Carlo method

[2]For charged particles, some approximations, discretization, and modelling are still necessary.

requires an algorithm that samples the reaction products for each possible reaction. If only the double-differential cross sections and the average multiplicities are given, as it is the case when we are solving a Boltzmann equation, then the algorithm must be consistent with these pieces of information, in the sense that the *average number* of sampled reaction products must be distributed in energy and angle according to the physical quantities. However, if we have access to more information about the reaction, it is entirely possible to incorporate this in the sampling algorithm. For example, if the reaction sampling algorithm correctly models the fluctuations and correlations of the physical reactions, then the Monte Carlo method will propagate this information to the simulation. This makes it possible to use Monte Carlo to answer questions about the radiation-transport problem that lie beyond the Boltzmann equation. For example, one might want to compute the probability that, given a source particle, the amount of energy deposited in a detector volume exceeds a given threshold. This observable cannot be derived from the solution of the Boltzmann equation, but it is accessible by suitable Monte Carlo simulations.

It may seem that the use of a sampling algorithm instead of cross sections requires more information about the physics of the elementary reactions. This is not correct. Extra information may be accommodated if needed, but it is not required. Quite the contrary: there are situations where the double-differential cross section and the average multiplicities are not known, but Monte Carlo is nevertheless applicable. This happens for example when the elementary reactions between the radiation field and the media are described by a **nuclear reaction model** that can be cast in the form of a sampling algorithm. For example, models for reactions induced by highly energetic nucleons or nuclei are often themselves solved using the Monte Carlo method[3]! Thus, Monte Carlo solves the transport problem, and relies on Monte Carlo models for sampling the elementary reactions, in an astounding *mise en abyme*. Additional Monte Carlo layers can even appear at the top or at the bottom of the stack. "Above" the radiation transport problem, we mention the problem of transport in stochastic geometries, where the geometry of the radiation transport problem itself is random; this is a special form of *total Monte Carlo*, where uncertainty on the input to the radiation transport problem is modelled using probability distributions and propagated to the calculation results by sampling. On the other (lower) end of the stack, Monte Carlo nuclear reaction models need to sample the outcome of collisions between the nuclear constituents; for exotic or high-energy collisions, dedicated Monte Carlo models exist and are sometimes employed by the nuclear reaction models. It is Monte Carlo all the way down.

The purpose of this manuscript is to be a guidebook for a leisurely tour of Monte Carlo particle transport. The document is divided in two parts. In the first part, which consists of Chapters 2 to 5, I provide some background matter about the subjects of particle transport, Monte Carlo, and nuclear reaction models, with a special focus on the class of intranuclear-cascade models. I feel obliged to justify the decision to preface the manuscript with a sizeable introductory part of background knowledge. It is my belief that the most remarkable achievements of my post-doctoral research career are fairly heterogeneous. As the Reader will discover in the following chapters, I have elected to write about the extension of nuclear-reaction models, about transport theory for neutral and charged particles, about variance-reduction techniques in the Monte Carlo method, and about simulations for reactor physics. As my career progressed and I expanded my interests to include new subjects, I had to acquire the necessary background knowledge in statistical physics, nuclear physics,

[3]It is possible to push the analogy even further: many nuclear reaction models are actually akin to transport problems at the microscopic scale of the atomic nucleus.

reactor physics, numerics, and computing. I wrote the first part of this manuscript thinking about all the gaps that I have filled in the fifteen years since my Ph.D. defense. I am confident that the Reader will also find this material helpful.

In the second part of the manuscript, we will retrace the descent from the macroscopic to the microscopic scale undertook in Part I. Following the milestones of my career in roughly chronological order, Chapter 6 presents a few extensions and developments that I brought to the physics of intranuclear-cascade models. Chapter 7 introduces a few challenging kinetic and dynamic neutron transport calculations applied to reactor physics. Finally, Chapter 8 presents the development and the analysis of a few advanced variance-reduction techniques. In these chapters, I describe what I consider to be the most noteworthy deeds of my research career. I believe that Part II also serves to highlight the coherence of my experience. Monte Carlo is, of course, the foremost recurring theme, as implied even by the title of this work. Random numbers will accompany us along the journey from the microscopic scale of nuclear reactions to the macroscopic scale of nuclear reactors. Along this path, I am convinced that the Reader will also distinctly perceive the dual nature of this document, which was written in the zoo of practical applications, in the shade of an ivory tower. It is my feeling that I have always searched for theory and generalization in the empirical multiplicity of my everyday simulation work, as Chapter 8 in particular shows; but, at the same time, I have always been preoccupied with keeping theory adherent to reality, as Chapters 6 and 7 demonstrate. In this respect, the central role played by Monte Carlo is not a happenstance. The choice of a method that is considered to be the golden standard for particle transport simulations, by its approximation-free nature, is a concrete testimony to my perpetual ambition to describe reality as faithfully as possible.

Finally, in Chapter 9, I submit my perspectives for the future developments of my research.

I think that the content of this document provides a fair overview of my achievements. Nevertheless, I also feel that I had to omit a few remarkable works from my exposition, for the sake of brevity. This manuscript is already too long as it is. I hope that for what I lack in concision, dear Reader, I make up for in breadth and rigor.

Part I

Background matter

Elements of particle transport

Broadly speaking, the problem of particle transport can be stated as the determination of the effect of matter on the propagation of particles and the effect of particles on the properties of matter. The approach we select for modelling this problem depends very much on the nature of the physical quantities that we seek to describe.

2.1 Neutral particles: definitions

Let us consider a specific example. In nuclear-reactor physics, fuel depletion (the evolution of the atomic composition of fuel) is driven by the nuclear reactions induced by the neutrons circulating in the reactor. In reality, the reaction events are stochastic: each neutron has some finite probability per unit time to induce a nuclear reaction. However, the number of neutrons circulating in a full-power reactor is so large that we can neglect the stochastic nature of the nuclear reactions. Let $n(\boldsymbol{r}, \hat{\boldsymbol{\Omega}}, E, t)$ represent the average number of neutrons per unit volume, energy and solid angle, present at position $\boldsymbol{r}$ with energy E and direction $\hat{\boldsymbol{\Omega}}$ at time t. This quantity is called the **neutron density**; in SI units, it is measured in $\mathrm{m}^{-3}\ \mathrm{J}^{-1}\ \mathrm{sr}^{-1}$, but in reactor physics it is usually rather given in $\mathrm{cm}^{-3}\ \mathrm{eV}^{-1}\ \mathrm{sr}^{-1}$. By modelling neutrons as a continuous field, we gain the ability to apply the standard tools of functional analysis to the study of the problem of neutron transport.

In order to describe the dynamics of the neutron density, we need to introduce the **collision density** $\psi_n(\boldsymbol{r}, \hat{\boldsymbol{\Omega}}, E, t)$, which is the average number of collisions per unit volume, time, energy and solid angle induced in a given position and at a given time by neutrons with a given energy and direction. Clearly, the collision density is locally proportional to the neutron density. For practical reasons which will become clear in the following, the factor of proportionality is written as the product of the neutron speed v (which is a function of the energy, E) and a function called the **total macroscopic cross section**, denoted as $\Sigma_t(\boldsymbol{r}, E, \hat{\boldsymbol{\Omega}}, t)$, having the dimensions of the inverse of a length:

$$\psi_n(\boldsymbol{r}, \hat{\boldsymbol{\Omega}}, E, t) = v(E) \cdot \Sigma_t(\boldsymbol{r}, \hat{\boldsymbol{\Omega}}, E, t) \cdot n(\boldsymbol{r}, \hat{\boldsymbol{\Omega}}, E, t). \tag{2.1}$$

The average number of neutrons that undergo collisions with the nuclei of the medium in the reactor (per unit time and unit volume) is called the **collision rate**. The collision rate (at position $\boldsymbol{r}$ and time t) is the integral of the collision density ψ_n over all energies and angles,

and it is given by

$$\begin{aligned}\tau(\boldsymbol{r},t) &= \int \psi_n(\boldsymbol{r},\hat{\boldsymbol{\Omega}},E,t)\,\mathrm{d}^2\hat{\boldsymbol{\Omega}}\,\mathrm{d}E \\ &= \int v\cdot\Sigma_t(\boldsymbol{r},\hat{\boldsymbol{\Omega}},E,t)\cdot n(\boldsymbol{r},\hat{\boldsymbol{\Omega}},E,t)\,\mathrm{d}^2\hat{\boldsymbol{\Omega}}\,\mathrm{d}E. \end{aligned} \tag{2.2}$$

The total macroscopic cross section Σ_t captures information about the interaction of the neutron with the medium. In an amorphous, unpolarized medium (which we will always assume), the cross section is independent of the direction $\hat{\boldsymbol{\Omega}}$ of the incident neutron; in a stationary medium, it is independent of time; in general, it depends on the composition and the temperature of the medium.

Similarly, it is possible to consider other types of reaction rates, associated to specific collision types or outcomes. For instance, it is possible to introduce the **fission density** ψ_f as the number of fission events induced by neutrons per unit time, volume, energy and solid angle. Again, clearly the fission density is locally proportional to the neutron density, which leads us to introduce the **macroscopic fission cross section** Σ_f:

$$\psi_f(\boldsymbol{r},\hat{\boldsymbol{\Omega}},E,t) = v\cdot\Sigma_f(\boldsymbol{r},\hat{\boldsymbol{\Omega}},E,t)\cdot n(\boldsymbol{r},\hat{\boldsymbol{\Omega}},E,t).$$

Likewise, the **fission rate** τ_f is the integral of the fission density over all incident energies and directions:

$$\tau_f(\boldsymbol{r},t) = \int \psi_f(\boldsymbol{r},\hat{\boldsymbol{\Omega}},E,t)\,\mathrm{d}^2\hat{\boldsymbol{\Omega}}\,\mathrm{d}E. \tag{2.3}$$

Integrals of the form of Eqs. (2.2) and (2.3) play an important role in transport theory. Therefore, it is customary to introduce the **angular flux** φ as the product of the neutron density and the speed:

$$\varphi(\boldsymbol{r},\hat{\boldsymbol{\Omega}},E,t) = v\cdot n(\boldsymbol{r},\hat{\boldsymbol{\Omega}},E,t). \tag{2.4}$$

With this definition, the collision rate, Eq. (2.2), can be rewritten as

$$\tau(\boldsymbol{r},t) = \int \Sigma_t(\boldsymbol{r},E,t)\,\varphi(\boldsymbol{r},\hat{\boldsymbol{\Omega}},E,t)\,\mathrm{d}^2\hat{\boldsymbol{\Omega}}\,\mathrm{d}E.$$

The **scalar flux** Φ is defined as the integral of the angular flux over the angular variables:

$$\Phi(\boldsymbol{r},E,t) = \int \varphi(\boldsymbol{r},\hat{\boldsymbol{\Omega}},E,t)\,\mathrm{d}^2\hat{\boldsymbol{\Omega}}. \tag{2.5}$$

If the total macroscopic cross section is independent of the neutron direction, the collision rate can be expressed as a functional of the scalar flux:

$$\tau(\boldsymbol{r},t) = \int \Sigma_t(\boldsymbol{r},E,t)\,\Phi(\boldsymbol{r},E,t)\,\mathrm{d}E.$$

The same considerations apply to the fission rate, Eq. (2.3), and to any other type of reaction rate. All the definitions given in this section can be extended to photons in a straightforward manner.

2.1.1 Relation between macroscopic and microscopic cross sections

In detail, how are macroscopic cross sections related to the properties of the medium? The collisions between neutrons and nuclei are described by the quantum-mechanical theory of nuclear reactions (Newton 1966; Wu and Ohmura 1962) in terms of **cross sections**. In the context of transport theory, cross sections are usually referred to as **microscopic cross sections**, to better distinguish them from macroscopic cross sections. We recall that microscopic cross sections are defined as reaction rates per unit incident flux and target nucleus. The microscopic cross sections are determined by the laws of quantum mechanics and describe the dynamics of the collision of a neutron of energy E on a nucleus at rest. For the concerns of particle transport, they are usually considered as given data (however, see Section 2.8 below).

The simplest case to consider is that of an amorphous, unpolarized medium consisting of I nuclides, at the temperature of 0 K. Let $\rho_i(\boldsymbol{r}, t)$ ($i \in \{1, \ldots, I\}$) be the **concentration** of the i-th nuclide at position $\boldsymbol{r}$ and time t, i.e. the number of nuclei of nuclide i present per unit volume. Under these assumptions, the relation between the total macroscopic and microscopic cross sections reads

$$\Sigma_t(\boldsymbol{r}, E, t) = \sum_{i=1}^{I} \rho_i(\boldsymbol{r}, t)\sigma_{t,i}(\boldsymbol{r}, E, t).$$

The sum runs over the isotopes present in the medium.

2.1.2 Doppler broadening

At finite temperatures, the nuclei in the medium cannot be considered at rest in the laboratory system because they are endowed with thermal motion. The microscopic cross section for the interaction of a neutron and a nucleus in motion is determined by the velocity of the neutron relative to the nucleus; this is a form of **Doppler effect**. Therefore, the effect of thermal motion on the microscopic cross sections is expressed by an effective, **Doppler-broadened** microscopic cross section, defined by the following equation (Bell and Glasstone 1970):

$$\sigma_{t,i}(\boldsymbol{r}, E, t; T) = \frac{1}{v} \int v_r \cdot \sigma_{t,i}(\boldsymbol{r}, E_r, t) \cdot P_T(\boldsymbol{v'})\, \mathrm{d}^3\boldsymbol{v'}. \tag{2.6}$$

Here $\boldsymbol{v'}$ is the velocity of the nucleus in the laboratory frame, v_r and E_r are respectively the velocity and the kinetic energy of the neutron in the rest frame of the nucleus, and $P_T(\boldsymbol{v'})$ is the thermal velocity distribution of the nuclei in the medium at temperature T, which depends on the structure of the material and its chemical properties, in addition to its temperature. We observe that the definition of the Doppler-broadened cross section involves an average of the microscopic cross sections over energies close to the energy of the neutron in the laboratory system.

It is possible to gain some insight into the phenomenology of Doppler broadening by modelling the medium as an ideal gas of atoms of mass M. We can write a non-relativistic Maxwell-Boltzmann form for P_T:

$$P_T(\boldsymbol{v'}) = \left(\frac{M}{2\pi k_B T}\right)^{3/2} \exp\left(-\frac{M v'^2}{2k_B T}\right),$$

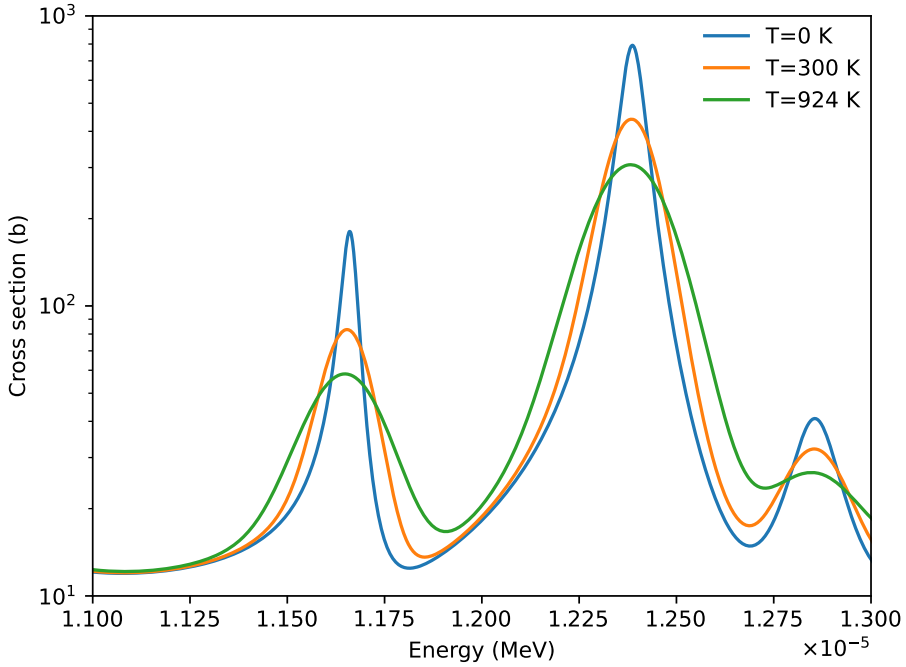

Figure 2.1: Excitation function for the $^{235}\mathrm{U}(n, f)$ cross section at three different temperatures. Data taken from the ENDF/B-VIII.0 library (D. A. Brown et al. 2018).

where k_B is Boltzmann's constant. Assuming non-relativistic kinematics for the neutron, too, and denoting the neutron mass as m, we can derive the expectation value of E_r, the kinetic energy of the neutron in the rest frame of the nucleus:

$$\begin{aligned}\mathbb{E}(E_r) &= \int \frac{m}{2}(\boldsymbol{v} - \boldsymbol{v'})^2 P_T(\boldsymbol{v'})\mathrm{d}^3\boldsymbol{v'} \\ &= \frac{m_n v^2}{2} + \frac{3mk_BT}{2M}.\end{aligned}$$

Therefore, the "effective" energy E_r differs from the nominal neutron energy E by a quantity of the order of k_BT. We can now state under what conditions the effects of Doppler broadening are negligible: if the microscopic cross section $\sigma_i(\boldsymbol{r}, E, t)$ exhibits little dependence on the incident energy E for variations of the order of k_BT, then the effect of Doppler broadening will be negligible. Note that it is not sufficient that the speed of the neutron in the lab frame be much larger than the thermal speed of the nucleus for Doppler broadening to be negligible; as an illustration, Fig. 2.1 shows the excitation function for the fission cross section of $^{235}\mathrm{U}$ at three different temperatures (0 K, 300 K, and 924 K). The plot shows a few resonances in the epithermal region and shows that the peak width increases as the temperature increases; this clarifies why we use the term "broadening" to refer to the effect of thermal motion.

Doppler broadening of neutron resonances is crucial for ensuring the stability of nuclear reactors and much theoretical and experimental effort has been devoted to modelling it, especially for materials relevant for nuclear energy.

For photon transport, the effect of Doppler broadening is negligible, for two reasons: first, photons always travel at the speed of light, which is much larger than the thermal speed of the atoms; second, photo-atomic cross sections do not exhibit sharp resonances as

a function of the photon energy.

2.2 Derivation of the Boltzmann transport equation

The equation that governs the dynamics of the particle flux can be written as a local balance equation for the losses and gains of particles in phase space. Let us consider an infinitesimal test volume $\mathrm{d}^3\boldsymbol{r}$ around position $\boldsymbol{r}$. The number of particles of energy E and direction $\hat{\boldsymbol{\Omega}}$ in the test volume at time t can vary with time for one of the following reasons:

C_1: particles leave or enter the test volume through its boundary;

C_2: particles disappear from the test volume because they undergo a collision;

C_3: new particles are produced by collisions in the test volume;

C_4: new particles are produced by an external source.

We will now derive a mathematical expression for each of these terms, and show that all of them are proportional to the test volume $\mathrm{d}^3\boldsymbol{r}$; this property is probably trivial for all contributions except C_1.

2.2.1 Leakage term

The first term to consider is the **leakage term**, representing contribution C_1. It is somewhat clearer to derive the form of the leakage term for a finite volume, and let the volume tend to zero at the end. So let us introduce a finite test volume V and let us define $\mathrm{d}L_V/\mathrm{d}t$ to be the *net* number of particles of direction $\hat{\boldsymbol{\Omega}}$ and energy E that *leave* the test volume per unit time. Since particles enter and leave through the boundary ∂V of the test volume, $\mathrm{d}L_V/\mathrm{d}t$ is naturally expressed as a surface integral on the boundary. Simple geometrical considerations, along with Eq. (2.4), lead to the expression

$$\frac{\mathrm{d}L_V}{\mathrm{d}t} = \oint_{\partial V} \hat{\boldsymbol{\Omega}} \cdot \hat{\boldsymbol{n}}\, \varphi(\boldsymbol{r}, \hat{\boldsymbol{\Omega}}, E, t)\, \mathrm{d}^2\boldsymbol{r}, \tag{2.7}$$

where $\hat{\boldsymbol{n}}$ is the surface normal. We cannot resist the temptation to invoke Gauss's theorem and rewrite Eq. (2.7) as

$$\begin{aligned}\frac{\mathrm{d}L_V}{\mathrm{d}t} &= \int_V \nabla \cdot \left(\varphi(\boldsymbol{r}, \hat{\boldsymbol{\Omega}}, E, t)\, \hat{\boldsymbol{\Omega}}\right) \mathrm{d}^3\boldsymbol{r} \\ &= \int_V \hat{\boldsymbol{\Omega}} \cdot \nabla\varphi(\boldsymbol{r}, \hat{\boldsymbol{\Omega}}, E, t)\, \mathrm{d}^3\boldsymbol{r}. \end{aligned} \tag{2.8}$$

Now the leakage term has the form of a volume integral, and we can let the test volume tend to zero. In this limit, the leakage density becomes

$$C_1 = \hat{\boldsymbol{\Omega}} \cdot \nabla\varphi(\boldsymbol{r}, \hat{\boldsymbol{\Omega}}, E, t), \tag{2.9}$$

which is the sought expression.

2.2.2 Collision term

The collision term C_2 tallies the number of particles per unit time, volume, energy and solid angle that undergo collisions at $\boldsymbol{r}$. This is exactly the definition of the collision density, Eq. (2.1). Therefore,

$$C_2 = \Sigma_t(\boldsymbol{r}, E, t)\, \varphi(\boldsymbol{r}, \hat{\boldsymbol{\Omega}}, E, t). \tag{2.10}$$

2.2.3 Production term

The third term, C_3, is defined as the number of particles per unit time, volume, energy and solid angle emerging from collisions at $\boldsymbol{r}$. This term can in principle include contributions from many different reactions channels. For the purpose of this illustration, we will limit ourselves to *scattering* and *fission*.

Scattering

Scattering encompasses all the channels that result in one or more outgoing particles[1], except fission. Note that the production terms tallies the particles that *emerge* from the collision with energy E and direction $\hat{\boldsymbol{\Omega}}$; thus, the particle that induced the reaction had a different energy E' and a different direction $\hat{\boldsymbol{\Omega}}'$, and all possible values of E' and $\hat{\boldsymbol{\Omega}}'$ need to be considered.

The information we need about scattering is encapsulated by two quantities. The first one is the **microscopic scattering cross section** for isotope i,

$$\sigma_{s,i}(E'),$$

which represents the number of scattering events per unit incident particle flux and target nucleus. Note that we have used E' as the energy variable. The second quantity is the **differential microscopic scattering cross section** for isotope i,

$$\frac{\mathrm{d}^3\sigma_{s,i}}{\mathrm{d}^2\hat{\boldsymbol{\Omega}}\,\mathrm{d}E}(\hat{\boldsymbol{\Omega}}' \to \hat{\boldsymbol{\Omega}}, E' \to E),$$

representing the number of particles emerging from scattering with direction $\hat{\boldsymbol{\Omega}}$ and energy E, per unit outgoing solid angle, unit outgoing energy, unit incident particle flux and target nucleus. Note that the integral of the differential cross sections over the outgoing variables E and $\hat{\boldsymbol{\Omega}}$ does not necessarily equal the scattering cross section; the **average scattering multiplicity**

$$\nu_{s,i}(E') = \frac{1}{\sigma_{s,i}(E')} \int \frac{\mathrm{d}^3\sigma_{s,i}}{\mathrm{d}^2\hat{\boldsymbol{\Omega}}\,\mathrm{d}E}(\hat{\boldsymbol{\Omega}}' \to \hat{\boldsymbol{\Omega}}, E' \to E)\, \mathrm{d}^2\hat{\boldsymbol{\Omega}}\,\mathrm{d}E$$

represents the average number of particles emerging from the scattering event. For example, if all scattering events are elastic, then $\nu_{s,i} = 1$; however, in the presence of scattering channels with higher multiplicity (such as $(n, 2n)$), this need not be the case and $\nu_{s,i}$ may be larger. We omit the dependence of $\nu_{s,i}$ on $\hat{\boldsymbol{\Omega}}'$ because we assume that the nucleus is unpolarized.

[1] The typical example is *elastic scattering*, which results in exactly one outgoing particle and no energy transfer to the internal degrees of freedom of the recoiling nucleus.

For the purpose of transport theory, it is practical to condense the information encoded by the scattering cross sections into a **macroscopic scattering cross section**,

$$\Sigma_s(\boldsymbol{r}, E', t) = \sum_{i=1}^{I} \rho_i(\boldsymbol{r}, t)\, \sigma_{s,i}(E'), \tag{2.11}$$

a **macroscopic scattering multiplicity**,

$$\nu_s(\boldsymbol{r}, E', t) = \frac{1}{\Sigma_s(\boldsymbol{r}, E', t)} \sum_{i=1}^{I} \rho_i(\boldsymbol{r}, t)\, \sigma_{s,i}(E')\, \nu_{s,i}(E') \tag{2.12}$$

and a **scattering kernel**,

$$\begin{aligned} &f_s(\boldsymbol{r}, \hat{\boldsymbol{\Omega}}' \to \hat{\boldsymbol{\Omega}}, E' \to E, t) \\ &\qquad = \frac{1}{\nu_s(\boldsymbol{r}, E', t)\Sigma_s(\boldsymbol{r}, E', t)} \sum_{i=1}^{I} \rho_i(\boldsymbol{r}, t) \frac{\mathrm{d}^3\sigma_{s,i}}{\mathrm{d}^2\hat{\boldsymbol{\Omega}}\, \mathrm{d}E}(\hat{\boldsymbol{\Omega}}' \to \hat{\boldsymbol{\Omega}}, E' \to E), \end{aligned} \tag{2.13}$$

which is easily verified to be normalized:

$$\int f_s(\boldsymbol{r}, \hat{\boldsymbol{\Omega}}' \to \hat{\boldsymbol{\Omega}}, E' \to E, t)\, \mathrm{d}^2\hat{\boldsymbol{\Omega}}\, \mathrm{d}E = 1.$$

Armed with these definitions, we can write the contribution of scattering to the production density as

$$C_{3,s} = \int \nu_s(\boldsymbol{r}, E', t)\, \Sigma_s(\boldsymbol{r}, E', t)\, f_s(\boldsymbol{r}, \hat{\boldsymbol{\Omega}}' \to \hat{\boldsymbol{\Omega}}, E' \to E, t)\, \varphi(\boldsymbol{r}, \hat{\boldsymbol{\Omega}}', E', t)\, \mathrm{d}^2\hat{\boldsymbol{\Omega}}'\, \mathrm{d}E'. \tag{2.14}$$

Fission

Fission can *almost* be described using the same formalism as scattering, as defined by Eqs. (2.11) to (2.13). However, a few important differences in the phenomenology suggest the use of a slightly different parametrization. Additionally, in many reactor-physics problems, fission plays a peculiar role, and it is necessary to formally distinguish it from the other scattering processes. The formalism described in this section only concerns neutron-induced fission.

Like scattering, fission is usually characterized by a **macroscopic fission cross section**

$$\Sigma_f(\boldsymbol{r}, E', t) = \sum_{i=1}^{I} \rho_i(\boldsymbol{r}, t) \sigma_{f,i}(\boldsymbol{r}, E', t),$$

representing the number of fission events per unit incident flux. Unlike scattering, fission neutrons may not emerge instantly from the collision. Neutrons that are produced immediately after fission (within very short delays of the order of a picosecond at most) are termed **prompt fission neutrons**. In a fraction of the events, neutrons are observed to emerge with much longer delays, ranging from a few milliseconds to a few seconds; these are called **delayed fission neutrons**.

Let us focus on prompt neutrons first. In reality, the number of neutrons emitted in a fission event may fluctuate from one event to another. The neutron energy distributions depend on the fissioning isotope and the energy of the incoming neutron, but also on the actual neutron multiplicity of the event; the energies of neutrons emitted during the same fission event are also correlated by the dynamics of fission. Luckily, for the purpose of establishing an equation for the neutron flux, it is not necessary to take this complexity into account, and it is sufficient to consider the differential cross section for the production of prompt neutrons, which we decompose as a product

$$\frac{\mathrm{d}^3\sigma_{fp,i}}{\mathrm{d}^2\hat{\mathbf{\Omega}}\,\mathrm{d}E}(\hat{\mathbf{\Omega}}' \to \hat{\mathbf{\Omega}}, E' \to E) = \nu_{p,i}(E') f_{p,i}(\hat{\mathbf{\Omega}}' \to \hat{\mathbf{\Omega}}, E' \to E),$$

where:

- $\nu_{p,i}(E')$ is the **average multiplicity of prompt neutrons**;
- $f_{p,i}(\hat{\mathbf{\Omega}}' \to \hat{\mathbf{\Omega}}, E' \to E)$ is the (normalized) **prompt fission spectrum**, which represents the energy-angle distribution of prompt neutrons emerging from fission.

Since fission is often isotropic, the angular distribution of the prompt neutrons is often written in a simpler form, with a slight abuse of notation:

$$f_{p,i}(\hat{\mathbf{\Omega}}' \to \hat{\mathbf{\Omega}}, E' \to E) = \frac{1}{4\pi} f_{p,i}(E' \to E).$$

Here $f_{p,i}(E' \to E)$ is the energy distribution of the prompt fission neutrons.

Inspired by the definitions given for scattering in the previous section, we introduce a **macroscopic prompt-neutron multiplicity**

$$\nu_p(\boldsymbol{r}, E', t) = \frac{1}{\Sigma_f(\boldsymbol{r}, E', t)} \sum_{i=1}^{I} \rho_i(\boldsymbol{r}, t)\, \sigma_{f,i}(E')\, \nu_{p,i}(E')$$

and a **prompt-fission kernel**

$$f_p(\boldsymbol{r}, \hat{\mathbf{\Omega}}' \to \hat{\mathbf{\Omega}}, E' \to E, t) = \frac{1}{\nu_p(\boldsymbol{r}, E', t)\Sigma_f(\boldsymbol{r}, E', t)} \sum_{i=1}^{I} \rho_i(\boldsymbol{r}, t)\nu_{p,i}(E') f_{p,i}(\hat{\mathbf{\Omega}}' \to \hat{\mathbf{\Omega}}, E' \to E),$$

which, like the scattering kernel, is normalized. We can now write the contribution of prompt fission neutrons to the production density as

$$C_{3,p} = \int \nu_p(\boldsymbol{r}, E', t)\, \Sigma_f(\boldsymbol{r}, E', t)\, f_p(\boldsymbol{r}, \hat{\mathbf{\Omega}}' \to \hat{\mathbf{\Omega}}, E' \to E, t)\, \varphi(\boldsymbol{r}, \hat{\mathbf{\Omega}}', E', t)\, \mathrm{d}^2\hat{\mathbf{\Omega}}'\, \mathrm{d}E', \tag{2.15}$$

which is formally identical to the expression of the scattering contribution. Eq. (2.14).

Let us turn now turn to delayed neutrons. The phenomenology of the emission of delayed neutrons is quite complex and involves the occasional evaporation of neutrons from fission fragments that de-excite along their decay path towards the stability valley. The nuclear data used in reactor physics take a pragmatic stance and model the emission of delayed neutrons as the (exponential) decay of fictitious nuclei, called **delayed-neutron precursors**, that are

assumed to be produced by fission. Precursors are grouped into *families*, each family being characterized by its own decay constant.

Let J be the number of precursor families[2]. We define a few important quantities:

- $c_j(\boldsymbol{r}, t)$ ($j = 1, \ldots, J$) is the **density** of precursors of the j-th family;
- $\nu_{d,ji}(E')$ is the average multiplicity of precursors of the j-th family produced by fission of the i-th isotope induced by a neutron of energy E';
- $\nu_{d,j}(\boldsymbol{r}, E', t)$ is the **macroscopic precursor multiplicity** for the j-th family:

$$\nu_{d,j}(\boldsymbol{r}, E', t) = \frac{1}{\Sigma_f(\boldsymbol{r}, E', t)} \sum_{i=1}^{I} \rho_i(\boldsymbol{r}, t)\, \sigma_{f,i}(E')\, \nu_{d,ji}(E')$$

- λ_j is the exponential **decay constant** for the j-th family[3].
- $f_{d,j}(E)$ is the **delayed-neutron spectrum**, i.e. the energy distribution of delayed neutrons emitted from the decay of precursors of the j-th family. The angular distribution is assumed to be isotropic.

We are already in a position to write the contribution of delayed neutrons to the production term:

$$C_{3,d} = \sum_{j=1}^{J} \lambda_j c_j(\boldsymbol{r}, t) \frac{f_{d,j}(E)}{4\pi}. \tag{2.16}$$

We need to complement this equation with an equation for the precursor density c_j. If we assume that precursors do not migrate[4], the differential equation that governs the evolution of c_j is rather straightforward:

$$\frac{\partial c_j}{\partial t}(\boldsymbol{r}, t) = -\lambda_j\, c_j(\boldsymbol{r}, t) + \int \nu_{d,j}(\boldsymbol{r}, E', t)\, \Sigma_f(\boldsymbol{r}, E', t)\, \varphi(\boldsymbol{r}, \hat{\boldsymbol{\Omega}}', E', t)\, \mathrm{d}^2\hat{\boldsymbol{\Omega}}'\, \mathrm{d}E' + Q_{c,j}(\boldsymbol{r}, t). \tag{2.17}$$

In this equation, the first term on the right-hand side represents the exponential decay of the precursor population; the second term represents the production of precursors from fission; finally, the third term represents an external source of precursors.

2.2.4 External source term

The final term of the balance equation is an external source term, which can simply be written as

$$C_4 = Q_n(\boldsymbol{r}, \hat{\boldsymbol{\Omega}}, E, t). \tag{2.18}$$

[2] At the time of writing, nuclear-data libraries typically use six or eight families.

[3] We assume that the precursor decay constant are independent of the fissioning nuclide. This follows the choice made by the JEFF-3.3 library for the major actinides (Plompen et al. 2020). Other nuclear-data libraries, such as ENDF/B-VIII.0 (D. A. Brown et al. 2018), use decay constants that depend on the fissioning nuclide. This simplification is not a major restriction for the formalism developed in this chapter. Additionally, the decay constant can in principle depend on the energy of the neutron that induces fission, although this possibility is rarely exploited in nuclear-data libraries.

[4] Note for example that it is necessary to account for migration of precursors in systems with liquid fuel.

2.2.5 The Boltzmann transport equation

We can express the conservation law of the number of particles by equating the net sum of all the contributions to zero. The balance equation for the particle density n reads

$$\frac{\partial n}{\partial t}(\boldsymbol{r}, \hat{\boldsymbol{\Omega}}, E, t) + C_1 + C_2 = C_{3,s} + C_{3,p} + C_{3,d} + C_4,$$

with the terms C_i given by Eqs. (2.9), (2.10), (2.14) to (2.16) and (2.18). Note that C_1 and C_2 conventionally appear on the left-hand side of the equation because they represent particle losses. By substituting the expressions of C_i, we finally obtain the **time-dependent Boltzmann transport equation** with precursors:

$$\begin{aligned}
&\frac{1}{v}\frac{\partial \varphi}{\partial t}(\boldsymbol{r}, \hat{\boldsymbol{\Omega}}, E, t) + \hat{\boldsymbol{\Omega}} \cdot \nabla \varphi(\boldsymbol{r}, \hat{\boldsymbol{\Omega}}, E, t) + \Sigma_t(\boldsymbol{r}, E, t)\, \varphi(\boldsymbol{r}, \hat{\boldsymbol{\Omega}}, E, t) \\
&\quad = \int \nu_s(\boldsymbol{r}, E', t)\, \Sigma_s(\boldsymbol{r}, E', t)\, f_s(\boldsymbol{r}, \hat{\boldsymbol{\Omega}}' \to \hat{\boldsymbol{\Omega}}, E' \to E, t)\, \varphi(\boldsymbol{r}, \hat{\boldsymbol{\Omega}}', E', t)\, \mathrm{d}^2\hat{\boldsymbol{\Omega}}'\, \mathrm{d}E' \\
&\quad + \int \nu_p(\boldsymbol{r}, E', t)\, \Sigma_f(\boldsymbol{r}, E', t)\, f_p(\boldsymbol{r}, \hat{\boldsymbol{\Omega}}' \to \hat{\boldsymbol{\Omega}}, E' \to E, t)\, \varphi(\boldsymbol{r}, \hat{\boldsymbol{\Omega}}', E', t)\, \mathrm{d}^2\hat{\boldsymbol{\Omega}}'\, \mathrm{d}E' \\
&\qquad\qquad + \sum_{j=1}^{J} \lambda_j c_j(\boldsymbol{r}, t) \frac{f_{d,j}(E)}{4\pi} + Q_n(\boldsymbol{r}, \hat{\boldsymbol{\Omega}}, E, t). \quad (2.19)
\end{aligned}$$

This equation must be complemented by initial conditions on the particle flux and the precursor densities, of the form

$$\varphi(\boldsymbol{r}, \hat{\boldsymbol{\Omega}}, E, t = 0) = \varphi_0(\boldsymbol{r}, \hat{\boldsymbol{\Omega}}, E) \quad (2.20a)$$

$$c_j(\boldsymbol{r}, t = 0) = c_j^0(\boldsymbol{r}). \quad (2.20b)$$

Equations (2.17) and (2.19), taken together, form a system of linear, non-homogeneous integro-differential equations for the angular flux, which is a function of seven variables, and the precursor densities, which are functions of four variables.

A word needs to be spent about the choice of the normalization for Eqs. (2.17) and (2.19). Let us assume an infinite system ($\boldsymbol{r} \in \mathbb{R}^3$). The most natural conditions to impose are of the L_1 class, that is: we require that the precursor populations are finite

$$\int |c_j(\boldsymbol{r}, t)|\, \mathrm{d}^3\boldsymbol{r} < \infty,$$

and that the total flux in the system is finite:

$$\int |\varphi(\boldsymbol{r}, \hat{\boldsymbol{\Omega}}, E, t)|\, \mathrm{d}^3\boldsymbol{r}\, \mathrm{d}^2\hat{\boldsymbol{\Omega}}\, \mathrm{d}E < \infty. \quad (2.21)$$

However, it would seem equally natural to require that the total neutron population be finite instead:

$$\int \frac{1}{v} |\varphi(\boldsymbol{r}, \hat{\boldsymbol{\Omega}}, E, t)|\, \mathrm{d}^3\boldsymbol{r}\, \mathrm{d}^2\hat{\boldsymbol{\Omega}}\, \mathrm{d}E < \infty, \quad (2.22)$$

or that the total collision rate be finite:

$$\int \Sigma_t(\boldsymbol{r}, E, t) |\varphi(\boldsymbol{r}, \hat{\boldsymbol{\Omega}}, E, t)|\, \mathrm{d}^3\boldsymbol{r}\, \mathrm{d}^2\hat{\boldsymbol{\Omega}}\, \mathrm{d}E < \infty. \quad (2.23)$$

These different choices are equivalent to the definition of different vector spaces for our unknown functions. In practical matters, the choice between Eq. (2.21), (2.22) and (2.23) is of little consequence, because nuclear data are anyway only available between a finite minimum and a finite maximum energy and the total cross section is usually bounded. Under these conditions, all the normalization conditions above are equivalent.

We conclude this section by stressing the fact that Eq. (2.19) is easily applicable to photon transport, with a few caveats. First, fission does not play such an important role in photon transport as it does in neutron transport; of course photons can multiply in collisions, but they do not gain energy in the process. Thus, these phenomena are usually treated as scattering. Second, delayed emission of photons exists (fluorescence is a form of delayed photon emission; fission products also emit delayed photons), but in reactor physics applications delayed photons play a less important role than delayed neutrons, which are crucial for determining the dynamical response of nuclear reactors at equilibrium.

2.3 Variations over the theme of the Boltzmann equation

In this section, we will explore some common (and some less common) variations over the main theme established by Eq. (2.19).

2.3.1 α-eigenvalue equation

Let us start by considering a system without any external source ($Q_n = Q_{c,j} = 0$) and assuming that all the cross sections and multiplicities are independent of time. Can such a system admit stationary (i.e. time-independent) solutions in general[5]? Intuitively, the answer should be no. For example, let us imagine a system where neutrons can only scatter or be captured, but never multiply (i.e. no fissile material is present). In such a system, it is clear that the size of the neutron population is doomed to decrease over time. If we suppress the external source term, the neutron population cannot possibly remain stable.

There are several ways to transform the time-dependent Boltzmann equation without an external source in such a way that the dependence on the time variable is removed. The first attempt (and probably the most natural one to a physicist) would be to apply the method of separation of variables. Following Betzler et al. (2012), we seek solutions of the form

$$\varphi(\boldsymbol{r}, \hat{\boldsymbol{\Omega}}, E, t) = T(t)\, \varphi(\boldsymbol{r}, \hat{\boldsymbol{\Omega}}, E) \tag{2.24a}$$

$$c_j(\boldsymbol{r}, t) = T(t)\, c_j(\boldsymbol{r}). \tag{2.24b}$$

Substituting these ansätze into Eqs. (2.17) and (2.19) and separating the variables yields the following equations for $T(t)$ and $c_j(\boldsymbol{r})$:

$$\frac{\mathrm{d}T}{\mathrm{d}t}(t) = \alpha T(t) \tag{2.25}$$

$$c_j(\boldsymbol{r}) = \frac{1}{\alpha + \lambda_j} \int \nu_{d,j}(\boldsymbol{r}, E')\, \Sigma_f(\boldsymbol{r}, E')\, \varphi(\boldsymbol{r}, \hat{\boldsymbol{\Omega}}', E')\, \mathrm{d}^2\hat{\boldsymbol{\Omega}}'\, \mathrm{d}E'.$$

[5] By "in general" we mean "for arbitrary choices of the cross sections and multiplicities".

We substitute the expression for $c_j(\boldsymbol{r})$ in the equation for $\varphi(\boldsymbol{r}, \hat{\boldsymbol{\Omega}}, E)$ and we obtain

$$\begin{aligned}
&\frac{\alpha}{v}\varphi(\boldsymbol{r}, \hat{\boldsymbol{\Omega}}, E) + \hat{\boldsymbol{\Omega}} \cdot \nabla\varphi(\boldsymbol{r}, \hat{\boldsymbol{\Omega}}, E) + \Sigma_t(\boldsymbol{r}, E)\, \varphi(\boldsymbol{r}, \hat{\boldsymbol{\Omega}}, E) \\
&\qquad = \int \nu_s(\boldsymbol{r}, E')\, \Sigma_s(\boldsymbol{r}, E')\, f_s(\boldsymbol{r}, \hat{\boldsymbol{\Omega}}' \to \hat{\boldsymbol{\Omega}}, E' \to E)\, \varphi(\boldsymbol{r}, \hat{\boldsymbol{\Omega}}', E')\, \mathrm{d}^2\hat{\boldsymbol{\Omega}}'\, \mathrm{d}E' \\
&\qquad + \int \nu_p(\boldsymbol{r}, E')\, \Sigma_f(\boldsymbol{r}, E')\, f_p(\boldsymbol{r}, \hat{\boldsymbol{\Omega}}' \to \hat{\boldsymbol{\Omega}}, E' \to E)\, \varphi(\boldsymbol{r}, \hat{\boldsymbol{\Omega}}', E')\, \mathrm{d}^2\hat{\boldsymbol{\Omega}}'\, \mathrm{d}E' \\
&\qquad\quad + \sum_{j=1}^{J} \frac{\lambda_j}{\alpha + \lambda_j} \frac{f_{d,j}(E)}{4\pi} \int \nu_{d,j}(\boldsymbol{r}, E')\, \Sigma_f(\boldsymbol{r}, E')\, \varphi(\boldsymbol{r}, \hat{\boldsymbol{\Omega}}', E')\, \mathrm{d}^2\hat{\boldsymbol{\Omega}}'\, \mathrm{d}E' \qquad (2.26)
\end{aligned}$$

This long equation is known as the α-**eigenvalue equation**. It is a linear integro-differential eigenvalue equation for the angular flux, φ; it is however non-linear in the eigenvalue α.

The physical meaning of α is very straightforward: as Eq. (2.25) indicates, solutions to the α-eigenvalue problem have a time dependence of the form

$$T(t) \propto \exp(\alpha t).$$

Therefore, α is the inverse of the exponential time constant. Unfortunately, it is not a generalized eigenvalue equation because it is not possible to cast it into the conventional form

$$\boldsymbol{A}\varphi = \lambda \boldsymbol{B}\varphi,$$

where $\boldsymbol{A}$ and $\boldsymbol{B}$ are linear operators acting on φ and λ would be some function of α. Moreover, the study of the spectral properties of Eq. (2.26) is somewhat complicated by the fact that the delayed-fission term is clearly discontinuous at $\alpha = -\lambda_j$. For these reasons, the analysis of the theoretical aspects of Eq. (2.26) is limited to simple systems or to systems without delayed neutrons ($\lambda_j = 0$) (Duderstadt and Martin 1979; Larsen 1979; Larsen and Zweifel 1974). Finally, translating Eq. (2.26) into an algorithm that can be efficiently solved with numerical methods is possible, but difficult.

For all these reasons, the use of Eq. (2.26) is somewhat uncommon in nuclear engineering.

2.3.2 k-eigenvalue equation

Again, we assume no external source ($Q_n = Q_{c,j} = 0$) and time-independent cross sections and multiplicities. Starting from Eq. (2.17), we remark that it is possible to write a formal solution to this equation by using the method of the integrating factor, i.e. as a convolution of the source term with the Green's function:

$$c_j(\boldsymbol{r}, t) = \int_{-\infty}^{t} \exp\left(\lambda_j(t' - t)\right) \int \nu_{d,j}(\boldsymbol{r}, E')\, \Sigma_f(\boldsymbol{r}, E')\, \varphi(\boldsymbol{r}, \hat{\boldsymbol{\Omega}}', E', t')\, \mathrm{d}^2\hat{\boldsymbol{\Omega}}'\, \mathrm{d}E'\, \mathrm{d}t'. \qquad (2.27)$$

Substituting Eq. (2.27) into Eq. (2.19) yields

$$\begin{aligned}
&\frac{1}{v}\frac{\partial\varphi}{\partial t}(\boldsymbol{r},\hat{\boldsymbol{\Omega}},E,t)+\hat{\boldsymbol{\Omega}}\cdot\nabla\varphi(\boldsymbol{r},\hat{\boldsymbol{\Omega}},E,t)+\Sigma_t(\boldsymbol{r},E)\,\varphi(\boldsymbol{r},\hat{\boldsymbol{\Omega}},E,t)\\
&\qquad=\int\nu_s(\boldsymbol{r},E')\,\Sigma_s(\boldsymbol{r},E')\,f_s(\boldsymbol{r},\hat{\boldsymbol{\Omega}}'\to\hat{\boldsymbol{\Omega}},E'\to E)\,\varphi(\boldsymbol{r},\hat{\boldsymbol{\Omega}}',E',t)\,\mathrm{d}^2\hat{\boldsymbol{\Omega}}'\,\mathrm{d}E'\\
&\qquad+\int\nu_p(\boldsymbol{r},E')\,\Sigma_f(\boldsymbol{r},E')\,f_p(\boldsymbol{r},\hat{\boldsymbol{\Omega}}'\to\hat{\boldsymbol{\Omega}},E'\to E)\,\varphi(\boldsymbol{r},\hat{\boldsymbol{\Omega}}',E',t)\,\mathrm{d}^2\hat{\boldsymbol{\Omega}}'\,\mathrm{d}E'\\
&\qquad\qquad+\sum_{j=1}^{J}\lambda_j\frac{f_{d,j}(E)}{4\pi}\int_{-\infty}^{t}\exp\left(\lambda_j(t'-t)\right)\\
&\qquad\qquad\int\nu_{d,j}(\boldsymbol{r},E')\,\Sigma_f(\boldsymbol{r},E')\,\varphi(\boldsymbol{r},\hat{\boldsymbol{\Omega}}',E',t')\,\mathrm{d}^2\hat{\boldsymbol{\Omega}}'\,\mathrm{d}E'\,\mathrm{d}t'. \quad (2.28)
\end{aligned}$$

Clearly, just like Eqs. (2.17) and (2.19), this equation cannot generally admit a time-independent solution. However, a stationary solution may exist for some very specific sets of cross sections and multiplicities. Intuitively, a stationary solution will exist if the number of neutrons produced by fission and scattering exactly compensate the losses due to leakage and absorption.

This remark suggests that it should be possible to transform Eq. (2.28) into a stationary equation by rescaling one of the production terms, all the production terms, or the absorption term. The most common choice, by far, is to rescale the fission terms. We introduce the **multiplication factor** k and we replace all occurrences of Σ_f with Σ_f/k in Eq. (2.28). This yields an equation of the form

$$\begin{aligned}
&\hat{\boldsymbol{\Omega}}\cdot\nabla\varphi(\boldsymbol{r},\hat{\boldsymbol{\Omega}},E)+\Sigma_t(\boldsymbol{r},E)\,\varphi(\boldsymbol{r},\hat{\boldsymbol{\Omega}},E)\\
&\qquad=\int\nu_s(\boldsymbol{r},E')\,\Sigma_s(\boldsymbol{r},E')\,f_s(\boldsymbol{r},\hat{\boldsymbol{\Omega}}'\to\hat{\boldsymbol{\Omega}},E'\to E)\,\varphi(\boldsymbol{r},\hat{\boldsymbol{\Omega}}',E')\,\mathrm{d}^2\hat{\boldsymbol{\Omega}}'\,\mathrm{d}E'\\
&\qquad+\frac{1}{k}\int\nu(\boldsymbol{r},E')\,\Sigma_f(\boldsymbol{r},E')\,f_f(\boldsymbol{r},\hat{\boldsymbol{\Omega}}'\to\hat{\boldsymbol{\Omega}},E'\to E)\,\varphi(\boldsymbol{r},\hat{\boldsymbol{\Omega}}',E')\,\mathrm{d}^2\hat{\boldsymbol{\Omega}}'\,\mathrm{d}E', \quad (2.29)
\end{aligned}$$

where we have introduced the **total fission multiplicity**

$$\nu(\boldsymbol{r},E')=\nu_p(\boldsymbol{r},E')+\nu_d(\boldsymbol{r},E')$$

and the **fission kernel**

$$\begin{aligned}
&f_f(\boldsymbol{r},\hat{\boldsymbol{\Omega}}'\to\hat{\boldsymbol{\Omega}},E'\to E)\\
&\qquad=\frac{1}{\nu(\boldsymbol{r},E')}\left[\nu_p(\boldsymbol{r},E')f_p(\boldsymbol{r},\hat{\boldsymbol{\Omega}}'\to\hat{\boldsymbol{\Omega}},E'\to E)+\nu_d(\boldsymbol{r},E')\sum_{j=1}^{J}\frac{f_{d,j}(E)}{4\pi}\right].
\end{aligned}$$

Equation (2.29) is known as the k**-eigenvalue equation**. To the extent of my knowledge, the analysis of the spectral properties of this equation has not been carried out in complete generality. In some special cases, such as one-speed transport with isotropic scattering in a slab or a sphere, it has been shown that the spectrum has an infinite number of discrete real eigenvalues, and it is bounded from above (Bell and Glasstone 1970). On physical grounds, however, it is commonly assumed that the set of eigenvalues is bounded from above in real part by a real eigenvalue. The largest eigenvalue is usually denoted as k_{eff} and it is called

the **effective multiplication factor** or the **fundamental eigenvalue** of the system. It is also assumed that the associated eigenfunction, which is determined up to a global factor because of the linearity of Eq. (2.29), can be normalized to be real and non-negative everywhere in phase space.

2.4 Integral formulation

It is time to introduce a more convenient notation for the equations defined in the previous sections. We will now embark on a quest to rewrite all the integro-differential equations above in integral form.

2.4.1 Flight operator

Let us start by considering this extremely simplified version of the Boltzmann transport equation, Eq. (2.19):

$$\frac{1}{v}\frac{\partial\varphi}{\partial t}(\boldsymbol{r},\hat{\boldsymbol{\Omega}},E,t)+\hat{\boldsymbol{\Omega}}\cdot\nabla\varphi(\boldsymbol{r},\hat{\boldsymbol{\Omega}},E,t)+\Sigma_t(\boldsymbol{r},E,t)\,\varphi(\boldsymbol{r},\hat{\boldsymbol{\Omega}},E,t)=Q_n(\boldsymbol{r},\hat{\boldsymbol{\Omega}},E,t). \quad (2.30)$$

This equation described the propagation of neutrons produced by an external source Q_n, travelling in straight lines with speed v until they are absorbed by the medium, which has a macroscopic total cross section Σ_t. Note that Eq. (2.30) is parametric in $\hat{\boldsymbol{\Omega}}$ and E, so we can temporarily suppress these variables from our notation (but we will reinstate them later).

If Eq. (2.30) holds everywhere, then in particular it holds along the line of flight of a particle (also called the **characteristic**), which is described by the parametric equations

$$\begin{aligned}\boldsymbol{r}' &= \boldsymbol{r}+\hat{\boldsymbol{\Omega}}s\\ t' &= t+\frac{s}{v}.\end{aligned}$$

We evaluate Eq. (2.30) along the characteristic to obtain

$$\begin{aligned}\frac{1}{v}\frac{\partial\varphi}{\partial t}\left(\boldsymbol{r}+\hat{\boldsymbol{\Omega}}s,t+\frac{s}{v}\right)+\hat{\boldsymbol{\Omega}}\cdot\nabla\varphi\left(\boldsymbol{r}+\hat{\boldsymbol{\Omega}}s,t+\frac{s}{v}\right)\\ +\Sigma_t\left(\boldsymbol{r}+\hat{\boldsymbol{\Omega}}s,t+\frac{s}{v}\right)\,\varphi\left(\boldsymbol{r}+\hat{\boldsymbol{\Omega}}s,t+\frac{s}{v}\right)=Q_n\left(\boldsymbol{r}+\hat{\boldsymbol{\Omega}}s,t+\frac{s}{v}\right). \quad (2.31)\end{aligned}$$

Now we observe that the first two terms are simply the total derivative of the angular flux along the characteristic:

$$\frac{1}{v}\frac{\partial\varphi}{\partial t}\left(\boldsymbol{r}+\hat{\boldsymbol{\Omega}}s,t+\frac{s}{v}\right)+\hat{\boldsymbol{\Omega}}\cdot\nabla\varphi\left(\boldsymbol{r}+\hat{\boldsymbol{\Omega}}s,t+\frac{s}{v}\right)=\frac{\mathrm{d}}{\mathrm{d}s}\left[\varphi\left(\boldsymbol{r}+\hat{\boldsymbol{\Omega}}s,t+\frac{s}{v}\right)\right].$$

This simplifies Eq. (2.31) to read

$$\begin{aligned}\frac{\mathrm{d}}{\mathrm{d}s}\left[\varphi\left(\boldsymbol{r}+\hat{\boldsymbol{\Omega}}s,t+\frac{s}{v}\right)\right]+\Sigma_t\left(\boldsymbol{r}+\hat{\boldsymbol{\Omega}}s,t+\frac{s}{v}\right)\,\varphi\left(\boldsymbol{r}+\hat{\boldsymbol{\Omega}}s,t+\frac{s}{v}\right)\\ =Q_n\left(\boldsymbol{r}+\hat{\boldsymbol{\Omega}}s,t+\frac{s}{v}\right).\end{aligned}$$

This equation is of the form

$$\frac{\mathrm{d}g}{\mathrm{d}s}(s) + a(s)g(s) = b(s)$$

and it can be solved by applying the method of the integrating factor to yield

$$g(s) = \int_{s_0}^{s} e^{-\int_{s'}^{s} a(s'')\mathrm{d}s''} b(s')\,\mathrm{d}s' + g(s_0),$$

for any s_0. If we assume that no flux is present in the system at times sufficiently far in the past, we can let s_0 go to $-\infty$ and drop the term $g(s_0)$. The solution to Eq. (2.31) can then be written as

$$\varphi\Big(\boldsymbol{r} + \hat{\boldsymbol{\Omega}}\, s, t + \frac{s}{v}\Big) = \int_{-\infty}^{s} e^{-\int_{s'}^{s} \Sigma_t\left(\boldsymbol{r}+\hat{\boldsymbol{\Omega}}\, s'', t+\frac{s''}{v}\right)\mathrm{d}s''} Q_n\left(\boldsymbol{r} + \hat{\boldsymbol{\Omega}}\, s', t + \frac{s'}{v}\right)\mathrm{d}s'.$$

Evaluating at $s = 0$, reinstating the missing variables and rearranging, we find

$$\varphi(\boldsymbol{r}, \hat{\boldsymbol{\Omega}}, E, t) = \int_{0}^{\infty} e^{-\int_{0}^{s'} \Sigma_t\left(\boldsymbol{r}-\hat{\boldsymbol{\Omega}}\, s'', E, t-\frac{s''}{v}\right)\mathrm{d}s''} Q_n\left(\boldsymbol{r} - \hat{\boldsymbol{\Omega}}\, s', \hat{\boldsymbol{\Omega}}, E, t - \frac{s'}{v}\right)\mathrm{d}s', \quad (2.32)$$

which is the formal solution to Eq. (2.30). This equation expresses the angular flux at position $\boldsymbol{r}$ and time t as the superposition of contributions from the source term at previous times and other positions along the characteristic, weighted by the exponential attenuation factor. The quantity that appears in the exponent,

$$\rho(\boldsymbol{r}, \hat{\boldsymbol{\Omega}}, E, t, s') = \int_{0}^{s'} \Sigma_t\left(\boldsymbol{r} - \hat{\boldsymbol{\Omega}}\, s'', E, t - \frac{s''}{v}\right)\mathrm{d}s'',$$

is known as the **optical length** seen by a particle travelling a distance s' from $\boldsymbol{r}$.

Although Eq. (2.32) is perfectly acceptable, it is more common in certain literature (for example Lux and Koblinger 2018) to rewrite it for the collision density ψ_n:

$$\begin{aligned}&\psi_n(\boldsymbol{r}, \hat{\boldsymbol{\Omega}}, E, t)\\ &\quad = \Sigma_t(\boldsymbol{r}, E, t) \int_{0}^{\infty} e^{-\int_{0}^{s'} \Sigma_t\left(\boldsymbol{r}-\hat{\boldsymbol{\Omega}}\, s'',, E, t-\frac{s''}{v}\right)\mathrm{d}s''} Q_n\left(\boldsymbol{r} - \hat{\boldsymbol{\Omega}}\, s', \hat{\boldsymbol{\Omega}}, E, t - \frac{s'}{v}\right)\mathrm{d}s' \quad (2.33)\end{aligned}$$

This equation shows that it is possible to regard the collision density as the result of the action of a linear operator $\boldsymbol{T}_n$ on the source term Q_n. The operator acts on a vector space of functions of seven real variables, $(\boldsymbol{r}, \hat{\boldsymbol{\Omega}}, E, t)$. It is called the **neutron flight operator** and it is defined as

$$\begin{aligned}&(\boldsymbol{T}_n\, g)(\boldsymbol{r}, \hat{\boldsymbol{\Omega}}, E, t)\\ &\quad = \Sigma_t(\boldsymbol{r}, E, t) \int_{0}^{\infty} e^{-\int_{0}^{s'} \Sigma_t\left(\boldsymbol{r}-\hat{\boldsymbol{\Omega}}\, s'', E, t-\frac{s''}{v}\right)\mathrm{d}s''} g\left(\boldsymbol{r} - \hat{\boldsymbol{\Omega}}\, s', \hat{\boldsymbol{\Omega}}, E, t - \frac{s'}{v}\right)\mathrm{d}s'. \quad (2.34)\end{aligned}$$

With this definition, Eq. (2.33) can be rewritten in shorthand form as

$$\psi_n = \boldsymbol{T}_n\, Q_n. \quad (2.35)$$

The same treatment can be applied to the precursor evolution equation, Eq. (2.17). To start, we neglect the delayed fission term, and we simplify the equation to read

$$\frac{\partial c_j}{\partial t}(\boldsymbol{r},t) + \lambda_j\, c_j(\boldsymbol{r},t) = Q_{c,j}(\boldsymbol{r},t). \tag{2.36}$$

By applying the method of the integrating factor and assuming no precursor in the system at times sufficiently far in the past, we can write the solution to Eq. (2.36) in integral form as

$$c_j(\boldsymbol{r},t) = \int_0^\infty e^{-\lambda_j t''}\, Q_{c,j}(\boldsymbol{r},t-t'')\,\mathrm{d}t''. \tag{2.37}$$

This leads us to introduce the **precursor decay density**

$$\psi_{c,j}(\boldsymbol{r},t) = \lambda_j\, c_j(\boldsymbol{r},t)$$

and the **precursor flight operator** $\boldsymbol{T}_{c,j}$

$$(\boldsymbol{T}_{c,j}\, g)(\boldsymbol{r},t) = \lambda_j \int_0^\infty e^{-\lambda_j t''}\, g(\boldsymbol{r},t')\mathrm{d}t'', \tag{2.38}$$

which acts on the vector space of functions of four real variables, $(\boldsymbol{r},t)$. With this notation, Eq. (2.37) reads

$$\psi_{c,j} = \boldsymbol{T}_{c,j}\, Q_{c,j}. \tag{2.39}$$

It is of course a bit silly to talk about precursor *flights*, because precursors do not actually move at all in our model. However, in a more general setting, precursors may actually move or diffuse; the precursor flight operator would then account for any displacement of the precursor between its creation site and its decay site.

2.4.2 Emission density

Equations (2.30) and (2.36) are simplified versions of respectively the full Boltzmann equation, Eq. (2.19), and the precursor evolution equation, Eq. (2.17). In spite of this, the flight operators defined by Eqs. (2.34) and (2.38) are very useful for representing the solutions to the full equations. Indeed, Eq. (2.30) has the form of the full Boltzmann equation, provided that one formally replaces Q_n with the **neutron emission density**:

$$\begin{aligned}
&\chi_n(\boldsymbol{r},\hat{\boldsymbol{\Omega}}',E',t)\\
&\quad= \int \frac{\nu_s(\boldsymbol{r},E',t)\,\Sigma_s(\boldsymbol{r},E',t)}{\Sigma_t(\boldsymbol{r},E',t)}\, f_s(\boldsymbol{r},\hat{\boldsymbol{\Omega}}'\to\hat{\boldsymbol{\Omega}},E'\to E,t)\,\psi_n(\boldsymbol{r},\hat{\boldsymbol{\Omega}}',E',t)\,\mathrm{d}^2\hat{\boldsymbol{\Omega}}'\,\mathrm{d}E'\\
&\quad+ \int \frac{\nu_p(\boldsymbol{r},E',t)\,\Sigma_f(\boldsymbol{r},E',t)}{\Sigma_t(\boldsymbol{r},E',t)}\, f_p(\boldsymbol{r},\hat{\boldsymbol{\Omega}}'\to\hat{\boldsymbol{\Omega}},E'\to E,t)\,\psi_n(\boldsymbol{r},\hat{\boldsymbol{\Omega}}',E',t)\,\mathrm{d}^2\hat{\boldsymbol{\Omega}}'\,\mathrm{d}E'\\
&\qquad\qquad+ \sum_{j=1}^{J} \frac{f_{d,j}(E)}{4\pi}\psi_{c,j}(\boldsymbol{r},t) + Q_n(\boldsymbol{r},\hat{\boldsymbol{\Omega}},E,t).
\end{aligned}$$

The formal developments leading to Eq. (2.35) remain unchanged and one finds

$$\psi_n = \boldsymbol{T}_n\, \chi_n. \tag{2.40}$$

Contrary to Eq. (2.35), however, this equation does not represent the solution to the Boltzmann equation in closed form, because the emission density χ_n depends on the precursor decay densities $\psi_{c,j}$ and on the collision density ψ_n itself. Therefore, Eq. (2.40) is actually an integral equation for the collision density and the precursor decay densities.

By applying similar tricks to the precursor evolution equation, Eq. (2.17), we obtain

$$\psi_{c,j} = \boldsymbol{T}_{c,j}\, \chi_{c,j}, \tag{2.41}$$

which is formally identical to Eq. (2.39), except that the source term $Q_{c,j}$ has been replaced by the **precursor emission density**

$$\chi_{c,j}(\boldsymbol{r}, t) = \int \frac{\nu_{d,j}(\boldsymbol{r}, E', t)\, \Sigma_f(\boldsymbol{r}, E', t)}{\Sigma_t(\boldsymbol{r}, E', t)}\, \psi_n(\boldsymbol{r}, \hat{\boldsymbol{\Omega}}', E', t)\, \mathrm{d}^2\hat{\boldsymbol{\Omega}}'\, \mathrm{d}E' + Q_{c,j}(\boldsymbol{r}, t),$$

which is a function of the collision density ψ_n. Thus, Eq. (2.41) represents a set of J integral equations for the precursor decay densities $\psi_{c,j}$. Equations (2.40) and (2.41), taken together, are equivalent to the set of $J+1$ integro-differential equations defined by Eqs. (2.17) and (2.19).

2.4.3 Collision operator

The integral equations (2.40) and (2.41) look deceptively simple, because we have succeeded at hiding part of the pain involved in the definition of the flight operators. However, the definitions of the emission densities χ_n and $\chi_{c,j}$ are still cumbersome. We will now rewrite these definitions too in a deceptively simple form.

The idea is simply to regard the emission densities as the result of the action of linear operators on the collision and decay densities. We introduce the **scattering operator**

$$\begin{aligned}&(\boldsymbol{S}\, g)(\boldsymbol{r}, \hat{\boldsymbol{\Omega}}, E, t)\\ &\quad = \int \frac{\nu_s(\boldsymbol{r}, E', t)\, \Sigma_s(\boldsymbol{r}, E', t)}{\Sigma_t(\boldsymbol{r}, E', t)}\, f_s(\boldsymbol{r}, \hat{\boldsymbol{\Omega}}' \to \hat{\boldsymbol{\Omega}}, E' \to E, t)\, g(\boldsymbol{r}, \hat{\boldsymbol{\Omega}}', E', t)\, \mathrm{d}^2\hat{\boldsymbol{\Omega}}'\, \mathrm{d}E',\end{aligned}$$

the **prompt fission operator**

$$\begin{aligned}&(\boldsymbol{F}_p\, g)(\boldsymbol{r}, \hat{\boldsymbol{\Omega}}, E, t)\\ &\quad = \int \frac{\nu_p(\boldsymbol{r}, E', t)\, \Sigma_f(\boldsymbol{r}, E', t)}{\Sigma_t(\boldsymbol{r}, E', t)}\, f_p(\boldsymbol{r}, \hat{\boldsymbol{\Omega}}' \to \hat{\boldsymbol{\Omega}}, E' \to E, t)\, g(\boldsymbol{r}, \hat{\boldsymbol{\Omega}}', E', t)\, \mathrm{d}^2\hat{\boldsymbol{\Omega}}'\, \mathrm{d}E',\end{aligned}$$

the **prompt collision operator**

$$\boldsymbol{C}_p = \boldsymbol{S} + \boldsymbol{F}_p,$$

the **precursor production operator**

$$\begin{aligned}&(\boldsymbol{P}_{d,j}\, g)(\boldsymbol{r}, t)\\ &\qquad = \int \frac{\nu_{d,j}(\boldsymbol{r}, E', t)\, \Sigma_f(\boldsymbol{r}, E', t)}{\Sigma_t(\boldsymbol{r}, E', t)}\, g(\boldsymbol{r}, \hat{\boldsymbol{\Omega}}', E', t)\, \mathrm{d}^2\hat{\boldsymbol{\Omega}}'\, \mathrm{d}E',\end{aligned}$$

and the **precursor decay operators**

$$(\boldsymbol{D}_j\, g)(\boldsymbol{r}, \hat{\boldsymbol{\Omega}}, E, t) = \frac{f_{d,j}(E)}{4\pi} g(\boldsymbol{r}, t).$$

With this notation, we can write the Boltzmann equation and the decay equations for the precursors (Eqs. (2.17) and (2.19)) in the remarkably compact form

$$\psi_n = \boldsymbol{T}_n \, \chi_n \tag{2.42a}$$
$$\psi_{c,j} = \boldsymbol{T}_{c,j} \, \chi_{c,j} \tag{2.42b}$$
$$\chi_n = \boldsymbol{C}_p \, \psi_n + \sum_{j=1}^{J} \boldsymbol{D}_j \, \psi_{c,j} + Q_n \tag{2.42c}$$
$$\chi_{c,j} = \boldsymbol{P}_{d,j} \, \psi_n + Q_{c,j}. \tag{2.42d}$$

Interestingly, the notation used in Eq. (2.42) is sufficiently powerful to allow us to concisely express other forms of the transport equation. For instance, the integral equivalent of the condensed transport equation, Eq. (2.28), can be recovered by substituting $\psi_{c,j}$ from Eq. (2.42b) and $\chi_{c,j}$ from Eq. (2.42d) into Eq. (2.42c), yielding

$$\psi_n = \boldsymbol{T}_n \, \chi_n \tag{2.43a}$$
$$\chi_n = \boldsymbol{C} \, \psi_n + Q_{\chi_n}, \tag{2.43b}$$

where we have introduced the **collision operator**

$$\begin{aligned} \boldsymbol{C} &= \boldsymbol{C}_p + \sum_{j=1}^{J} \boldsymbol{D}_j \, \boldsymbol{T}_{c,j} \, \boldsymbol{P}_{d,j} \\ &= \boldsymbol{S} + \boldsymbol{F}, \end{aligned}$$

the **fission operator**

$$\boldsymbol{F} = \boldsymbol{F}_p + \sum_{j=1}^{J} \boldsymbol{F}_{d,j},$$

the **delayed fission operators**

$$\boldsymbol{F}_{d,j} = \boldsymbol{D}_j \, \boldsymbol{T}_{c,j} \, \boldsymbol{P}_{d,j},$$

and the **neutron emission source**

$$Q_{\chi_n} = Q_n + \sum_{j=1}^{J} \boldsymbol{D}_j \, \boldsymbol{T}_{c,j} \, Q_{c,j}.$$

If we assume $Q = 0$, we can repeat the argument made in the derivation of Eq. (2.28). It is clear here that, in general, Eq. (2.43) only admit the trivial solution $\psi_n = \chi_n = 0$, which is the same conclusion we reached in Section 2.3.2 above.

As another example, it is also rather common to write Eq. (2.42) in the following form, which only involves the emission densities:

$$\chi_n = \boldsymbol{C}_p \, \boldsymbol{T}_n \, \chi_n + \sum_{j=1}^{J} \boldsymbol{D}_j \, \boldsymbol{T}_{c,j} \, \chi_{c,j} + Q_n \tag{2.44a}$$
$$\chi_{c,j} = \boldsymbol{P}_{d,j} \, \boldsymbol{T}_n \, \chi_n + Q_{c,j}. \tag{2.44b}$$

These equations are obtained by substituting Eqs. (2.42a) and (2.42b) in (2.42c) and (2.42d). Similarly, the standalone form for the collision densities reads

$$\psi_n = \boldsymbol{T}_n \boldsymbol{C}_p \psi_n + \sum_{j=1}^{J} \boldsymbol{T}_n \boldsymbol{D}_j \psi_{c,j} + \boldsymbol{T}_n Q_n \tag{2.45a}$$

$$\psi_{c,j} = \boldsymbol{T}_{c,j} \boldsymbol{P}_{d,j} \psi_n + \boldsymbol{T}_{c,j} Q_{c,j}. \tag{2.45b}$$

It is again possible to condense these systems of equations down to a single equation for a single unknown function. From Eq. (2.44), the equation for the neutron emission density reads

$$\chi_n = \boldsymbol{C}\boldsymbol{T}_n \chi_n + Q_{\chi_n}. \tag{2.46}$$

From Eq. (2.45), the equation for the neutron collision density reads

$$\psi_n = \boldsymbol{T}_n \boldsymbol{C} \psi_n + Q_{\psi_n}, \tag{2.47}$$

with

$$Q_{\psi_n} = \boldsymbol{T}_n Q_{\chi_n}.$$

Finally, we can use our new compact notation to rewrite the k-eigenvalue equation, Eq. (2.29). If we restrict our functional space to time-independent functions, most of our operator definitions are unaffected, because they act locally in time. The only operator that is non-local in time is the precursor flight operator $\boldsymbol{T}_{c,j}$, defined by Eq. (2.38), which simplifies to the identity when restricted to time-independent functions. Thus, the fission operator simplifies to

$$\boldsymbol{F} = \boldsymbol{F}_p + \sum_{j=1}^{J} \boldsymbol{D}_j \boldsymbol{P}_{d,j},$$

and the k-eigenvalue equation can be written in integral form as

$$\psi_n = \boldsymbol{T}\chi_n \tag{2.48a}$$

$$\chi_n = \left(\boldsymbol{S} + \frac{\boldsymbol{F}}{k}\right) \psi_n, \tag{2.48b}$$

where the n subscripts on operators have been omitted for the sake of conciseness. This system of integral equations for χ_n and ψ_n can be further condensed into one integral equation for either function by applying simple algebraic manipulations. For instance, by replacing χ_n in Eq. (2.48a) with its definition in Eq. (2.48b), we obtain the following equation for ψ_n:

$$\psi_n = \boldsymbol{T}\left(\boldsymbol{S} + \frac{\boldsymbol{F}}{k}\right) \psi_n. \tag{2.49}$$

In spite of all the effort that has gone into molding the integro-differential form of (2.17) and (2.19) into the integral shape of Eq. (2.42), we have not made one inch of progress towards the *solution* of these equations. However, the integral formulation provides the natural theoretical tools to analyze the properties of the Monte Carlo method, which will be outlined in Chapter 3.

2.4.4 Form of the integral kernels

Among the operators that we have introduced, some of them (like $\boldsymbol{T}_n$ or $\boldsymbol{S}$) map functions of seven variables $(\boldsymbol{r}, \hat{\boldsymbol{\Omega}}, E, t)$ to functions of the seven variables; some ($\boldsymbol{P}_{d,j}$) map functions of seven variables to functions of four variables $(\boldsymbol{r}, t)$; some ($\boldsymbol{D}_j$) map functions of four variables to functions of seven variables; and, finally, some ($\boldsymbol{T}_{c,j}$) map functions of four variables to functions of four variables. This means that we are working with at least two different functional spaces: one for neutron densities and one for precursor densities.

It may be convenient to embed the space of precursor densities in the space of neutron densities. Simply put, we can regard precursor densities as neutron densities with extra (dummy) direction and energy variables. The integral operators become endomorphisms of the unified functional space and all of them can be expressed in a common form, i.e.

$$(\boldsymbol{O}\, g)(P') = \int O(P, P') g(P)\, \mathrm{d}P.$$

Here we have introduced the shorthand notation $P = (\boldsymbol{r}, \hat{\boldsymbol{\Omega}}, E, t)$, $P' = (\boldsymbol{r}', \hat{\boldsymbol{\Omega}}', E', t')$, and integrals are understood to extend over the whole phase space:

$$\int \mathrm{d}P = \int \mathrm{d}^3\boldsymbol{r}\, \mathrm{d}^2\hat{\boldsymbol{\Omega}}\, \mathrm{d}E\, \mathrm{d}t.$$

The function $O(P, P')$ is known as the **integral kernel** associated to operator $\boldsymbol{O}$. In the best (or worst?) tradition of nuclear engineering, we play fast and loose with functional analysis without ironing out the formal details.

As an example of this notation, we provide the expression of the **neutron flight kernel**:

$$T_n(P, P') = \Sigma_t(\boldsymbol{r}', E', t') \exp\left[- \int_0^{|\boldsymbol{r}-\boldsymbol{r}'|} \Sigma_t\Big(\boldsymbol{r}' - \hat{\boldsymbol{\Omega}}\, s, E', t' - \frac{s}{v}\Big)\, \mathrm{d}s \right] \cdot \frac{\delta(\hat{\boldsymbol{\Omega}} - \frac{\boldsymbol{r}-\boldsymbol{r}'}{|\boldsymbol{r}-\boldsymbol{r}'|})}{|\boldsymbol{r} - \boldsymbol{r}'|^2} \cdot \delta(\hat{\boldsymbol{\Omega}} - \hat{\boldsymbol{\Omega}}') \cdot \delta(E - E') \cdot \delta\left(t - t' - \frac{|\boldsymbol{r} - \boldsymbol{r}'|}{v}\right). \quad (2.50)$$

This approach may seem unnecessarily clumsy at the moment, but it will prove its worth in due time (see Chapter 8).

2.5 Adjoint transport equation

For the sake of concreteness, let us now restrict our attention to the space of time-independent functions and let us consider the integral form of the k-eigenvalue equation, Eq. (2.48), which we rewrite here for the convenience of the Reader:

$$\begin{aligned} \psi &= \boldsymbol{T}\, \chi \\ \chi &= \left(\boldsymbol{S} + \frac{\boldsymbol{F}}{k}\right) \psi. \end{aligned}$$

2.5.1 Mathematical definition of the adjoint operators

Let us denote by $\mathcal{B}$ the functional space where ψ and χ live. If we impose a normalization condition of the L_1 type, like we discussed in Section 2.2.5, then $\mathcal{B}$ is a Banach space, but not a Hilbert space; that is, there is no natural definition of a scalar product (also known as an inner product) between functions. This point is sometimes overlooked in textbooks about transport theory (Bell and Glasstone 1970; Duderstadt and Martin 1979; Prinja and Larsen 2010), which define adjoint operators by introducing the inner product between two functions.

A more principled way to introduce adjoint operators is to consider the *dual* vector space $\mathcal{B}^*$ of our Banach space $\mathcal{B}$. The dual space is defined as the space of **continuous linear functionals** over $\mathcal{B}$, i.e. continuous linear maps from $\mathcal{B}$ to the reals; the term **covector** is also used. For concreteness, let $\boldsymbol{A} : \mathcal{B} \to \mathcal{B}$ denote a linear operator on our functional space, $f \in \mathcal{B}$ a generic function in its domain and $g^\dagger \in \mathcal{B}^*$ a generic linear functional. We use the notation $\langle g^\dagger, f \rangle$ to denote the action of the linear functional $g^\dagger$ on f; by the definition given above, $\langle g^\dagger, f \rangle$ is a real number. The adjoint operator $\boldsymbol{A}^\dagger$ is the[6] linear operator on $\mathcal{B}^*$ defined by the identity

$$\langle \boldsymbol{A}^\dagger g^\dagger, f \rangle = \langle g^\dagger, \boldsymbol{A} f \rangle \qquad \forall f \in \mathcal{B}.$$

In order to relate this definition to the usual introduction of adjoint operators of nuclear engineering textbooks, we need to invoke the Riesz-Markov-Kakutani representation theorem (Theorem 6.19 in Rudin 2013), which essentially states that any linear functional $g^\dagger \in \mathcal{B}^*$ can be represented as a unique regular Borel measure $\mathrm{d}\mu_g$, in the sense that

$$\langle g^\dagger, f \rangle = \int_{\mathbb{R}^n} f(P)\, \mathrm{d}\mu_g \qquad \forall f \in \mathcal{B}.$$

By a traditional abuse of notation, the integration against the Borel measure is usually written as

$$\langle g^\dagger, f \rangle = \int_{\mathbb{R}^n} f(P)\, g(P)\, \mathrm{d}P \qquad \forall f \in \mathcal{B}. \tag{2.51}$$

for some generalized function g, which may of course be a Dirac delta or any other sort of mathematical curiosity; it can be shown that $g(P)$ is a regular function if and only if $g^\dagger$ is bounded (or, equivalently, continuous) (Theorem 6.16 in Rudin 2013). By the same token, the action of $g^\dagger$ on f, represented by Eq. (2.51), is usually referred to as "the scalar product of $g(P)$ and $f(P)$" in transport theory textbooks.

When $g^\dagger$ is represented by a regular function $g(P)$, the integral in Eq. (2.51) is simply a Lebesgue integral over $\mathbb{R}^n$. It is clear, however, that the functional space that $g(P)$ lives in is not the same as $\mathcal{B}$. For instance, if we choose $\mathcal{B} = L_p(\mathbb{R}^n)$, then the convergence of the integral in Eq. (2.51) requires that g must be in $L_q(\mathbb{R}^n)$, with $q = p/(p-1)$; in particular, in the common case of $\mathcal{B} = L_1(\mathbb{R}^n)$, g must be in $L_\infty(\mathbb{R}^n)$.

Thus, we have stated the fundamental result: given a linear operator $\boldsymbol{O}$ on $L_p(\mathbb{R}^n)$, its **adjoint** $\boldsymbol{O}^\dagger$ is defined as the linear operator on $L_q(\mathbb{R}^n)$ ($q = p/(p-1)$) that satisfies the identity

$$\int_{\mathbb{R}^n} (\boldsymbol{O} f)(P)\, g(P)\, \mathrm{d}P = \int_{\mathbb{R}^n} f(P)\, (\boldsymbol{O}^\dagger g)(P)\, \mathrm{d}P. \tag{2.52}$$

[6] The mathematical definition requires much more attention to technical details. The interested Reader is invited to consult Kreyszig (1989).

In the notation of Section 2.4.4, it is remarkably simple to express the action of the adjoint operators. Let $\boldsymbol{O}$ be characterized by a kernel $O(P, P')$, i.e.

$$(\boldsymbol{O}\, f)(P') = \int O(P, P')\, f(P)\, \mathrm{d}P.$$

It is easy to show, by inverting the order of the integrals in Eq. (2.52), that the adjoint operator $\boldsymbol{O}^\dagger$ admits the integral representation

$$(\boldsymbol{O}^\dagger g)(P) = \int O(P, P')\, g(P')\, \mathrm{d}P';$$

in other words, the kernel $O^\dagger(P, P')$ of the adjoint operator $\boldsymbol{O}^\dagger$ is simply

$$O^\dagger(P, P') = O(P', P).$$

In particular, all the linear operators that we defined above, such as the flight operators, collision operators, etc., define corresponding adjoint operators. Given for example the form of the integral kernel for the neutron flight operator $\boldsymbol{T}_n$, Eq. (2.50), we can also regard it as the functional form of the kernel of the adjoint neutron flight operator $\boldsymbol{T}_n^\dagger$, provided that we exchange the roles of P and P'.

The adjoint flight and collision operators define a set of **adjoint transport equations**. For example, the fixed-source adjoint problem is

$$\chi^\dagger = \boldsymbol{T}^\dagger\, \psi^\dagger \tag{2.53a}$$

$$\psi^\dagger = \boldsymbol{C}^\dagger\, \chi^\dagger + Q^\dagger_{\psi^\dagger}. \tag{2.53b}$$

and the adjoint k-eigenvalue problem is

$$\chi^\dagger = \boldsymbol{T}^\dagger\, \psi^\dagger \tag{2.54a}$$

$$\psi^\dagger = \left(\boldsymbol{S}^\dagger + \frac{\boldsymbol{F}^\dagger}{k^\dagger}\right) \chi^\dagger. \tag{2.54b}$$

These equations should be compared to Eqs. (2.43) and (2.48). Note that we have used $k^\dagger$ for the eigenvalue in Eq. (2.54), to distinguish it from the eigenvalue k of Eq. (2.48). Like for Eq. (2.48), it is assumed that Eq. (2.54) admit a real dominant eigenvalue, and that the associated dominant eigenvector can be normalized to be real and non-negative everywhere in phase space.

Suppose now that ψ and χ are solutions of Eq. (2.48) with eigenvalue k. Likewise, let $\psi^\dagger$ and $\chi^\dagger$ be solutions of Eq. (2.54) with eigenvalue $k^\dagger$. By taking the scalar product of Eq. (2.48a) with $\psi^\dagger$, taking the scalar product of Eq. (2.48b) with $\chi^\dagger$ and summing, we obtain

$$\left\langle \psi^\dagger, \psi \right\rangle + \left\langle \chi^\dagger, \chi \right\rangle = \left\langle \psi^\dagger, \boldsymbol{T}\, \chi \right\rangle + \left\langle \chi^\dagger, \left(\boldsymbol{S} + \frac{\boldsymbol{F}}{k}\right) \psi \right\rangle.$$

Similarly, if we take the scalar product of Eq. (2.54a) with χ and the scalar product of Eq. (2.54b) with ψ, we find

$$\left\langle \chi^\dagger, \chi \right\rangle + \left\langle \psi^\dagger, \psi \right\rangle = \left\langle \boldsymbol{T}^\dagger \psi^\dagger, \chi \right\rangle + \left\langle \left(\boldsymbol{S}^\dagger + \frac{\boldsymbol{F}^\dagger}{k^\dagger}\right) \chi^\dagger, \psi \right\rangle.$$

Subtracting and using Eq. (2.52), we can conclude that

$$\left(\frac{1}{k} - \frac{1}{k^\dagger}\right) \left\langle \chi^\dagger, \boldsymbol{F}\, \psi \right\rangle = 0.$$

Therefore, either $k = k^\dagger$ or $\left\langle \chi^\dagger, \boldsymbol{F}\, \psi \right\rangle = 0$. In other words, either direct and adjoint eigenvectors share the same eigenvalue, or they are "orthogonal", in the sense of $\left\langle \chi^\dagger, \boldsymbol{F}\, \psi \right\rangle = 0$. In the particular case of the dominant eigenvectors of Eqs. (2.48) and (2.54), the scalar product cannot vanish because ψ and $\chi^\dagger$ are non-negative everywhere in phase space. Therefore, Eqs. (2.48) and (2.54) have the same dominant eigenvalue, k_{eff}.

2.6 Transport equations for charged particles

So far, we have only concerned ourselves with the formalism for the transport of electrically neutral particles. Most of the mathematical aspects of the formalism still apply to charged particles, but the phenomenology is sensibly different. Charged particles (defined as electrons or atomic nuclei for the purpose of this document) are tightly coupled with the atomic electrons of the medium that they traverse. The electromagnetic interaction can lead to **elastic scattering** of the charged particle off the atomic nuclei or the electrons of the medium. Inelastic collisions are also possible, and typically involve the **excitation** of the atomic electrons or the **ionization** of the atom; in some cases (high energy, light particles) inelastic collisions may also involve the emission of **bremsstrahlung** photons.

The distinguishing feature of charged-particle transport is that electromagnetic interactions with the electrons of the medium are characterized by very large cross sections, typically several orders of magnitude larger than the largest cross sections involved in neutron transport. For the sake of illustration, let us compare the largest cross sections involved in neutron transport with the smallest cross sections involved in electron transport. The total cross section for the $n + {}^{235}\text{U}$ reaction at 25 meV is of the order of 700 b (D. A. Brown et al. 2018; Plompen et al. 2020), which results in a mean free path of about 300 µm in uranium with 100 % ${}^{235}\text{U}$ enrichment. For contrast, the interaction of a 1 MeV electron in water is characterized by a total cross section of about 1.2 Mb (1.2×10^6 b!) with the water molecule (Perkins et al. 1991), for a mean free path of the order of 250 nm. Thus, the cross sections for electron transport are at least three orders of magnitude larger than the largest cross sections involved in neutron transport. The ratio is even larger for lower energies and heavier materials.

In practice, let $\Sigma_s(\boldsymbol{r}, E, T, \mu)$ be the differential scattering cross section for a particle of energy E losing an amount of energy T and being deflected by an angle $\arccos \mu$ in a collision (azimuthal symmetry is assumed). The integral of the scattering cross section over all possible energy losses and angular deflections is the total scattering cross section:

$$\Sigma_s(\boldsymbol{r}, E) = 2\pi \int_0^E \mathrm{d}T \int_{-1}^1 \mathrm{d}\mu\, \Sigma_s(\boldsymbol{r}, E, T, \mu).$$

For incident electrons up to a few tens of MeV, the scattering cross section is essentially equal to the total cross section, i.e. absorption is negligible compared to scattering. The same remark holds for protons and ions; it is however worth stressing that reaction events, albeit rare, are catastrophic in nature because they may lead to the disappearance of the primary particle and to the conversion into other particle species. For the sake of illustration, the

reaction cross section for protons on ^{7}Li at 5 MeV is of the order of 500 mb (with (p, n) being the only open inelastic channel at this energy). This is completely negligible with respect to the atomic excitation and ionization cross sections for a 5 MeV proton in lithium, which are of the same order of magnitude as the electron cross sections above (tens to hundreds of kb) (Paul and Sacher 1989). However, the $^7\mathrm{Li}(p, n)$ cross section is the only open channel that leads to the production of neutrons at 5 MeV. Even if this process has a negligible impact on the energy and momentum loss of the primary proton, it is clearly of paramount importance for neutron production.

It is common to decompose the scattering cross section Σ_s as the sum of two components:

$$\Sigma_s(\boldsymbol{r}, E, T, \mu) = \Sigma_{s,\text{nucl}}(\boldsymbol{r}, E, T, \mu) + \Sigma_{s,\text{atom}}(\boldsymbol{r}, E, T, \mu).$$

The first term, $\Sigma_{s,\text{nucl}}$, represents the electromagnetic interaction of the particle with the atomic nucleus. For incident electrons and light ions, the amount of energy lost to scattering with a large atomic nucleus is very small because of the large mass difference. The second term, $\Sigma_{s,\text{atom}}$, describes the interactions of the particle with the atomic electrons. In many practical cases, the atomic cross section is sharply forward-peaked, even for incident electrons. This phenomenon is so pronounced that the reference data library for atomic electron cross sections, the Evaluated Electron Data Library (EEDL) (Perkins et al. 1991), provides separate evaluations for the total elastic cross section, integrated over $\mu \in [-1, 1]$, and the "large-angle" scattering cross section, integrated over $\mu \in [-1, 0.999999]$. In the common **straight-ahead approximation**, the atomic scattering cross section is written as

$$\Sigma_{s,\text{atom}}(\boldsymbol{r}, E, T, \mu) = \Sigma_{s,\text{atom}}(\boldsymbol{r}, E, T)\, \delta(\mu - 1). \tag{2.55}$$

Moreover, the typical energy loss in an atomic collision is of the order of the atomic binding energy (a few tens of eV), which is usually much smaller than the particle energy E.

2.6.1 The continuous slowing-down approximation

This example makes it clear that the number of collisions involved in the transport of charged particles is very large. However, most of the collisions actually result in very little energy and momentum transfer between the particle and the medium. This makes it possible to formulate effective transport theories where most (or all) of the "soft" particle-matter interactions are replaced with approximate continuous processes. As an example, we derive the continuous slowing-down approximation (CSDA), which amounts to replacing the energy loss due to elastic and inelastic particle-atom collisions with a continuous energy-loss process.

We start by writing out the integro-differential form of the stationary Boltzmann equation for electrons:

$$\begin{aligned}\hat{\boldsymbol{\Omega}} \cdot \nabla\varphi(\boldsymbol{r}, \hat{\boldsymbol{\Omega}}, E) + [\Sigma_{s,\text{atom}}(\boldsymbol{r}, E) + \Sigma_{s,\text{nucl}}(\boldsymbol{r}, E)]\, \varphi(\boldsymbol{r}, \hat{\boldsymbol{\Omega}}, E) \\ = C_{\text{atom}}(\boldsymbol{r}, E, \hat{\boldsymbol{\Omega}}) + C_{\text{nucl}}(\boldsymbol{r}, E, \hat{\boldsymbol{\Omega}}) + Q(\boldsymbol{r}, \hat{\boldsymbol{\Omega}}, E).\end{aligned} \tag{2.56}$$

Here $C_{\text{atom}}(\boldsymbol{r}, E, \hat{\boldsymbol{\Omega}})$ and $C_{\text{nucl}}(\boldsymbol{r}, E, \hat{\boldsymbol{\Omega}})$ are respectively the atomic and nuclear collision

terms:

$$C_{\text{atom}}(\boldsymbol{r}, E, \hat{\boldsymbol{\Omega}}) = \int \mathrm{d}E' \int \mathrm{d}^2\hat{\boldsymbol{\Omega}}'\, \Sigma_{s,\text{atom}}(\boldsymbol{r}, E', E'-E, \hat{\boldsymbol{\Omega}}'\cdot\hat{\boldsymbol{\Omega}})\, \varphi(\boldsymbol{r}, \hat{\boldsymbol{\Omega}}', E') \tag{2.57}$$

$$C_{\text{nucl}}(\boldsymbol{r}, E, \hat{\boldsymbol{\Omega}}) = \int \mathrm{d}E' \int \mathrm{d}^2\hat{\boldsymbol{\Omega}}'\, \Sigma_{s,\text{nucl}}(\boldsymbol{r}, E', E'-E, \hat{\boldsymbol{\Omega}}'\cdot\hat{\boldsymbol{\Omega}})\, \varphi(\boldsymbol{r}, \hat{\boldsymbol{\Omega}}', E'). \tag{2.58}$$

Inspired by Zheng-Ming and Brahme (1993), we make use of the following identity involving Fourier transforms:

$$f(E) = \frac{1}{2\pi} \int \mathrm{d}\omega\, e^{i\omega E} \int \mathrm{d}X\, e^{-i\omega X} f(X).$$

Applying this to Eq. (2.57), we obtain

$$C_{\text{atom}}(\boldsymbol{r}, E, \hat{\boldsymbol{\Omega}}) = \frac{1}{2\pi} \int \mathrm{d}\omega\, e^{i\omega E} \int \mathrm{d}X\, e^{-i\omega X} \int \mathrm{d}E' \int \mathrm{d}^2\hat{\boldsymbol{\Omega}}'\, \Sigma_{s,\text{atom}}(\boldsymbol{r}, E', E'-X, \hat{\boldsymbol{\Omega}}'\cdot\hat{\boldsymbol{\Omega}})\, \varphi(\boldsymbol{r}, \hat{\boldsymbol{\Omega}}', E').$$

We exchange the order of the integrals, and we change the integration variable from X to $T = E' - X$:

$$C_{\text{atom}}(\boldsymbol{r}, E, \hat{\boldsymbol{\Omega}}) = \frac{1}{2\pi} \int \mathrm{d}\omega\, e^{i\omega E} \int \mathrm{d}E'\, e^{-i\omega E'} \int \mathrm{d}^2\hat{\boldsymbol{\Omega}}'\, \varphi(\boldsymbol{r}, \hat{\boldsymbol{\Omega}}', E') \int \mathrm{d}T\, e^{i\omega T}\, \Sigma_{s,\text{atom}}(\boldsymbol{r}, E', T, \hat{\boldsymbol{\Omega}}'\cdot\hat{\boldsymbol{\Omega}}).$$

We now invoke the smallness of the energy transfer T by developing the $e^{i\omega T}$ term to first order in T:

$$e^{i\omega T} \simeq 1 + i\omega T. \tag{2.59}$$

Thus, the collision term is approximated as

$$C_{\text{atom}}(\boldsymbol{r}, E, \hat{\boldsymbol{\Omega}}) \simeq \frac{1}{2\pi} \int \mathrm{d}\omega\, e^{i\omega E} \int \mathrm{d}E'\, e^{-i\omega E'} \int \mathrm{d}^2\hat{\boldsymbol{\Omega}}'\, \varphi(\boldsymbol{r}, \hat{\boldsymbol{\Omega}}', E') \int \mathrm{d}T\, (1 + i\omega T)\, \Sigma_{s,\text{atom}}(\boldsymbol{r}, E', T, \hat{\boldsymbol{\Omega}}'\cdot\hat{\boldsymbol{\Omega}}),$$

which simplifies to

$$C_{\text{atom}}(\boldsymbol{r}, E, \hat{\boldsymbol{\Omega}}) = \int \mathrm{d}T \int \mathrm{d}^2\hat{\boldsymbol{\Omega}}' \left[\Sigma_{s,\text{atom}}(\boldsymbol{r}, E, T, \hat{\boldsymbol{\Omega}}'\cdot\hat{\boldsymbol{\Omega}})\, \varphi(\boldsymbol{r}, \hat{\boldsymbol{\Omega}}', E) + T\, \frac{\partial \left(\Sigma_{s,\text{atom}}(\boldsymbol{r}, E, T, \hat{\boldsymbol{\Omega}}'\cdot\hat{\boldsymbol{\Omega}})\, \varphi(\boldsymbol{r}, \hat{\boldsymbol{\Omega}}', E) \right)}{\partial E} \right].$$

If we now invoke Eq. (2.55), we can simplify this expression further to

$$C_{\text{atom}}(\boldsymbol{r}, E, \hat{\boldsymbol{\Omega}}) = \Sigma_{s,\text{atom}}(\boldsymbol{r}, E)\, \varphi(\boldsymbol{r}, \hat{\boldsymbol{\Omega}}, E) + \frac{\partial}{\partial E} \left(S_{\text{atom}}(\boldsymbol{r}, E)\, \varphi(\boldsymbol{r}, \hat{\boldsymbol{\Omega}}, E) \right), \tag{2.60}$$

where we have introduced the **atomic stopping power**

$$S_{\text{atom}}(\boldsymbol{r}, E) = 2\pi \int_0^E \mathrm{d}T \int_{-1}^1 \mathrm{d}\mu \, T \, \Sigma_{s,\text{atom}}(\boldsymbol{r}, E, T, \mu), \tag{2.61}$$

which represents the average energy loss of the primary particle per unit distance travelled.

Note that the first term of Eq. (2.60) is exactly the atomic collision density that appears on the left-hand side of Eq. (2.56). Thus, Eq. (2.56) may be rewritten as

$$\hat{\boldsymbol{\Omega}} \cdot \nabla \varphi(\boldsymbol{r}, \hat{\boldsymbol{\Omega}}, E) - \frac{\partial (S_{\text{atom}} \varphi)}{\partial E}(\boldsymbol{r}, \hat{\boldsymbol{\Omega}}, E) + \Sigma_{s,\text{nucl}}(\boldsymbol{r}, E)\, \varphi(\boldsymbol{r}, \hat{\boldsymbol{\Omega}}, E) = C_{\text{nucl}}(\boldsymbol{r}, E, \hat{\boldsymbol{\Omega}}) + Q(\boldsymbol{r}, \hat{\boldsymbol{\Omega}}, E). \tag{2.62}$$

This approximated form of the Boltzmann equation is much simpler to treat than Eq. (2.56): the problematic atomic collision term, which is characterized by extremely large cross sections, has been replaced by a much simpler differential term, which captures the average energy loss of the electron in atomic collisions and which represents a *continuous* change of the electron energy along its line of flight. The cross sections associated to the remaining nuclear collision term are not as large as atomic cross sections.

2.6.2 Going beyond the continuous slowing-down approximation

Equation (2.62) should really be regarded as only the starting point of an *efficient* and *accurate* theory of electron transport. There are a number of improvements that can be brought. First of all, the straight-ahead approximation introduced by Eq. (2.57) is rather crude. In reality, atomic collisions do introduce small angular deviations, especially for light particles. Collisions typically result in very small angular deviations, but they are extremely numerous. The cumulative effect of many small angular deviations is called **angular straggling** and it is described by a number of approximate models (Goudsmit and Saunderson 1940; Ivanchenko et al. 2010; H. W. Lewis 1950; Molière 1948; Urbàn 2002; E. J. Williams and Chadwick 1939).

Furthermore, the CSDA formalism revolves around the concept of stopping power, defined in Eq. (2.61), which is the average energy loss per unit distance travelled by the particle. The definition of stopping power can be seen as the first instance of a hierarchy of statistical moments that characterize the energy loss. In practice, the energy loss experienced by a particle over a certain flight path is subject to fluctuations around the average value described by the stopping power. This phenomenon is called **energy straggling**, and plays a major role in the determination of the distribution of the penetration depth for particles. Like for angular straggling, the effect of energy straggling is usually modelled, and different models address different regimes of particle transport (Blunck and Leisegang 1950; Landau 1944; Vavilov 1957).

Finally, atomic collisions may occasionally result in catastrophic events characterized by large scattering angles and/or energy losses. These events should be handled carefully because, despite their rare occurrence, they lead to very large changes in the energy and direction of the incident particle. This remark has motivated the formulation of "mixed" theories (Schneider and Cormack 1959), where catastrophic collisions are individualized, while soft collisions are treated collectively. The formulation of mixed theories is tightly connected with the emergence of Monte Carlo calculations for charged particles (Andreo and Brahme 1984; Berger et al. 1963).

For further details about the formulation of more sophisticated transport theories for charged particles, the interested Reader is invited to consult Andreo and Brahme (1984), Berger et al. (1963), Salvat (2015), and Zheng-Ming and Brahme (1993), as well as the references therein.

2.7 Non-linear variations over the theme of the Boltzmann equation

All the transport equations that we have analyzed so far, be it in integro-differential or integral form, are linear. In this section, we wish to briefly explore a few non-linear variations of the transport equation that are of some relevance for the rest of this manuscript.

2.7.1 Particle-particle collisions

First and foremost, the first transport equation, as formulated by Ludwig Boltzmann in his kinetic theory of gases (Boltzmann 1872), is non-linear. Boltzmann was concerned with the problem of writing an equation for the single-particle density of a gas of identical hard spheres of mass m and radius a moving in a box with perfectly reflecting walls. Following Uffink and Valente (2015), if we use $n(\boldsymbol{r},\boldsymbol{p},t)\,\mathrm{d}^3\boldsymbol{r}\,\mathrm{d}^3\boldsymbol{p}$ to denote the number of particles having position between $\boldsymbol{r}$ and $\boldsymbol{r}+\mathrm{d}^3\boldsymbol{r}$ and momentum between $\boldsymbol{p}$ and $\boldsymbol{p}+\mathrm{d}^3\boldsymbol{p}$, then Boltzmann's transport equation reads

$$\frac{\partial n}{\partial t}(\boldsymbol{r},\boldsymbol{p},t)+\frac{\boldsymbol{p}}{m}\cdot\nabla n(\boldsymbol{r},\boldsymbol{p},t)= \\ \frac{Na^2}{m}\int \mathrm{d}^3\boldsymbol{p}'\int_{(\boldsymbol{p}-\boldsymbol{p}')\cdot\hat{\boldsymbol{\omega}}\geq 0}\mathrm{d}^2\hat{\boldsymbol{\omega}}\,((\boldsymbol{p}-\boldsymbol{p}')\cdot\hat{\boldsymbol{\omega}})\left[n(\boldsymbol{r},\boldsymbol{p}_c,t)n(\boldsymbol{r},\boldsymbol{p}_c',t)-n(\boldsymbol{r},\boldsymbol{p},t)n(\boldsymbol{r},\boldsymbol{p}',t)\right]. \quad (2.63)$$

Here $\boldsymbol{p}$ and $\boldsymbol{p}'$ represent the momenta of the spheres that are about to collide, $\hat{\boldsymbol{\omega}}$ is the unit vector pointing from the center of the sphere having momentum $\boldsymbol{p}$ to the center of the sphere having momentum $\boldsymbol{p}'$, and $\boldsymbol{p}_c$ and $\boldsymbol{p}_c'$ are shortcut notations for the momenta after the collision, which are determined by the incoming momenta and the direction of closest approach as

$$\boldsymbol{p}_c=\boldsymbol{p}-((\boldsymbol{p}-\boldsymbol{p}')\cdot\hat{\boldsymbol{\omega}})\,\hat{\boldsymbol{\omega}} \\ \boldsymbol{p}_c'=\boldsymbol{p}+((\boldsymbol{p}-\boldsymbol{p}')\cdot\hat{\boldsymbol{\omega}})\,\hat{\boldsymbol{\omega}}.$$

The collision term of Eq. (2.63) is non-linear, because it involves the product of the single-particle density evaluated at different momenta, which represents the number of pairs of spheres that are just about to collide or have just emerged from a collision. More specifically, the quadratic form is a consequence of the assumption of molecular chaos (Boltzmann's famous *Stoßzahlansatz*) and the shape of the integral is related to the assumed kinematics of collisions between hard spheres.

In general, non-linear collision terms can be interpreted as approximated contributions from particle-particle collisions. Even though neutrons can scatter off other neutrons, no such term was included in the neutron transport equations outlined in this chapter; the justification for this is that neutron-neutron scattering is completely negligible compared to

neutron-nucleus scattering in ordinary matter. We can convince ourselves of this fact by a simple order-of-magnitude calculation. If we assume a neutron-neutron scattering length at low energy $a_{nn} = -18.6\,\text{fm}$ (Machleidt and Slaus 2001), we obtain a scattering cross section $\sigma_{nn} = 4\pi a_{nn}^2 = \simeq 43\,\text{b}$ for thermal neutrons. Given a thermal flux $\Phi \simeq 10^{14}\,\text{cm}^{-2}\,\text{s}^{-1}$ and a thermal velocity $v_{\text{th}} \simeq 10^3\,\text{cm}\,\text{s}^{-1}$, we can estimate the density of the neutron gas to be $\rho = \Phi/v_{\text{th}} \simeq 10^{11}\,\text{cm}^{-3}$. We find a "macroscopic cross section" for thermal neutrons moving in a thermal neutron gas of

$$\Sigma_{nn} = \frac{\sigma_{nn}\Phi}{v_{\text{th}}} \simeq 4 \times 10^{-12}\,\text{cm}^{-1},$$

which is about eight order of magnitudes smaller than the total macroscopic cross section for thermal neutrons in air (about $5 \times 10^{-4}\,\text{cm}^{-1}$).

For neutron-neutron collisions to be important, the neutron density needs to be much higher. One situation where this happens is in the atomic nucleus. In a ^{208}Pb nucleus, for example, 82 protons and 126 neutrons are packed in a sphere of roughly 6.5 fm radius. This corresponds to a nucleon density of the order of $\rho_{^{208}\text{Pb}} = 1.8 \times 10^{38}\,\text{cm}^{-3}$. For collisions of a thermal neutron with neutrons bound in nuclei, as a very rough approximation we can assume the cross section to be given by the neutron-proton total cross section at the Fermi energy (about 40 MeV), which is of the order of 0.2 b (D. A. Brown et al. 2018), yielding a mean free path in nuclear matter of the order of

$$\lambda = \frac{1}{\rho_{^{208}\text{Pb}}} \simeq 0.25\,\text{fm},$$

which is sensibly smaller than the nuclear radius. This goes to show that multiple interactions between nucleons in nuclear matter cannot be neglected. This point is at the basis of the nuclear reaction models that will be discussed in more detail in Chapter 5.

2.7.2 Physical feedbacks

There are other phenomena that can introduce non-linearities in the Boltzmann neutron transport equation. We have assumed so far that the macroscopic cross sections are given for the transport problem. In a nuclear reactor, however, the number of circulating neutrons is so large that their presence has macroscopic effects on matter. First, nuclear reactions are so numerous that they can sensibly modify the isotopic composition of the medium. Second, the power released by neutron-nucleus reactions (especially fission) is so large that it can affect the temperature of the medium. Both processes modify the macroscopic cross sections and make them dependent on the past history of the neutron population. An accurate model of depletion and thermal feedbacks is very important for practical applications of transport theory to nuclear reactors; the production of heat through fission, in particular, is really the *raison d'être* of many nuclear reactors. A detailed discussion of the algorithms and techniques involved in the solution of the non-linear problems arising from the different feedback mechanisms is outside the scope of this document; here we will limit ourselves to illustrating the emergence of non-linearity in the transport equation.

For the sake of concreteness, let us start by considering the evolution of the isotopic composition of the medium. As stipulated above, let $\rho_i(\boldsymbol{r}, t)$ be the concentration of the i-th nuclide at position $\boldsymbol{r}$ and time t. We need to allow for the possible presence of radioactive nuclides, so let us denote as $\lambda_{i\to j}$ the decay constant for a nucleus of species i to yield a nucleus

of another species j. Finally, let us write as $\tau_{i\to j}$ the rate of occurrence of neutron-induced reactions on nuclei of species i yielding nuclei of species j; we can write this quantity as the product of the scalar flux and a cross section:

$$\begin{aligned}\tau_{i\to j}(\boldsymbol{r},t) &= \int \Phi(\boldsymbol{r},E,t)\Sigma_{i\to j}(\boldsymbol{r},E,t)\mathrm{d}E \\ &= \left(\int \Phi(\boldsymbol{r},E,t)\sigma_{i\to j}(\boldsymbol{r},E,t)\mathrm{d}E\right)\cdot\rho_i(\boldsymbol{r},t),\end{aligned}$$

where the scalar flux has been defined in Eq. (2.5). The microscopic cross section $\sigma_{i\to j}$ may involve the sum of several reaction channels (for example (n,d) reactions and (n,pn) reactions lead to the production of the same residual nucleus).

A few remarks are in order. Note that our model assumes that the nucleus j is produced at the same position as the initial nucleus i, and that it does not migrate. This assumption may be violated if the reaction products can move through the medium, either because they are gaseous and can diffuse away, or because the medium is a liquid or a gas. If this is the case, we need to supplement our neutron transport equation with transport equations for the isotopes. Additionally, we are also neglecting the fact that the reaction products gain some recoil from the nuclear reaction; this is usually unimportant for fission products, which have micrometric ranges in ordinary matter, but it may be relevant for light reaction products such as protons or alpha particles.

We can write the rate of change of the concentration of the i-th nuclide as follows:

$$\frac{\partial\rho_i}{\partial t} = \sum_{j\neq i}\left[\left(\lambda_{j\to i}+\int\Phi\,\sigma_{j\to i}\,\mathrm{d}E\right)\rho_j - \left(\lambda_{i\to j}+\int\Phi\,\sigma_{i\to j}\,\mathrm{d}E\right)\rho_i\right],$$

where we have omitted the arguments of the functions for the sake of conciseness. These equations, in their simplest form, are due to Ernest Rutherford (Rutherford 1905) and are known as the **Bateman equations** (Bateman 1908). They involve the scalar flux Φ, which results from the solution of one of the Boltzmann transport equations (typically the k-eigenvalue equation, Eq. (2.29)). The Boltzmann equation, in turn, involve the macroscopic cross sections, which depend on the isotopic concentrations ρ_i. Therefore, the Boltzmann-Bateman equations must be regarded as a system of coupled non-linear equations for the neutron flux and the isotopic concentrations.

We conclude with a few words about the non-linearities that arise from temperature feedback. Most of the power deposited by neutrons in a nuclear reactor is located in the fuel, but heat is quickly transported outside the fuel and into the moderator/coolant. Even if heat diffusion is assumed to be linear in the source power (assuming constant material properties), and even if thermal-hydraulics is linearized, the cross sections are highly non-linear functions of the medium temperature, as we pointed out in Section 2.1.2. Therefore, the thermal feedback loop is much more intricate than the simple quadratic non-linearity of the Boltzmann-Bateman equations.

2.8 Non-Boltzmann observables and high-energy particle transport

The Boltzmann equation and the theory that we have sketched in this chapter have some limitations. First, the Boltzmann equation is an equation for the particle flux or the average

phase-space density of particles, i.e. the average number of particles contained in a given phase-space volume. The information contained in the particle flux or density, however, is not sufficient to describe any possible physical observable. For example, the probability that a particle deposits more than some given energy ΔE in a detector is not accessible via the Boltzmann equation; another example is the average of the square of the number of particles contained in a given phase-space volume. By convention, we call **Boltzmann observables** the physical quantities which can be deduced from the solution of the Boltzmann equation. The mathematical description of non-Boltzmann observables requires a more general theory.

Another limitation of the theory is that we have consistently assumed that the microscopic cross sections are given data for the problem at hand. In practice, this assumption is reasonable for neutrons and protons of energy lower than a few tens of MeV and for photons of energy lower than about 150 MeV (D. Brown et al. 2010; D. A. Brown et al. 2018; Plompen et al. 2020); luckily, this ranges cover all the energies of interest for nuclear reactor physics (see Section 4.1 for a more detailed discussion on this point). Above these energies, the number of open reaction channels becomes so large that measuring all the necessary experimental data and producing accurate evaluations for the differential cross sections becomes unfeasible. Thus, even though the theory is still correct at high energy, it is of no practical use because of the lack of elementary nuclear data.

Based on these remarks, one would probably expect that the solution of low-energy problems, on one side, and high-energy or non-Boltzmann problems, on the other side, should require quite different techniques. This is true only to a certain point; perhaps surprisingly, Monte Carlo is a very commonly used tool on either side of the divide. In the following chapter, we will present the basic ideas of Monte Carlo and how they relate to the solution of the Boltzmann equation at low energy. However, we will return to high-energy particle transport in Chapter 4 and discuss how Monte Carlo is actually much more than a solver for the Boltzmann transport equation.

The Monte Carlo method

3

If all other methods fail, a Monte Carlo calculation may be attempted.

Bell and Glasstone (1970)

In the previous chapter, we have shown that the Boltzmann equation for neutron transport can be cast in the form of a system of coupled integral equations. Depending on the specific problem considered, the equations are either inhomogeneous equations, as in Eq. (2.47),

$$\psi_n = \boldsymbol{T}_n \boldsymbol{C}\, \psi_n + Q_{\psi_n}, \tag{3.1}$$

or eigenvalue equations, as in Eq. (2.49):

$$\psi_n = \boldsymbol{T} \left(\boldsymbol{S} + \frac{\boldsymbol{F}}{k} \right) \psi_n. \tag{3.2}$$

Inhomogeneous equations like Eq. (3.1) are classified by mathematicians as **Fredholm equations of the second kind**. They have the general form

$$f = \alpha \boldsymbol{K} f + g, \tag{3.3}$$

where f and g are (possibly vector) function over some measure space[1], α is a (given) scalar, and $\boldsymbol{K}$ is an integral operator.

The Monte Carlo method provides a very natural way to solve Fredholm equations of the second kind. Besides allowing us to determine the unknown function f, the Monte Carlo method actually provides direct access to any linear functional over f, i.e. any quantity O of the form

$$O = \left\langle w_O^\dagger, f \right\rangle \tag{3.4}$$

for a given covector $w_O^\dagger$. As special cases, this class includes the value of f at some point P

$$O = f(P),$$

[1]Mathematicians tread carefully and only use the name "Fredholm equation" if the functions involved are defined over the real numbers. In this manuscript we will use the term more loosely, to refer to any integral equation of the form of Eq. (3.3).

the integral of f over some region V

$$O = \int_V f(P)\,\mathrm{d}P,$$

and the convolution of f with some **response function** η

$$O = \int f(P)\,\eta(P)\,\mathrm{d}P. \tag{3.5}$$

Any quantity that can be calculated by Monte Carlo is called an **observable**; in the spirit of the remarks made at the end of the previous chapter, observables of the form of Eq. (3.4) are called **Boltzmann observables**.

In this chapter we will present the main ideas of the Monte Carlo method for the solution of Fredholm equations of the second kind, and therefore of all linear integral transport equations derived in Chapter 2. Before diving into the methodological details, we need to make a quick digression into the mathematical theory of Monte Carlo, which is the subject of Section 3.1. Section 3.2 introduces the Liouville-Neumann series, which is both an important conceptual tool for the study of Fredholm equations and a commonly used numerical device to construct a solution. Its importance for Monte Carlo is demonstrated in Section 3.3. In the following sections we describe a few techniques for the construction of Monte Carlo games; in particular, Section 3.4 discusses the probabilistic interpretation of the source term of a Fredholm equation; Section 3.5 introduces the key concept of statistical weight; Section 3.6 shows how different forms of transition probabilities can be handled in this context. A concrete example of a Monte Carlo solution of a Fredholm equation of the second kind in presented in Section 3.8. We generalize the Monte Carlo approach to eigenvalue equations in Section 3.7. Finally, partial conclusions about Monte Carlo are drawn in Section 3.9.

We will assume that the Reader is familiar with the following items, which are the bread and butter of any Monte Carlo technique:

- pseudo-random number generators;
- sampling from simple one-dimensional distributions;
- computing integrals using Monte Carlo.

For a refresher on these topics and a deeper dive into the subject of this chapter, eager Readers are encouraged to consult Carter and Cashwell (1975), Lux and Koblinger (2018), and Spanier and Gelbard (2008), in this order.

3.1 Markov processes in less than two pages

The mathematical formulation of Monte Carlo involves the following main ingredients:

- a set of states;
- a Markov process;
- an estimator for each observable that we wish to calculate.

Let us go into each of these elements in detail.

3.1.1 Set of states

The set of states Π is the stage where Monte Carlo is performed. We do not wish to delve into the details of the mathematical structure that is required of the set of states; we limit ourselves to observe that the set of states can be discrete or continuous, finite or infinite. For particle transport, the set of states often (but not always!) coincides with the phase space of the system, which is parametrized by the particle position, direction of motion, energy and time, so that $\Pi = \mathbb{R}^7$ and states P are parameterized by $(\boldsymbol{r}, \hat{\boldsymbol{\Omega}}, E, t)$.

3.1.2 Definition of a Markov process

A Markov process is a specific type of stochastic process. Broadly speaking, a **stochastic process** is a set of rules that define **transitions** between system states. Transitions can be continuous or discrete, giving rise to continuous-time and discrete-time stochastic processes, respectively. More importantly, transitions are allowed to be *stochastic*, i.e. it is generally possible to reach more than one state (with various probabilities) in a single step. In this sense, stochastic processes can be seen as a generalization of (continuous or discrete) *dynamical systems*, for which the "next" state is uniquely determined by the current one. In a stochastic process, the "next" state is a random variable.

Inspired by the analogy with dynamical systems, we define a **history** to be any set of states sampled according to the rules of the process. This concept is basically an extension of the idea of *trajectory* of a dynamical system. However, while the initial conditions of a dynamical system uniquely determine its trajectory, many histories are possible for a given initial condition in a stochastic process, because of the stochastic nature of transitions.

Let us assume that we are sampling a history of our stochastic process, and let us call P the most recently visited state. In general, the probability to access another state P' from P is a function not only of P, but also of all the other previously visited states. In most (if not all) of the cases of interest for particle transport, however, transition probabilities depend only on the most recent state, P. This property is called the **Markov property**, after the name of the Russian mathematician Andrey Andreyevich Markov.

As an example, let us concentrate on discrete-time Markov processes. Such a process is uniquely specified by a conditional transition probabilities $\mathscr{P}(P'|P)$ and by a probability distribution $\mathscr{P}(P_0)$ for the initial state P_0. Given these ingredients, we can generate a history. We start by sampling[2] the initial state P_0 from $\mathscr{P}(P_0)$. The next state, P_1, is sampled from $\mathscr{P}(P_1|P_0)$; in general, the $(n+1)$-th state P_{n+1} of the process is obtained by sampling the distribution $\mathscr{P}(P_{n+1}|P_n)$. Any number of histories can be generated by repeating this process.

According to the description that we have given above, a history of a Markov process never really terminates; as soon as we reach a state P_n, we are urged to move forward to a new state P_{n+1}. It is however possible to model finite histories by formally extending the state space with an extra state P_{final}, with the proviso that the new state is "absorbing":

$$\begin{aligned} \mathscr{P}(P_{\text{final}}|P_{\text{final}}) &= 1 \\ \mathscr{P}(P|P_{\text{final}}) &= 0 \qquad \forall P \neq P_{\text{final}}. \end{aligned}$$

[2] We assume working knowledge of the techniques involved in random sampling of discrete and continuous variables. Keen Readers may refer to Spanier and Gelbard (2008) for a refresher.

In the extended model, $\mathscr{P}(P_{\text{final}}|P)$ represents the probability that the history ends at P. In practice, this formal extension is always implicitly understood and histories are allowed to have a finite length.

3.1.3 Estimators

Consider a history

$$\gamma = \{P_0, P_1, \ldots, P_{k-1}\};$$

since γ visits k states before terminating, it is an element of Π^k. If all histories eventually terminate (which we will assume), then the space of all possible histories is the union

$$\Gamma = \bigcup_{k=1}^{\infty} \Pi^k.$$

The generic history γ can be regarded as a random variable on Γ. Its probability distribution $\mathscr{P}(\gamma)$ depends on the Markov process, i.e. on the probability distribution $\mathscr{P}(P_0)$ for the initial state and on the transition probabilities, $\mathscr{P}(P_{n+1}|P_n)$. We formally write the probability distribution of γ over Γ as $\mathscr{P}(\gamma)$, but the implicit dependence on the Markov process should be borne in mind.

Now let $h : \Gamma \to \mathbb{R}$ be a function that maps histories to real numbers. Such a function is called an **estimator**. If γ denotes a random history, then $\hat{h} = h(\gamma)$ is a random variable on $\mathbb{R}$, characterized by its probability distribution $\mathscr{P}\left(\hat{h}\right)$, and possibly its expected value $\mathbb{E}(\hat{h})$ and its variance $\mathbb{V}(\hat{h})$.

3.2 The Liouville-Neumann series

Equipped with these basic notions about Markov processes, we now turn to the problem of using them to solve a Fredholm equation of the second kind. First, we need to write the sought solution in a form that can be easily interpreted in probabilistic terms. The most straightforward approach to solve Eq. (3.3) is to write the solution as a sum of successive contributions. Let us introduce a sequence of functions f_n satisfying the recurrence relation

$$f_{n+1} = \alpha \boldsymbol{K} f_n,$$

with $f_0 = g$. Now consider the following series

$$f = \sum_{n=0}^{\infty} f_n = g + \alpha \boldsymbol{K} g + \alpha^2 \boldsymbol{K}^2 g + \ldots, \tag{3.6}$$

with $\boldsymbol{K}^n g$ representing the composition of n applications of operator $\boldsymbol{K}$. Suppose that the series in Eq. (3.6) converges. It is easy then to verify that f is a solution of Eq. (3.3):

$$\alpha \boldsymbol{K} f = \alpha \boldsymbol{K} \sum_{n=0}^{\infty} f_n = \sum_{n=0}^{\infty} \alpha \boldsymbol{K} f_n = \sum_{n=0}^{\infty} f_{n+1} = \sum_{n=1}^{\infty} f_n = f - g,$$

provided that we can exchange the integral (the application of $\boldsymbol{K}$) and the summation.

```
history ← [] ;
P ← sample(g(·));                                  // sample first state
loop
    append P to history;
    ξ ← sample(U[0, 1]);
    if ξ < α then
        P ← sample(K(·, P)) ;                      // survival, sample next state
    else
        break;                                     // history dies
    end
endLoop
```

Algorithm 3.1: Sampling a history using the "natural" Markov process.

Equation (3.6) is known as the **Liouville-Neumann series**. If we assume that the integrals cover some finite range $[a, b]$, then a sufficient condition for its convergence is (Arfken et al. 2012)

$$|\alpha| \cdot |b - a| \cdot \max_{x,y} |K(x, y)| < 1, \tag{3.7}$$

where $K(x, y)$ is the kernel of $\boldsymbol{K}$. In what follows, we will always assume that the series converges, unless noted otherwise.

3.3 From the Liouville-Neumann series to a Markov process

The Liouville-Neumann series lends itself well to a probabilistic interpretation. Indeed, if we regard $g(P')$ as the probability to find a particle in P' and $K(P, P')$ as the probability distribution for the transition from P' to P, then

$$(\boldsymbol{K}g)(P) = \int K(P, P')\, g(P')\, \mathrm{d}P'$$

would just be the average number of particles in P after exactly one transition. Additionally, if $0 < \alpha < 1$, we can interpret α as a **survival probability**, i.e. the probability for the particle to survive the current transition[3]. Thus, $f_n(P)$ is the average number of particles that are found at P and have undergone exactly n transitions, and $f(P)$ is the average number of particles found at P. Algorithm 3.1 summarizes how to generate a history.

Note that the probabilistic interpretation naturally led us to the construction of a Markov process: the set of states of the process is the measure space on which the functions f and g are defined; the transition probabilities are represented by the kernel $K(P', P)$, and the initial probability distribution is given by g. This construction relies on a number of assumptions. For example, regarding $g(P)$ as a probability distribution requires that $g(P) \geq 0$ and that $\int g(P)\mathrm{d}P = 1$. Some of these assumptions will be lifted below.

To complete our discussion, we need to clarify in what sense the Markov process solves Eq. (3.3).

[3] In the notation of Section 3.1.2, $\mathscr{P}(P_{\text{final}}|P) = 1 - \alpha$.

3.3.1 Observables and estimators

Let $\{P_0, P_1, \ldots, P_{k-1}\}$ denote the k states visited by a history γ (k being a random variable), and let us consider an estimator of the form

$$h(\gamma) = \sum_{i=0}^{k-1} \eta(P_i), \tag{3.8}$$

which is entirely defined by the one-point function $\eta(P)$. As explained in Section 3.1, $h(\gamma)$ is a real random variable, and it can be sampled by evaluating h on histories of the Markov process. It is possible to show (Lux and Koblinger 2018) that the expectation value of $h(\gamma)$ is

$$\mathbb{E}(h) = \int f(P)\, \eta(P)\, \mathrm{d}P, \tag{3.9}$$

where f is the solution to Eq. (3.3). Therefore, any linear functional of the form (Eq. (3.5)):

$$O = \int f(P)\, \eta(P)\, \mathrm{d}P$$

can be estimated with Monte Carlo as follows:

1. generate N histories of the Markov process;

2. convert the histories into a sample of N real numbers by applying the function

$$h(\gamma) = \sum_{i=0}^{k-1} \eta(P_i);$$

3. apply the standard methods of statistical inference to the sample to produce an estimate of the expectation value of $h(\gamma)$ and an associated confidence interval.

To summarize, given any *response function* η, Eq. (3.8) yields an unbiased Monte Carlo estimator for $\int f(P)\eta(P)\mathrm{d}P$. However, note that this the estimator defined by Eq. (3.8) is not unique; there are actually infinitely many possible estimators for the same response function. A detailed discussion of this point, in the context of particle transport, can be found in Spanier and Gelbard (2008).

3.3.2 Remarks

A few remarks are in order:

- The Monte Carlo "solution" is approximation-free, in the sense that it does not require any discretization of the Fredholm equation. The trade-off is that the "solutions" are random variables. The statistical uncertainty on the estimates of the sought expectation value, however one chooses to evaluate it, is inversely proportional to the square root of the number of histories. This means that convergence is typically slow: halving the statistical uncertainty requires sampling four times as many histories.

- There are infinitely many Markov processes that "solve" a given Fredholm equation. All the ingredients can be modified: the initial condition, the transition probabilities, the estimators, and even the set of states. All the different possible Monte Carlo games solve the same problem, but, in general, they are *not* equivalent in terms of efficiency. The problem of formulating the optimal Monte Carlo game is a very interesting one, and it will be discussed further in Chapter 8.

- The family of linear functionals defined by Eq. (3.5) does not actually include point values of f, such as $f(P)$. It is possible to approximate point values by linear functionals that integrate f over some small volume δP around P:

$$h_{P,\delta P}(\gamma) \simeq \frac{1}{\delta P} \sum_{i=0}^{k-1} \mathbb{1}_{\delta P}(P_i);$$

  here $\mathbb{1}_{\delta P}(P)$ represents the indicator function for the integration volume δP. Clearly, this estimator is not unbiased. One may be tempted to make the bias as small as possible by taking the integration volume as small as possible. However, when doing so, the associated Monte Carlo estimators becomes very inefficient, in the sense that the statistical uncertainty associated with any given set of histories increases. This is due to the fact that, as the integration volume is reduced, the number of histories that contribute a non-zero value to the estimate is also reduced.

  Unbiased estimators for point values of f exist, and they do not suffer from the problems discussed here (although they suffer from other problems). Their definition is outside the scope of this manuscript, but the interested Reader is encouraged to consult Lux and Koblinger (2018, paragraph 4.V.D.3).

Finally, the Reader probably suspects that there are many things that can go wrong with the "natural" construction of a Markov process outlined in above. For example, it may not be possible to interpret g as a probability distribution at all; the function $g(P)$ may take negative values for some P, or it may not be normalized to 1. Similar problems may arise if one insists on interpreting $K(P', P)$ as a transition probability. Remarkably, however, it is often possible to refine the construction of the Markov process to work around most of the limitations of the "natural" construction. In the rest of this chapter, we will somewhat heuristically propose strategies to handle the most common ones.

3.4 Source term

Suppose that the source term is not normalized to 1:

$$\int g(P)\,\mathrm{d}P = N_g$$
$$g(P) \geq 0$$

for some $N_g > 0$, $N_g \neq 1$. We can interpret g as the average number of source particles emitted at P. Let f be the unknown solution of Eq. (3.3). Let $g' = g/N_g$. Linearity implies that $f' = f/N_g$ is a solution of the Fredholm equation

$$f' = \alpha \boldsymbol{K} f' + g'.$$

By construction, however, the source term for this equation is normalized to 1; we can apply the natural construction of the Markov process to it, solve for f' and recover $f = f' \cdot N_g$. Therefore, we can assume that g is normalized to 1 without loss of generality.

This trick cannot be applied if $N_g = 0$:

$$\int g(P)\,\mathrm{d}P = 0$$

We have to consider two cases here: If $g(P) = 0$ everywhere, then in general[4] Eq. (3.3) only admits the trivial solution $f = 0$. If $g(P)$ does *not* vanish everywhere, then we define two auxiliary source functions, representing the positive and the negative parts of g:

$$\begin{aligned} g_+(P) &= \max\left(g(P), 0\right) \\ g_-(P) &= \max\left(-g(P), 0\right). \end{aligned}$$

By construction, $g = g_+ - g_-$. Both functions $g_\pm$ are non-negative; therefore, we can use the natural construction to solve the Fredholm equations

$$f_\pm = \alpha \boldsymbol{K} f_\pm + g_\pm.$$

Then, by linearity, the solution to the original equation is given by $f = f_+ - f_-$. This strategy actually works for any situation in which $g(P)$ changes sign, even if its integral does not vanish.

3.5 Statistical weights

Before discussing transition probabilities, we need to introduce the concept of **statistical weight**. The idea is to associate a real number w_i to each state visited by a history. Weighted histories have the form

$$\gamma = \{(P_0, w_0), (P_1, w_1), \ldots, (P_{k-1}, w_{k-1})\}.$$

Intuitively, the weight w_i can be used to represent the fact that a given state P_i was visited by a fraction of a process. This generalization has consequences on the structure of estimators: for example, one-point estimators of the form of Eq. (3.8) need to be generalized to

$$h(\gamma) = \sum_{i=0}^{k-1} w_i \cdot h_1(P_i). \tag{3.10}$$

Statistical weights are a crucial tool for Monte Carlo. Essentially any attempt to improve the efficiency of Monte Carlo relies on the introduction of suitable statistical weights; in practice, efficient Monte Carlo schemes try to spend as much time as possible on the simulation of "interesting" events, and they use statistical weights to compensate and keep the game fair. Methods that aim to improve the efficiency of Monte Carlo are collectively known as **variance-reduction techniques** and constitute a lively field of ongoing research.

[4]The form of Eq. (3.3) without a source term is actually better interpreted as an eigenvalue equation, but we will not pursue this matter.

```
1 history ← [] ;
2 weight ← 1 ;                                   // initialize weight
3 P ← sample(g(·));
4 loop
5 |   append (P, weight) to history;
6 |   weight ← weight × α ;        // multiply by survival probability
7 |   P ← sample(K(·, P));
8 endLoop
```

Algorithm 3.2: Sampling a history using survival biasing. This algorithm never terminates.

As an example of the use of statistical weights, consider how survival of the history is sampled in the natural Markov process of Algorithm 3.1. Clearly, at any step, the average fraction of histories that survive is α. We can represent survival by modifying the weight: in Line 6 of the algorithm, we can let the history unconditionally continue, and keep track of the survival probability by multiplying the current weight of the history by α. This leads to Algorithm 3.2, which is known as **survival biasing**. Note that the history starts from the source with a weight of 1 and accumulates a factor of α at each step, so that the weight after i transitions is given by

$$w_i = \alpha^i.$$

In this form, survival biasing is problematic because it produces infinitely long histories. Note that the statistical weight decreases exponentially with the number of steps; therefore, states visited after many steps are expected to yield small contributions to estimators of the form of Eq. (3.8). One may be tempted to truncate the histories once the weight falls below a fixed threshold value; however, this will lead to biased estimates. A commonly used and unbiased alternative is **Russian roulette**: in the simplest implementation of this method, when the weight w of the history drops below a fixed threshold w_{RR}, the history is randomly killed with probability $1 - w$; if the history survives, its current weight is reset to 1. This ensures that histories will eventually terminate, and at the same time guarantees that weight is conserved on average and that any estimator will remain unbiased (Lux and Koblinger 2018). The inclusion of Russian roulette leads to Algorithm 3.3.

3.6 Transition probabilities

Let us now consider the case where the kernel $K(P', P)$ is always positive, but it cannot be interpreted as a conditional probability distribution for P' because

$$\int K(P', P)\mathrm{d}P' = N_K(P)$$

for some $N_K(P) > 0$, $N_K(P) \neq 1$. Define

$$K'(P', P) = \frac{K(P', P)}{N_K(P)} \tag{3.11}$$

and observe that $\int K'(P', P)\mathrm{d}P' = 1$, by construction. Thus, $K'(P', P)$ can be interpreted as a probability distribution. By substituting this definition into Eq. (3.3), we obtain

$$f = (\alpha\, N_K)\boldsymbol{K'} f + g. \tag{3.12}$$

```
history ← [] ;
weight ← 1 ;
P ← sample(g(·));
loop
    append (P, weight) to history;
    weight ← weight × α;
    if weight < weight_RR then  // below threshold, must play roulette
        ξ ← sample(Uniform_[0,1]);
        if ξ < weight then
            weight ← 1 ;                          // survived roulette
        else
            break;                                    // history dies
        end
    end
    P ← sample(K(·, P));
endLoop
```

Algorithm 3.3: Sampling a history using survival biasing and Russian roulette.

The brackets highlight the fact that this equation is similar in form to Eq. (3.3), except for the fact that the scalar $\alpha\, N_K(P)$ now depends on P. If $0 \leq \alpha\, N_K(P) \leq 1$, then this value can be regarded as a state-dependent survival probability. In this case, the natural Markov process construction for Eq. (3.12) can proceed as normal.

As we have seen before, the survival probability can also be handled by introducing statistical weights and using survival biasing and Russian roulette. This solution also works for the state-dependent survival probability of Eq. (3.12): instead of randomly deciding whether the history should survive, with probability $\alpha\, N_K(P)$, we multiply the current weight by $\alpha\, N_K(P)$ and apply Russian roulette, leading to Algorithm 3.4.

The Reader should try to convince themselves that Algorithm 3.4 is actually applicable for *any* value of $\alpha\, N_K(P)$. Indeed, if $\alpha\, N_K(P) > 1$, then the weight will occasionally increase for the given transition, but this is not necessarily a problem; as long as the weight keeps decreasing most of the time, histories will eventually terminate. It is worth stressing in passing the similarity between the sufficient condition for the convergence of the Liouville-Neumann series, Eq. (3.7), and the fact that the weight needs to decrease "most of the time" for the Monte Carlo histories to terminate. This is more than just a coincidence: the convergence of the Liouville-Neumann series expresses the fact that the average density of particles is finite. However, the connection is subtle because it is possible to imagine Monte Carlo games with finitely long histories but infinite particle densities; conversely, a non-terminating Monte Carlo game may well simulate a Fredholm equation characterized by a converging Liouville-Neumann series (see Algorithm 3.2 for example).

More interestingly, let us consider the case where $K(P', P)$ is always negative. The normalized kernel, Eq. (3.11), can still be interpreted as a probability distribution; however, the weight multiplier $\alpha\, N_K(P)$ becomes negative and the weight sign alternates at each step. A negative weight is difficult to interpret in terms of fractions of histories, but it does not pose any serious practical difficulty, as long as one modifies Russian roulette in such a way that negative values are handled correctly. Algorithm 3.4 uses the absolute value of the weight to perform roulette; in case the particle survives, its weight keeps its sign and its

```
history ← [] ;
weight ← 1 ;
P ← sample(g(·));
loop
    append (P, weight) to history;
    // multiply weight by the state-dependent survival
       probability
    weight ← weight × α N_K(P);
    // the rest is the same as before
    if |weight| < weight_RR then
        ξ ← sample(Uniform_[0,1]);
        if ξ < |weight| then
            weight ← weight/|weight|;
        else
            break;
        end
        P ← sample(K(·, P));
    end
endLoop
```

Algorithm 3.4: Sampling a history using survival biasing and Russian roulette, with a state-dependent survival probability. This algorithm is applicable to any value of $\alpha\, N_K(P)$.

magnitude is reset to 1.

Kernels without a definite sign can be handled by defining their positive and negative parts,

$$K_+(P', P) = \max\left(K(P', P), 0\right)$$
$$K_-(P', P) = \max\left(-K(P', P), 0\right),$$

so that

$$K(P', P) = K_+(P', P) - K_-(P', P). \tag{3.13}$$

We assume that the positive and the negative parts can be separately normalized:

$$K'_+(P', P) = \frac{K_+(P', P)}{N_{K_+}(P)} \tag{3.14a}$$

$$K'_-(P', P) = \frac{K_-(P', P)}{N_{K_-}(P)}, \tag{3.14b}$$

with

$$N_{K_+}(P) = \int K_+(P', P)\mathrm{d}P'$$
$$N_{K_-}(P) = \int K_-(P', P)\mathrm{d}P'.$$

The equation can then be rewritten as

$$f = \alpha\left(N_{K_+} + N_{K_-}\right)\left[\frac{N_{K_+}}{N_{K_+} + N_{K_-}}\boldsymbol{K}'_+ f - \frac{N_{K_-}}{N_{K_+} + N_{K_-}}\boldsymbol{K}'_- f\right] + g. \tag{3.15}$$

```
1  history ← [] ;
2  weight ← 1 ;
3  P ← sample(g(·));
4  loop
5  |  append (P, weight) to history;
   |  // multiply weight by the state-dependent survival
   |     probability
6  |  weight ← weight × α (N_{K+}(P) + N_{K−}(P));
   |  // play Russian roulette with weight, omitted
7  |  ξ ← sample(Uniform_{[0,1]});
8  |  if ξ < N_{K+}(P)/(N_{K+}(P) + N_{K−}(P)) then
9  |  |  P ← sample(K+(·, P));
10 |  else
11 |  |  P ← sample(K−(·, P));
12 |  |  weight ← −weight;
13 |  end
14 endLoop
```

Algorithm 3.5: Algorithm for sampling a history for a transition kernel without a definite sign. The kernel K is written as a difference of two positive kernels K_+ and K_-, which are selected and sampled at random. Russian roulette is applied, but omitted for the sake of conciseness.

Equation (3.15) highlights that the transition can be sampled as follows: first, we select a "positive" or a "negative" transition with respective probabilities

$$P_{K_\pm}(P) = \frac{N_{K_\pm}(P)}{N_{K_+}(P) + N_{K_-}(P)}.$$

If a positive transition is selected, then the final state is sampled from the kernel $K'_+(P', P)$. If a negative transition is selected, then the final state is sampled from the kernel $K'_-(P', P)$ *and* we flip the sign of the statistical weight. In either case, we multiply the statistical weight by $\alpha\,(N_{K_+} + N_{K_-})$. The procedure is summarized in Algorithm 3.5.

A moment's thought will reveal that Algorithm 3.5 is actually applicable to *any* decomposition of the form

$$\begin{gathered} K(P', P) = K_+(P', P) - K_-(P', P) \\ K_\pm(P', P) \geq 0 \\ N_{K_\pm}(P) = \int K_\pm(P', P)\mathrm{d}P' < \infty, \end{gathered}$$

regardless of the fact that K_+ and K_- represent the positive and negative parts of the kernel. More generally, if the kernel can be written as a sum of finitely many positive and negative

components of finite norm,

$$K(P', P) = \sum_i K_{+,i}(P', P) - \sum_i K_{-,i}(P', P)$$
$$K_{\pm,i}(P', P) \geq 0$$
$$N_{K_{\pm,i}}(P) = \int K_{\pm,i}(P', P)\mathrm{d}P' < \infty,$$

then it is possible to sample K by first selecting a sub-kernel according to the probability distribution

$$P_{K_{\pm,i}}(P) = \frac{N_{K_{\pm,i}}(P)}{\sum_i N_{K_{+,i}}(P) + \sum_i N_{K_{-,i}}(P)}$$

and then sampling the corresponding normalized sub-kernel. Finally, we must remember to apply the weight multiplier

$$\alpha \cdot \left(\sum_i N_{K_{+,i}}(P) + \sum_i N_{K_{-,i}}(P) \right)$$

and to flip the sign of the weight if one of the negative sub-kernels was selected. This procedure actually generalizes fairly easily to kernels that can be expressed as linear combinations of finitely many sub-kernels,

$$K(P', P) = \sum_i K_{+,i}(P', P) - \sum_i \int K_{-,i}(P', P),$$

provided that the sub-kernels can be individually normalized,

$$N_{K_{\pm,i}}(P) = \int K_{\pm,i}(P', P)\mathrm{d}P' < \infty,$$

and provided that the normalization constants $|N_{K_{\pm,i}}(P)|$ can be interpreted as a probability distribution for the choice of the sub-kernel.

3.7 Eigenvalue equations and power iteration

The algorithms outlined so far can be used to solve Fredholm equations of the second kind. Let us however go back to Eq. (3.2):

$$\psi_n = \boldsymbol{T} \left(\boldsymbol{S} + \frac{\boldsymbol{F}}{k} \right) \psi_n.$$

This integral equation is not a Fredholm equation of the second kind, but rather an eigenvalue equation. On physical grounds, we know that this equation admits a set of discrete eigenvalues $\{k^{(0)}, k^{(1)}, \ldots\}$, with $k^{(0)}$ real and bounding the spectrum from above:

$$k^{(0)} > \mathrm{Re}(k^{(i)}) \quad \forall i > 0.$$

We are generally interested in determining the dominant eigenvalue $k^{(0)}$ and the associated eigenfunction. Can we adapt our heuristic construction of the Markov process above to this

problem? The solution is provided by a classic algorithm called **power iteration**, which is an adaptation of the power method from linear algebra.

Let us consider more abstractly the following eigenvalue equation:

$$\alpha \cdot (f - \boldsymbol{K} f) = \boldsymbol{F} f. \tag{3.16}$$

Here α is the eigenvalue and f is the unknown. Since this equation is homogeneous, the solution f is determined up to an arbitrary normalization constant, which we assume to be fixed by the following (L^1) normalization condition:

$$\|\boldsymbol{F} f\| = \int |\boldsymbol{F} f(P)| \mathrm{d}P = 1. \tag{3.17}$$

Suppose that we replace the right-hand side of Eq. (3.16) with an initial guess g_0,

$$\alpha \cdot (f - \boldsymbol{K} f) = g_0; \tag{3.18}$$

we assume g_0 to be non-negative and normalized, for coherence with Eq. (3.17):

$$\|g_0\| = \int g_0(P) \, \mathrm{d}P = 1.$$

Equation (3.18) is a Fredholm equation of the second kind, of the form of Eq. (3.3); g_0 is the source term and the unknown is $f' = \alpha f$. We can solve it by constructing a Markov chain as outlined in the previous section. Let f'_0 be the solution to the equation

$$f'_0 - \boldsymbol{K} f'_0 = g_0.$$

This yields the first estimate of the eigenfunction:

$$f_0 = \frac{f'_0}{\|\boldsymbol{F} f'_0\|}.$$

We can now iterate. At the n-th step, we solve the equation

$$f'_n - \boldsymbol{K} f'_n = \boldsymbol{F} f_{n-1}.$$

This yields the recurrence relation

$$f'_n = \frac{(1 - \boldsymbol{K})^{-1} \boldsymbol{F} f'_{n-1}}{\|\boldsymbol{F} f'_{n-1}\|},$$

which can be cast in the explicit form

$$f'_n = \frac{\left[(1 - \boldsymbol{K})^{-1} \boldsymbol{F}\right]^n f'_0}{\prod_{i=0}^{n-1} \|\boldsymbol{F} f'_i\|}. \tag{3.19}$$

It is legitimate to ask whether this sequence of functions converges, and what it converges to if it does. We will give a heuristic argument here. Suppose Eq. (3.16) admits a complete set of discrete eigenvalue/eigenfunction pairs[5]:

$$\alpha^{(i)} \cdot \left(f^{(i)} - \boldsymbol{K} f^{(i)}\right) = \boldsymbol{F} f^{(i)};$$

[5]This condition is not necessary, but it simplifies the following exposition.

thus,

$$\alpha^{(i)} f^{(i)} = (1 - \boldsymbol{K})^{-1} \boldsymbol{F} f^{(i)}.$$

Assume that the eigenvalues are bounded in magnitude from above, that the eigenpairs are labelled so that

$$|\alpha^{(0)}| \geq |\alpha^{(1)}| \geq |\alpha^{(2)}| \geq \ldots,$$

and that the eigenfunctions are normalized:

$$\int |\boldsymbol{F} f^{(i)}(P)| \mathrm{d}P = 1.$$

By completeness, any function can be expressed as a linear combination of the functions $f^{(i)}$. In particular, the function f'_0 can be decomposed as

$$f'_0(P) = \sum_{i=0}^{\infty} c_n^{(i)} f^{(i)}(P).$$

Equation (3.19) yields

$$\begin{aligned} f'_n &= \frac{\left[(1 - \boldsymbol{K})^{-1} \boldsymbol{F}\right]^n \sum_{i=0}^{\infty} c_n^{(i)} f^{(i)}}{\prod_{i=0}^{n-1} \|\boldsymbol{F} f'_i\|} \\ &= \frac{\sum_{i=0}^{\infty} c_n^{(i)} {\alpha^{(i)}}^n f^{(i)}}{\prod_{i=0}^{n-1} \|\boldsymbol{F} f'_i\|}. \end{aligned}$$

Therefore, if n is sufficiently large and $c^{(0)} \neq 0$, the ${\alpha^{(0)}}^n f^{(0)}$ term eventually dominates the sum and we get

$$f'_n \propto f^{(0)}.$$

This shows that the power iteration algorithm converges to the dominant eigenfunction of the generalized eigenvalue equation, Eq. (3.16).

The Monte Carlo version of the power iteration algorithm is based on the very same ideas. Taking Eq. (3.2) as an example, the algorithm is adapted as follows:

1. Sample N unit-weight particles from an arbitrary source distribution; this starts the first *generation* (or *cycle*).

2. Solve the fixed-source problem for the propagation of the source particles, *assuming that fission is treated as absorption.*

3. Sample particles emitted from fission during the propagation of the source particles.

4. Somehow resample and/or renormalize the fission particles so that their weight (and possibly their number) is equal to N. This provides the particle source for the next generation/cycle.

5. Go to step 2.

As iterations develop, the distribution of the source particles approaches the distribution described by the dominant eigenfunction $f^{(0)}$. There are many strategies to monitor the convergence of the iteration, which we will not discuss here (F. B. Brown 2009). Suffice it to say that once convergence has been attained, the source particles can be collectively seen as a representative sample from the dominant eigenfunction $f^{(0)}$. From this point on, further iterations do not modify the distribution of the source particles. Linear functionals of the collision or emission density can then be estimated by applying the usual Monte Carlo estimators. Care must however be taken in evaluating confidence intervals for the Monte Carlo estimators, because particles from different generations are not independent (F. B. Brown 2009; Miao et al. 2018).

3.8 An example

We wish to provide a concrete example of the techniques developed in the sections above by applying them to the solution of a specific Fredholm equation of the second kind. The equation that we have selected is

$$f(x) = \alpha \int_0^x (\beta\,(x-y) - 1)\,\Sigma\,\exp\left(-\Sigma\,(x-y)\right)\,f(y)\,\mathrm{d}y + \delta(x). \tag{3.20}$$

The parameters β, Σ, and α are assumed to be positive. This equation admits an analytical solution (Polyanin and Manzhirov 2008, §2.2-2, Eq. 25):

$$f(x) = \delta(x) + \frac{\alpha\Sigma\,e^{-(\frac{\alpha}{2}+1)\Sigma x}}{k}\left[\left(\frac{k^2}{\alpha\Sigma} + \frac{\alpha\Sigma}{4}\right)\sinh(k\,x) - k\cosh(k\,x)\right], \tag{3.21}$$

with

$$k = \frac{1}{2}\sqrt{\alpha\Sigma(4\beta + \alpha\Sigma)}.$$

We will use this equation as a reference for our Monte Carlo simulation.

The kernel of this equation is actually a function of $s = x - y$ only and reads

$$K(s) = \begin{cases} (\beta\,s - 1)\,\Sigma\,\exp\left(-\Sigma\,s\right) & \text{if } s > 0 \\ 0 & \text{otherwise} \end{cases} \tag{3.22}$$

Following Algorithm 3.5, we split K into its positive and negative parts:

$$K_+(s) = \begin{cases} K(s,0) & \text{if } s > \beta^{-1} \\ 0 & \text{otherwise} \end{cases}$$

$$K_-(s) = \begin{cases} -K(s,0) & \text{if } 0 < s \leq \beta^{-1} \\ 0 & \text{otherwise} \end{cases}.$$

A primitive of K is

$$\begin{aligned} N(s) &= \int_0^s K(s')\mathrm{d}s' \\ &= \frac{\beta}{\Sigma} + \left(1 - \beta\,s - \frac{\beta}{\Sigma}\right)\exp(-\Sigma\,s) - 1. \end{aligned}$$

Procedure `sampleKernelPN()`

$\xi_1 \leftarrow$ `sample(`$\mathsf{Uniform}_{[0,1]}$`);`

$\xi_2 \leftarrow$ `sample(`$\mathsf{Uniform}_{[0,1]}$`);`

if $\xi_1 < N_{K_+}(P)/(N_{K_+}(P) + N_{K_-}(P))$ **then**

$$s \leftarrow \frac{1}{\beta} - \frac{W_{-1}\left(\frac{\xi_2 - 1}{e}\right) + 1}{\Sigma};$$

else

$$s \leftarrow \frac{1}{\beta} - \frac{W_0\left((1-\xi_2)\left(\frac{\Sigma}{\beta} - 1\right)\exp\left(\frac{\Sigma}{\beta} - 1\right) - \frac{\xi_2}{e}\right) + 1}{\Sigma};$$

weight $\leftarrow -$weight;

end

return s;

endProcedure

Algorithm 3.6: Procedure for sampling Eq. (3.22) by splitting it into a positive and a negative part.

This yields the norms of the positive and negative parts,

$$N_{K_+} = N(+\infty) - N(\beta^{-1}) = \frac{\beta}{\Sigma}\exp\left(-\frac{\Sigma}{\beta}\right)$$
$$N_{K_-} = -N(\beta^{-1}) = 1 - \frac{\beta}{\Sigma}\left[1 - \exp\left(-\frac{\Sigma}{\beta}\right)\right],$$

and their sum:

$$N_{K_+} + N_{K_-} = 1 - \frac{\beta}{\Sigma}\left[1 - 2\exp\left(-\frac{\Sigma}{\beta}\right)\right].$$

The normalized version of the kernels, Eq. (3.14), are omitted for the sake of brevity.

We will need to separately sample K_+ and K_-. We will use inverse transform sampling (Spanier and Gelbard 2008). For the positive part, we need to solve the following equation for s:

$$N(s) - N(\beta^{-1}) = \xi\, N_{K_+},$$

where ξ is a standard pseudo-random number. The solution is

$$s = \frac{1}{\beta} - \frac{W_{-1}\left(\frac{\xi - 1}{e}\right) + 1}{\Sigma}.$$

Here W_{-1} is the secondary real-valued branch of the Lambert function[6]. The choice of the branch stems from the requirement that the solution must take the limiting values $s = \beta^{-1}$

[6]The Lambert function is defined as the solution of the following (complex) equation:

$$W(z)e^{W(z)} = z.$$

It has a countably infinite number of branches, denoted $W_n(z)$. The $n = -1$ and $n = 0$ branches are real-valued, i.e they take up real values for some range of real arguments.

```
1  Procedure sampleKernelEL()
2      ξ1 ← sample(Uniform[0,1]);
3      if ξ1 < β/(β + Σ) then
           // linear-exponential part selected
4          ξ2 ← sample(Uniform[0,1]);
5          ξ3 ← sample(Uniform[0,1]);
6          s ← −(log ξ2 + log ξ3)/Σ;
7      else
           // exponential part selected
8          ξ2 ← sample(Uniform[0,1]);
9          s ← −log ξ2/Σ;
10         weight ← −weight;
11     end
12     return s;
13 endProcedure
```

Algorithm 3.7: Procedure for sampling Eq. (3.22) by splitting it into an exponential part and a linear-exponential part.

and $s = +\infty$ for $\xi \to 0$ and $\xi \to 1$, respectively. For the negative part, the equation to solve is

$$N(s) = \xi \, N_{K_-},$$

and the solution reads

$$s = \frac{1}{\beta} - \frac{W_0\left((1-\xi)\left(\frac{\Sigma}{\beta} - 1\right)\exp\left(\frac{\Sigma}{\beta} - 1\right) - \frac{\xi}{e}\right) + 1}{\Sigma}, \tag{3.23}$$

where W_0 is the principal branch of the Lambert function. Equation (3.23) correctly yields $s = 0$ for $\xi \to 0$ and $s = \beta^{-1}$ for $\xi \to 1$. We summarize this sampling strategy for the transition kernel in Algorithm 3.6.

An alternative sampling strategy directly leverages the structure of Eq. (3.22). Indeed, the kernel can be written as

$$K(s) = \begin{cases} K_1(s) - K_0(s) & \text{if } s > 0 \\ 0 & \text{otherwise} \end{cases},$$

where

$$K_0(s) = \Sigma \, \exp\left(-\Sigma \, s\right)$$
$$K_1(s) = \beta \, \Sigma \, s \, \exp\left(-\Sigma \, s\right).$$

The sub-kernels satisfy

$$K_i(P', P) \geq 0, \qquad i = 0, 1$$

and

$$N_{K_0}(P) = 1$$
$$N_{K_1}(P) = \frac{\beta}{\Sigma}$$
$$.$$

Therefore, we can sample K using Algorithm 3.7.

Regardless of how we choose to sample the transition kernel, we need to define the estimators that we will apply to the histories generated by Algorithm 3.5. Since our goal is to "solve" Eq. (3.20), we want to construct estimators for $f(x)$. To this end, we first define an interval of interest, say $x \in [0, x_{\text{max}}]$, and we partition it into $B = 100$ equal bins of size $\delta x = x_{\text{max}}/B$. For each bin $[x_i, x_i + \delta x]$, we define a one-point estimator $h^{(i)}(\gamma)$ following Eq. (3.10), with

$$h_1^{(i)}(x) = \frac{\mathbb{1}_{[x_i, x_{i+1}]}(x)}{\delta x}.$$

Up to a factor, the estimator $h^{(i)}(\gamma)$ keeps a weighted count of how many particles have landed into the i-th bin during history γ. By virtue of Eq. (3.9), the expectation value of $h^{(i)}$ is

$$\mathbb{E}(h^{(i)}) = \frac{1}{\delta x} \int_{x_i}^{x_i + \delta x} f(x)\, \mathrm{d}x, \tag{3.24}$$

which approximates the value of $f(x)$ in the bin.

Finally, for completeness, we need to mention the fact that sampling the source term of Eq. (3.20) is trivial; for our Monte Carlo simulation, a Dirac delta simply means that all our particles start at $x = 0$. For the sake of clarity of illustration, the first point of each history (the source point) is excluded from the count. This is done in order to improve the readability of the plots, which would otherwise be marred by a large peak at $x = 0$. For coherence, we likewise exclude the $\delta(x)$ term of Eq. (3.21) from our plots below.

I have written a small Monte Carlo solver for Eq. (3.20) according to the rules outlined in this chapter. The code is released as free software (Mancusi 2023). The positions of the walkers generated by the Monte Carlo solver are tallied on a grid of 100 equal bins between $x = 0$ and $x = 10$. Figure 3.1 shows the result of two Monte Carlo simulations of 10^8 histories each; the difference between the Monte Carlo calculations lies in the kernel sampling algorithm used (positive-negative, Algorithm 3.6, or linear-exponential, Algorithm 3.7). In the top part of Fig. 3.1, the dots represent the sample averages $\bar{h}^{(i)}$ of the estimators $h^{(i)}$, plotted as a function of the position; the error bars represent the standard errors $\bar{\sigma}_{h^{(i)}}$. The continuous green line represents the analytical solution, Eq. (3.21), with the $\delta(x)$ term excluded. The agreement between the Monte Carlo results and the expected solution can be somewhat quantified by inspecting the studentized residuals

$$t^{(i)} = \frac{\bar{h}^{(i)} - f(x_i + \delta x/2)}{\bar{\sigma}_{h^{(i)}}}.$$

If the number of simulated histories is sufficiently large, then each residual $t^{(i)}$ is expected to follow a standard normal distribution (zero mean, unit variance). The bottom part of Fig. 3.1 shows the studentized residuals as a function of position.

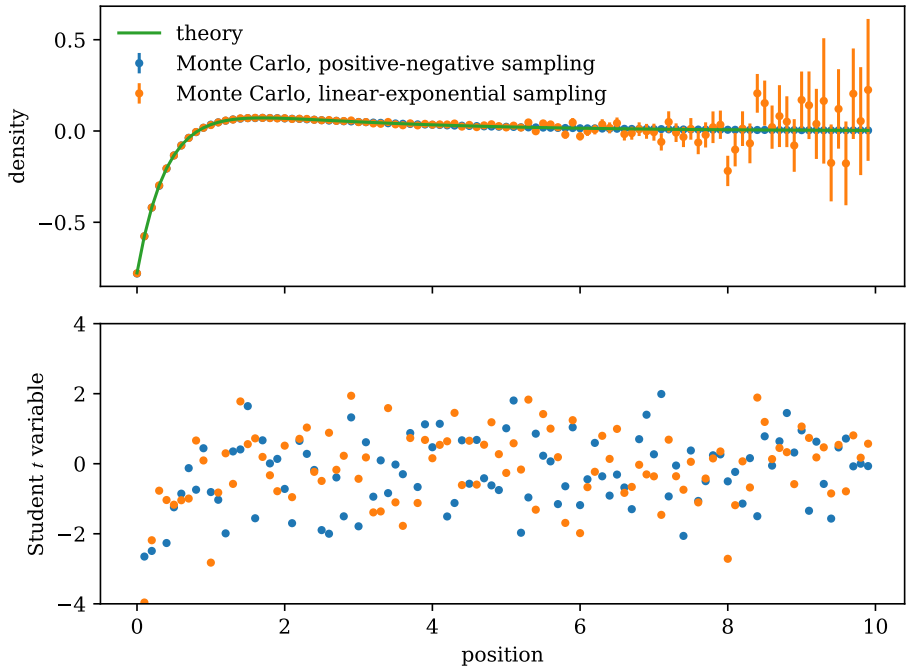

Figure 3.1: Comparison between Eq. (3.21), which is the solution to Eq. (3.20), and the result of two Monte Carlo simulations. The simulations use different sampling strategies for the transition kernel.

It is immediately evident from Fig. 3.1 that both Monte Carlo calculations are in very good agreement with the theory. The residual plot shows a cloud of points that are mostly contained within the $-2 < t^{(i)} < 2$ interval. Towards the beginning of the curve, around $x \lesssim 1$, the magnitude of the residuals becomes somewhat larger. However, we should remember that our estimators $h^{(i)}$ are not pointwise estimators for the values of the solution, but they actually estimate the average of the solution over the bin, Eq. (3.24). By developing $f(x)$ in Taylor series around the bin midpoint $x_i + \delta x/2$, it is possible to argue that the value of $f(x_i + \delta x/2)$ differs from the average over the bin by an amount proportional to the second derivative of the solution, $f''(x_i + \delta x/2)$. This is consistent with the somewhat larger values of the residuals for $x \lesssim 1$.

We should also stress the fact that both kernel sampling methods (positive-negative and linear-exponential) yield results in good agreement with the theory. However, the error bars in the top part of Fig. 3.1 are clearly larger for linear-exponential sampling. This illustrates the fact that there may be reasons to prefer one sampling method over another "equivalent" one; besides the variance of the results, one should certainly take into account at least the total CPU time required by the sampling method and the simplicity of the algorithm.

3.9 Conclusions and insights

Even though this chapter did not to provide a rigorous construction of a Markov-process-based solution to a Fredholm equation, the content presented here will hopefully suffice to convince the Reader that a whole host of situations actually prove to be treatable by making ingenious use of statistical weights. Since the goal of this chapter is not to provide a grimoire

of every possible "trick", my exposition will stop here. I am not aware of the existence of an exhaustive collection of Monte Carlo "tricks", but I would be very interested in reading one if it exists.

I wish to conclude this chapter by raising a final question. We have mentioned for example in Section 3.6 that a linear combination of transition sub-kernels without a definite sign can be treated in the Monte Carlo framework if *(i)* the sub-kernels can be individually normalized, and *(ii)* the magnitudes of the normalization constants can be interpreted as a probability distribution for the choice of the sub-kernel. What happens if these conditions do not hold?

Consider the kernel

$$K(s) = K_+(s) - K_-(s) \tag{3.25}$$

with

$$K_+(s) = \begin{cases} \dfrac{1}{\sin s} & \text{if } 0 < s < 1 \\ 0 & \text{otherwise} \end{cases}$$

$$K_-(s) = \begin{cases} \dfrac{1}{s} & \text{if } 0 < s < 1 \\ 0 & \text{otherwise} \end{cases}.$$

Here $K(s)$ is perfectly well-behaved: it has a finite limit at $s = 0^+$ (in fact, $\lim_{s\to 0^+} K(s) = 0$) and it has a finite normalization constant, but condition *(i)* is broken, because

$$\int_0^1 K_+(s)\,\mathrm{d}s = \int_0^1 K_-(s)\,\mathrm{d}s = \infty.$$

As an example of a kernel that breaks condition *(ii)* but not condition *(i)*, consider

$$K(s) = \sum_{n=1}^{\infty} (-1)^{n+1}\,\Sigma \exp(-n\Sigma s) \qquad s \geq 0. \tag{3.26}$$

This well-known series (which provides a counterexample to the Fubini-Tonelli theorem) can be summed to yield the Fermi-Dirac function,

$$K(s) = \frac{1}{1 + \exp(\Sigma s)},$$

which can be normalized:

$$\int_0^\infty K(s)\,\mathrm{d}s = \log 2.$$

The sub-kernels

$$K_n(s) = (-1)^{n+1}\,\Sigma \exp(-n\Sigma s)$$

are individually normalizable:

$$N_n = \int_0^\infty K_n(s)\,\mathrm{d}s = \frac{(-1)^{n+1}}{n}.$$

However, the normalization constants cannot be interpreted as a probability distribution because

$$\sum_{n=1}^{\infty} |N_n| = \sum_{n=1}^{\infty} \frac{1}{n} = \infty.$$

Arguably, these two examples highlight problems with our decompositions into sub-kernels, rather than problems with the method itself. In fact, there is no need to decompose Eq. (3.25) into sub-kernels, since the kernel is always non-negative. Equation (3.26) is better decomposed by combining terms in pairs:

$$\begin{aligned} K(s) &= \Sigma \sum_{\substack{n=1 \\ n \text{ odd}}}^{\infty} [\exp(-n\Sigma s) - \exp(-(n+1)\Sigma s)] \\ &= \Sigma \sum_{n=1}^{\infty} \exp(-2n\Sigma s) \left[\exp(\Sigma s) - 1\right]. \end{aligned}$$

The norms of the sub-kernels

$$\hat{K}_n(s) = \Sigma \exp(-2n\Sigma s) \left[\exp(\Sigma s) - 1\right]$$

are

$$\hat{N}_n = \int_0^{\infty} \hat{K}_n(s) \, \mathrm{d}s = \frac{1}{2n(2n-1)}$$

and their sum converges:

$$\sum_n \hat{N}_n = \log 2.$$

The need for nuclear reaction models

The application of the Monte Carlo method to the resolution of the Boltzmann equation requires access to a certain number of elementary data, such as cross sections, multiplicities, double-differential scattering kernels, fission spectra, precursor production multiplicities and decay constants, etc., for all the nuclides present in our system and for all the temperatures and energies of interest (see Chapter 2). So far, we have assumed that these nuclear data are always available. In practice, there are situations where this may not be the case.

4.1 Exhaustiveness of nuclear data

Exhaustive nuclear data are typically unavailable for nuclear reactions at incident energies above 100 MeV to 150 MeV, which we take as our definition of *high energy* for the purpose of this manuscript. The reason for this is that the number of open reaction channels and the average particle multiplicities increase very quickly with increasing incident energy. By consequence, the coverage of experimental data becomes scarcer and scarcer as the energy increases, and the evaluation of nuclear data becomes under-constrained. Nuclear data libraries still provide the cross sections for the most common channels (total, elastic, total inelastic), but most of the other channels are just omitted from the evaluation. For example, according to the online version[1] of the JANIS software provided by IAEA (Soppera et al. 2014), the $n + {}^{208}$Pb entry of the ENDF/B-VIII.0 library (D. A. Brown et al. 2018) contains double-differential particle emission cross sections (`MF=6`) for 112 distinct reaction channels (counting each discrete inelastic channel as a different one). According to the AME2016 nuclear mass evaluation (Wang et al. 2017), there are 862 combinations of ejectiles that are energetically accessible by the $n + {}^{208}$Pb reaction at 150 MeV. Note that a given combination of ejectiles may be realized by more than one reaction channel. Thus, it is clear then that traditional nuclear data evaluations are far from being able to provide all the information that is necessary for particle-transport codes at high energy.

For these reasons, Monte Carlo particle transport codes have to resort to another solution in order to sample the outcomes of high-energy collisions. One possibility, which has been thoroughly explored in the last ten to fifteen years by the TENDL library (Koning et al. 2019), is to extend the coverage of evaluated nuclear data by making ample use of many adjustable nuclear reaction models. To quote from Koning et al. (2019), "[t]he TENDL library [...] striv[es] for completeness and quality of nuclear data files for all isotopes, evaluation methods, processing and applied performance". However, I feel that it is hard to formulate

[1] Information retrieved on the 4th April 2022 from `https://www.oecd-nea.org/janisweb/`.

strong *a priori* guarantees about the quality of the evaluation if the available experimental datasets are few and far between.

The other option, which represents the subject of the present chapter, is to rely on few, **frugal** nuclear reaction models to generate the information necessary for the Monte Carlo calculation. A model is frugal if it is able to explain a large body of experimental evidence with relatively few adjustable parameters. The free parameters can be adjusted to *globally* reproduce the available experimental datasets. The advantage of a frugal model is that it is expected to have more *predictive power* than a model with a large number of adjustable parameters. In other words, a model with many free parameters will in general provide a better fit to the available experimental data, but it will also generalize badly to new experimental data. In the jargon of statistical inference, this problem is known as *overfitting*.

4.2 Nuclear reaction models as event generators

The use of evaluated nuclear data library is fraught with another limitation. The nuclear reaction models that are used to build the evaluated nuclear data libraries often guarantee that the fundamental conservation laws (energy, momentum, angular momentum, etc.) are respected. However, when these models are used to build a library, part of this information is lost. This happens in particular in the evaluation of "singles" spectra for channels with more than one outgoing particle. For example, neutron emission in an $(n, 2n)$ reaction is fully described by a sextuple-differential cross section $\mathrm{d}^6\sigma_{n,2n}/\mathrm{d}E_1\mathrm{d}\hat{\mathbf{\Omega}}_1\mathrm{d}E_2\mathrm{d}\hat{\mathbf{\Omega}}_2$, where E_1 and E_2 are the energies of the outgoing neutrons and $\hat{\mathbf{\Omega}}_1$ and $\hat{\mathbf{\Omega}}_2$ are their directions[2]. Indeed, the energies and momenta of the outgoing neutrons are correlated by the dynamics of then nuclear reaction, so (for example) not all energies E_2 are accessible if the first neutron has an energy E_1. However, evaluated nuclear data library typically only provide the "singles" cross section

$$\begin{aligned}\frac{\mathrm{d}^3\sigma_{n,2n}}{\mathrm{d}E\mathrm{d}\hat{\mathbf{\Omega}}} = &\frac{1}{2}\int \frac{\mathrm{d}^6\sigma_{n,2n}}{\mathrm{d}E_1\mathrm{d}\hat{\mathbf{\Omega}}_1\mathrm{d}E_2\mathrm{d}\hat{\mathbf{\Omega}}_2}\delta(E-E_1)\delta(\hat{\mathbf{\Omega}}-\hat{\mathbf{\Omega}}_1)\mathrm{d}E_1\mathrm{d}\hat{\mathbf{\Omega}}_1\mathrm{d}E_2\mathrm{d}\hat{\mathbf{\Omega}}_2 \\ &+\frac{1}{2}\int \frac{\mathrm{d}^6\sigma_{n,2n}}{\mathrm{d}E_1\mathrm{d}\hat{\mathbf{\Omega}}_1\mathrm{d}E_2\mathrm{d}\hat{\mathbf{\Omega}}_2}\delta(E-E_2)\delta(\hat{\mathbf{\Omega}}-\hat{\mathbf{\Omega}}_2)\mathrm{d}E_1\mathrm{d}\hat{\mathbf{\Omega}}_1\mathrm{d}E_2\mathrm{d}\hat{\mathbf{\Omega}}_2,\end{aligned}$$

where E and $\hat{\mathbf{\Omega}}$ are the energy and direction of a single neutron. The fact that two neutrons are simultaneously emitted is accounted for using a channel multiplicity of 2. The reason for this choice is obvious: the amount of storage required to describe the differential cross section for a reaction channel increases exponentially with the channel multiplicity. Besides, the singles cross section is sufficient for the calculation of Boltzmann observables (see Chapter 3), because the $(n, 2n)$ production term of the Boltzmann equation is anyway proportional to

$$S_{n,2n} = 2\int \mathrm{d}E'\mathrm{d}\hat{\mathbf{\Omega}}' \int \mathrm{d}E\mathrm{d}\hat{\mathbf{\Omega}}\,\frac{\mathrm{d}^3\sigma_{n,2n}}{\mathrm{d}E\mathrm{d}\hat{\mathbf{\Omega}}}\varphi(\boldsymbol{r},\hat{\mathbf{\Omega}}',E',t).$$

However, the Monte Carlo calculation of non-Boltzmann observables cannot be carried out using the singles cross section. Indeed, non-Boltzmann observables are in principle sensitive to the state of all the particles present in the system at all times, and therefore they are

[2]Note that our kinematic variables do not include the energy and direction of the recoiling nucleus, which are determined by energy and momentum conservation.

indirectly affected by the particle-particle correlations in reaction channels that produce several particles. In the example of an $(n, 2n)$ reaction, the best a Monte Carlo code can do is to independently sample two neutron energies E_1 and E_2 from the singles spectrum provided in the evaluated nuclear data. Consider the recoil energy of the target nucleus E_{recoil}, which can be defined by conservation:

$$E_{\text{recoil}} = E_{\text{in}} - E_1 - E_2 - Q_{n,2n};$$

here E_{in} is the energy of the incident neutron and $Q_{n,2n}$ is the Q-value of the $(n, 2n)$ reaction. Because of statistical independence, the sampled energies do *not*, in general, satisfy the appropriate conservation law; this will lead to unphysical values for E_{recoil}, which can even be negative. Therefore, if we wish to estimate for example the probability that the recoil energy exceeds a certain threshold, the neutron energies *cannot* be independently sampled. However, if we are interested in the *average* recoil energy, then independent sampling is fine, because the singles spectrum has the correct average energy. This example goes to indicate that the nature (Boltzmann or non-Boltzmann) of the observables that we wish to calculate is crucial. Unfortunately, in many high-energy physics applications of particle transport, it is very common that the relevant observables are non-Boltzmann; as an example, consider energy deposition in calorimeters (Fabjan and Gianotti 2003). Non-Boltzmann observables are sometimes relevant even in low-energy applications, such as nuclear safeguards (Swinhoe et al. 1991).

Instead of using a nuclear reaction model to produce an evaluated nuclear data library, which in turn can be used in a Monte Carlo particle-transport code, it is sometimes possible to directly use nuclear reaction models in Monte Carlo codes as **event generators**. For the purpose of this manuscript, we will define an event generator as a program that accepts as input a projectile type, a particle energy, and a target nucleus, and outputs a sampled final state (i.e. a collection of particles) for a given reaction channel. Different event generators can describe different reaction types.

In practice, each time a collision must be sampled, the Monte Carlo transport code delegates the sampling of the final state of the collision to a suitable event generator. In the case of event generators that are themselves based on the Monte Carlo method, it is arguably more natural to call them directly from the transport calculation than to use them to build a cross section library. In addition, the direct solution has the added benefit of preserving all the properties of the event generator in the transport calculation; for instance, if the event generator guarantees energy conservation, then the transport calculation can also attempt to provide the same guarantee.

There are two main disadvantages to event generators, compared to evaluated nuclear data. The first one is that event generators typically require more computing time than nuclear data. This is not unexpected, in view of the fact that, as we have seen, nuclear data contain less information than the output of an event generator. The second, perhaps surprising, disadvantage is that some information about the reaction is only accessible via evaluated nuclear data, and not via event generators. For example, an event generator for (say) elastic scattering makes it possible to sample the angular distribution of the scattered particle, but generally does not provide any access to the distribution function for the scattering angle. As a consequence, certain types of sophisticated Monte Carlo estimators, such as next-event estimators (Spanier and Gelbard 2008), are not available when event generators are used.

Event generators are a cornerstone of Monte Carlo particle transport codes for high-energy physics. The archetypical example of a high-energy particle-transport code is proba-

bly Geant4 (Allison et al. 2016), which offers a customizable palette of event generators for hadronic and electromagnetic physics, from thermal energy up to several TeV. Geant4 also includes a module for nuclear-data-driven low-energy neutron transport (*Geant4 Physics Reference Manual* 2022). I think it is telling that the Geant4 documentation refers to the module as a "model", and I hasten to add that I like this unusual choice of terminology.

In the following chapter, I wish to focus on a particular class of event generators for nuclear reactions, which was the main focus of my research for a few years.

Event generators for high-energy nuclear reactions

5

As we have mentioned in the previous chapter, the number of emitted particles grows very rapidly with the energy of the incident particle. Niels Bohr had foreseen this in his well-known 1936 article about neutron capture (Bohr 1936):

> Even if we could experiment with neutrons or protons of energies of more than a hundred million volts, we should still expect that the excess energy of such particles, when they penetrate into a nucleus of not too small mass, would in the first place be divided among the nuclear particles with the result that a liberation of any of these would necessitate a subsequent energy concentration. Instead of the ordinary course of nuclear reactions we may, however, in such cases expect that in general not one but several charged or uncharged particles will eventually leave the nucleus as a result of the encounter.

At the time, the cyclotron had just been invented, and particle beams were limited to energies of about 10 MeV. A few years later, as 200 MeV deuteron and 400 MeV ^{4}He particle beams became available at the Berkeley cyclotron (Brobeck et al. 1947), physicists confirmed that high-energy reactions did indeed lead to abundant emission of charged and neutral particles. However, the mechanism that led to the emission was not what Bohr had imagined. In modern language, Bohr expected that reactions at several hundred MeV would proceed via the formation of a **compound nucleus**, i.e. an excited nucleus that forms when the target nucleus captures the projectile nucleon and absorbs its energy; the energy is then *thermalized*, in the sense that it is shared among all the nuclear degrees of freedom. Eventually (and this is Bohr's model in a nutshell) random fluctuations concentrate enough energy on a single particle (usually a neutron) to allow it to escape from the nucleus; we refer to this process as **evaporation** (Bohr 1937; Frenkel 1936), by analogy with the process that leads to the preferential emission of faster-than-average molecules from a liquid. Evaporation repeats until the compound nucleus has exhausted all the available excitation energy. This is the appropriate picture for neutron capture, which was Bohr's concern at the time.

Bohr's model is the prototype of **statistical de-excitation models**. Their main, common assumption is that particle emission is due to a system that is in quasi-static equilibrium, which makes it possible to use the tools of statistical mechanics to make predictions about the lifetime and the features of the emitted particles. In particular, evaporation is characterized by a soft and isotropic particle-emission spectrum, with relatively small fluctuations in the multiplicity of the emitted particles. Therefore, evaporation also results in the production of a relatively small number of different reaction products. By contrast, early experimental evidence immediately showed that the reaction products of high-energy proton-nucleus re-

actions span a range of several tens of mass units (Batzel et al. 1951; O'connor and Seaborg 1948). This and other observations could not be explained in the framework of Bohr's compound-nucleus model.

The first successful model for high-energy proton-nucleus reactions was created by Robert Serber (1947), former member of the Manhattan project[1] and head of the theoretical division of the Berkeley laboratory at the time. Today, Serber's model is still at the core of our current understanding of high-energy nuclear reactions. In this chapter we will review the main tenets of this model, its limitations and its numerous variants and extensions.

5.1 The two-stage reaction model

The central idea of Serber's model is that a collision between a high-energy nucleon and a nucleon at rest is short compared to the typical timescale of the movement of the nucleons in the target nucleus. To illustrate this point with some orders of magnitude, a Fermi energy of $E_F = 38\,\text{MeV}$ corresponds to an orbit period of $T = \hbar/E_F \simeq 1.7 \times 10^{-23}\,\text{s}$. If we assume that the nuclear forces have a range $a = 1\,\text{fm}$ (as can be estimated from rough cross section measurements), and if we assume that the incident nucleon moves at the speed of light, then the interaction will last about $t = a/c \simeq 3.3 \times 10^{-24}\,\text{s}$. Thus, we have $T/t \simeq 5$, i.e. the collision time is smaller than the duration of a "nuclear orbit", but not by a large factor.

We can also compare the de Broglie wavelength of the incoming particle to the radius of the nucleus. A proton with an incident kinetic energy $E = 1\,\text{GeV}$ has a wavelength $\lambda = \hbar/p \simeq 5.7 \times 10^{-16}\,\text{m}$. The radius of a lead nucleus is of the order of $R = 6.5\,\text{fm}$. Thus, we have roughly $R/\lambda \simeq 10$, i.e. the proton wavelength is smaller than the size of the nucleus, but again not by much.

Finally, we can compare the mean free path for the incident particle in nuclear matter with the size of the nucleus. If we assume that the nucleon-nucleon cross section is of the order of the square of the range of nuclear forces, we obtain $\sigma = \pi a^2 \simeq 31\,\text{mb}$. The average nuclear density (number of nucleons per unit volume) for a ^{208}Pb nucleus is $\rho = 208/(4\pi R^3/3) \simeq 0.18\,\text{fm}^{-3}$. Thus, the mean free path for a high-energy nucleon in a nucleus is of the order of $(\rho\sigma)^{-1} \simeq 1.8\,\text{fm}$, which is slightly smaller than, but definitely comparable to the nuclear radius.

It is now clear why Bohr's picture fails. In that model, the target nucleus absorbs the high-energy nucleon and results in the formation of a compound nucleus. However, at high energy, the nucleus is too transparent to completely stop the projectile. Note also that one collision is not sufficient to absorb a high-energy projectile and dissipate its kinetic energy. First, because of kinematic constraints, at most half of the projectile energy can be transferred at any collision; second, the typical momentum transfer is actually of the order of $\Delta p = \hbar/a \simeq 200\,\text{MeV}/c$, and the typical energy transfer is of the order of 25 MeV.

The picture painted by our back-of-the-envelope calculations is not as clear as one could hope for. Nevertheless, a somewhat reasonable model seems to emerge. The collisions between the incident particle and the target nucleons can be treated as collisions between free nucleons, to a first approximation. However, the momenta of particles in the nucleus are of the order of the Fermi momentum, $p_F = 270\,\text{MeV}$; since the typical momentum transfer in collisions is $\Delta p \simeq 200\,\text{MeV}/c$, the target nucleons cannot really be regarded

[1] In his memoirs, Serber claims to be the person that suggested the code names for the bombs that were dropped on Hiroshima and Nagasaki, "Little boy" and "Fat man" (Serber and Crease 1998).

as free. The binding of the target nucleons is expected to manifest itself in several ways. First, the kinematics will deviate from the free kinematics because the target nucleons are not at rest. Second, the presence of a degenerate gas of nucleons is expected to suppress soft collisions, which would lead to violations of the Pauli exclusion principle; this also results in an increase of the nucleon mean free path.

The secondary nucleons arising from the first collision can in turn induce further nucleon-nucleon collisions. For collisions that take place near the surface of the nucleus, escape is also possible. Eventually, the nucleons that could not escape will redistribute their energy over all the nuclear degrees of freedom and result in the formation of a thermalized nucleus, which is also called **remnant nucleus** in this context. At this point, we can apply Bohr's evaporation model to describe the de-excitation of the remnant; however, the mass, charge, excitation energy, and spin of the remnant are not determined by the absorption of the projectile nucleus, but rather by the dynamics of the first stage.

To summarize, Serber's model consists of two stages. In the first stage, called **intranuclear cascade** (INC), the incident nucleon triggers an avalanche of binary nucleon-nucleon collisions, leading to the emission of particles *before* thermal equilibrium is reached. The INC stage leaves behind a remnant nucleus with an excess of excitation energy, which is subsequently evacuated according to Bohr's evaporation model.

It immediately became clear that the intranuclear-cascade model lent itself well to a Monte Carlo-based implementation. Indeed, cascade particles are assumed to follow quasi-classical trajectories between collisions and undergo collisions with the nuclear medium; this is exactly the dynamics described by the Boltzmann equation (Chapter 2). The earliest calculations with this model were performed by hand (Goldberger 1948), and the earliest computer implementations date back to at least 1958 (Metropolis, Bivins, Storm, Miller, et al. 1958; Metropolis, Bivins, Storm, Turkevich, et al. 1958). The devil, of course, is in the details. In the seventy-five years that have elapsed since Serber's seminal publication, we have had the opportunity to explore several variations over the common theme of the two-stage model. Many INC models have been implemented since. In the following sections, I will make a non-exhaustive attempt at identifying the most common themes that have since been researched.

5.2 Theoretical foundations and domain of validity

Intranuclear cascade, as described by Serber, is essentially a semi-classical and semi-empirical model based on reasonable assumptions about the physics of the nucleon-nucleon collisions. The conditions for the validity of the model, although plausible, were not rigorously specified; moreover, the model lacked a solid theoretical foundation. These matters were clarified towards the end of the 1980s by a series of papers that represented the culmination of a large amount of theoretical effort (Bunakov and Matvejev 1985; Goldberger and Watson 1964). Our exposition is inspired in particular by Bunakov and Matvejev (1985) and by Cugnon's lucid review (Cugnon 2012, and references therein).

The initial condition for our system represents a set of A bound nucleons in a Fermi sea, plus a free incident nucleon. At each collision, a nucleon is promoted from the Fermi sea into the continuum, leaving behind a hole state in the sea. The probability to observe the system in a state where K particles have been promoted to the continuum, in a semi-classical approximation, can be written as a probability distribution function $f^{K,\alpha}(t, P_1, \ldots, P_K)$,

where α is the $(K-1)$-tuple of the quantum numbers of the hole states[2], and $P_i = (\boldsymbol{r}_i, \boldsymbol{p}_i)$ are the quasi-classical phase-space coordinates of the i-th excited nucleon. Starting from the Dyson formulation of the many-body Schrödinger equation, Bunakov and Matvejev (1985) showed that the dynamics of the K-body distribution functions $f^{K,\alpha}$ can be approximately described by a system of Boltzmann equations of the form

$$\left(\frac{\partial}{\partial t} + \sum_{i=1}^{K} \frac{\boldsymbol{p}_i}{m} \cdot \frac{\partial}{\partial \boldsymbol{r}_i} - \frac{\partial U(\boldsymbol{r}_i)}{\partial \boldsymbol{r}_i} \cdot \frac{\partial}{\partial \boldsymbol{p}_i}\right) f^{K,\alpha} = \sum_{i=1}^{K-1} \sum_{\alpha'} \int \mathrm{d}P_i' \, f^{K-1,\alpha'}(P_1, \ldots, P_i', \ldots, P_{K-1}) \, W(P_i' \to P_i, \alpha' \to (\alpha, P_K)) - \sum_{i=1}^{K} f^{K,\alpha}(P_1, \ldots, P_i, \ldots, P_K) \sum_{\alpha'} \int \mathrm{d}P_i' \mathrm{d}P_{K+1}' \, W(P_i \to P_i', \alpha \to (\alpha', P_{K+1}')). \quad (5.1)$$

The left-hand side of this equation is the usual drift term for particles of mass m moving in a common potential $U(\boldsymbol{r})$. On the right-hand side, we have a gain term and a loss term. The gain term has the structure of an external source: it is proportional to $f^{K-1,\alpha'}$, which is assumed to be known when solving for $f^{K,\alpha}$. The function $W(P_i' \to P_i, \alpha' \to (\alpha, P_K))$ represents the transition probability for the collision of the i-th nucleon; before the transition, the i-th nucleon is at P_i' and the Fermi sea configuration is given by the $(K-1)$-tuple α'; after the transition, the i-th nucleon has coordinates P_i, the Fermi-sea configuration is α, and the newly promoted nucleon has coordinates P_K. The loss term is the transition rate from the observed K-particle, $(K-1)$-hole state to any other state.

Equation (5.1) is valid under the following conditions:

- *semi-classical approximation*: particle trajectories between collisions can be treated classically;
- *no collision interference*: the wave function of a scattered nucleon reaches its asymptotic state before undergoing a new scattering event.

Interestingly, these conditions essentially ensure that the wave packet formed by the cascading nucleons is well localized in space and in time. Localization in space is important for the semi-classical form of the drift term; it amounts to requiring that the wave packet is small compared to the typical length scale of variation of the potential $U(\boldsymbol{r})$. Localization in time is important for the collision term, because it guarantees that the collision integral can be written as an incoherent sum of individual, quasi-free scatterings.

Quantitatively, the conditions for the validity of Eq. (5.1) are the plain-language translation of the following quantitative conditions:

$$\Delta p \cdot d > \hbar \quad (5.2a)$$

$$\Delta E \cdot \tau_{\text{free}} > \hbar \quad (5.2b)$$

$$p > \Delta p \quad (5.2c)$$

$$E > \Delta E. \quad (5.2d)$$

Here p and E are the momentum and kinetic energy of the cascading nucleon, Δp is its momentum dispersion, ΔE is its energy dispersion, d is the typical length scale of variation of

[2] If K nucleons are above the Fermi sea, then the system must contain exactly $K-1$ holes.

the potential $U(\boldsymbol{r})$, and τ_{free} is the mean free time between collisions. Numerically, we have $d \simeq 0.5\,\text{fm}$ (a typical value of the diffuseness parameter for the Woods-Saxon potential). For the mean free time between collisions, we can relate it to the mean free path

$$\tau_{\text{free}} = \frac{1}{v\,\sigma_{nn}(E)\rho},$$

where $v = p/m$ is the (non-relativistic) nucleon speed, σ_{nn} is the nucleon-nucleon cross section and $\rho \simeq 0.18\,\text{fm}^{-3}$ is the nucleon density for cold nuclear matter. Equation (5.2b) can be rewritten as

$$\Delta E > \frac{p}{m}\hbar\,\sigma_{nn}(E)\rho.$$

If we assume that $\Delta E \simeq p\,\Delta p/m$, we obtain

$$\Delta p > \hbar\,\sigma_{nn}(E)\rho \tag{5.3}$$

which should be compared to Eq. (5.2a):

$$\Delta p > \frac{\hbar}{d}.$$

Numerically, $\sigma_{nn}(E)\rho \simeq 0.7\,\text{fm}^{-1}$, assuming that the cross section takes its high-energy limiting value of $\approx 40\,\text{mb}$. Thus, for nucleon-nucleus reactions, the inequality given by Eq. (5.2a) is marginally tighter than Eq. (5.3) or, equivalently, than Eq. (5.2b).

In summary, Eq. (5.2), taken together, imply

$$E > \frac{\hbar^2}{2md^2}.$$

When the numerical values for m and d are substituted, one obtains

$$E \gtrsim 85\,\text{MeV}.$$

This number is slightly smaller than the values that are typically derived from *a priori* arguments (Cugnon 2012), but of course it should only be taken as an order-of-magnitude estimate.

Does the comparison with experimental data confirm the domain of validity inferred from first principles? As Cugnon (2012) notes, the predictions of INC models are indeed in excellent agreement with the evidence for incident kinetic energies above some 200 MeV. Interestingly, in double-differential particle-emission spectra, the agreement is very good for essentially any energy of the ejectiles (Leray et al. 2011). This is illustrated by Fig. 5.1, which shows a typical comparison of double-differential cross sections for neutron emission from $1.2\,\text{GeV}p + {}^{56}\text{Fe}$ reactions. The experimental data are taken from Leray et al. (2002), and the calculations were performed with the INCL4.5-ABLA07 model (Boudard, Cugnon, David, et al. 2013; Kelić et al. 2008). The agreement with the experimental data for the emission of low-energy neutrons is a bit surprising, in light of the fact that the conditions of Eq. (5.2) should apply to all the cascading nucleons, and not just the incident one; therefore, even at energies of the order of 100 MeV, where conditions Eq. (5.2) are barely satisfied, one should expect marginal agreement with the experimental data. At energies below some 20 MeV, most of the neutrons are not emitted during the intranuclear-cascade phase (see Section 5.3); therefore, no conclusions can be drawn on the validity of the model

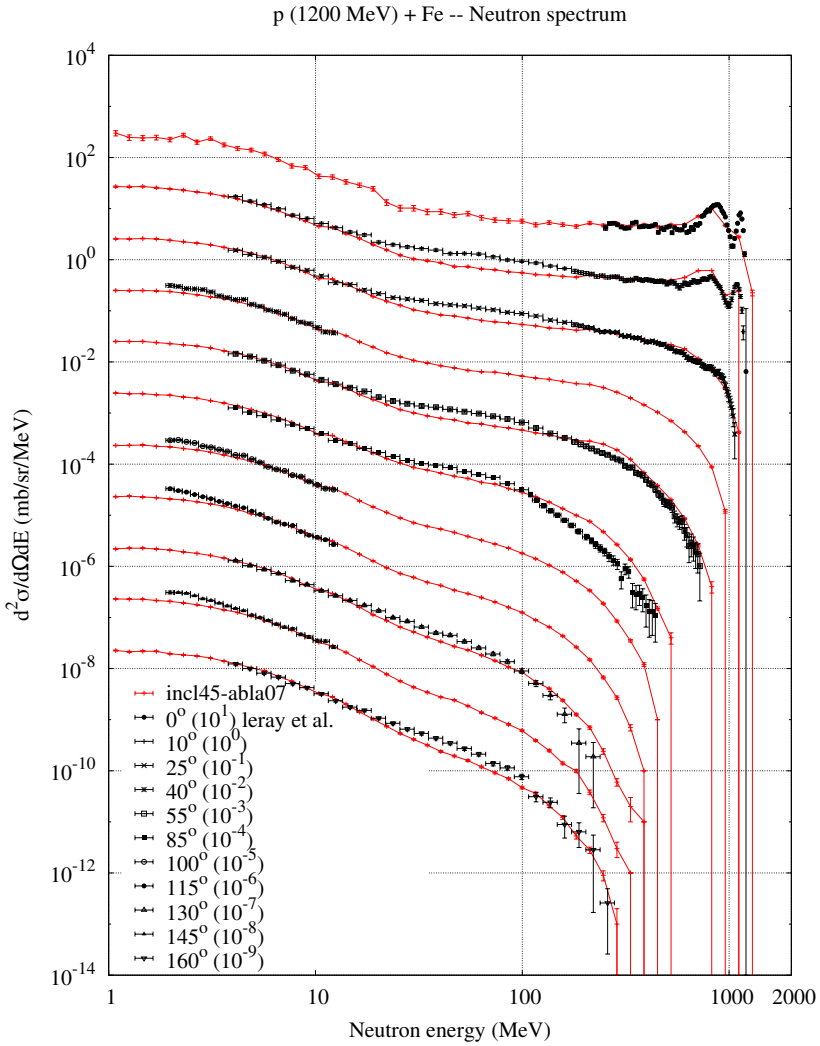

Figure 5.1: Double-differential neutron emission spectra for the 1.2 GeV p+^{56}Fe reaction, as measured by Leray et al. (2002) and calculated by the INCL4.5-ABLA07 model (Boudard, Cugnon, David, et al. 2013; Kelić et al. 2008). Image retrieved from the website of the IAEA benchmark of spallation models (*IAEA Benchmark of Spallation Models* 2022; Leray et al. 2011).

from those data. The low-energy behavior of the model can also be explored by decreasing the energy of the incident nucleon. As expected, the quality of the model predictions deteriorates below 200 MeV; however, the model remains remarkably accurate, even at incident kinetic energies of the order of 40 MeV to 50 MeV (Leray et al. 2011).

There is no general agreement about the reason why INC/de-excitation models work reasonably well, even in conditions where they should not. The matter has been mostly discussed by Yariv, Aoust, et al. (2007) and Cugnon (2012). As the energy of the projectile is reduced, the total nucleon-nucleon cross section increases; however, it is possible to argue that the mean free time between collisions τ_{free} actually *increases*, for the following reason: at low energy, the typical momentum transfer is small and most collisions are suppressed by the Pauli exclusion principle in the Fermi sea. Thus, Eq. (5.2b) may be violated at lower energy than what one would expect based on the calculations above. Additionally, the dynamics of low-energy reactions is actually fairly simple. For collisions with central impact parameters, the most likely outcome is the absorption of the incoming nucleon; the details of the dynamics leading to absorption do not matter, since the final state of INC is fully determined by the conservation laws. On the other hand, for sufficiently peripheral collisions, the dynamics is dominated by one collision, for which INC is rather well suited. Therefore, INC provides a reasonable description for both small and large impact parameters, and arguably this constrains the behavior at intermediate impact parameters, too.

Finally, we should spend a few words about the high-energy limit of INC models. The question here is less controversial, as it is clear that high-energy collisions eventually excite the internal degrees of freedom of the nucleons (baryonic resonances, meson production, etc.). The production and decay of the first few resonances can be easily accommodated into the standard INC picture, leading to models that are accurate up to a few GeV; this limit can be pushed to even higher energies if more resonances are taken into account (Folger et al. 2004; Niita, Sato, et al. 2006; Wright and Kelsey 2015). Alternatively, it is possible to argue that heavy baryonic and mesonic resonances are generally[3] so short-lived on the timescale of INC that they need not be treated individually. An effective model for multiple pion production in high-energy collisions was shown to be quite efficient at reproducing integral and differential pion yields from nucleon-nucleus and pion-nucleus reactions above 3 GeV (Pedoux and Cugnon 2011). At very high energies, the (proper) time between collisions becomes comparable to the hadronization time of the nucleon-nucleon collisions (Ferreres-Solé and Sjöstrand 2018); at that point, the hypothesis of independent collision breaks down and the model is no longer directly applicable.

5.3 Pre-equilibrium and statistical de-excitation

After numerous collisions, the kinetic energy of the projectile will degrade and the nucleus will reach thermal equilibrium; at that point we stop the INC phase. The exact stopping criteria for INC vary between the models. In some cases (Folger et al. 2004; Mashnik, Gudima, et al. 2008; Wright and Kelsey 2015), the final state of the INC phase becomes the input of an intermediate stage, called **pre-equilibrium** or **pre-compound model** (Griffin 1966). In pre-equilibrium models, the phase-space picture of INC is abandoned in favor of a model that describes the relaxation of the nuclear remnant towards thermal equilibrium in

[3] With the notable exception of the lightest strange resonances, which are constrained to decay by weak interaction.

terms of the dynamics of excitons and holes in the Fermi sea. The argument in favor of a pre-equilibrium model is easy to see: as we have discussed in the previous section, the INC approximation degrades as the energy of the cascading nucleons decreases, and is downright unjustified for most of the struck target nucleons. Pre-equilibrium models try to bridge the gap between the semi-classical INC picture and the statistical framework of de-excitation models, discussed below. When a pre-equilibrium model is used, the INC phase is typically stopped rather early, often using a criterion based on the energies of the cascading nucleons; the idea is to avoid handling low nucleon energies, for which INC is ill-suited.

Albeit pre-equilibrium tries hard to avoid the "language" of INC, the elementary ingredients of the model are nevertheless influenced by and tightly connected with it. The transition rates for exciton-hole annihilation and generation are more or less directly inspired by the same physical picture that underlies INC, namely transport and collisions of fermions over a Fermi-sea background. In introducing a new model, it is clear that we can improve the agreement with the known experimental data; after all, we are giving ourselves new degrees of freedom, in the form of the free parameters of the new model. However, it is necessary to evaluate if the improved predictions on known experimental data are offset by a loss of predictive power on unknown experimental data. As we have already discussed in Section 4.1, frugal models, with fewer free parameters, usually generalize better.

For these reasons, some INC models made the choice to forgo an intermediate pre-equilibrium stage (Yariv and Fraenkel 1979; Yariv and Fraenkel 1981). In these cases, the INC phase usually runs a little longer. The case of the Liège Intranuclear Cascade model (Boudard, Cugnon, David, et al. 2013) is rather unique, insofar as its stopping criterion is *i)* based on the time since the beginning of the cascade, and not on the energies of the nucleons, and *ii)* self-consistently determined from the dynamics of the INC phase itself.

Regardless of the use of an intermediate pre-equilibrium model, the nuclear reaction results in the production of an excited, thermalized remnant nucleus, which is entirely characterized by its conserved quantities: mass, charge, momentum, angular momentum and excitation energy. The thermalized nucleus is also frequently referred to as a **compound nucleus**, although this term actually comes from (and makes most sense in the context of) low-energy neutron capture. For the sake of clarification, the timescale leading to the emission of a new particle is assumed to be much longer than the typical internal timescales of the nucleus. Therefore, we are led to assume that further particle emission proceeds via a sequence of quasi-static states. The transition rates and the emission spectra are described by **statistical de-excitation models**.

5.3.1 Evaporation

The oldest example of a statistical de-excitation model is probably the Weisskopf-Ewing evaporation model (Weisskopf 1937; Weisskopf and Ewing 1940). In this model, the rate for the emission of a neutron of energy ϵ by a nucleus with A nucleons and excitation energy E^* is determined by *detailed balance*, i.e. by assuming that the emission rate would be equal to the absorption rate for a neutron of energy ϵ, $A-1$ nucleons, and the appropriate excitation energy. These assumptions lead to the following equation for the *energy-differential transition width* $\Gamma_n(\epsilon)$:

$$\Gamma_n(\epsilon) = \sigma_{A-1}(E^* - S_n - \epsilon, \epsilon)\frac{2\,m_n\,\epsilon}{\pi^2\hbar^2}\frac{\rho_{A-1}(E^* - S_n - \epsilon)}{\rho_A(E^*)}. \tag{5.4}$$

Here $\Gamma_n(\epsilon)\,\mathrm{d}\epsilon/\hbar$ represents the probability per unit time to emit a neutron with energy between ϵ and $\epsilon + \mathrm{d}\epsilon$; $\sigma_B(E,\epsilon)$ is the cross section for the absorption of a neutron of energy ϵ by a nucleus of mass number B and excitation energy E; m_n is the neutron mass; S_n is the neutron separation energy for the emitting nucleus; and, finally, $\rho_B(E)$ is the *level density* for a nucleus of mass number B and excitation energy E, i.e. $\rho_B(E)\,\mathrm{d}E$ is the number of levels found between excitation energies E and $E + \mathrm{d}E$.

The connection with evaporation can be made more conspicuous by introducing the *entropy*, i.e. the logarithm of the level density:

$$S_B(E) = \log \rho_B(E).$$

Equation (5.4) then reads

$$\Gamma_n(\epsilon) = \sigma_{A-1}(E^* - S_n - \epsilon, \epsilon)\frac{2\,m_n\,\epsilon}{\pi^2\hbar^2}\exp\left[S_{A-1}(E^* - S_n - \epsilon) - S_A(E^*)\right]. \tag{5.5}$$

If we assume that $S_A(E)$ and $S_{A-1}(E)$ are the same function, and that the excitation energy E^* is large with respect to the separation energy S_n and the neutron emission energy ϵ, then we can develop

$$S_{A-1}(E^* - S_n - \epsilon) \simeq S_A(E^*) - (S_n + \epsilon)\frac{\mathrm{d}S_A(E^*)}{\mathrm{d}E^*}.$$

The quantity $\mathrm{d}S_A/\mathrm{d}E^*$ has the dimensions of the inverse of an energy, which can be interpreted as a *nuclear temperature* T_A:

$$\frac{1}{T_A} = \frac{\mathrm{d}S_A}{\mathrm{d}E^*}.$$

Replacing in Eq. (5.5), we obtain the characteristic evaporation formula,

$$\Gamma_n(\epsilon) = \sigma_{A-1}(E^* - S_n - \epsilon, \epsilon)\frac{2\,m_n\,\epsilon}{\pi^2\hbar^2}\exp\left(-\frac{S_n}{T_A}\right)\exp\left(-\frac{\epsilon}{T_A}\right),$$

which shows that the energy distribution for the evaporating neutrons is proportional to

$$\frac{\Gamma_n(\epsilon)}{\int \Gamma_n(\epsilon)\,\mathrm{d}\epsilon} \propto \sigma_{A-1}(E^* - S_n - \epsilon, \epsilon)\cdot\epsilon\cdot\exp\left(-\frac{\epsilon}{T_A}\right).$$

If we assume that the cross section is independent of the excitation energy and has the typical k/v shape as a function of the energy of the neutron, we can derive an approximate expression for the total evaporation width:

$$\Gamma_n = \int \Gamma_n(\epsilon)\,\mathrm{d}\epsilon = \frac{m_n\,k\,T_A^{3/2}}{\pi^{3/2}\hbar^2}\exp\left(-\frac{S_n}{T_A}\right). \tag{5.6}$$

5.3.2 Fission

Statistical models have also been applied to the description of nuclear fission. In the semiclassical liquid-drop nuclear structure model, the spherical shape corresponds to the state

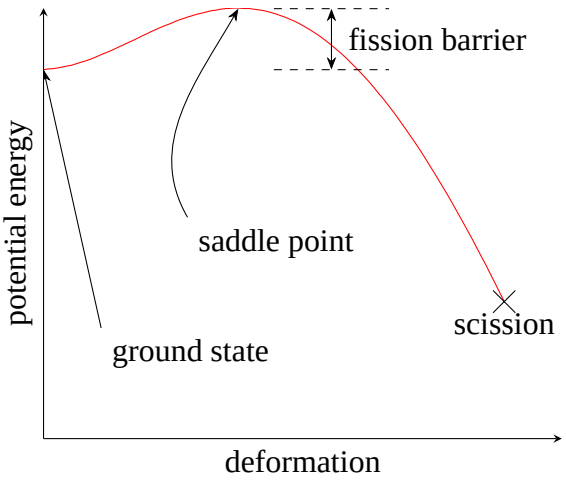

Figure 5.2: Schematic picture of the structure of the fission barrier in a liquid drop model (without any shell correction).

with the lowest energy if the charge is sufficiently small[4]. Figure 5.2 shows a schematic outline of the shape of the potential energy predicted by the liquid-drop model for a fissile nucleus, as a function of the deformation of the nucleus along a particular axis. In this model, the equilibrium point corresponds to no deformation. The equilibrium shape is stable under small shape perturbations, i.e. the potential has a minimum around the state with no deformation. However, the potential reaches an extremum for a certain value of the deformation. The configuration corresponding to the extremum value of the potential is called *saddle point*, and the difference between the potential energy at the saddle point and the ground-state energy is called *fission barrier*. Beyond the saddle point, the nucleus gains energy by increasing its deformation. At some critical deformation value, the nucleus splits into two fragments (*scission*).

Although fission is exothermic for sufficiently large nuclei, the presence of the fission barrier suppresses the transition to the scission state. Quantum-mechanical tunneling effects make spontaneous fission possible even for nuclei in their ground state, but the corresponding half-lives are generally very large. However, the tunneling probability increases very quickly with the excitation energy of the nucleus. When the excitation energy becomes larger than the fission barrier, quantum-mechanical effects stop playing an important role. At this point, fission starts to efficiently compete against evaporation in the dynamics of de-excitation.

The first model for describing the fission rate of an excited nucleus was conceived by Bohr and Wheeler (1939). Bohr and Wheeler build on Weisskopf's statistical formalism and on Wigner's concept of *transition states* (Wigner 1938), i.e. states of the excited nucleus that inevitably lead to fission when they are visited. These states conceptually correspond to the saddle point of Fig. 5.2. For an excited nucleus of mass number A and excitation energy E^*, Bohr and Wheeler's fission width reads

$$\Gamma_f = \frac{1}{2\pi\rho_A(E^*)} \int \rho_A^*(E^* - B_f - K)\,\mathrm{d}K,$$

where K is the kinetic energy along the deformation degree of freedom, B_f is the height of

[4]For large values of the nuclear charge, the liquid-drop model predicts that spherical nuclei becomes unstable and spontaneously fission.

the fission barrier, and $\rho_A^*(E)$ is the level density of transition states, i.e. the level density at the saddle point.

Compared to the Weisskopf-Ewing evaporation formula, Eq. (5.4), Bohr and Wheeler's fission width leaves several unanswered questions. First of all, one may wonder how to determine the fission barrier, B_f. The existence of fission induced by thermal neutrons is direct evidence that this quantity cannot be larger than a few MeV; indeed, the excitation energy of the compound nucleus formed by the absorption of a thermal neutron is equal to the Q-value for absorption, which is of the order of 6 MeV in actinides. More quantitative evidence about the height of the fission barrier can be extracted from the analysis of fission excitation curves, but the resulting values are in general model-dependent. Sierk (1986) used a refined version of the liquid-drop model to predict the values of the fission barrier for essentially all the relevant nuclei, for any value of the nuclear angular momentum. However, fission barriers based on the liquid-drop model neglect shell and pairing effects, and are only applicable if the internal excitation energy is sufficiently large. I hasten to add that shell and pairing effects are far from being negligible: in several nuclei (notably the actinides) the simplified picture of Fig. 5.2 does not hold. First, the ground state has a non-vanishing deformation. Second, the fission barrier actually has a double hump, which allows for the existence of metastable states in the pocket between the humps (Bjørnholm and Lynn 1980). Double-humped fission barriers can be handled in the context of a generalized Bohr-Wheeler model, with a set of transition states for each barrier hump. For certain nuclides, the existence of a triple-humped fission barrier is also well established.

The other mysterious ingredient of the Bohr-Wheeler formula is the level density of transition states, ρ_A^*. This quantity is well-defined only if we assume that the collective motion along the axis of deformation is *adiabatic*, in the sense that the dynamics of the nucleons inside the nucleus is in quasi-static equilibrium at all times. Within this approximation, we can consider the set of quantum states for nucleons moving in a nucleus at the saddle point deformation, and their level density ρ_A^*. As for the fission barrier, experimental data only provide indirect, model-dependent indications about the saddle-point level density. Therefore, ρ_A^* is often described by semi-empirically modifying the parameters of models for the (unconditional) level density (*Handbook for Calculations of Nuclear Reaction Data Reference Input Parameter Library* 1998; Ignatyuk et al. 1975), adjusting them to the available experimental data.

In the same spirit as in Section 5.3.1, we can derive a simplified expression for the fission width by introducing the entropies for the level densities $S_A(E)$ and $S_A^*(E)$. Again, we need to assume some relation between the saddle-point level density and the ground-state level density. In actinides, the saddle-point configuration is actually very close to spherical (excluding shell effects); therefore, it is reasonable to assume that $S_A^*(E) \simeq S_A(E)$. By developing $S_A^*(E^* - B_f - K)$ in power series around E^*, we obtain

$$\Gamma_f = \frac{T_A}{2\pi} \exp\left(-\frac{B_f}{T_A}\right),$$

which should be compared to the approximate expression for the total evaporation width Eq. (5.6), obtained under similar assumptions:

$$\Gamma_n = \int \Gamma_n(\epsilon)\,\mathrm{d}\epsilon = \frac{m_n\, k\, T_A^{3/2}}{\pi^{3/2}\hbar^2} \exp\left(-\frac{S_n}{T_A}\right).$$

The ratio of the fission width to the evaporation width is therefore proportional to

$$\frac{\Gamma_n}{\Gamma_f} \propto \exp\left(\frac{B_f - S_n}{T_A}\right).$$

This shows that, at least in this approximate model, the dominant de-excitation mechanism is determined by the relative values of the fission barrier and the neutron separation energy.

Once the saddle point is reached, it is generally assumed that the nucleus will inevitably progress towards fission. However, a certain amount of time might still be required for the nucleus to reach the scission configuration. During this time, the system may cool down by emitting more particles, especially if the excitation energy is large. Thus, the mass, charge and total energy available at the scission point may be different from what was available at the saddle point. In this model, it is generally assumed that the scission configuration is selected relatively late during the descent from saddle to scission (Benlliure, Grewe, et al. 1998; Kruglov et al. 2002; Schmidt et al. 2008); the details about the sharing of mass, charge, energy and angular momentum at scission are influenced by shell effects in the nascent fission fragments, which are responsible for the notorious asymmetric fission yields of actinides. If the residual excitation energy is sufficiently large, the fission fragments may undergo further de-excitation.

5.3.3 Production of intermediate-mass fragments

Neutron evaporation and fission are not the only mechanisms available for nuclear de-excitation. First, evaporation is not restricted to neutrons; there is clear evidence that the de-excitation spectra of many light particle types can be accurately described by an evaporation formalism. For light charged particles, such as protons, deuterons, alpha particles, etc., it is important to take into account the presence of the Coulomb barrier, which suppresses the emission of low-energy particles. In the Weisskopf-Ewing formalism, the Coulomb barrier modifies the inverse absorption cross section σ_{A-1}.

One of the limitations of the Weisskopf-Ewing formalism is that it does not track the evolution of the angular momentum of the nucleus, which must also be conserved. If the angular momentum is large, then the angular distribution of the evaporated particles is expected to be anisotropic. Moreover, the energy reservoir available for evaporation only contains thermal energy; when the angular momentum is large, a significant fraction of the total excitation energy is locked in a collective mode and is not available to the evaporating particles. These effects can be handled within the framework of the Hauser-Feshbach evaporation model (Hauser and Feshbach 1952). In this formalism, the energy-differential evaporation width is expressed as

$$\Gamma_n(\epsilon) = \frac{1}{2\pi\rho_A(U, S_A)} \sum_{S_{A-1}=0}^{\infty} \sum_{J=S_A-S_{A-1}}^{S_A+S_{A-1}} \sum_{\ell=|J-1/2|}^{J+1/2} T_\ell(\epsilon)\, \rho_{A-1}(E^* - S_n - \epsilon, S_{A-1}),$$

where S_A is the spin of the evaporating nucleus, S_{A-1} is the spin of the daughter nucleus, J is the total angular momentum of the evaporated neutron, ℓ is its orbital angular momentum, $T_\ell(\epsilon)$ is the transmission coefficient for an incoming spherical wave of angular momentum ℓ, and $\rho_{A-1}(E, S)$ is the level density of the daughter nucleus with excitation energy E and spin S[5]. The Hauser-Feshbach formula keeps track of all the possible combinations of

[5]Note that the only levels with spin S are counted in this definition of the level density.

spin and angular momentum that can result in the emission of a neutron. As a result, the evaluation of the evaporation width is more cumbersome, because a triple sum needs to be evaluated.

An interesting question arises about the relationship between fission fragments and evaporation. One can extend the evaporation formalism to handle the emission of particles of essentially any mass. For example, the Generalized Evaporation Model by Furihata (2000) considers ejectiles up to ^{24}Mg and finds that the evaporation width decreases with increasing charge number, mostly because of the effect of the Coulomb barrier. At the same time, the fission fragment distribution has a tail that extends down to very small mass numbers. It is legitimate to ask which formalism should be used to describe the emission of ejectiles in the overlap.

The reconciliation of evaporation and fission was discussed by Moretto (Moretto 1975) and Świątecki (Świątecki 1983). I personally feel that it is not even clear whether the two formalism are actually describing the same phenomenon. The question is difficult to settle in part because evaporation relates the emission rate to the asymptotic ejectile + remnant state; in fission, on the other hand, the rate is expressed as a function of the characteristics of the transition state (the saddle-point configuration), which is unobserved. Additionally, the fission fragments retain some excitation energy, but Furihata's generalized evaporation formalism (Furihata 2000) only considers ejectiles in their ground-state configuration. This assumption is surely justified for neutrons, protons, and probably alpha particles (due to the latter's large energy gap between the ground state and the first excited state), but it is less obvious that it applies to heavier ejectiles, that may have many low-lying excited states. The formalism can be straightforwardly extended to handle excited ejectiles, but the inverse absorption cross section is not known for excited ejectiles. These considerations further complicate the comparison with fission. Finally, since the definition of the saddle-point level density is a bit nebulous, it is my feeling that it is difficult to say much about the relationship between the two formalisms.

In fission, it is difficult to relate the characteristics of the transition state to those of the scission state. In order to clarify the meaning of this statement, we need to parametrize the nuclear shape with a set of deformation coordinates q_i and introduce the nuclear potential energy surface $V(q_i)$ (neglecting pairing and shell effects for a moment) (Nix and Swiatecki 1965). The saddle point and the ground state are both characterized as solutions of the equation

$$\frac{\partial V}{\partial q_i} = 0.$$

In the example of thermal fission of ^{235}U, the saddle-point configuration is almost spherical and relatively close to the ground state, whereas the scission configuration is characterized by the distinct presence of two fragments. It is well-known however that nuclei with a low value of the fissility parameter have dumbbell-shaped saddle-point configurations; moreover, the lower the fissility parameter is, the more constrained the neck between the fragment becomes. Thus, in non-fissile nuclei, the saddle-point configuration and the scission configuration are very close in the space of deformation parameters; in other terms, the saddle-point configuration essentially defines the mass asymmetry of the split. This suggests that binary "fission" of non-fissile nuclei should be described by a modified Bohr-Wheeler formalism, where the transition state however is characterized by a well-specified mass/charge asymmetry. This idea was introduced by Moretto (1975) and Moretto and

Wozniak (1988), who suggested the use of the following formula:

$$\Gamma_f(y) = \frac{1}{2\pi\rho_A(E^*)} \int \rho^*_{A,y}(E^* - B_f(y) - K)\,\mathrm{d}K.$$

Here y is a parameter measuring the charge asymmetry and $\rho_{A,y}(E)$ is the level density at the *conditional saddle point*, i.e. the saddle point seen along a line of constant y. This formalism goes under the somewhat confusing name of **asymmetryic fission**, where the term "asymmetric" does not refer to the symmetry of the fragment mass or charge distribution, but rather to the fact that the saddle-point is constrained to be asymmetric. Moretto's formalism was later extended by Charity, McMahan, et al. (1988) to saddle points with fixed mass and charge asymmetries, and was proved to be quite successful in describing the yields of light particles and complex fragments from fusion reactions (Charity 2010; Charity, Jing, et al. 1990). Perhaps unexpectedly, asymmetric fission is also applied to the description of the yields of very asymmetric splits of fissile nuclei, which are similarly characterized by short saddle-to-scission distances (Thomas et al. 1985).

Part II

Highlighted research

The Liège intranuclear cascade model

6

The intranuclear-cascade model has seen many incarnations since its inception, which differ in several details. In what follows, I wish to discuss in particular the Liège intranuclear cascade model (INCL), which is one of the most sophisticated models for nucleon-nucleus reactions on the market and has been the object of a great deal of development. In this chapter we will first give a description of the most specific aspects of INCL in Section 6.1, and then we will focus on a few recent selected topics which I actively contributed to; these are the emission of composite particles from the INC phase (Section 6.2), the extension of INCL to nucleus-nucleus reactions (Section 6.3) and the improvement of the description of proton-nucleus reactions where exactly one nucleon is removed from the target nucleus (Section 6.4).

6.1 Model description

The Liège intranuclear cascade model (INCL) was conceived by Cugnon (1980) and developed with the help of many collaborators over the years (Boudard, Cugnon, David, et al. 2013; Boudard, Cugnon, Leray, et al. 2002; Cugnon 1982; Cugnon 1987; Cugnon 1992; Cugnon, Deneye, et al. 1989; Cugnon, Deneye, et al. 1990; Cugnon and Lombard 1984; Cugnon, Mizutani, et al. 1981; Cugnon, Volant, et al. 1997; Mancusi, Boudard, Cugnon, et al. 2014; Mancusi, Boudard, Carbonell, et al. 2015; Pedoux and Cugnon 2011). We will now briefly touch upon the characteristics of the Liège model that set it apart from the other incarnations of the INC model.

We mentioned in Chapter 5 that intranuclear cascade results from certain approximations to the K-body Schrödinger equation (Bunakov and Matvejev 1985). In this context, intranuclear cascade describes the propagation of energetic nucleons in a nucleus; the energetic nucleons are semi-classically described by their phase-space coordinates, while the nucleus is represented as a Fermi sea of nucleons. The incident particle can undergo collisions with the Fermi sea and excite particle-hole states; the secondary cascading nucleons are also treated semi-classically, while the hole states are identified by their quantum numbers.

This picture is more or less faithfully reproduced by most implementations of INC models, with a few variations. In many INC models, the nucleus is represented as a continuous Fermi sea (Mashnik, Gudima, et al. 2008; Yariv and Fraenkel 1979; Yariv and Fraenkel 1981). In the Liège model, on the other hand, the Fermi sea is realized as a semi-classical collection of nucleons, which are assumed to be bound in a potential representing the mean

field of the nucleon-nucleon interaction. There is no real distinction between cascading and target nucleons in INCL.

The semi-classical representation is admittedly difficult to justify for the Fermi-sea nucleons, which have wavelengths of the order of the nuclear size. However, one can argue that the traditional representation of the nucleus as a continuous Fermi sea is unable to model any correlation between the target nucleons, while the semi-classical representation is able to naturally capture at least part of the correlations. Indeed, continuous models need to resort to ad-hoc recipes aimed at capturing correlations. In the ISABEL model (Yariv and Fraenkel 1979; Yariv and Fraenkel 1981), for instance, a collision between a cascading nucleon and a Fermi-sea nucleon punches a "hole" in the Fermi sea, i.e. it slightly depletes the nuclear density around the collision point. The size of the hole and its lifetime are free parameters of the model and need to be adjusted on a phenomenological basis. In contrast, the Liège model does not need to introduce any specific treatment, because depletion is (again, at least partially) accounted for by the semi-classical representation.

In the mean-field picture, nucleons move around in a potential that varies smoothly with the particle position. Due to the short range of the nuclear forces, the shape of the potential resembles the shape of the nuclear density distribution (De Vries et al. 1987). Clearly, a smooth density distribution is important for the description of peripheral reactions, which are dominated by collisions happening at the surface of the nucleus. However, a smoothly varying potential well induces curved trajectories, which require numerical integration techniques for propagation. Because of this, INCL uses a simpler nuclear potential model. Instead of a smoothly varying potential, each nucleon sees a spherical potential well. The smooth density distribution is recovered via a clever superposition of potential wells of different radii. Specifically, the radius of the well is assumed to depend on the nucleon kinetic energy; Boudard, Cugnon, Leray, et al. (2002) showed that any spherically symmetric density distribution can be modelled this way, on condition that the radial distribution is monotonically decreasing.

Further details about the reference version of the INCL model can be found in Boudard, Cugnon, Leray, et al. (2002).

6.2 Cluster production

High-energy nucleon-nucleus reactions are well known for *spallation*, which is generally intended as the production of a large amount of small fragments[1]. The most commonly occurring fragments are neutrons and protons, as it is known since the inception of the accelerator era (Serber 1947). However, it is an experimentally established fact that spallation reactions also lead to the emission of heavier fragments, such as deuterons, tritons, ^{3}He and ^{4}He nuclei (Bertrand and Peelle 1973; Cowley et al. 1996; Guertin et al. 2005; Herbach et al. 2006; Letourneau et al. 2002; PISA Collaboration, Bubak, et al. 2007; PISA Collaboration, Budzanowski, et al. 2008; PISA Collaboration, Budzanowski, et al. 2009). Emission of heavier nuclei is also possible. In the context of spallation reactions, the emission of such particles is often referred to as **cluster production**. Clusters go by many other names in the literature, often with slightly different connotations. Among the most commonly employed terms we cite *light ions*, *light nuclei*, *intermediate mass fragments* (IMFs, especially

[1]The term was imported from solid mechanics, where it is used to describe the ejection of splinters from the impact between a projectile and a target.

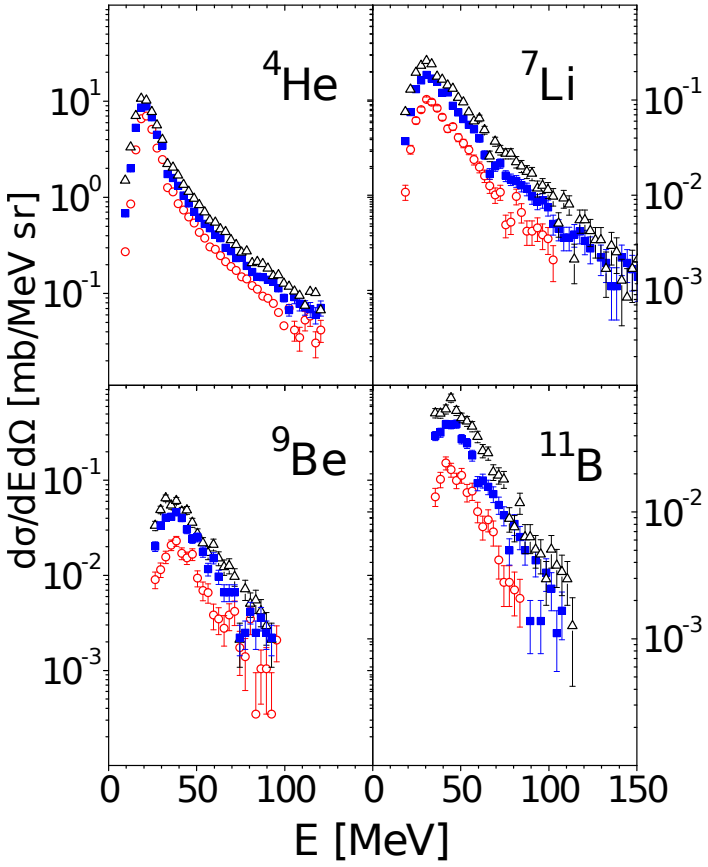

Figure 6.1: Typical spectra of ^{4}He, ^{7}Li, ^{9}Be, and ^{11}B ejectiles (upper left, upper right, lower left, and lower right parts of the figure, respectively) measured at 35° for three energies of the proton beam (1.2 GeV, 1.9 GeV, and 2.5 GeV) impinging onto an Au target. Open circles represent the lowest energy, full squares represent the intermediate energy, and open triangles represent the highest energy. Adapted from PISA Collaboration, Budzanowski, et al. (2008), with permission.

in the context of de-excitation models), *composite particles*, *light charged particles*, and *light heavy ions* (yes, really: Brandan and Satchler 1997).

Similarly to neutron and proton emission, the production of clusters in spallation reactions appears to be due to multiple mechanisms. Figure 6.1 shows several examples of experimental double-differential cross sections for the emission of light nuclei from high-energy proton-nucleus reactions. Such spectra are known to be broadly compatible with phenomenological moving source emission mechanism (PISA Collaboration, Bubak, et al. 2007; PISA Collaboration, Budzanowski, et al. 2008; PISA Collaboration, Budzanowski, et al. 2009). In this framework, the shape of the spectra are interpreted as the superposition of a thermal particle sources at rest in the laboratory frame, and one or more moving thermal particle sources.

It is of course very tempting to look at the moving sources through the lens of the two-stage reaction model of Section 5.1. Indeed, the source at rest can be naturally identified with the statistical de-excitation stage, which involves emission from a thermalized source with a very small recoil velocity. The out-of-equilibrium nuclear-reaction stage (involving intranuclear-cascade and possibly pre-equilibrium models) would then be responsible for the emission of the moving sources.

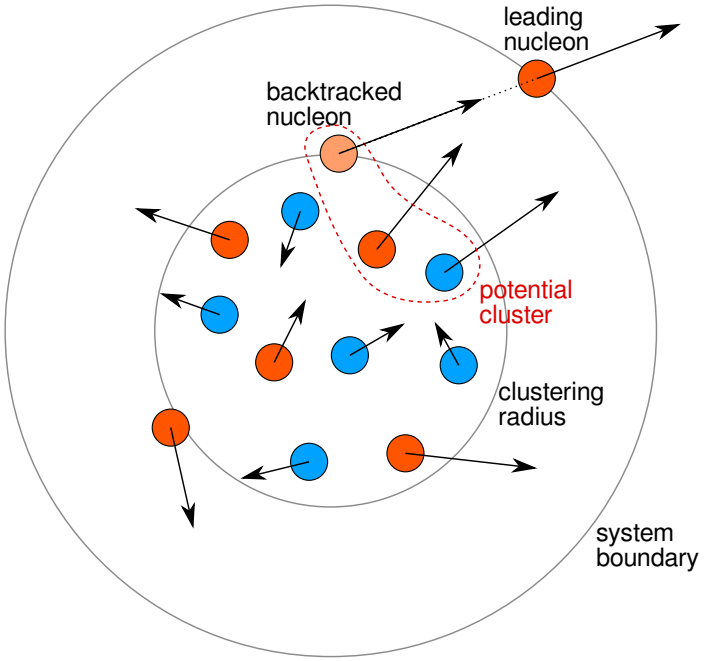

Figure 6.2: Schematic view of the INCL clustering model. Arrows represent the nucleon momenta.

Historically, there have been many attempts to generalize INC, pre-equilibrium and statistical de-excitation models to accommodate the emission of light clusters (Charity, McMahan, et al. 1988; Kelić et al. 2008; Toneev and Gudima 1983; Wright and Kelsey 2015). In this section, I wish to focus in particular on the extension of the INCL model (Boudard, Cugnon, David, et al. 2013).

6.2.1 The INCL coalescence model

Cluster production in INCL proceeds via **coalescence**, a term which broadly refers to any model where clusters are produced by aggregating several nucleons in the system. In some coalescence models (Toneev and Gudima 1983), clusters are formed *ex post*, using the nucleons emitted during the INC phase. Typically, nucleons are assumed to coalesce if they are "close" in momentum space; the critical momentum distance is typically a free parameter of such models.

The INCL coalescence model is more sophisticated, because coalescence takes place in *phase space*; the distance in both momentum space and configuration space plays a role. This choice does not really increase the number of free parameters of the model. The INCL clustering model is schematically represented in Fig. 6.2. Clustering is triggered when a nucleon reaches the system boundary (a sphere of radius R_{max}) and is about to leave the system. However, the position of the leading nucleon considered by the clustering algorithm is not the position on the system boundary. In fact, since R_{max} is typically much larger than the nuclear radius[2], the region around the leading nucleon will be relatively devoid of nucleons. Besides, if we were to use the leading nucleon as a coalescence seed, the result of the clustering procedure would depend on the radius of the system boundary, which is

[2]In a proton-nucleus reactions at 1 GeV, for instance, $R_{\text{max}} = 12.2$ fm, which should be compared to a typical half-density radius for ^{208}Pb of 6.6 fm.

parameter	value
h	1 fm
$h_0(2)$	424 fm MeV/c
$h_0(3)$	300 fm MeV/c
$h_0(4)$	300 fm MeV/c
$h_0(A)$ ($A > 4$)	210 $A^{1/3}$ fm MeV/c
$\mu_{\text{cl}}^{\text{min}}$	0.7

Table 6.1: Free parameters of the INCL clustering model.

only a calculation parameter and does not have any physical meaning. For this reason, the leading nucleon first backtracks along its line of flight until it meets the *clustering sphere*; the clustering radius D is a free parameter of the model, and it is fixed as $D = R_0 + h$, where R_0 is the half-density nuclear radius and $h = 1$ fm.

Next, *all* potential clusters are incrementally constructed, starting with the backtracked leading nucleon (which is considered as a cluster of mass $A_{\text{cl}} = 1$) and up to some maximum cluster mass $A_{\text{cl}}^{\text{max}}$. Let $\boldsymbol{j} = \{j_1, \ldots, j_{A_{\text{cl}}}\}$ be the indices of the A_{cl} selected nucleons, $\boldsymbol{r}_{\text{cl}}(\boldsymbol{j})$ the coordinates of the center of mass of the cluster and $\boldsymbol{p}_{\text{cl}}(\boldsymbol{j})$ the total momentum of the cluster. The i-th nucleon is assumed to coalesce with the cluster if the following phase-space proximity condition is satisfied:

$$|\boldsymbol{r}_i - \boldsymbol{r}_{\text{cl}}(\boldsymbol{j})| \cdot |\boldsymbol{p}_i - \boldsymbol{p}_{\text{cl}}(\boldsymbol{j})| < h_0(A+1).$$

Here h_0 is a free parameter. Its values for $A \leq 4$ are explicitly fixed, and a simple systematics is used for $A > 4$, as given in Table 6.1.

Once all the clusters have been built, the "less virtual" cluster is selected. Let $\sqrt{s}(\boldsymbol{j})$ be the Mandelstam variable representing the total center-of-mass energy of the cluster. We consider the "virtuality"

$$v(\boldsymbol{j}) = \left[\sqrt{s}(\boldsymbol{j}) - \sum_{j \in \boldsymbol{j}} m_j - B_{\text{cl}}(Z_{\text{cl}}, N_{\text{cl}})\right] \Big/ A_{\text{cl}}. \tag{6.1}$$

Here m_j is the mass of the j-th nucleon, Z_{cl} and N_{cl} are respectively the numbers of protons and neutrons in the cluster, and $B_{\text{cl}}(Z, N)$ is the experimental binding energy. The cluster that minimizes $v(\boldsymbol{j})$ is selected. Eq. (6.1) can be interpreted as the excitation energy per nucleon of the cluster, diminished by twice the binding energy per nucleon. The introduction of this quantity is largely phenomenological and is solely justified by the relative success of the model.

The candidate cluster is only emitted if three conditions are met:

1. The total kinetic energy of the cluster must be positive, i.e.

$$T_{\text{cl}} = \sum_{j \in \boldsymbol{j}} (T_j - V_j) - B_{\text{cl}} > 0,$$

   where T_j and V_j are the kinetic and potential energy of the j-th nucleon in the nucleus.

2. The cluster must penetrate the Coulomb barrier.

3. Emission of the candidate cluster must be "radial": the angle θ_{cl} between the total cluster momentum and the radial direction must satisfy $\cos\theta_{\mathrm{cl}} > \mu_{\mathrm{cl}}^{\mathrm{min}}$. This condition, which can be qualitatively justified by considering that clusters are unlikely to survive a long time in the nuclear surface, is admittedly required to suppress an otherwise abundant cluster emission at low energies.

If any of these tests fails, execution of the INCL code resumes as normal by considering the possibility of emitting the leading nucleon, according to the standard INCL rules (Boudard, Cugnon, Leray, et al. 2002).

This clustering model is admittedly highly phenomenological. It has six free parameters, plus a number of more or less arbitrary choices. However, it is perhaps worth stressing that a much simpler model is actually sufficient for the reproduction of high-energy data only (Boudard, Cugnon, Leray, et al. 2004). In the simplified model, for example, only one free phase-space parameter is used, and priority is always given to the heaviest possible cluster. The extended clustering model is only necessary if one wishes INCL to describe cluster emission at low energy (< 200 MeV), a phenomenon which is at the limit of the domain of validity of intranuclear cascade.

6.2.2 Results

We present here a few results obtained with the INCL coalescence model. Since clusters can also be produced during the de-excitation phase, it is necessary to couple INCL to a statistical de-excitation model in order to perform a meaningful comparison with the experimental data. These results were obtained with INCL/ABLA07, ABLA07 being the traditional companion de-excitation model to INCL (Kelić et al. 2008). Without going into too much detail about its ingredients, suffice it to say that ABLA07 models the emission of light nuclei as generalized evaporation. The model considers all possible ejectiles up to the Businaro-Gallone maximum of the mass-asymmetry-dependent barrier (Businaro and Gallone 1955a; Businaro and Gallone 1955b).

Figure 6.3 shows a plot of the double-differential cross section for the emission of ^{2}H, ^{3}H, ^{2}He, and ^{4}He, from a high-energy proton-induced reaction (p + ^{197}Au). Analysis of the calculation results shows that the spectra are characterized by two components. The evaporation component is roughly isotropic and it is characterized by an energy of the order of 10 MeV to 20 MeV. The cascade component is forward-peaked and it extends to very high energies; for this particular reaction, the INCL model predicts that clusters can be emitted at essentially any energy up to the beam energy, albeit the cross section drops quickly above $\sim$ 150 MeV. Unfortunately, experimental data are not available above the same energy. However, it is reasonable to assume that the emission of such high-energy clusters is sensitive to the details of the momentum distribution of the target nucleons in the surface, at momenta close to the surface of the Fermi sea. The INCL nuclear model is probably too simple to account for these phenomena (although see Section 6.4 below).

The overall agreement between the calculation and the experimental data can be considered to be quite good. The global trend of the experimental data is correctly reproduced, with occasional discrepancies of up to a factor of 2. However, the low-energy part of all the spectra is somewhat underestimated, although the impact on the integrated cross section is probably small. This effect is probably due to the modelling of the Coulomb barrier for cluster emission in ABLA07.

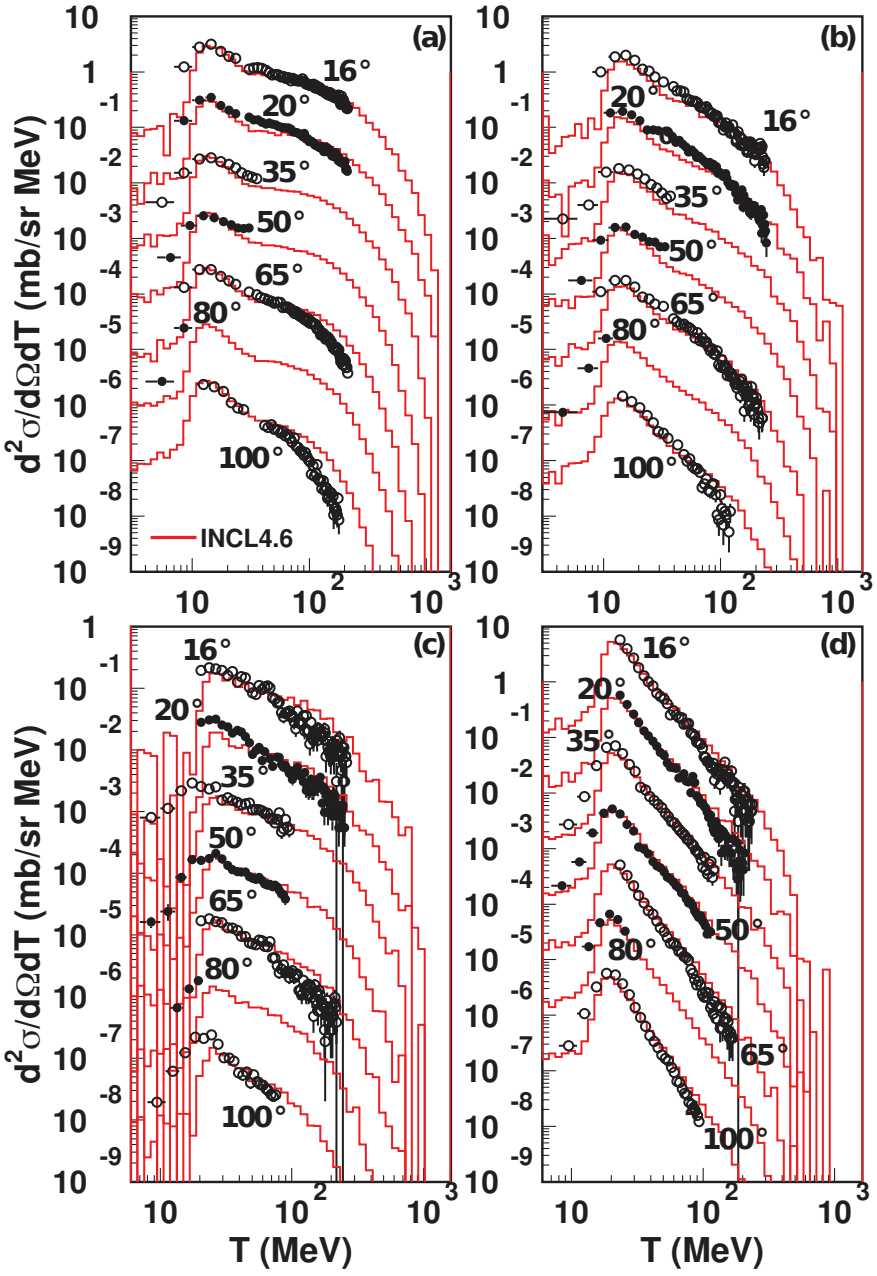

Figure 6.3: Double-differential energy-angle cross section for the emission of ^{2}H (a), ^{3}H (b), ^{3}He (c) and ^{4}He (d) from a 1.2 GeV p + ^{197}Au reaction. The points are experimental data (PISA Collaboration, Budzanowski, et al. 2008). The red lines represent the result of an INCL/ABLA07 calculation. In order to fit all the data on the same figure, the spectra are multiplied by 10^{0}, 10^{-1}, 10^{-2}, etc., for increasing angles, starting at the lowest angle. Adapted from Boudard, Cugnon, David, et al. (2013), with permission.

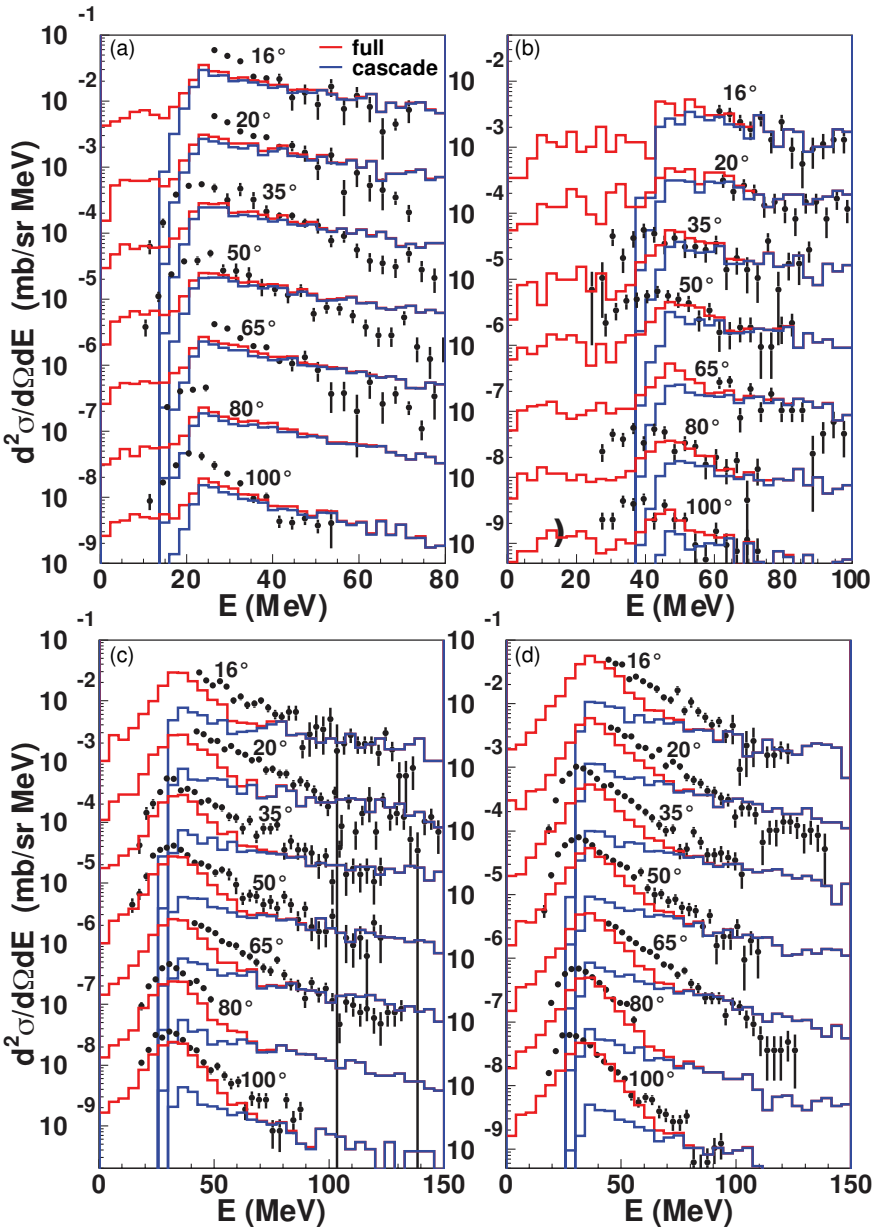

Figure 6.4: Double-differential energy-angle cross section for the emission of ^{6}He (a), ^{7}Be (b), ^{6}Li (c) and ^{7}Li (d) from a 1.2 GeV p + ^{197}Au reaction. The points are experimental data (Herbach et al. 2006). The red lines represent the result of an INCL/ABLA07 calculation. The blue lines represent the contribution of the INCL stage alone. Spectra are rescaled according to the same convention as in Fig. 6.3. Adapted from Boudard, Cugnon, David, et al. (2013), with permission.

ejectile	$1.2\,\mathrm{GeV p} + {}^{197}\mathrm{Au}$		$63\,\mathrm{MeV p} + {}^{208}\mathrm{Pb}$	
	cascade	evaporation	cascade	evaporation
^{2}H	$\mathbf{5.05 \times 10^{-1}}$	1.66×10^{-1}	$\mathbf{3.35 \times 10^{-2}}$	3.5×10^{-4}
^{3}H	$\mathbf{1.24 \times 10^{-1}}$	8.1×10^{-2}	$\mathbf{1.02 \times 10^{-2}}$	1.1×10^{-4}
^{3}He	$\mathbf{4.6 \times 10^{-2}}$	6.7×10^{-3}	$\mathbf{1.47 \times 10^{-3}}$	0
^{4}He	1.67×10^{-1}	$\mathbf{3.52 \times 10^{-1}}$	1.41×10^{-2}	1.36×10^{-2}

Table 6.2: Average multiplicity of clusters produced in cascade and in evaporation stages for two systems, as given by the INCL/ABLA07 model. The numbers in boldface indicate the dominant component, if it is clearly defined. Adapted from Boudard, Cugnon, David, et al. (2013), with permission.

Similar conclusions can be drawn from the analysis of the spectra for heavier clusters. Figure 6.4 shows the spectra for ^{6}He, ^{7}Be, ^{6}Li, and ^{7}Li, from the same p + ^{197}Au reaction. Again, the experimental data stop around 150 MeV, which makes it hard to evaluate the accuracy of the high-energy part of the cascade component. Nevertheless, the model predictions are roughly in the ballpark. This is not a trivial result, since the integrated cross sections for the production of heavy clusters are sensibly different; for instance, the ^{6}He yield is about an order of magnitude larger than the ^{7}Be yield, and about two orders of magnitude smaller than the ^{4}He yield. Cascade dominates the integrated ^{6}He and ^{7}Be yields; it is also the dominating mechanism for the production of high-energy (> 60 MeV) ^{6}Li and ^{7}Li. The shape of the spectra is generally reasonably reproduced, although the cascade component appears to be too hard; these observations seems to be confirmed by other calculations at lower incident energies (~ 200 MeV), but these results are not shown here for the sake of conciseness.

All things considered, the coalescence mechanism is relatively successful in describing the production of clusters from high-energy reactions, although not all the details of the spectra are correctly reproduced. This suggests that coalescence is more than a modelling "trick"; it is a physical mechanism that participates in the production of high-energy clusters.

We conclude this section with a brief incursion in the realm of low-energy reactions, which is generally considered to be out of reach for INC models. Figure 6.5 shows double-differential spectra for the productions of the four light clusters ($A \leq 4$) from p + ^{208}Pb at 63 MeV. At such incident energy, the excitation energy of the cascade remnant is fairly small, hindering charged-particle evaporation. Thus, cascade largely dominates the production of clusters. The global trend of the data is remarkably well reproduced by INCL. Discrepancies with the experimental data are most apparent in the low-energy and high-energy ends of the spectra. At low energy, it appears like the Coulomb barrier used by INCL is too high, and perhaps too sharp; the barrier for ^{4}He, for instance, is of the order of 25 MeV, while the evaporation barrier is of the order of 15 MeV. At high energy, the spectra show a forward-peaked structure that is clearly due to coherent scattering mechanisms; as such, we do not expect it to be reproducible by INC. Finally, it is worth stressing that cluster yields at low incident energy are heavily influenced by the "radial emission" cut described in Section 6.2.1 above. Without this criterion, the production of clusters is much larger than the experimental observations.

As discussed in Section 5.2, the relative success of INCL at low energy is somewhat surprising. The intranuclear-cascade model is not justified in this energy range, and it is not expected to be able to describe the production of composite particles; and yet, it manages

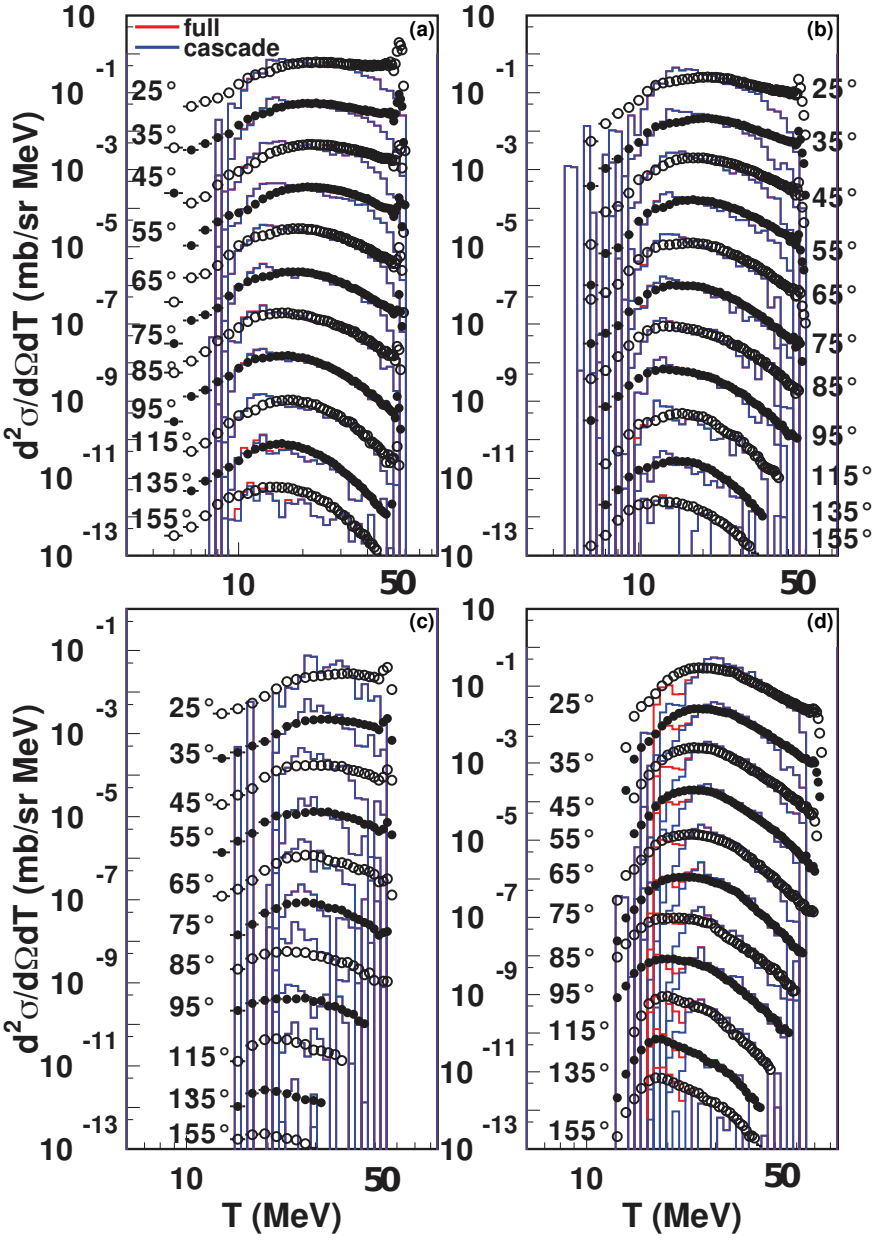

Figure 6.5: Double-differential energy-angle cross section for the emission of ^{2}H (a), ^{3}H (b), ^{3}He (c) and ^{4}He (d) from a 63 MeV p + ^{208}Pb reaction. The points are experimental data (Guertin et al. 2005). The red lines represent the result of an INCL/ABLA07 calculation. The blue lines represent the contribution of the INCL stage alone. Spectra are rescaled according to the same convention as in Fig. 6.3. Adapted from Boudard, Cugnon, David, et al. (2013), with permission.

to capture the essential features of this phenomenon.

More comprehensive comparisons with experimental data for cluster emission were performed in the context of the Benchmark of Spallation Models (David 2015), an international intercomparison effort organized under the auspices of IAEA in 2008 involving 17 nuclear-reaction codes. Among these, we included the results of couplings between INCL and other statistical de-excitation models (Botvina et al. 1987; Charity, McMahan, et al. 1988; Mancusi, Charity, et al. 2010), which fared quite well overall. Many different observables were considered. The intercomparison results are invaluable to evaluate the sensitivity of the various reaction observables to the ingredients of the INC state and the de-excitation stage.

6.3 Extension to nucleus-nucleus reactions

Reactions involving light nuclei play an important role in several applications. In hadrontherapy, for instance, cancer patients are treated using accelerated beams of protons or light nuclei (Kraft 1990; Kraft 2000). Nuclear reactions between the beam particles and the body of the patient can be responsible for dose deposition outside the clinical target volume, which is undesirable. The radiation environment in space also involves energetic protons and heavy ions (Durante 2002). The Galactic Cosmic Rays are one of the contributing sources to radiation in the Solar System; their hadronic component mainly consists of protons and alpha particles, but ions as heavy as iron are known to yield sizable contributions to the equivalent dose absorbed by space crews. Nuclear reactions induced by light nuclei are also involved in the production of beams of unstable nuclei. The in-flight projectile-fragmentation method (Morrissey and Sherrill 1998) is often realized using ^{9}Be production targets. Radioactive beams produced with the ISOL method (Ravn 1998) typically rely on light charged particles (LCPs) to induce spallation or fission in the production target. In either case, the luminosity of the secondary beam crucially depends on the fragment yields in light-ion-induced reactions. Reactions on light nuclei are also often used in fundamental research at the limits of nuclear stability, for instance in the quest for very neutron-rich or neutron-poor residues (e.g. Alvarez-Pol et al. 2010; Benlliure, Fernández-Ordóñez, et al. 2008; Benlliure, Kurtukian-Nieto, et al. 2007; Blank et al. 1994; Kurcewicz et al. 2006; Stolz et al. 2002).

The applications listed above typically involve projectile energies of the order of a few tens to several hundreds or even thousands of MeV per nucleon. Since INC in general, and INCL in particular, is quite successful in describing several observables of nucleon-nucleus reactions in this energy range, it is quite natural to consider the possibility to extend the model to light incident nuclei. This is not a novel idea: INC models have a long tradition of nucleus-nucleus extensions (e.g. Yariv and Fraenkel 1979; Yariv and Fraenkel 1981), with mixed success. As far as INCL is concerned, a simple extension to light-ion-induced reactions, based on an old FORTRAN77 version of the model, was attempted in 2011 (Kaitaniemi et al. 2011). The model yielded promising physical results, but maintaining the code quickly grew to the proportions of a formidable task. This was mainly due to the fact that the FORTRAN77 version was monolithic, hardly flexible and not very legible from the start. This is one of the motivations that led us to redesign the INCL code from scratch and cast it in modern, object-oriented C++.

I wish to spend just a few words on the rewriting of the INCL code. The FORTRAN77 version (INCL4.6) stood at about 19 kSLOC (physical source lines of code, excluding blanks

and comments). According to a Basic Constructive Cost Model (Basic COCOMO, Kemerer 1987), this corresponds to an effort of about 4 person-years; of course this only accounts for software development, and not for the research effort in nuclear physics. The initial C++ conversion, targeting the same set of features as INCL4.6, resulted in a slightly smaller code base, of the order of 16 kSLOC. Basic COCOMO yields again a development effort of the order of 4 person-years. Reviving old, unmaintainable scientific software by rewriting it in a more modern language is a crucial task that needs to be performed every so often; however, it is very difficult for young researchers to draw any value from this kind of work in the form of publications, grants, and so on. The C++ incarnation of INCL is the fruit of the effort of several persons, and it is my personal opinion that it deserved better recognition than a short paragraph in an article on another subject (Mancusi, Boudard, Cugnon, et al. 2014).

6.3.1 Challenges

Let us go back to the main topic of this section, which is the extension of INCL to reactions induced by light ions. The treatment of nucleus-nucleus reactions in an INC framework poses several challenges that do not apply to nucleon-nucleus reactions. First and foremost, there is no natural way of accounting for the binding of the projectile nucleus within the INC scheme. The cascade takes place in a single mean-field potential, which is typically assumed to be that of the target nucleus; this essentially amounts to neglecting the mean-field interaction between the projectile constituents. This approximation might be tenable for central collisions of a light projectile on a heavy target, which rarely lead to the emission of a projectile-like fragment; however, it is clear that no model can describe projectile fragmentation if the binding of the projectile nucleons is neglected. Second, INC models typically do not treat the mean-field potentials as dynamical quantities and assume that they do not evolve during the cascade phase. This is justifiable for nucleon-nucleus reactions, where only a relatively small fraction of the nucleons directly participates in the reaction, but it is clear that pre-fragments produced in nucleus-nucleus reactions can be very different from the initial reaction partners. Therefore, any collective rearrangement of the mean field is beyond the reach of traditional INC models. Third, nucleons in nuclei are endowed with Fermi motion. A realistic description of the intrinsic momentum content of both reaction partners is necessary for an accurate description of certain observables. This is somewhat at odds with the independent-particle Fermi-gas model that is typically used to describe the structure of the reaction partners, especially for light nuclei. The definition of Pauli blocking is unambiguous only if the initial momentum distribution of the nucleons is assumed to be a hard, uniform Fermi sphere. It is well-known however that nucleons in light nuclei exhibit smoother distributions (de Witt Huberts 1990), which manifest themselves (among other things) in the momenta of nucleons from the break-up of the projectile.

Clearly, a faithful description of the collective behavior of symmetric nucleus-nucleus reactions is beyond the reach of any INC model. It is possible however to obtain a reasonably accurate phenomenological description of reactions induced by light nuclei with a few practical decisions and a bit of suspension of disbelief. The approach taken by INCL is to constrain the model predictions via the respect of global conservation laws. For the sake of conciseness, we will only detail the most important aspects of the nucleus-nucleus extension below. The interested Reader is encouraged to consult Mancusi, Boudard, Cugnon, et al. (2014) for a painstakingly detailed description of all the relevant modelling choices

made in INCL.

6.3.2 The projectile nucleus

The first step in the simulation of a light-ion-induced reaction is the preparation of the projectile and target nuclei. Since the preparation of the target is standard for INCL, we refer the Reader to Boudard, Cugnon, Leray, et al. (2002) and we limit ourselves to describing the preparation of the projectile in its center-of-mass frame.

We assume that the density distribution for the nucleons is given. The positions $\boldsymbol{\rho}_i$ of the nucleons in the center-of-mass frame are determined in such a way that the first and second central moments of their distribution are "correct", i.e. the first moment vanishes and the second moment is equal to the second moment of the assumed empirical density distribution. Also, the $\boldsymbol{\rho}_i$ vectors roughly follow the assumed distribution. Deviations from the shape of the assumed distribution are smaller if the number of nucleons is larger; if the assumed distribution is Gaussian, then the $\boldsymbol{\rho}_i$ vectors exactly follow the assumed distribution. The center-of-mass momenta of the projectile nucleons $\boldsymbol{\pi}_i$ are constructed in a similar way. Since the momentum distributions are taken to be Gaussian for all projectile nuclei, the generated momenta are normally distributed with the correct width parameter and sum up to zero total momentum, as appropriate for the center-of-mass system.

We choose to account for the projectile binding by putting the nucleons off their mass shell. It is assumed that the center-of-mass nucleon energies ε_i are given by

$$\varepsilon_i = \sqrt{{\boldsymbol{\pi}_i}^2 + m^2} - V_p,$$

where m is the common proton-neutron mass used in INCL and V_p is the *dynamical pseudopotential*. This quantity is used to enforce the nominal dispersion law for the projectile nucleus in the center-of-mass frame and in the laboratory frame, namely:

$$\begin{aligned} \sum \varepsilon_i &= M_p, && \text{(center of mass)} \\ \sum \boldsymbol{\pi}_i &= 0. \end{aligned}$$

and

$$\begin{aligned} \sum e_i &= E_p && \text{(laboratory)} \\ \sum \boldsymbol{p}_i &= \boldsymbol{P}_p, \end{aligned}$$

with M_p, E_p and $\boldsymbol{P}_p$ being the nominal mass, energy and momentum of the projectile nucleus in the laboratory frame, and $(e_i, \boldsymbol{p}_i)$ being the four-momenta of the nucleons in the laboratory frame. Although the dynamical pseudopotential is merely a unphysical calculation device, it has the right order of magnitude for light nuclei (a few tens of MeV) and it is always positive (see Mancusi, Boudard, Cugnon, et al. 2014, for more details).

An important ingredient of the nucleus-nucleus extension is the assumption that projectile nucleons propagate with the (Coulomb-distorted) collective velocity of the projectile beam until they undergo a collision. As a consequence, projectile nucleons can immediately be divided in two classes: those whose trajectory intersects the INCL calculation volume are labeled as *geometrical participants*; the others are called *geometrical spectators*. The distinction between geometrical participants and spectators is not physical, because it is a

consequence of the finite radius of the INCL calculation volume, $R_{\max}$, which is *not* a physical parameter. Ideally, the model predictions (e.g. cross sections) should be completely independent of $R_{\max}$ (for sufficiently large values of $R_{\max}$). In reaction models such as quantum molecular dynamics (QMD; Aichelin 1991), there is no difference between projectile and target nucleons. The nuclear force is modeled as the result of pairwise nucleon interactions, which naturally generate the projectile and the target mean fields. In INC-type models, as discussed above, it is difficult to treat the mean field as a true dynamic quantity. The complexity of the projectile preparation algorithm described here reflects this limitation of INC. One of the main concerns of the INCL nucleus-nucleus extension is therefore to blur the distinction between the treatment of projectile and target nuclei. In regard to geometrical spectators and participants in particular, they should be treated on exactly the same footing, but this is not always possible in INCL (see below).

6.3.3 The INC phase

The INC phase of nucleus-nucleus reactions is pretty similar to standard INCL. The main differences concern the entrance and the exit of nucleons from the calculation volume. In particular, nucleons that enter the calculation volume undergo two modifications. First, their energy is adjusted to accommodate the Q-value for the transfer reaction from the projectile nucleus to the target nucleus, and possibly the energy transferred to the projectile nucleus, which may be left in an excited state. These corrections are necessary in order to ensure that the energy conservation law holds, taking into account the real particle masses. Second, since cascading nucleons in INCL are always assumed to be on mass shell, the entering nucleons are put on mass shell by rescaling their momenta. These modifications are only applied to particles that enter the calculation volume; in particular, they are never applied to geometrical spectators. Clearly, this breaks the desirable symmetry of treatment between geometrical spectators and participants.

At the end of the intranuclear cascade, a projectile pre-fragment may be defined if some nucleons missed the calculation volume (geometrical spectators) or traversed the calculation volume without undergoing any collision (dynamical spectators). If no dynamical spectators are present, the mass, charge, excitation energy and state of motion of the projectile pre-fragment are already defined (they are those of the geometrical spectators) and are guaranteed to satisfy four-momentum conservation. However, if dynamical spectators are present and are to be merged back into the projectile-like pre-fragment, some adjustment is necessary to make sure that the resulting pre-fragment is well-defined. Indeed, the application of empirical thresholds for particle absorption/emission may result in a net energy transfer between the dynamical spectators and the target, possibly resulting in negative projectile excitation energies.

We then tentatively define the pre-fragment four-momentum as the sum of the four-momenta of the dynamical and geometrical spectators. If the resulting four-momentum leads to a negative excitation energy, we apply a greedy iterative procedure to determine the maximal number of dynamical spectators that can be incorporated in the pre-fragment without leading to negative excitation energy. This is done as follows: we start from a candidate pre-fragment consisting of A nucleons, with negative excitation energy. We remove the dynamical spectator that maximizes the excitation energy of the remaining $A - 1$ nucleons. If the resulting excitation energy is non-negative, we stop; otherwise, we keep removing dynamical participants until either the excitation energy of the pre-fragment is non-negative

or we have removed all the dynamical spectators. In the latter case, the excitation energy of the projectile-like pre-fragment reduces to that of the geometrical spectators, which is guaranteed to be non-negative.

From our discussion it clearly emerges that, despite our efforts, dynamical and geometrical spectators are not (and cannot) be treated on exactly the same footing. The crucial reason for this is that the four-momenta of dynamical spectators are perturbed when they enter the target nucleus. Indeed, their energy is corrected to keep the energy balance satisfied and to possibly make room for some excitation energy of the projectile-like pre-fragment.

6.3.4 Low-energy fusion model

So far, we have implicitly assumed that the transfer of one nucleon from the projectile to the target is always possible. However, serious conceptual and technical complications arise if the kinetic energy of one of the entering nucleons is lower than the Fermi energy of the target. One would expect such a process to be forbidden by the Pauli exclusion principle, especially for the first projectile nucleon entering the unperturbed target Fermi sea. This difficulty has already been encountered in the extension of the FORTRAN version of INCL to light incident clusters (Kaitaniemi et al. 2011). In that case, it was observed that the problematic circumstance is most likely to occur when the projectile kinetic energy per nucleon is comparable to or smaller than the dynamical projectile pseudopotential. Under these conditions, it seems reasonable to assume that, independently of the details of the dynamics, most of the incoming nucleons will be trapped by the target potential well, resulting in (possibly incomplete) fusion of the projectile and the target. This argument is especially cogent for reactions between a light composite particle ($A \leq 4$) and a large nucleus.

Therefore, for problematic events, INCL abandons normal INC in favor of a simple geometrical fusion model if, at any moment during the intranuclear cascade, the particle-entry procedure (see above) endows the entering projectile nucleon with a kinetic energy lower than the target Fermi energy. Normal intranuclear cascade is then abandoned, but the information about the initial position and momenta of the projectile nucleons is retained. In the spirit of critical-distance fusion models (Bass 1974; Galin et al. 1974), we define an *interaction radius* R_{int} and we prescribe that only nucleons whose collective trajectory intersects the sphere of radius R_{int} will fuse with the target nucleus. The interaction radius is defined as

$$R_{\text{int}} = R_0 + d_{\text{int}}$$

in terms of the *interaction distance* d_{int},

$$d_{\text{int}} = \sqrt{\max\left(\sigma_{pp}, \sigma_{nn}, \sigma_{pn}\right)/\pi},$$

where the elementary nucleon-nucleon cross sections σ_i are calculated at the nominal kinetic energy per nucleon of the light-ion projectile.

Nucleons that miss the interaction sphere are assumed not to fuse with the target and are collectively considered as a projectile-like pre-fragment. This defines another (possibly excited) source and is expected to mimic incomplete fusion. The four-momentum of the compound nucleus (the source composed of the target and the fusing nucleons) is defined as the difference between the initial total four-momentum and the four-momentum of the projectile-like pre-fragment. If the compound-nucleus four-momentum corresponds to

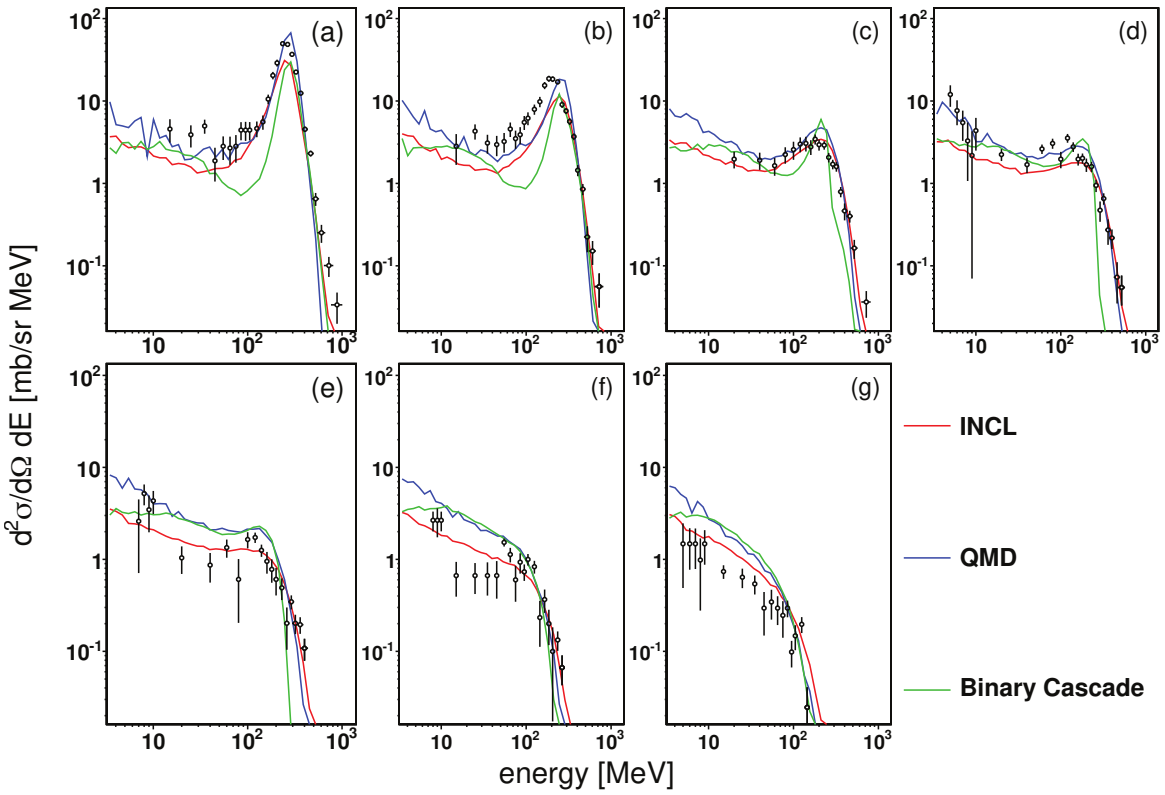

Figure 6.6: Double-differential cross sections for neutron production at (a) 5°, (b) 10°, (c) 20°, (d) 30°, (e) 40°, (f) 60° and (g) 80°, from a 290 A MeV $^{12}\mathrm{C} + \mathrm{C}$ reaction, as calculated by INCL, QMD, and BIC. All models are coupled to G4ExcitationHandler. Experimental data are taken from Iwata et al. (2001). Adapted from Mancusi, Boudard, Cugnon, et al. (2014), with permission.

negative excitation energy, the event is discarded and treated as a non-reaction. As a consequence, and in accordance with known phenomenology, incomplete fusion at low projectile kinetic energy is automatically suppressed because energetically forbidden.

6.3.5 Results

We illustrate the predictions of the INCL nucleus-nucleus extension with a few examples. Figure 6.6 shows the predictions for the double-differential cross section for neutron production for the $^{12}\mathrm{C} + \mathrm{C}$ reaction at 290 MeV per nucleon. Figure 6.7 shows the same observable for the $^{4}\mathrm{He} + \mathrm{Cu}$ reaction at 230 MeV per nucleon. The INCL results are compared to the results of other Geant4 reaction models: the Binary Cascade model (BIC, Folger et al. 2004) and Quantum Molecular Dynamics (QMD, Mancusi, Niita, et al. 2009; Niita, Chiba, et al. 1995). For the $^{4}\mathrm{He} + \mathrm{Cu}$ reaction, we also show the results of the Bertini+PreCompound model (Wright and Kelsey 2015). All models are coupled to the G4ExcitationHandler statistical de-excitation model (Quesada et al. 2011), except Bertini+PreCompound, which includes its own internal de-excitation model.

One notices that the BIC predictions are generally in less good agreement with the experimental data than INCL. The QMD results are everywhere comparable to or worse than the INCL calculation, except at the forward-most angle, which were shown to be improvable in INCL by using the empirical Fermi momentum (Mancusi, Boudard, Cugnon, et al.

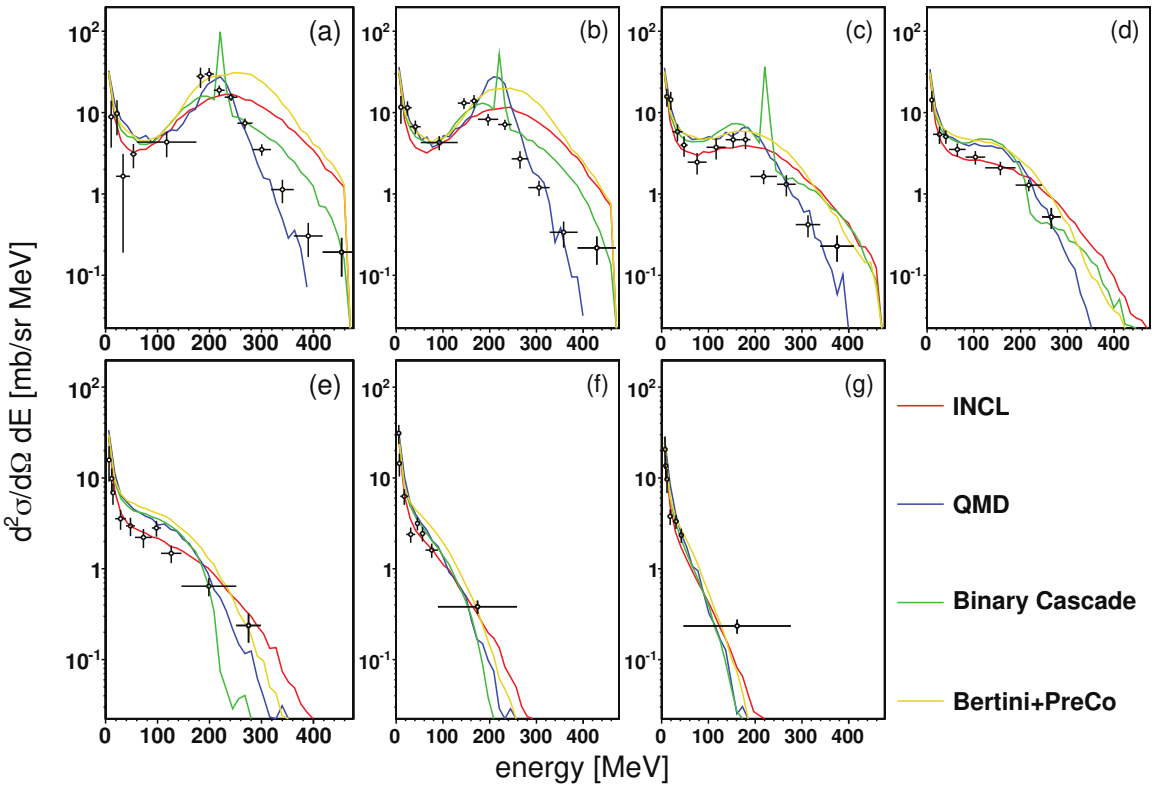

Figure 6.7: Double-differential cross sections for neutron production at (a) 4°, (b) 9°, (c) 20°, (d) 30°, (e) 40°, (f) 60° and (g) 80°, from a 230 A MeV ^{4}He + Cu reaction, as calculated by INCL, QMD, BIC, and Bertini+PreCompound. All models are coupled to G4ExcitationHandler, except Bertini+PreCompound which uses its own internal de-excitation module. Experimental data are taken from Heilbronn et al. (2007). Adapted from Mancusi, Boudard, Cugnon, et al. (2014), with permission.

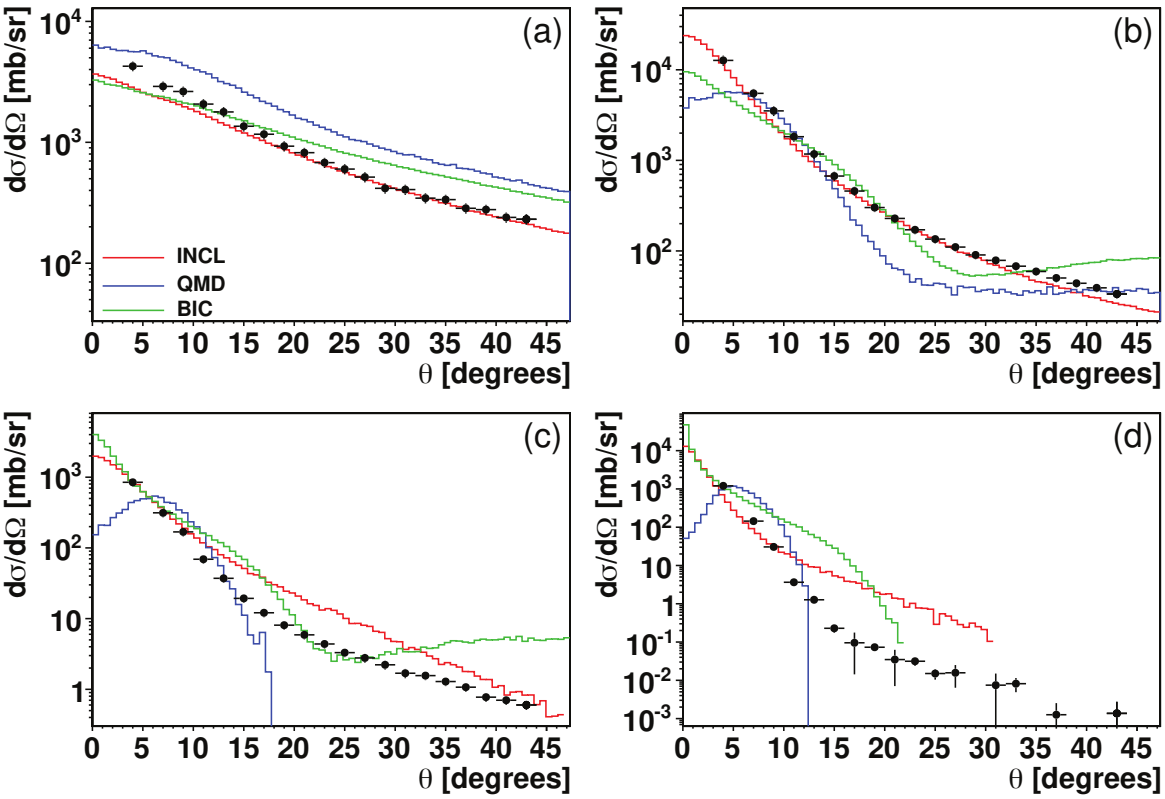

Figure 6.8: Angle-differential cross section for the production of (a) protons, (b) ^{4}He, (c) ^{7}Li and (d) ^{11}C from the 95 A MeV ^{12}C + ^{12}C reaction. Calculations with INCL , QMD and BIC are shown; all models except are coupled to G4ExcitationHandler. Experimental data are taken from Dudouet, Juliani, et al. (2013a) and Dudouet, Juliani, et al. (2013b). Adapted from Mancusi, Boudard, Cugnon, et al. (2014), with permission.

2014). Note also that the CPU time for QMD is about two orders of magnitude larger than for INCL. All the other models fail to describe the ^{4}He fragmentation peak, which (in view of the above) might suggest that they also employ unrealistic Fermi momenta for this projectile. In addition, the BIC model shows some unphysical structures at small angles for the ^{4}He + Cu system.

We now turn to the production of charged particles. We focus in particular on an experiment by Dudouet, Juliani, et al. (2013a) and Dudouet, Juliani, et al. (2013b), who measured double-differential cross sections for the production of several charged particles from reactions induced by a 95 A MeV ^{12}C beam on targets ranging from hydrogen to titanium. We are mostly interested in the carbon-target data for the purpose of verifying the INCL nucleus-nucleus extension. Calculations with some Geant4 models have been presented in Dudouet, Cussol, et al. (2014), where however the authors used an old version of the INCL model, which was shown above to be affected by serious drawbacks for the ^{12}C + ^{12}C reaction (Mancusi, Boudard, Cugnon, et al. 2014). Our results should be considered as the reference.

First, we observe that the incident energy (95 A MeV) is rather low. The conditions for the applicability of the intranuclear-cascade hypothesis (independent binary nucleon-nucleon collisions) are not very well fulfilled here. Moreover, INCL's low-energy fusion sector is responsible for 43% of the reaction cross section, which is far from negligible.

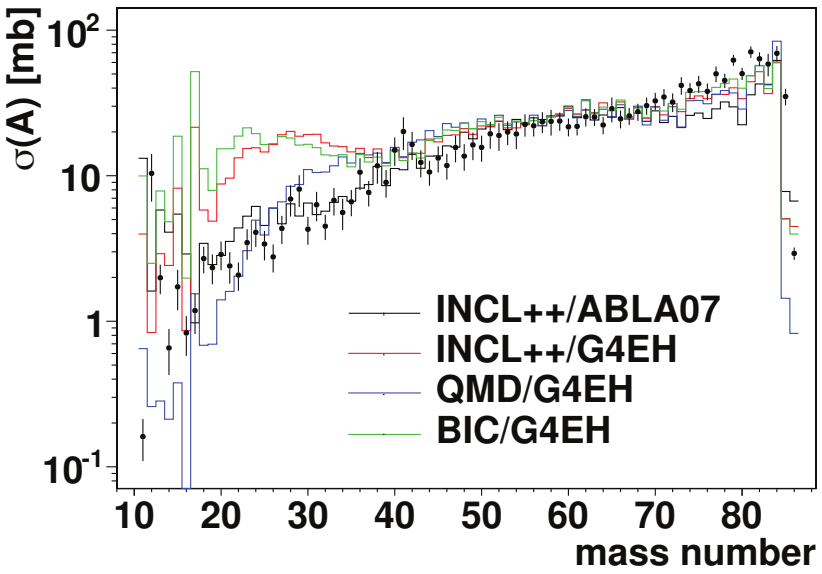

Figure 6.9: Fragmentation cross sections for the 500 A MeV $^{86}\mathrm{Kr} + {}^{9}\mathrm{Be}$ reaction, as a function of the fragment mass number. Model calculations are compared to the data taken from Weber et al. (1994). In the plot legend, *G4EH* stands for G4ExcitationHandler. Adapted from Mancusi, Boudard, Cugnon, et al. (2014), with permission.

Given the empirical nature of the fusion sector, we do not expect very accurate predictions.

Figure 6.8 shows angular-differential cross sections for the production of protons, ^{4}He, ^{7}Li, and ^{11}C. For each angle, the calculated ejectile energy distributions were integrated above the detection thresholds reported by Dudouet, Juliani, et al. (Table IV in 2013b). It is striking that none of the considered models can accurately reproduce all the experimental data (see however calculations with LAQGSM in Mashnik, Kerby, et al. 2014). The proton angular distributions predicted by INCL are quite close to the experimental data. The agreement progressively degrades as the mass of the ejectile increases. Dudouet, Juliani, et al. (2013b) showed that the experimental angular distributions can be represented as a sum of a Gaussian and an exponential contribution, and claimed (Dudouet, Cussol, et al. 2014) that no model can reproduce this trend. Figure 6.8 shows that this is incorrect: although the exponential tail of the angular distribution might be quantitatively incorrect (especially for ^{11}C), INCL is clearly the only model that can capture the trend of the experimental data. In spite of the crudeness of the model ingredients, the agreement with the experimental data is remarkable, except for the case of ^{11}C. As far as the other models are concerned, QMD seems to systematically underpredict the fragment yields at small angles. In general, the shape of the angular distribution is very different from the experimental result. Even for protons, one can observe a sizable overestimation of the yield. The BIC results manage to capture at least some qualitative features of the experimental data, but its predictions are in general less accurate than those of INCL.

We conclude this section by analyzing some results for fragmentation cross sections. Weber et al. (1994) measured isotopic fragmentation cross sections for 500 A MeV $^{86}\mathrm{Kr} + {}^{9}\mathrm{Be}$. For this system, we also show calculations with the ABLA07 de-excitation model (Kelić et al. 2008). The reason for this is that fragmentation cross sections are clearly very sensitive to de-excitation. Figure 6.9 shows that INCL/ABLA07 can reproduce most of the experimental data fairly well, but it underestimates the production of fragments close to the

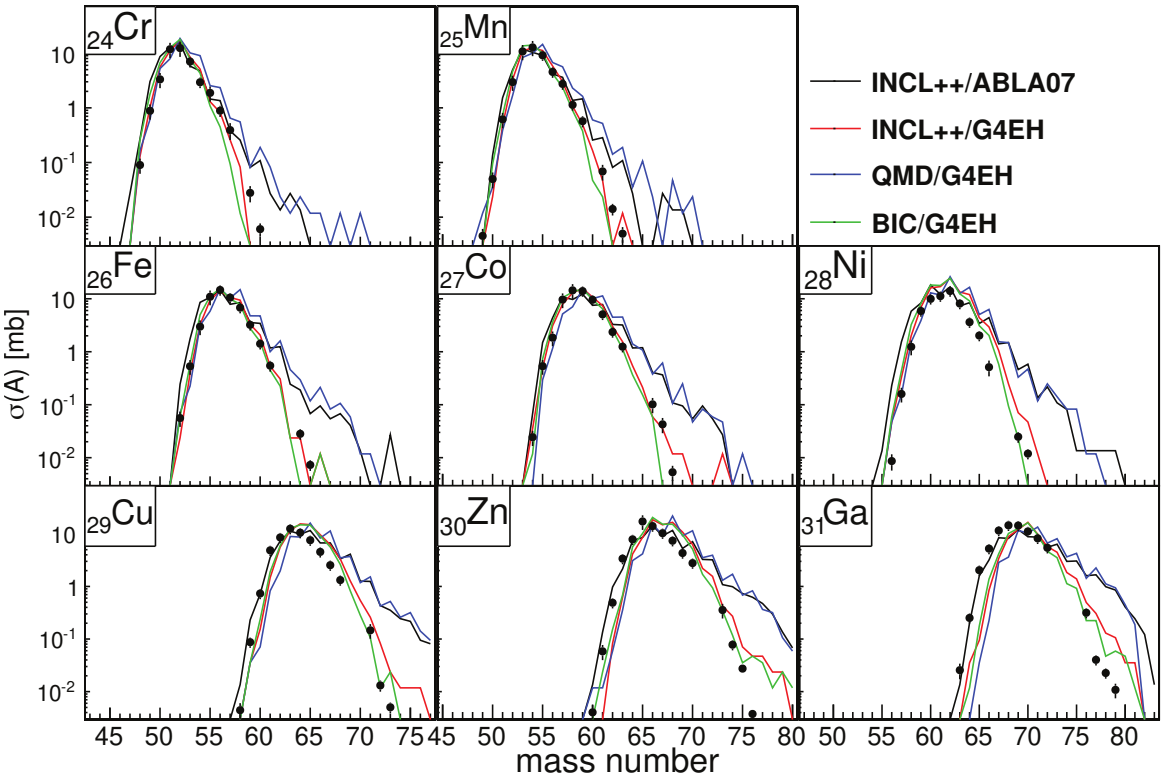

Figure 6.10: Isotopic fragmentation cross sections for the 500 A MeV ^{86}Kr+^{9}Be reaction, as a function of the fragment mass number, for different values of the fragment charge number. Model calculations are compared to the data taken from Weber et al. (1994). In the plot legend, *G4EH* stands for G4ExcitationHandler. Adapted from Mancusi, Boudard, Cugnon, et al. (2014), with permission.

projectile ^{86}Kr. QMD performs slightly better close to the projectile but slightly worse at intermediate mass ($A \simeq 35$). The INCL/G4ExcitationHandler and BIC/G4ExcitationHandler couplings well reproduce the data for $A > 40$, but overestimate the cross sections for lighter fragments.

The isotopic distributions in Fig. 6.10 illustrate that INCL/ABLA07 is affected by a defect. The yields for neutron-rich isotopes of $Z > 25$ nuclei are systematically overestimated. This defect might be correlated with the underestimation of the cross sections for the heaviest fragments. INCL/G4ExcitationHandler does not exhibit the same defect, but QMD/G4ExcitationHandler does. The emerging picture is unclear and no conclusion can be drawn. We have anyway verified that the overestimation of the neutron-rich isotopes is not due to the neglect of Pauli blocking on the first collision in the projectile. This is reasonable in the light of the QMD/G4ExcitationHandler results, which are surprisingly similar to those of INCL/ABLA07 on the neutron-rich sides of the isotopic distributions, but must be generated by a completely different dynamics.

In summary, we have described the crucial elements of the extension and we have discussed the limitations of our approach, which is admittedly more phenomenological than the core of the model. A broad comparison with heterogeneous observables has shown that, in spite of the conceptual difficulties, the extended INCL model yields predictions in fair agreement with the considered experimental data. In comparison to other models for nucleus-nucleus reactions available in Geant4, INCL stands out as one of the most viable options. We conclude that our extended model is successful at capturing the physics that is essential for the description of inclusive observables from reactions induced by light nuclei.

6.4 One-nucleon-removal reactions

The last topic I wish to discuss is the description of one-nucleon removal reactions in INC models. It has been known for some time that these models systematically, and in a somewhat puzzling manner, fail to describe inclusive cross sections for the removals of few nucleons (see for example Audirac et al. 2013; Jacob and Markowitz 1975). Note that, in general, the prediction of the inclusive one-nucleon-removal cross sections at high energy can reasonably be tackled only with a two-step dynamical/de-excitation model. The dynamical stage may be described by INC or by other models, such as the Boltzmann-Uehling-Uhlenbeck (BUU) or Vlasov-Uehling-Uhlenbeck (VUU) approaches (Remler and Sathe 1975), or models from the family of quantum molecular dynamics (QMD) (Aichelin 1991; Niita, Chiba, et al. 1995; Sorge et al. 1989). These models are all "INC-like" insofar as they superimpose a cascade of binary collisions on some kind of particle dynamics. For the sake of simplicity, in what follows we will always refer to INC models, but most of the following analysis can be generalized to other classes of dynamical models.

In this section we will briefly present how INC fails to describe one-nucleon removal reactions, and we will concentrate on the solution that my collaborators and I first proposed in 2015 (Mancusi, Boudard, Carbonell, et al. 2015), and subsequently refined a few years later (Rodríguez-Sánchez et al. 2017).

6.4.1 Failure of INC for one-nucleon removal

Figure 6.11 shows the experimental data for one-nucleon removal in proton-induced reactions at energies $\gtrsim 500$ MeV, as a function of the target mass (all targets are close to the sta-

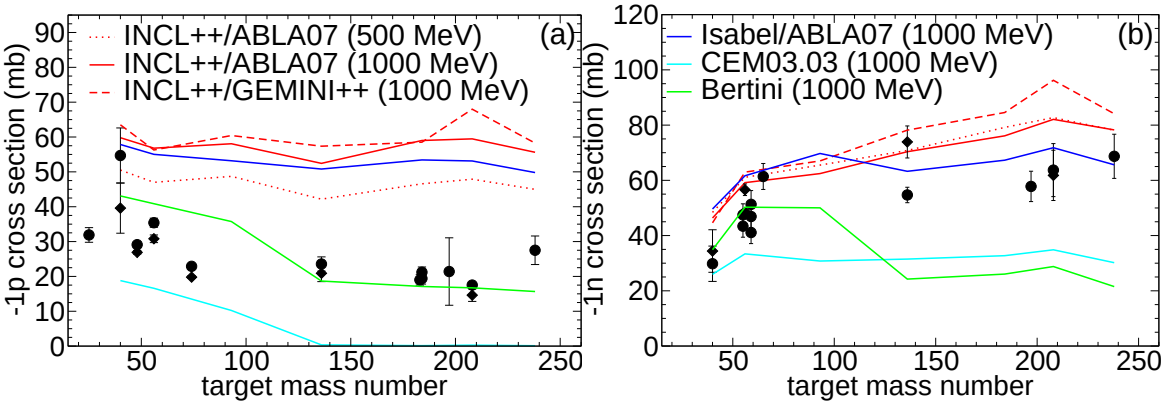

Figure 6.11: Experimental data for one-proton- (a) and one-neutron-removal cross sections (b) in proton-nucleus reactions above 500 MeV incident energy, as a function of the target mass. Diamonds refer to experimental beam energies between 500 MeV and 750 MeV, while circles represent energies above 750 MeV. The solid lines represent calculations with INCL/ABLA07 (red), ISABEL/ABLA07 (blue), CEM03.03 (cyan) and Geant4's Bertini+PreCompound model (green) at 1000 MeV. The dashed red lines represent INCL/GEMINI++ calculations at 1000 MeV. The dotted red lines represent INCL/ABLA07 calculations at 500 MeV. Adapted from Mancusi, Boudard, Carbonell, et al. (2015), with permission.

bility valley). For comparison, we also show calculations with INCL/ABLA07 at 500 MeV and 1000 MeV, and with other INC/de-excitation models at 1000 MeV. It is clear that the INCL/ABLA07 predictions are in the right ballpark for neutron removal, but they overestimate the proton-removal data by a factor that can be as large as 3–4 for heavy nuclei.

The role played by de-excitation can be clarified by comparing the INCL/ABLA07 calculations with the INCL/GEMINI++ calculations (Charity, McMahan, et al. 1988; Mancusi, Charity, et al. 2010). The resulting cross sections (shown in Fig. 6.11 as dashed red lines) are within 20% of the INCL/ABLA07 values and indicate that the influence of de-excitation is rather mild. Therefore, it seems unlikely that de-excitation can be held responsible for the gross overestimation of proton-removal cross sections. Other models exhibit different biases, but no model can reproduce all the experimental data trends (Mashnik, Gudima, et al. 2008; Wright and Kelsey 2015; Yariv and Fraenkel 1979).

The calculations presented in Fig. 6.11 globally demonstrate that INC models have difficulty in correctly predicting the inclusive one-nucleon-removal cross sections. This is rather surprising on two counts. First, one-nucleon-removal cross sections are among the largest isotopic cross sections, they are only modestly influenced by de-excitation and they vary slowly with the target mass and the projectile energy; thus, they represent an excellent test bench for INC models, but they seem to have attracted little attention so far. Second, one-nucleon removal reactions are typically dominated by very peripheral impact parameters, which probe regions of the nucleus with large mean free path (low density); in addition, the collision partners are somewhat localized in the nuclear surface, i.e. they are loosely bound. One would expect the INC approximation to be fully justified under these conditions. The failure illustrated by Fig. 6.11 suggests that INC models might be affected by a fundamental defect.

There are other remarkable features of the INC failure. One might expect even more conspicuous mispredictions for the removal of a larger number of nucleons, but one instead

finds that the models can generally reproduce most of the isotopic distributions rather well (David 2015). This should be understood as a consequence of the larger excitation energies associated with the emission of several nucleons. Since large excitation energies can be realized in numerous ways, some averaging takes place and the predictions become less sensitive to the details of the initial conditions. At the same time, it should be stressed that discrepancies do seem to increase for the removal of e.g. several protons from stable nuclei (Audirac et al. 2013). This is consistent, inasmuch as the constraints on the excitation energy in that case are even stricter than for one-proton removal, as evidenced by the smallness of the associated cross sections.

Note that the experimental cross sections do not seem very sensitive to the reaction parameters, such as the beam energy and the target species. This suggests that the details of the level structure of the individual nuclides involved do not play an important role. Therefore, it might be possible to amend INC and describe these observables, but it is probably necessary to go beyond the naive semi-classical model of the nuclear surface. We will do so in the following sections, but we first need to clarify the mechanism that leads to proton and neutron removal within the INC framework.

Let us first concentrate our attention on proton removal. The analysis of the INC/de-excitation calculations indicates that proton removal is dominated (about 90% of the cross section) by events with only one proton-proton collision. The two protons leave the nucleus, which however retains some excitation energy. If only one collision takes place, the excitation energy is simply given by the depth of the proton hole, i.e. the difference between the Fermi energy and the initial energy of the ejected proton. In any case, the excitation energy remaining at the end of cascade is evacuated during the de-excitation phase.

Note that, for most β-stable, non-fissile nuclei, particle emission at low excitation energy is largely dominated by neutron evaporation. If the excitation energy is lower than the neutron separation energy S_n, no particle can be evaporated and the energy will be evacuated as gamma rays. This is also true at energies slightly larger than S_n, as long as gamma-ray emission outcompetes neutron evaporation; thus, the effective neutron-evaporation threshold S_n^* is slightly larger than S_n. Therefore, the proton-removal channel is populated *if and only if* exactly one proton was ejected during INC and the excitation energies at the end of cascade lies below S_n^*. If the excitation energy allows for neutron evaporation, the final residue will be lighter (target minus one proton minus x neutrons).

Thus, the proton-removal cross section is extremely sensitive to the excitation energy left in the nucleus after the ejection of a proton during INC. More precisely, the cross section is determined by the probability that the ejection of a proton during INC deposits an excitation energy smaller than S_n^*. Furthermore, there is a subtle difference between proton and neutron removal. Neutron removal can be realized in two ways: either as a neutron ejection during INC followed by no evaporation (this is the analog of the proton-removal mechanism), or as no neutron ejection during INC followed by evaporation of one neutron. In the latter scenario, it is of course required that the incoming proton undergoes at least one binary collision and that it succeeds in escaping from the target; some conditions on the excitation energy also apply.

In either case, the fate of the de-excitation stage is essentially determined by the excitation energy at the end of INC and by the neutron separation energies in the region of the nuclide chart around the target. In this sense, our results are essentially independent of the choice of the de-excitation model, as far as all of them employ very similar separation energies for stable nuclei. The second-order dependence on the de-excitation model (see

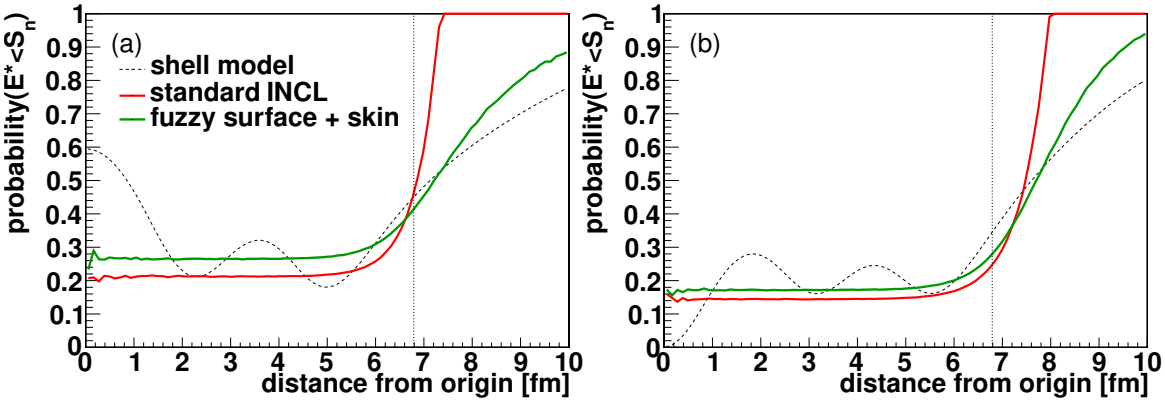

Figure 6.12: Probability that a proton (a) or neutron (b) hole in ^{208}Pb results in an excitation energy smaller than the shell-model neutron separation energy, as a function of the distance of the hole from the center of the nucleus. The dashed line denotes the result of the shell-model calculation. The solid red line represent the standard INCL initial condition, while the solid green line represents the improved initial condition. One-proton removal is dominated by impact parameters to the left of the vertical dotted lines. Adapted from Mancusi, Boudard, Carbonell, et al. (2015), with permission.

the ABLA07/GEMINI++ difference) can be ascribed to differences in the neutron-gamma competition, i.e. by slightly different values of the effective neutron-evaporation thresholds S_n^*.

It is clear then that the smallness of the excitation energy at the end of INC, especially in the proton-removal case, is the crucial element that determines one-nucleon-removal cross sections. Comparison with the experimental data (Fig. 6.11) seems to suggest that INCL largely underestimates the excitation energy associated with the ejection of a proton.

The nuclear surface in the INCL initial conditions is predominantly populated by nucleons whose energy is close to the Fermi energy. The ejection of one such nucleon during INC results in little excitation energy for the cascade remnant. However, in the quantum-mechanical square-well problem, the density outside the well does not vanish, even for states close to the bottom of the well. This means that there is a non-zero probability to find deeply bound particles outside the well, and eject them. This genuine quantum phenomenon is missing in the naive INC nuclear picture[3]. Another detail that is usually neglected in the INC picture is the presence of neutron (or proton) skins in certain nuclei. It is for instance rather well ascertained that ^{208}Pb exhibits a neutron skin thickness (defined as the difference of the neutron and proton root-mean-square radii) of about 0.2 fm (Zenihiro et al. 2010). For grazing collisions, this means that the local neutron density is several times larger than the proton density, leading to an enhanced probability for collisions on neutrons.

These observations suggest that the INCL predictions for proton-removal cross sections can be improved by refining the description of the nuclear surface. In order to bolster our

[3]A word of caution is due. In a purely quantum-mechanical treatment, the surface diffuseness is at least partly due to the penetration of the nucleon wave functions into the classically forbidden region; in spite of this, the INC initial conditions typically *do* account for a realistic diffuseness of the nuclear surface (e.g. the space density of the INCL model is a realistic Woods-Saxon distribution), although this is entirely enforced by a *classical* correlation between the particle position and energy. The failure of the INC initial conditions is therefore more subtle. It does not concern the presence of the tail of the spatial density but rather its energy density.

confidence in this interpretation, we compared the energy content of the nuclear surface in the INCL nuclear model with the result of an independent-particle shell-model calculation. Figure 6.12 shows the probability that a proton or neutron hole punched in the Fermi sea of a ^{208}Pb nucleus, at a given distance from the center, results in a small excitation energy (smaller than the neutron separation energy). In the standard INCL model, the probability for shallow holes becomes equal to 1 beyond a certain radius. This is due to the fact that there is a strict minimum kinetic energy for nucleons that are found beyond a given radius. In contrast, the shell-model calculation predicts that the probability to punch a deep hole is sensibly different from zero even very far out in the surface. How can INCL accommodate this phenomenology?

6.4.2 Neutron skin and surface fuzziness

Ideally, we would like to use the shell-model proton and neutron densities as inputs for our INC calculation; however, the particle densities in INCL cannot be described by an arbitrary function, so we must somehow adapt the shell-model densities. We choose to fit them with Woods-Saxon distributions. The best-fit parameters show that the shell-model densities for ^{208}Pb exhibit a neutron skin, although its thickness is slightly larger than the experimentally accepted value; this is a well-known defect of mean-field calculations (Friedman and Gal 2007).

We thus decouple the INCL parameters describing the neutron space density from those describing the proton space density. We choose not to modify the proton densities (because they are already given by fits to the experimental charge radii), but we adjust the neutron parameters relative to the proton parameters by the amounts indicated by the shell-model calculations. This is the first refinement that we apply to the INCL nuclear model.

As mentioned in Section 6.1 above, an INCL nucleon moves in a square-well potential whose radius $R(T)$ depends on the kinetic energy of the nucleon. The function $R(T)$ is uniquely determined by the choice of the space density $\rho(r)$ and by the assumption that nucleon momenta are uniformly distributed in the Fermi sphere. We have shown above that this construction results in excitation energies for one-collision reactions that are much smaller than those resulting from the shell model and, arguably, than those suggested by the available experimental data.

We refine the INCL initial conditions by allowing fluctuations in $R(T)$. We introduce a *fuzziness parameter* f ($0 \leq f \leq 1$) and a *fuzzy* square-well radius $R(T; f)$. The precise choice of $R(T; f)$ is not very important (see Mancusi, Boudard, Carbonell, et al. 2015, for more details); what matters are its properties. First, $R(T; f)$ is a random variable, described by a conditional probability distribution $P(R|T; f)$. Second, for $f = 0$ fluctuations are suppressed, and we recover the standard sharp radius-energy correlation:

$$R(T; 0) = R(T)$$
$$P(R|T; f = 0) = \delta(R - R(T)).$$

Third, for a given value of T, fluctuations in $R(T; f)$ are small if f is close to zero and they are large if f is close to one; in other words, $P(R|T; f)$ interpolates between the standard sharp radius-energy correlation at $f = 0$ and statistical independence of R and T at $f = 1$. Fourth, the fluctuations are constructed in such a way that the space density is still given by $\rho(r)$ and the momentum density is still given by a uniform Fermi sphere. The construction of the fuzzy INCL nucleus is analogous to the standard preparation algorithm (Boudard,

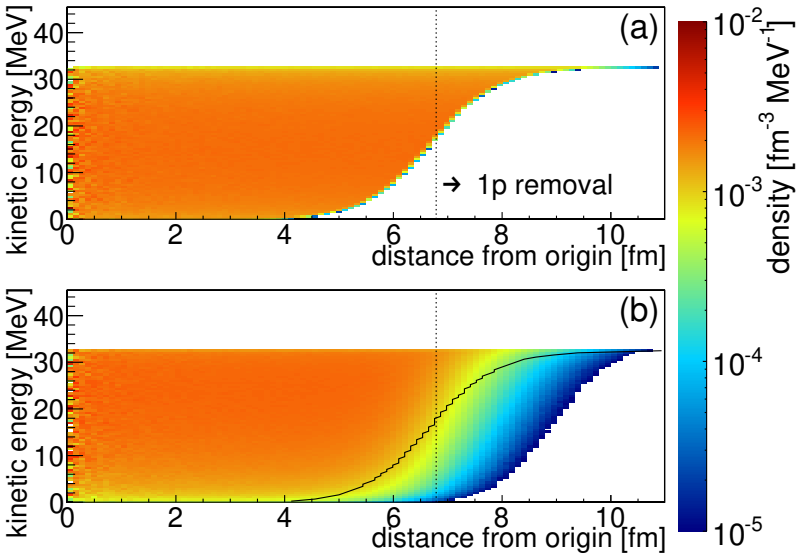

Figure 6.13: Space–kinetic-energy density of protons in ^{208}Pb in the standard INCL initial conditions (a) and in the refined initial conditions with $f = 0.5$ (b). The dotted vertical lines indicate the region of impact parameters which dominates one-proton removal. The contour of the colored shape in panel (a) represents the inverse of the function $R(T)$ and is reported as a solid black line in panel (b). Adapted from Mancusi, Boudard, Carbonell, et al. (2015), with permission.

Cugnon, Leray, et al. 2002). The only difference is that the radius of the square-well potential is no longer in one-to-one correspondence with the nucleon energy.

The phase-space structure of the fuzzy initial conditions is illustrated by Fig. 6.13(b), which refers to protons in ^{208}Pb with fuzziness parameter $f = 0.5$. Contrary to Fig. 6.13(a), we see that the density does not sharply drop to zero. Instead, protons of a given kinetic energy can sometimes be found at much larger distances than in the standard initial conditions [Fig. 6.13(a)]. By construction, the marginal kinetic-energy and space distributions of the fuzzy initial conditions are identical to those of the standard initial conditions. The fluctuations in one of the variables disappear when integrating over the full domain of the other one. Note however that different results are obtained if one limits the integration domain to some sub-range. This is illustrated by the dotted lines in Fig. 6.13, which indicate the region of impact parameters which dominates one-proton removal. The distribution of the standard initial conditions vanishes below a certain energy, while the fuzzy initial conditions extend much deeper in the Fermi sea.

6.4.3 Results

We turn now to the analysis of the results of the refined INC model. First, the introduction of the neutron skin in ^{208}Pb boosts the neutron-removal cross section, as expected. This is however undesired, since the cross section calculated by standard INCL is already in moderate excess of the experimental value. Second, surface fuzziness suppresses the cross sections for both channels. Third, neither effect is sufficient to compensate for the overestimation of the proton-removal cross section in ^{208}Pb *if considered alone*.

When the two refinements are simultaneously applied to ^{208}Pb, the effect of surface

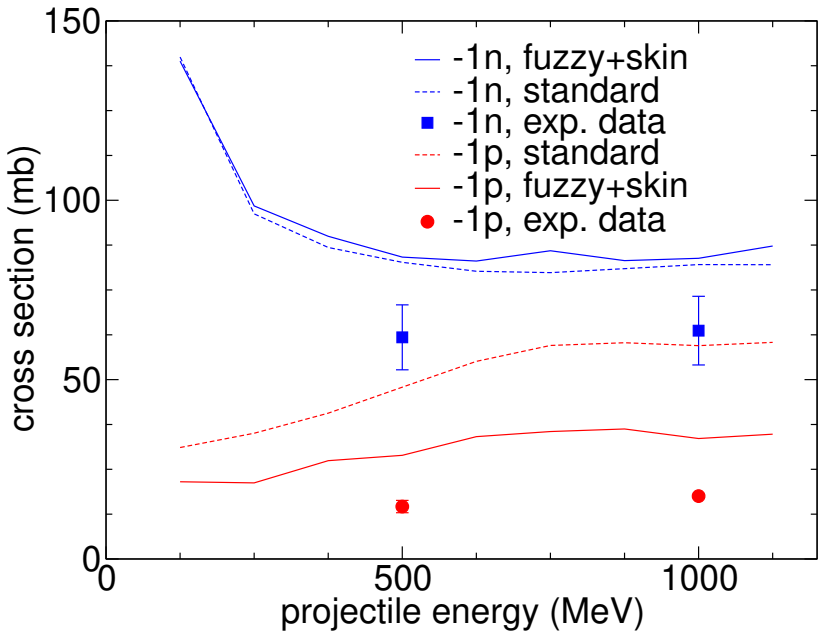

Figure 6.14: Excitation function for neutron- (blue) and proton-removal (red lines) cross sections in p + ^{208}Pb, as calculated with the standard INCL version (dashed lines) and with the refined treatment of the nuclear surface (solid lines). Adapted from Mancusi, Boudard, Carbonell, et al. (2015), with permission.

fuzziness for neutron removal almost exactly compensates the effect of the neutron skin, and the final result (83.8 mb) is very close to the value calculated with standard INCL (82.1 mb), which is within two standard deviations (about 30 %) of the experimental value. The proton-removal cross section, on the other hand, is reduced by almost a factor of two, which brings it much closer to the experimental value, but not quite in agreement with it.

The excitation curves for one-nucleon removal are shown in Fig. 6.14. The refined predictions are globally similar to the standard ones for neutron removal; for proton removal, the excitation function is roughly rescaled as a whole by a factor of ~ 0.6. This brings the prediction in better agreement with the trend shown by the experimental data.

The INCL results based on the shell-model densities and correlations are promising, but not entirely satisfactory. However, it was later shown that a more sophisticated nuclear model brings further improvements to the cross-section predictions. Indeed, one of the limitations of the shell model is that is only applicable to magic or almost magic nuclei. Rodríguez-Sánchez et al. (2017) removed this limitation by performing Hartree-Fock-Bogoliubov (HFB) calculations for all the nuclei between the proton and neutron drip lines. Woods-Saxon and Modified-Harmonic-Oscillator density shapes were used to fit the HFB densities and were injected in INCL. Surface fuzziness was found to be roughly independent of the nucleus, so constant values of the fuzziness parameter f were used (different parameters were used for neutrons and protons). With this setup, the INCL predictions were found to improve for proton- and neutron-removal cross sections; this was by design. However, the refinement also improved predictions for proton-proton coincidence detection, for isotopic residue production cross sections, and even for reaction cross sections in nucleus-nucleus reactions. This unexpected side-product strengthens our confidence in the appropriateness of the physical model.

References

The work presented in this chapter is based on the following publications:

Boudard, A., J. Cugnon, J.-C. David, et al. (2013). *New Potentialities of the Liège Intranuclear Cascade (INCL) Model for Reactions Induced by Nucleons and Light Charged Particles*. In: *Phys. Rev. C* 87.1, p. 14606. DOI: 10/gg89jj.

Kaitaniemi, P. et al. (2011). *INCL Intra-Nuclear Cascade and ABLA de-Excitation Models in Geant4*. In: *Prog. Nucl. Sci. Technol.* 2.0, pp. 788–793. DOI: 10.15669/pnst.2.788.

Mancusi, D., A. Boudard, J. Cugnon, et al. (2014). *Extension of the Liège Intranuclear-Cascade Model to Reactions Induced by Light Nuclei*. In: *Phys. Rev. C* 90.5, p. 54602. DOI: 10/gg89jt.

Mancusi, D., R. J. Charity, and J. Cugnon (2010). *Unified Description of Fission in Fusion and Spallation Reactions*. In: *Phys. Rev. C* 82.4, p. 44610. DOI: 10/dbvzss.

Mancusi, D., A. Boudard, J. Carbonell, et al. (2015). *Improving the Description of Proton-Induced One-Nucleon Removal in Intranuclear-Cascade Models*. In: *Phys. Rev. C* 91.3, p. 034602. DOI: 10.1103/PhysRevC.91.034602.

Mancusi, D., K. Niita, et al. (2009). *Stability of Nuclei in Peripheral Collisions in the JAERI Quantum Molecular Dynamics Model*. In: *Phys. Rev. C* 79.1, p. 014614. DOI: 10.1103/PhysRevC.79.014614.

Rodríguez-Sánchez, J. L. et al. (2017). *Improvement of One-Nucleon Removal and Total Reaction Cross Sections in the Liège Intranuclear-Cascade Model Using Hartree-Fock-Bogoliubov Calculations*. In: *Phys. Rev. C* 96.5, p. 054602. DOI: 10.1103/PhysRevC.96.054602.

Kinetics and dynamics in Monte Carlo neutron transport

In many technological applications, encompassing reactor start-up analysis and reactivity measurements, one is interested in determining the time behavior of the neutron flux φ in a system, starting from a given initial condition. The full description of such behavior is provided by the time-dependent Boltzmann equation, Eq. (2.19), which we reproduce here for the convenience of the Reader:

$$\begin{aligned}\frac{1}{v}\frac{\partial\varphi}{\partial t}(\boldsymbol{r},\hat{\boldsymbol{\Omega}},E,t)+\hat{\boldsymbol{\Omega}}\cdot\nabla\varphi(\boldsymbol{r},\hat{\boldsymbol{\Omega}},E,t)+\Sigma_t(\boldsymbol{r},E,t)\,\varphi(\boldsymbol{r},\hat{\boldsymbol{\Omega}},E,t)\\ =\int M_s(\boldsymbol{r},E',t)\,\Sigma_s(\boldsymbol{r},E',t)\,f_s(\boldsymbol{r},\hat{\boldsymbol{\Omega}}'\to\hat{\boldsymbol{\Omega}},E'\to E,t)\,\varphi(\boldsymbol{r},\hat{\boldsymbol{\Omega}}',E',t)\,\mathrm{d}^2\hat{\boldsymbol{\Omega}}'\,\mathrm{d}E'\\ +\int \nu_p(\boldsymbol{r},E',t)\,\Sigma_f(\boldsymbol{r},E',t)\,f_p(\boldsymbol{r},\hat{\boldsymbol{\Omega}}'\to\hat{\boldsymbol{\Omega}},E'\to E,t)\,\varphi(\boldsymbol{r},\hat{\boldsymbol{\Omega}}',E',t)\,\mathrm{d}^2\hat{\boldsymbol{\Omega}}'\,\mathrm{d}E'\\ +\sum_{j=1}^{J}\lambda_j c_j(\boldsymbol{r},t)\frac{f_{d,j}(E)}{4\pi}+Q_n(\boldsymbol{r},\hat{\boldsymbol{\Omega}},E,t).\end{aligned}\tag{7.1}$$

This equation must be coupled with Eq. (2.17) for the precursors concentrations c_j:

$$\frac{\partial c_j}{\partial t}(\boldsymbol{r},t)+\lambda_j\,c_j(\boldsymbol{r},t)=\int\nu_{d,j}(\boldsymbol{r},E',t)\,\Sigma_f(\boldsymbol{r},E',t)\,\varphi(\boldsymbol{r},\hat{\boldsymbol{\Omega}}',E',t)\,\mathrm{d}^2\hat{\boldsymbol{\Omega}}'\,\mathrm{d}E'+Q_{c,j}(\boldsymbol{r},t).\tag{7.2}$$

The goal of **kinetic Monte Carlo methods** is to address the solution of the full time-dependent Boltzmann Eq. (7.1), coupled to the precursor equations, Eq. (7.2). The first attempts at solving these two equations were proposed by Kaplan (1958) but they were soon somewhat forgotten because of limitations in computer power. They were later revived by Legrady and Hoogenboom (2008), Sjenitzer and Hoogenboom (2013), and Sjenitzer (2013).

It is uncommon but somewhat natural to distinguish between the *kinetics* and the *dynamics* of neutron transport. The distinction hinges on the presence of multi-physics feedback mechanisms. In what follows, I will use the term "kinetics" to refer to the time evolution of a free system, as described by Eqs. (7.1) and (7.2). I will use "dynamics" to refer to the time evolution of a system in which the physical parameters that appear in Eqs. (7.1) and (7.2) (cross sections, scattering kernels, etc.) are not time-independent, but are rather determined by some other physics, which is not described by the Boltzmann equation.

In this chapter, I wish to highlight the main challenges of kinetic and dynamic Monte Carlo for particle transport, along with the contributions that my collaborators and I have

brought to the field. Most of the work described in this chapter is extracted from my student Margaux Faucher's Ph.D. thesis (Faucher 2019).

7.1 Kinetic Monte Carlo for neutron transport

The greatest difficulty for kinetic Monte Carlo is the presence of largely different timescales. Indeed, the characteristic timescale of the precursor population (i.e. the average decay time $1/\lambda \sim 0.1\,\text{s}$ to $10\,\text{s}$) is much longer than the typical neutron timescale (i.e. the mean generation time; $\Lambda \sim 10^{-5}\,\text{s}$ in a typical PWR). In spite of the fact that the delayed neutron fraction is very small ($\beta \sim 0.7\%$), precursors are much more abundant than neutrons in, say, a PWR at equilibrium. The typical ratio $\beta/(\lambda\Lambda)$ is of the order of 10^4.

In the context of kinetic Monte Carlo, the timescales manifest themselves as *fluctuations*[1]. In a system close to criticality, each neutron chain on average produces a single precursor, which in turn induces a neutron chain by decaying to a delayed neutron. Due to the large separation between the neutron and precursor timescales, during the time between the creation of a precursor and its decay to a delayed neutron, no particle is produced (Legrady and Hoogenboom 2008). In a real system at full power, the number of fission events per unit time is so large ($\sim 10^{19}\,\text{s}^{-1}$) that fission chains will thoroughly superpose by the mere effect of statistics (Sjenitzer 2013). In Monte Carlo simulations, the number of simulated chains has to be much smaller than in real reactors because of limitations on CPU time and memory. Hence, ingenious algorithms are required to handle the presence of the two timescales and suppress the appearance of large fluctuations in the neutron population.

Sjenitzer and Hoogenboom (2013) proposed to use stratified sampling of precursor decay to curb the appearance of large fluctuations. To this aim, they introduced a time grid in the Monte Carlo simulation. Let $t_0 < t_1 < \ldots < t_K$ be the time grid, with $t_0 = 0$ representing the initial simulation time and t_K representing the final simulation time. At the beginning of each time step, each precursor is split into two particles; one of them is forced to decay before the end of the time step, while the other is forced to survive without decaying until the end of the time step. The statistical weights of the surviving precursor and of the delayed neutron produced by precursor decay are adjusted in order to ensure a fair game. Specifically, let $t \in [t_k, t_{k+1}[$ represent the current time step, j be the index of the precursor family[2] and $w_j(t)$ be the weight of a precursor particle at time t. The surviving precursor is forced to jump to the final time t_{k+1} with weight

$$w_j(t_{k+1}) = w_j(t) \exp\left[-\lambda_j(t_{k+1} - t)\right],$$

where λ_j is the decay constant for the j-th family (see Eq. (2.16)). By conservation of probability, the delayed neutron needs to be assigned an average weight of

$$\mathbb{E}(w_{\text{delayed}}) = w_j(t) - w_j(t_{k+1}).$$

The forced-decay time t_{decay} is assumed to be uniformly distributed between t and t_{k+1}. In order to keep the game unbiased, the neutron weight must be adjusted by the importance

[1] The presence of different timescales is also problematic in deterministic solvers. In numerical analysis, systems of differential equations that are characterized by vastly different scales are called *stiff*. Stiff systems are hard to solve numerically because they require very small integration time steps.

[2] Sjenitzer and Hoogenboom (2013) prefer the use of *condensed precursors*, which treat the decay of several families at once. For the sake of the simplicity, we have omitted this detail from our exposition, but the interested Reader may consult Faucher, Mancusi, et al. (2018).

ratio, i.e. by the ratio of the PDFs for decay:

$$\begin{aligned} w_{\text{delayed}}(t_{\text{decay}}) &= w_j(t)\frac{\lambda_j \exp\left[-\lambda_j(t_{\text{decay}}-t)\right]}{\frac{1}{t_{k+1}-t}} \\ &= w_j(t)\lambda_j\left(t_{k+1}-t\right)\exp\left[-\lambda_j(t_{\text{decay}}-t)\right]. \end{aligned}$$

One can easily verify that weight is conserved on average:

$$\begin{aligned} \mathbb{E}(w_{\text{delayed}}) &= \int_t^{t_{k+1}} \frac{1}{t_{k+1}-t} w_{\text{delayed}}(t_{\text{decay}})\mathrm{d}t_{\text{decay}} && (7.3)\\ &= w_j(t)\int_t^{t_{k+1}} \lambda_j \exp\left[-\lambda_j(t_{\text{decay}}-t)\right]\mathrm{d}t_{\text{decay}} && (7.4)\\ &= w_j(t)\left[1-\exp\left(-\lambda_j(t_{k+1}-t)\right)\right] && (7.5)\\ &= w_j(t) - w_j(t_{k+1}). && (7.6) \end{aligned}$$

In addition to the forced-decay scheme, kinetic Monte Carlo requires other important ingredients. For example, one often wishes to simulate the kinetic response to some perturbation of a critical system at equilibrium. This requires an algorithm to sample the source for the kinetic phase from the stationary distribution of neutrons in a critical system. Another important element of kinetic simulations is population control. In sub-critical or super-critical systems, the number of simulated particles either approaches zero or grows without bound. Neither outcome is desirable for Monte Carlo; thus, the size of the simulated population must be artificially controlled. We will not dwell on these aspects here, but the interested Reader may consult Faucher, Mancusi, et al. (2018) for more details.

Note that the Sjenitzer-Hoogenboom forced-decay scheme is *unbiased*. It does not introduce any discretization of the time evolution of the system. The purpose of the time grid is simply to perform *variance reduction* on the transport calculation. The choice of the grid affects the efficiency of the calculation, but it does not modify the expected value of any (linear) observable. But how should one choose the time grid to achieve good variance reduction? The scheme provides no guidance in this respect.

Consider indeed the case where one wishes to study the population kinetics on a timescale that is short compared to the typical precursor lifetimes (i.e. $t_K \lesssim \lambda_j^{-1}$). Such is the case, for instance, of transients related to reactivity insertion accidents (RIA). In this case one may develop the exponential in Maclaurin series in Eq. (7.6), yielding

$$\mathbb{E}(w_{\text{delayed}}) \simeq w_j(t)\lambda_j\left(t_{k+1}-t\right).$$

Thus, for small time steps, the average weight of the delayed neutron is approximately proportional to the length of the time step. Once the weight drops below the threshold for Russian roulette, the scheme becomes unable to force decays and loses much of its efficiency. If we are interested in short transients, then we are on the horns of a dilemma. If we use short time steps, then Russian roulette will kill most of our delayed neutrons, resulting in a large number of missed opportunities for variance reduction. Using large time steps does not force enough precursor decays and does not help with reducing the variance of the calculation. Either alternative is unsatisfactory.

7.2 Neutron-precursor importance sampling

In 2018, my collaborators and I introduced a refinement of the Sjenitzer-Hoogenboom scheme that paves the way towards more efficient kinetic calculations on short timescales; the scheme was implemented in the TRIPOLI-4 code (Brun et al. 2015). The intuition behind this method is that kinetic Monte Carlo à la Sjenitzer-Hoogenboom is inefficient because it allocates computational resources to neutrons and precursors proportionally to the size of the respective populations. Precursors are much more abundant than neutrons, and therefore represent the vast majority of the considered particles; however, basically all the detector responses of interest (reaction rates, power deposition, etc.) are sensitive to neutrons only. Thus, it stands to reason that neutrons should be favored over precursors in the simulation.

For this purpose, we introduce an *importance-sampling* scheme[3]. We wish to define a global importance value for the neutron population, I_N, and for the precursor population, I_C. Let us denote the total neutron weight as W_N and the total precursor weight as W_C; these are the *physical* particle weights. We wish to replace them with *simulation weights*, which are defined as

$$\bar{W}_N = W_N\, I_N \tag{7.7a}$$
$$\bar{W}_C = W_C\, I_C. \tag{7.7b}$$

We require that their sum equals the sum of the physical weights:

$$\bar{W}_N + \bar{W}_C = W_N + W_C. \tag{7.8}$$

With this constraint, the simulation weights can be rewritten as

$$\bar{W}_N = (W_N + W_C)\,\frac{R\,W_N}{R\,W_N + W_C}$$
$$\bar{W}_C = (W_N + W_C)\,\frac{W_C}{R\,W_N + W_C}.$$

Here we have introduced the *importance ratio*

$$R = \frac{I_N}{I_C}, \tag{7.9}$$

which is the only free parameter of the scheme; indeed, the importance values are expressed as

$$I_N = R\frac{W_N + W_C}{R\,W_N + W_C}$$
$$I_C = \frac{W_N + W_C}{R\,W_N + W_C}.$$

The rules of the importance sampling scheme are as follows.

[3]The notation used in this section is slightly different from the one used in Faucher, Mancusi, et al. (2018) and Faucher, Mancusi, et al. (2019). The main difference with respect to the published articles is that I prefer to use $1/I_N$ and $1/I_C$ where the articles use I_N and I_C, respectively. My definition of the importance ratio R is the same as the article (Eq. (7.9)), but the numerical values are obviously different. The reason for this change is that, for short time steps, my choice results in importance ratios much larger than one. This lends itself better to the intuition that neutrons are more important than precursors on short timescales. It also fits better with the interpretation of the importance as expected contribution to the detector and solution of the adjoint Boltzmann equation (see Chapters 2 and 8).

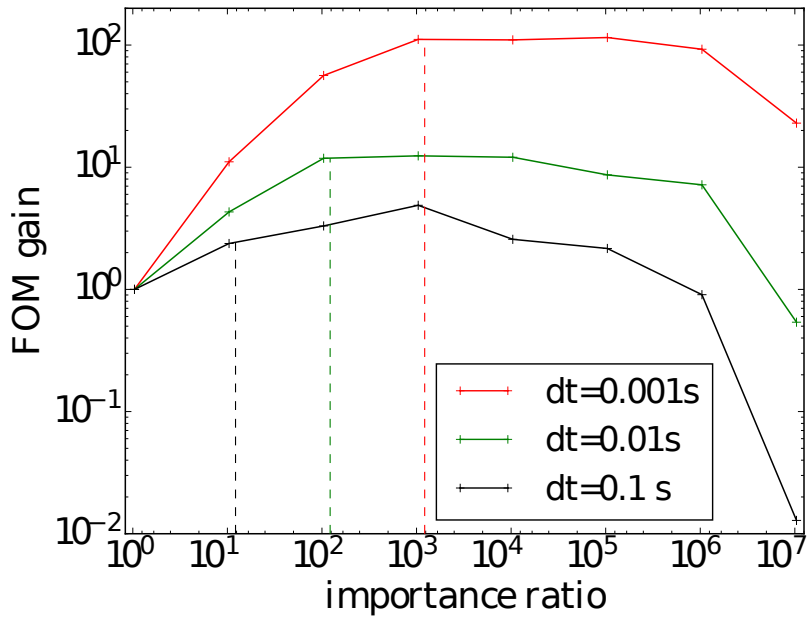

Figure 7.1: Figure of merit for the integral neutron flux in a PWR fuel assembly, for different values of the time step duration, as a function of the value of the neutron/precursor importance ratio. The dashed vertical lines represent the optimal values of the importance ratio, according to Eq. (7.10). Adapted from Faucher, Mancusi, et al. (2019).

- The weights of the source particles are multiplied by the corresponding population importance (Eq. (7.7)), which converts them to simulation weights. The populations are resampled so that Eq. (7.8) is respected.
- When neutrons produce precursors or precursors decay into neutrons, particle weights need to be adjusted to take into account the population importance values. The weight of a delayed neutron created by a precursor decay is multiplied by R.
- Similarly, when a neutron creates a precursor by fission, the precursor weight is divided by R.
- In order to keep the result unbiased, neutron and precursor scores are respectively divided by the importance factors I_N and I_C.

All these steps are rather standard for importance sampling.

The scheme can also be generalized to piecewise-constant, time-dependent importance ratios. Indeed, if we wish to change the importance ratio from R to R' at time t, we stop the particles and modify their simulation weights. Let us denote as $\bar{W}'_{N,C}$ the simulation weights after the change of importance. The relation between $\bar{W}_{N,C}$ and $\bar{W}'_{N,C}$ can be derived by first converting all the simulation weights to physical weights using the old importance ratio R, and then reconverting the physical weights to simulation weights using the new importance ratio R'. Note that the population weights need to be adjusted only if the importance ratio changes (nothing needs to be done if $R' = R$).

It remains to discuss how the importance ratio should be chosen. The intuition is that the importance ratio should somehow depend on the length of the time step. Indeed, consider a time step of length δt and consider that we wish to estimate some physical neutron observable integrated over the time step, for instance the energy deposited in the core. Let us

denote by δE_N the average amount of energy deposited by a typical neutron. Since precursors do not directly contribute to the energy deposition, they first need to decay into delayed neutrons. For a precursor decay constant λ (typically of the order of a few ms to a few s), the decay probability is

$$p_{\text{decay}} = 1 - \exp(-\lambda\,\delta t) \simeq \lambda\,\delta t$$

for short time steps. Once the precursor has decayed, the expected contribution of the delayed neutron is of the same order of magnitude as the contribution of a typical neutron. Therefore, the expected precursor contribution is given by

$$\delta E_C \simeq \delta E_N\,\lambda\,\delta t.$$

Keeping in mind the interpretation of importance as the expected contribution to some detector response (here energy deposition), the optimal importance ratio can be estimated as

$$R_{\text{opt}} \simeq \frac{\delta E_N}{\delta E_C} \simeq \frac{1}{\lambda\,\delta t}. \tag{7.10}$$

In order to estimate the efficiency of the Monte Carlo calculation for a particular observable, we can use the **figure of merit** (FOM), which is defined as

$$\text{FOM} = \frac{1}{\sigma^2 T},$$

where σ is the (estimated) standard error of the observable and T is the duration of the simulation. Figure 7.1 shows the figure of merit for the estimation of the total neutron flux, for different values of the importance ratio, as measured in a TRIPOLI-4 kinetic calculation in a reflected fuel assembly, for three different values of the duration of the time step. For each curve, the values of the figure of merit are normalized to the value for $R = 1$, which corresponds to no importance sampling. Thus, Fig. 7.1 shows the gain in figure of merit that can be realized with importance sampling in this particular case.

All the curves have similar shapes. As the importance ratio increases, the figure of merit initially increases, then reaches a plateau, and finally decreases. The plateau value depends on the time step duration, and it is roughly inversely proportional to the length of the time step; for $\delta t = 10^{-1}$ s the maximum FOM gain is around 3, while for $\delta t = 10^{-3}$ s it is around 100.

The curve shapes can be understood as the result of two competing effects. In the natural simulation ($R = 1$), neutrons are under-represented, relative to their importance; thus, values of the importance ratio larger than one favor the appearance of neutrons and improve the Monte Carlo estimate. It is interesting to remark that the saturation of the FOM approximately coincides with the optimal value of the importance ratio, as given by Eq. (7.10). The FOM starts decreasing for large values of the importance ratio (around 10^6), apparently independently of the time step duration. This is probably due to the occurrence of excessive precursor splitting or neutron roulette.

We will come back on the subject of the variance-reduction scheme in Chapter 8, where we will discuss the relationship between the sampling scheme discussed in this section and the optimal sampling scheme for kinetic simulations. We now turn to the illustration of the kinetic capabilities of TRIPOLI-4 in more realistic settings.

7.3 Dynamic simulations of reactor cores

The goal of this section is to illustrate simulations that are reasonably achievable in reactor physics with a kinetic Monte Carlo code today. We performed extensive tests of the kinetic capabilities of TRIPOLI-4 (Faucher 2019; Faucher, Mancusi, et al. 2018; Ferraro, Faucher, et al. 2019), but I will not dwell on these calculations in this manuscript. Instead, I wish to present *dynamic* calculations, that include the effect of physical feedback mechanisms. Kinetics without feedback is arguably of limited practical use. The calculations presented in this section were performed with a coupling between the TRIPOLI-4 code (Brun et al. 2015) and the sub-channel thermohydraulics code SUBCHANFLOW (Imke and V. H. Sanchez 2012).

In order to verify and test the dynamic capabilities of Monte Carlo codes, the participants of the McSAFE EU project (Sanchez-Espinoza et al. 2021) selected a few reference configurations, which are illustrated in Fig. 7.2. The first one is a 3×3 mini-core based on TMI-1 fuel assemblies (Ferraro, Faucher, et al. 2019); the second one is SPERT III E-core, a small research reactor that was used to perform several experiments on reactivity insertion accidents in the 1960s in the United States (Mancusi, Faucher, et al. 2022). For each system, a handful of reactivity insertion scenarios were studied.

For the TMI-1 mini-core, the benchmark specifies the precise configuration to be tested, in the interest of simplifying code-to-code comparisons. The benchmark specifies a few transient configurations that can be simulated with or without thermal-hydraulics feedbacks. As an example of purely kinetic (no feedback) results, Fig. 7.3 shows a power ramp induced by the movement of the control rods in the central assembly, as calculated by TRIPOLI-4 and Serpent2 (Leppänen et al. 2015). The rods are removed from the mini-core between $t = 0.2\,\mathrm{s}$ and $t = 1.2\,\mathrm{s}$. In the absence of feedback effects, the total power diverges. The TRIPOLI-4 and Serpent2 calculations show some mild discrepancy for large times, but are overall in fairly good agreement. Since the TRIPOLI-4 and Serpent2 implementations are independent, this result strengthens our confidence in the correctness of the implementations. It should be borne in mind that quantitative comparisons of time-dependent calculations can be a delicate matter, for two reasons. First, results obtained in different time steps are not statistically independent, especially in supercritical scenarios (like the one under consideration); neutrons have a tendency to positively correlate estimates in consecutive time steps. Second, the error bars in Fig. 7.3 were not estimated with ensemble averages but with ergodic averages over the power iteration; they underestimate the true uncertainty of the Monte Carlo calculation. All things considered, there is no reason to be concerned about the disagreement in Fig. 7.3.

A few examples of transient calculations with thermal-hydraulic feedback are shown in Fig. 7.4 (Faucher, Mancusi, et al. 2021). Simulations were performed for two scenarios, which differ for the total length of the control rod movement (30 cm or 40 cm). The calculation for the 30 cm scenario is comparable to the kinetic calculation in Fig. 7.3. Comparison of Figs. 7.3 and 7.4 highlights the stabilizing role of thermal-hydraulic feedback: the excess reactivity is absorbed by the Doppler effect, and the total power quickly drops back to roughly the initial level.

The SPERT III E-core calculations with TRIPOLI-4 are shown in Fig. 7.5; the Serpent2 results can be found in Ferraro, García, et al. (2020). The TRIPOLI-4/SUBCHANFLOW calculations differ in the initial condition (total power of 19 MW vs. 20 MW) or in the way the initial control-rod extraction event is modelled (sudden vs. gradual extraction). The

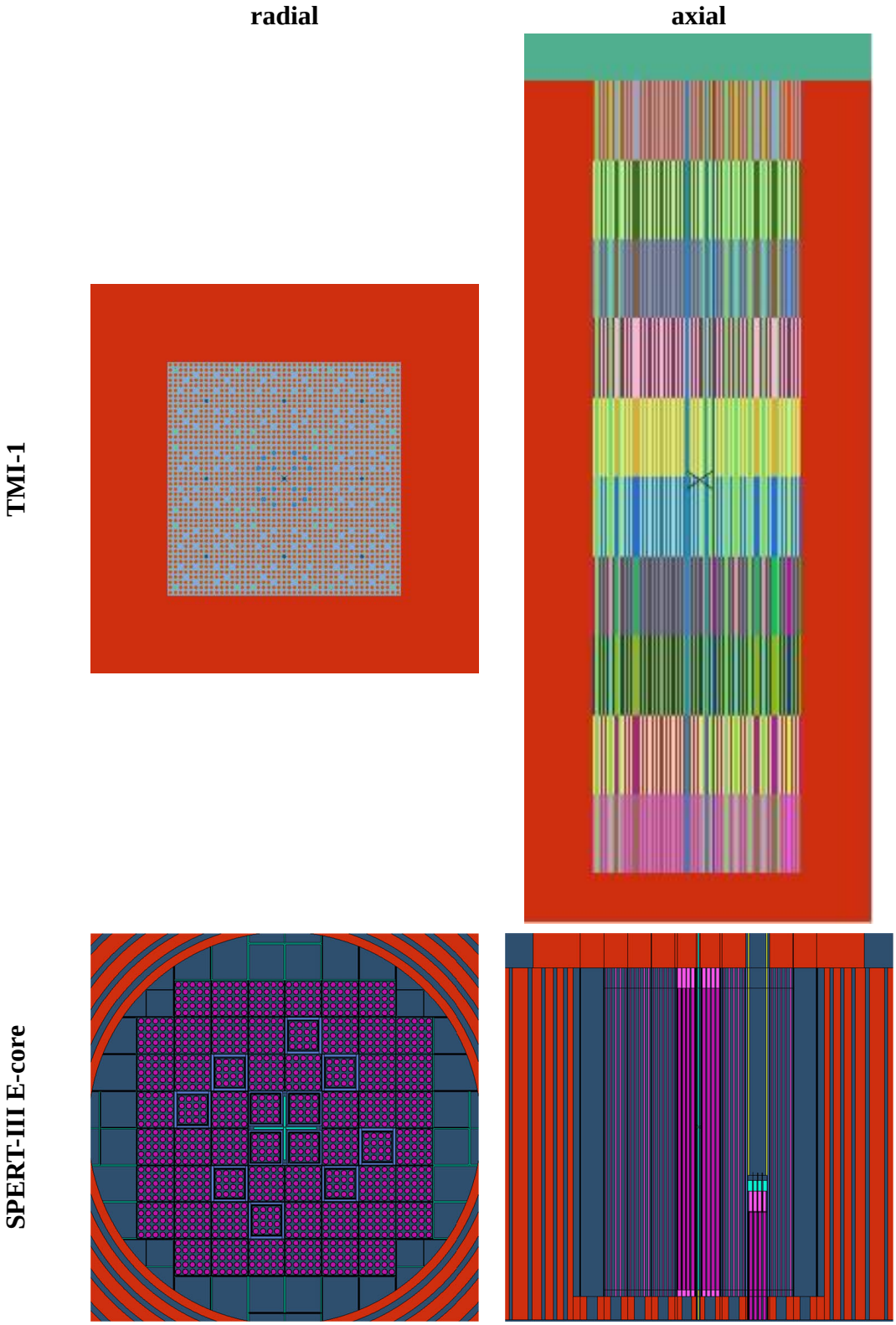

Figure 7.2: Geometries of the systems used for validating dynamic calculations with TRIPOLI-4. Top: TMI 3×3 mini-core (Ferraro, Faucher, et al. 2019). Bottom: SPERT III E-core (Mancusi, Faucher, et al. 2022). Left column: radial cuts. Right column: axial cuts. Adapted from Mancusi, Faucher, et al. (2022), with kind permission of the European Physical Journal (EPJ).

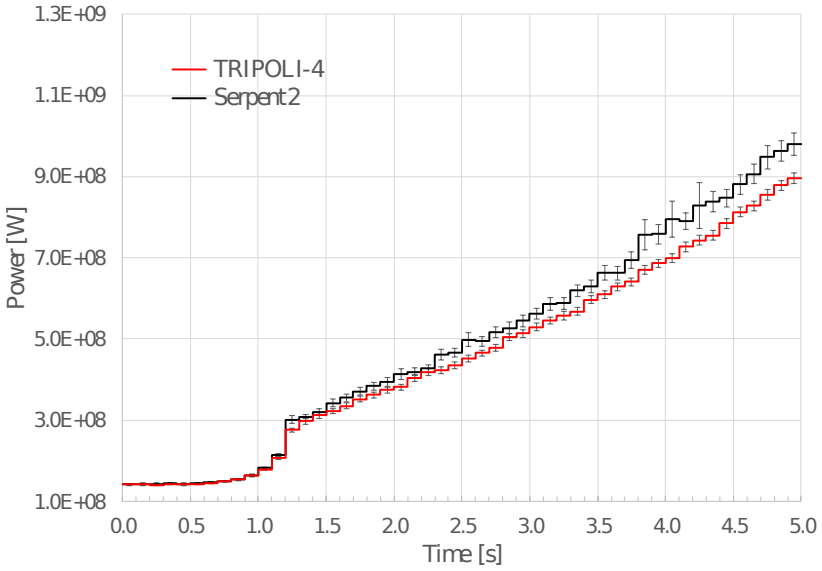

Figure 7.3: Results of kinetic simulations of a reactivity insertion in the TMI-1 mini-core, as performed with Serpent2 (black) and TRIPOLI-4 (red). Adapted from Ferraro, Faucher, et al. (2019), with permission.

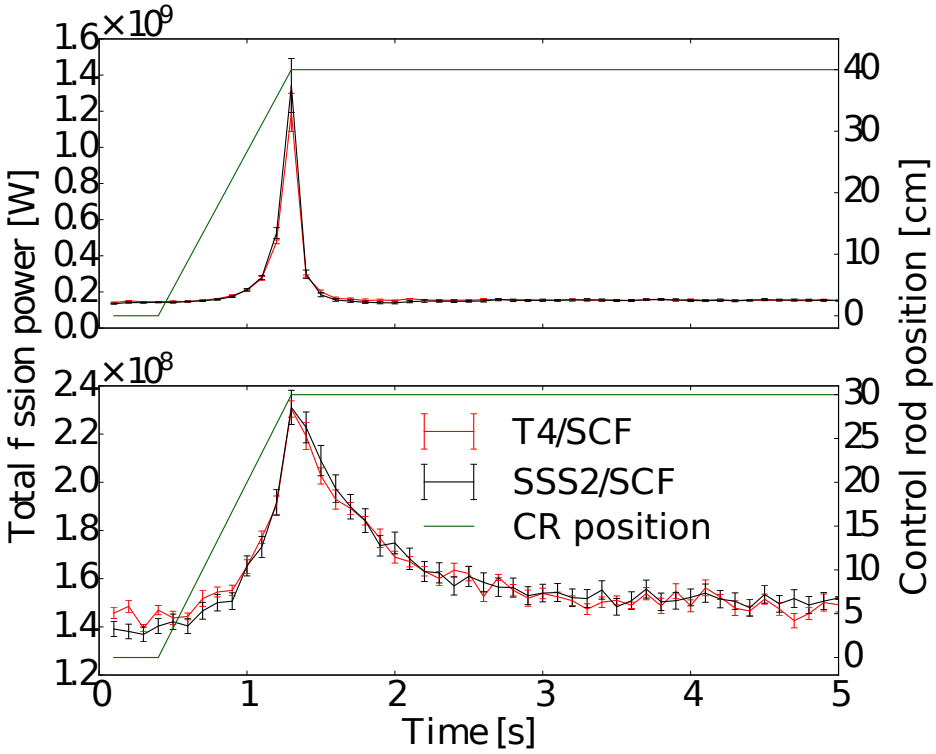

Figure 7.4: Results of dynamic simulations of a reactivity insertion in the TMI-1 mini-core, as performed with Serpent2/SUBCHANFLOW (black) and TRIPOLI-4/SUBCHANFLOW (red), for two different scenarios. The green lines represent the position of the control rods, and refer to the scale on the right-hand side of the plots. Top: 40 cm control-rod extraction. Bottom: 30 cm control-rod extraction. Adapted from Faucher, Mancusi, et al. (2021).

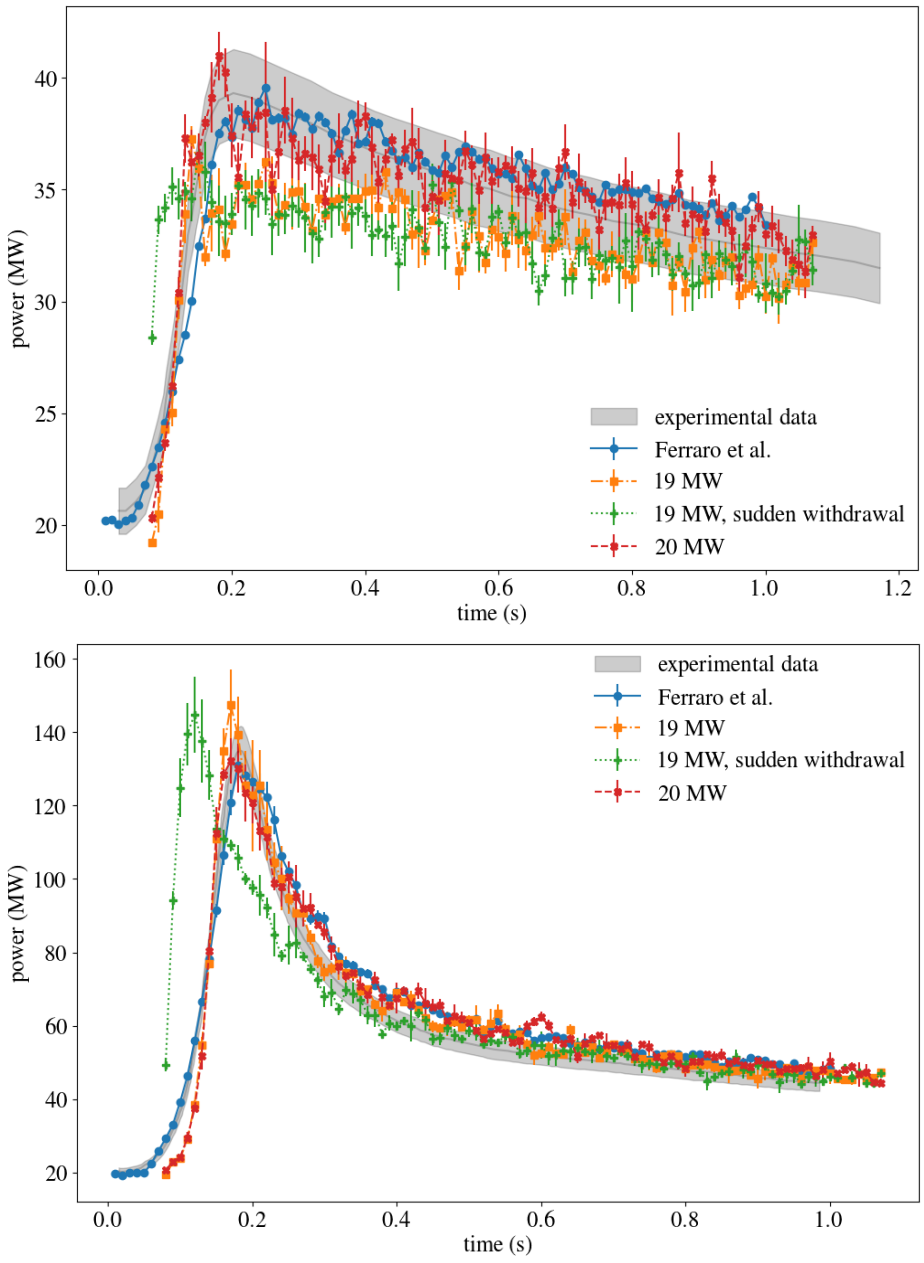

Figure 7.5: Results of dynamic simulations of reactivity insertion transients in the SPERT III E-core, as performed with Serpent2/SUBCHANFLOW (blue) and TRIPOLI-4/SUBCHANFLOW (orange, green, red), for two different scenarios (top: 0.47 $ reactivity insertion; bottom: 0.84 $ reactivity insertion). Experimental data are represented as a gray band. The Serpent2/SUBCHANFLOW calculation results are taken from Ferraro, García, et al. (2020). Adapted from Mancusi, Faucher, et al. (2022), with kind permission of the European Physical Journal (EPJ).

variations in the initial condition and in the withdrawal speed reflect the uncertainty in the initial condition of the experiment. The experimental data are displayed as a gray band, whose width represents the nominal experimental uncertainty. Finally, the Serpent2/SUBCHANFLOW results are displayed as blue lines. Both calculations are in good agreement with the experimental data.

The agreement between the TRIPOLI-4 and Serpent2 is surprisingly good, especially for the 20 MW initial condition. This is partly explained by the fact that the system response exhibits little sensitivity to the details of the model, as shown in more detail in Mancusi, Faucher, et al. (2022). Unlike the TMI-1 mini-core, the Serpent2 and TRIPOLI-4 models for SPERT III are sensibly different. In particular, the static reactivity of the Serpent2 model differs from the nominal values of up to 3000 pcm, while the TRIPOLI-4 model yields static reactivities within a few hundred pcm of the experimental values. These large differences between the models are reabsorbed in the adjustment of the system parameters (mostly the control-rod positions) that are required for the dynamic simulations, where they seem to leave very little trace. Thus, in spite of the large differences in the static characterization of the models, the kinetic behavior is very similar.

It is worth to conclude this chapter with a few observations about the efficiency and the cost of the dynamic simulations presented here. The comparison between the TRIPOLI-4 and Serpent2 kinetic calculations showed that the efficiency of the two codes is very similar. The SPERT III transients of Fig. 7.5 cost 10 $\mathrm{kh_{core}}$ to 15 $\mathrm{kh_{core}}$ each, which corresponds to a 24 h run on about 500 cores. The maximum (apparent) uncertainty on the integral power distribution is of the order of 8 %; this value comes from an ergodic average and therefore is surely underestimated. Arguably this precision is insufficient for high-fidelity simulations, which we (somewhat arbitrarily) define as calculations with less than 1 % uncertainty. In addition, a reliable estimate of error bars would require multiple independent replicas. Today, the actual cost of a high-fidelity Monte Carlo calculation of a SPERT III transient is probably of the order of 0.5 $\mathrm{Mh_{core}}$ to 1 $\mathrm{Mh_{core}}$.

We can perform a back-of-the-envelope estimate of the expected calculation time for a larger reactor by scaling by the volume ratio. For a large commercial pressurized water reactor (e.g. an EPR), this yields an estimate of about 100 $\mathrm{Mh_{core}}$, barring possible complications due to the large dominance ratio of the reactor. Such calculations are practically unattainable today. Even a cost of the order of 10 $\mathrm{Mh_{core}}$ (ten times smaller than our estimate) is unrealistically large for routine validation of deterministic transient calculations. If we are to apply Monte Carlo methods to transient simulations on the scale of a commercial reactor core, we need another breakthrough in calculation efficiency.

References

The work presented in this chapter is based on the following publications:

Faucher, M., D. Mancusi, and A. Zoia (2018). *New Kinetic Simulation Capabilities for Tripoli-4®: Methods and Applications*. In: *Ann. Nucl. Energy* 120, pp. 74–88. DOI: 10.1016/j.anucene.2018.05.030.

— (2019). *Variance-Reduction Methods for Monte Carlo Kinetic Simulations*. In: International Conference on Mathematics and Computational Methods Applied to Nuclear Science and Engineering, M&C 2019, pp. 130–139.

Faucher, M., D. Mancusi, and A. Zoia (2021). *Multi-Physics Transient Simulations with TRIPOLI-4®*. In: *EPJ Web Conf.* International Conference on Physics of Reactors (PHYSOR2020): Transition to a Scalable Nuclear Future. Vol. 247. EDP Sciences, p. 07019.

Ferraro, D., M. Faucher, et al. (2019). *Serpent and Tripoli-4® Transient Calculations Comparisons for Several Reactivity Insertion Scenarios in a 3D PWR Minicore Benchmark.* In: International Conference on Mathematics and Computational Methods Applied to Nuclear Science and Engineering, M&C 2019, pp. 1734–1743.

Mancusi, D., M. Faucher, and A. Zoia (2022). *Monte Carlo Simulations of the SPERT III E-core Transient Experiments*. In: *Eur. Phys. J. Plus* 137.1, p. 127. DOI: 10/gn42qs.

The content of this chapter is drawn from the Ph.D. thesis of my student Margaux Faucher (Faucher 2019).

Variance-reduction schemes for particle-transport Monte Carlo

Variance reduction encompasses all the techniques that aim at improving the efficiency of Monte Carlo calculations (thereby "reducing the variance" for a given computational effort). The universal metric for this purpose is the **figure of merit** (FOM). This quantity has already been introduced in Chapter 7, but given the crucial role that it plays in variance reduction, we will repeat the definition here.

Let $h(\gamma)$ be a Monte Carlo estimator (see Chapter 3), mapping a Monte Carlo history γ to a real number. Let us consider K independently and identically distributed histories $\{\gamma_1, \ldots, \gamma_K\}$. The empirical average is

$$\bar{h} = \frac{1}{K} \sum_{k=1}^{K} h(\gamma_k).$$

By independence of the γ_k, the variance of the average $\bar{h}$ is given by

$$\mathbb{V}(\bar{h}) = \frac{1}{K} \mathbb{V}(h).$$

This shows that, if the variance of the estimator is finite, then the variance of the empirical average decreases as the inverse of the number of histories[1]. Now let T be the total simulation time. On average, T is proportional to K. Therefore, the figure of merit

$$\text{FOM} = \frac{1}{\mathbb{V}(\bar{h})\, T}$$

is approximately independent of the number of histories. For a given simulation time, the FOM is larger if the variance is smaller, i.e. larger FOMs correspond to more efficient simulations. The goal of variance reduction is to maximize the figure of merit for one or more given Monte Carlo estimates.

In this chapter, I wish to focus on two items of my work that are related to variance reduction. The first one concerns the optimization of variance reduction for kinetic Monte Carlo (Section 8.1). The second one concerns the development and application of weight cancellation techniques (Section 8.2).

[1] Sometimes people invoke the central limit theorem to justify this trivial fact, but clearly this is not necessary, unless one wishes to convert the estimate of the variance of the mean into a confidence interval for the mean.

8.1 Zero-variance schemes for kinetic Monte Carlo

As we saw in the previous chapter, kinetic Monte Carlo calculations are not going to be applicable to the scale of a full reactor core in the short term, unless a major methodological breakthrough drastically improves the efficiency of these calculations. In this context, it makes sense to turn to the theory to seek guidance on the optimization of the simulation.

A noteworthy class of variance-reduction techniques is represented by **importance sampling**. This term embraces all the techniques that somehow modify the sampling rules of the Monte Carlo game in order to improve its efficiency (Lux and Koblinger 2018). We have seen in Chapter 3 that the resolution of integral equations with Monte Carlo requires interpreting the kernels of the integral operators as probability distributions. The probability distributions involved in transport simulations are related to

- the source distributions $Q_n(P)$ and $Q_{c,j}(P)$;
- the flight kernels $T_n(P, P')$ and $T_{c,j}(P, P')$;
- the collision kernel $C(P, P')$; or, equivalently, the scattering, fission, precursor production and decay kernels.

The Reader should refer to Chapter 2 for the definition of these quantities. Importance-sampling techniques consist in replacing any or all of the *natural* source and kernels with *modified* quantities:

- modified source distributions $\hat{Q}_n(P)$ and $\hat{Q}_{c,j}(P)$;
- modified flight kernels $\hat{T}_n(P, P')$ and $\hat{T}_{c,j}(P, P')$;
- a modified collision kernel $\hat{C}(P, P')$.

In the modified game, instead of sampling from the natural probability distributions, we sample from the modified distributions, and we correct the statistical weight of the history to take into account the modification in the sampling[2]; this is necessary because we want to constrain the importance-sampling game to be unbiased.

8.1.1 Optimal Monte Carlo schemes in stationary conditions

Among the unbiased importance-sampling games, it makes sense to search for the optimal one, i.e. the game that would result in the most efficient simulation for the observable(s) of interest. To fix the ideas, let us limit our attention to the stationary Boltzmann equation (so that $P = (\boldsymbol{r}, \hat{\boldsymbol{\Omega}}, E)$) and let R denote some linear functional of the neutron collision density

$$R = \int \psi_n(P)\eta_{\psi_n}(P)\,\mathrm{d}P. \tag{8.1}$$

We assume that we want to construct the optimal Monte Carlo simulation for the estimation of R. To this aim, we introduce a one-point (collision) estimator $h_R(P)$ for R (Section 3.3.1).

[2]This is done according to the well-known rule of importance sampling; if we should sample from $f(P)$, but we choose to sample from $g(P)$ instead, then the statistical weight of the sample is $f(P)/g(P)$. This also requires that $g(P) \neq 0$ wherever $f(P) \neq 0$; otherwise, importance sampling is biased. See Mancusi and Zoia (2020).

Note that a possible choice for $h_R(P)$ is $\eta_{\psi_n}(P)$, but that this is not the only possibility. Let $\hat{R}$ be the estimate of R produced by the Monte Carlo simulation. We restrict our attention to the *unbiased* Monte Carlo games, i.e. games such that $\mathbb{E}(\hat{R}) = R$. The following remarkable theorem holds: for a given estimator h_R, there exist an unbiased modified Monte Carlo game that yields an estimator $\hat{R}$ with a variance of *zero*, i.e. $\mathbb{V}(\hat{R}) = 0$. Games with this property are called **zero-variance schemes**.

Before discussing the practical feasibility of the zero-variance scheme, there is an important question we have to treat: is the zero-variance scheme the optimal one? This question is legitimate because efficiency is defined in terms of the figure of merit, not variance. Of course, any zero-variance scheme that terminates in finite time will yield an infinite figure of merit, and is optimal. However, some zero-variance schemes generate infinitely long histories. For this case, it is necessary to consider modified Monte Carlo games that are *close* (in some sense) to the zero-variance scheme, and study how the figure of merit changes as the zero-variance scheme is approached. If it diverges, then it can be reasonably argued that the zero-variance scheme is optimal. All the zero-variance schemes that I have studied are optimal in this sense, but I am not aware of a systematic discussion of this point (there is a very brief mention in Lux and Koblinger (2018, Sec. 5.VIII.I)). In what follows, I will assume that the zero-variance scheme is optimal, in the sense given above.

8.1.2 Practical feasibility

The astute Reader may be suspicious about the possibility of practically realizing a zero-variance scheme, which seems too good to be true. For the sake of this discussion, we need to look at the precise shape of the zero-variance scheme. For the sake of simplicity, let us consider the condensed prompt-delayed Boltzmann equation. In the notation of Chapter 2, Eq. (2.43), it reads (omitting the n subscript for the sake of conciseness)

$$\psi = \boldsymbol{T}\,\chi \tag{8.2a}$$

$$\chi = \boldsymbol{C}\,\psi + Q_\chi, \tag{8.2b}$$

Consider the following modified forms of the kernels and of the source term:

$$\hat{T}(P, P') = T(P, P')\frac{h_R(P') + \int C(P', P'')\, I(P'')\,\mathrm{d}P''}{I(P)} \tag{8.3a}$$

$$\hat{C}(P', P'') = C(P', P'')\frac{I(P'')}{\int C(P', P'')\, I(P'')\,\mathrm{d}P''} \tag{8.3b}$$

$$\hat{Q}(P) = Q(P)\frac{I(P)}{\int I(P')\, Q(P')\,\mathrm{d}P'}. \tag{8.3c}$$

Here $I(P)$ is a hitherto unspecified function of the phase-space coordinates, which we call **importance map**. If the appropriate importance-sampling weight correction rules are applied, the Monte Carlo game defined by Eq. (8.3) is unbiased for any reasonable choice of the importance map[3].

The shapes of the kernels given by Eq. (8.3) can be justified as follows. Let us interpret $I(P)$ as an estimate of the contribution to the detector of a particle starting a flight at P.

[3]By "reasonable" we essentially mean that the importance map is not allowed to vanish on any state that can be visited by the Monte Carlo game.

The interpretation for $\hat{C}$ is rather straightforward: each possible states after the collision P' is weighted by the estimate of their future contribution to the detector. The denominator in the definition of $\hat{C}$ is just a normalization factor to keep the kernel normalized. The interpretation of $\hat{Q}$ is similar: each possible particle state at the source is weighted by $I(P)$, and a global normalization factor is applied. Now consider $\hat{T}(P, P')$. How much do we estimate the particle to contribute to the detector response after its flight from P to P'? Well, the particle always contributes $h_R(P')$ at the end of its flight at P'; in addition, after the collision, each possible final state P'' is estimated to contribute $I(P'')$. If we put together these terms, we can conclude that we estimate the flight from P to P' to contribute $h_R(P') + \int C(P', P'')\, I(P'')\, \mathrm{d}P''$. Thus, the interpretation for the flight kernel is the same as for the collision kernel and the source term: each state after the transition is weighted proportionally to the estimated future contribution to the detector response. This rule is the centerpiece of zero-variance schemes (T. E. Booth 1989).

It can be shown (Lux and Koblinger 2018) that the zero-variance scheme for R and h_R is realized by a particular choice of the importance map. Given the Boltzmann observable R defined above, Eq. (8.1), consider the adjoint Boltzmann equation, Eq. (2.53), with η_ψ playing the role of the source term $Q_{\psi^\dagger}$:

$$\chi^\dagger = \boldsymbol{T}^\dagger\, \psi^\dagger \tag{8.4a}$$

$$\psi^\dagger = \boldsymbol{C}^\dagger\, \chi^\dagger + \eta_\psi. \tag{8.4b}$$

The zero-variance scheme simply corresponds to the choice $I = \chi^\dagger$. Thus, the zero-variance source term and kernels depend on the solution $\chi^\dagger$ of Eq. (8.4), the adjoint Boltzmann equation, and there's the rub: solving these equations is at least as difficult as solving the original transport problem for R.

Does this observation relegate zero-variance schemes to the realm of theoretical curiosities of little practical interest? Not at all! Suppose that we have an algorithm that produces an approximate solution $\tilde{\chi}^\dagger$ of Eq. (8.4). Since the unbiasedness of the modified Monte Carlo game does not depend on the choice of I, we can set $I = \tilde{\chi}^\dagger$ in Eq. (8.3) and obtain a Monte Carlo game that will be close (in some sense) to the optimal one. One hopes that this game will be efficient for the estimation of R. This idea has indeed been put into practice by using deterministic solvers to obtain a practical approximation of the adjoint flux, and injecting the resulting solution as importance maps in modified Monte Carlo games, with great success (Munk and Slaybaugh 2019; Wagner and Haghighat 1998).

The practical applications of zero-variance schemes are fraught with other difficulties, but none of them are as severe as the somewhat circular dependence between the optimal Monte Carlo game and the solution to the adjoint Boltzmann equation. A common misconception, perpetuated even by Hoogenboom (2008), is that all zero-variance schemes result in infinitely long histories. Of course, practical applications always involve some form of population control (e.g. Russian roulette and splitting), which truncates infinitely long histories; therefore, infinitely long histories would never be a problem in practice anyway. However, there actually exist zero-variance schemes that do *not* result in infinitely long histories, even in the absence of population control. We demonstrated this in Mancusi and Zoia (2020) (see Section 8.1.5 for more details and for a discussion of the schemes with this property).

8.1.3 Zero-variance schemes for kinetics

In Mancusi and Zoia (2020) we extended the construction of zero-variance schemes to the time-dependent form of the Boltzmann equation. We note that the time-dependent Boltzmann equation, in integral form, is formally identical to the stationary form, Eq. (8.2). This result is key, because it suggests that the strategy that yields the zero-variance scheme for the stationary problem should also yield the zero-variance scheme for the time-dependent problem. Indeed, we found that the zero-variance kernels and source term for kinetics are formally identical to those of stationary problems:

$$\hat{T}(P,P') = T(P,P')\frac{h_R(P,P') + \int C(P',P'')\,\chi^\dagger(P'')\,\mathrm{d}P''}{\chi^\dagger(P)} \tag{8.5a}$$

$$\hat{C}(P',P'') = C(P',P'')\frac{\chi^\dagger(P'')}{\int C(P',P'')\,\chi^\dagger(P'')\,\mathrm{d}P''} \tag{8.5b}$$

$$\hat{Q}(P) = Q(P)\frac{\chi^\dagger(P)}{\int \chi^\dagger(P')\,Q(P')\,\mathrm{d}P'}. \tag{8.5c}$$

Here we are working in a slightly more general framework where we allow the estimator h_R to be a function of the start and end points of the flight, P and P'.

There are two notable differences with Eq. (8.3). First, here P involves the time variable too: $P = (\boldsymbol{r}, \hat{\boldsymbol{\Omega}}, E, t)$. Second, in the presence of precursors, the collision operator $C(P',P'')$ is *non-local* in time. Indeed, it is given by

$$C(P',P'') = C_p(P',P'') + C_d(P',P''),$$

where the prompt (local) part C_p is given by

$$C_p(P',P'') = \left[\frac{\Sigma_s(\boldsymbol{r}',E')}{\Sigma_t(\boldsymbol{r}',E')} f_s(\hat{\boldsymbol{\Omega}}', E' \to \hat{\boldsymbol{\Omega}}'', E'') + \frac{\nu_p \Sigma_f(\boldsymbol{r}',E')}{\Sigma_t(\boldsymbol{r}',E')} \cdot \frac{f_p(E'')}{4\pi}\right] \cdot \delta(t'-t'') \cdot \delta(\boldsymbol{r}'-\boldsymbol{r}''),$$

and the delayed (non-local) part C_d is given by

$$C_d(P,P') = \sum_j \frac{\nu_d^j \Sigma_f(\boldsymbol{r}',E')}{\Sigma_t(\boldsymbol{r}',E')} \cdot \frac{f_d^j(E'')}{4\pi} \cdot \lambda_j \exp\left[-\lambda_j(t''-t')\right] \cdot \delta(\boldsymbol{r}'-\boldsymbol{r}'').$$

Note that both prompt and delayed parts are already non-local in energy and angle, even in stationary problems.

8.1.4 Sampling the zero-variance kernels

A remarkable result, which holds under very mild conditions[4], is that the zero-variance flight kernel, Eq. (8.5a), admits a general decomposition of the form

$$\hat{T}(P,P') = p_U(P)\,U(P,P') + [1-p_U(P)]\,V(P,P'). \tag{8.6}$$

[4]The estimator is required to be partially unbiased and non-negative. The condition of partial unbiasedness is

$$\int T(P,P')\,h_R(P,P')\,\mathrm{d}P' = \int T(P,P')\,\eta_{\psi_n}(P')\,\mathrm{d}P'.$$

See Mancusi and Zoia (2020) for the details.

Here U and V are normalized probability distributions for P' given P, and p_U is a probability ($0 \leq p_U \leq 1$) given by

$$p_U(P) = \frac{\eta_\chi(P)}{\chi^\dagger(P)},$$

where we have introduced the response function η_χ for the emission density:

$$R = \int \chi(P)\, \eta_\chi(P)\, \mathrm{d}P.$$

It is easy to show in general that η_χ and η_ψ are related by

$$\eta_\chi = \boldsymbol{T}^\dagger\, \eta_\psi.$$

The kernels U and V are related to the analogue flight kernel T:

$$U(P, P') = T(P, P') \frac{h_R(P, P')}{\eta_\chi(P)} \tag{8.7a}$$

$$V(P, P') = T(P, P') \frac{\psi^\dagger(P') - \eta_\psi(P')}{\chi^\dagger(P) - \eta_\chi(P)}. \tag{8.7b}$$

This decomposition lends itself to a relatively simple interpretation. First of all, for a flight starting at P, the quantity $p_U(P) = \eta_\chi(P)/\chi^\dagger(P)$ represents the expected fraction of the detector response due to the flight that we are about to sample; we might call this the *importance* of the next flight. Accordingly, if we select the U kernel, then the next flight must be sampled by weighting the analogue flight kernel by the contribution of the flight itself, i.e. by the estimator $h_R(P, P')$. Otherwise, if we select the V kernel, then we must weight the analogue flight kernel by the quantity $\psi^\dagger(P') - \eta_\psi(P')$. Equation (8.4b) tells us that

$$\psi^\dagger(P') - \eta_\psi(P') = \int C(P', P'')\, \chi^\dagger(P'')\, \mathrm{d}P'';$$

therefore, the weighting factor represents the expected detector response summed over all the flights *after* the flight from P to P'. One can then see that there is a clear correspondence between the importance of the flight and the kernel that should be used to sample the flight itself.

Equation (8.6) is also interesting because it shows that the zero-variance kernel can be sampled (at least in principle) with the following algorithm:

1. Evaluate the probability $p_U(P)$, which only depends on the initial coordinates P of the flight;
2. Select the kernel U with probability p_U, and the kernel V with the complementary probability $1 - p_U$;
3. Sample P' from the selected kernel.

In practice, sampling from U or V may require the use of rejection or delta tracking (Woodcock et al. 1965).

It is more difficult to devise an equivalent sampling algorithm for the zero-variance collision kernel, Eq. (8.5b), even in the case of stationary problems. The most straightforward approach consists in sampling from the analogue collision kernel $C(P', P'')$ and treating the

importance function $\chi^\dagger$ as a rejection factor. It is easy to show that the expected number of analogue samplings required before accepting a collision is

$$\langle n_{\text{coll}} \rangle = \frac{\int C(P', P'')\, \mathrm{d}P'' \cdot X(P')}{\int C(P', P'')\, \chi^\dagger(P'')\, \mathrm{d}P''},$$

where $X(P')$ is an estimate of the maximum value that $\chi^\dagger$ achieves over the states that can be reached via a collision at P':

$$X(P') \geq \max_{\substack{P'' \\ C(P',P'')\neq 0}} \chi^\dagger(P''). \tag{8.8}$$

Even assuming that the inequality in Eq. (8.8) is tight (i.e. $X(P')$ takes its smallest possible value), the number of required collisions may still be large if $\chi^\dagger$ is sharply peaked. For these and other reasons, the zero-variance collision kernel is seldom sampled from in practical applications.

8.1.5 On the length of zero-variance histories

We are now in a position to provide an informal characterization of the zero-variance games that result in finitely long histories. Suppose that the zero-variance flight kernel $\hat{T}$ leads the particle into a state P' such that no further contribution to the detector response is possible after visiting it. By virtue of the interpretation provided above, this is expressed by the condition

$$\psi^\dagger(P') - \eta_\psi(P') = \int C(P', P'')\, \chi^\dagger(P'')\, \mathrm{d}P'' = 0.$$

If this happens, then $\chi^\dagger$ and $\psi^\dagger$ must vanish for any state that can be possibly reached from P' (remember that $\chi^\dagger$ and $\psi^\dagger$ integrate the contribution of all possible future histories). At this point, the history can safely be terminated without biasing the response and without introducing any variance. Informally, we can think of points with this property as points outside the system.

Now consider again the decomposition of Eq. (8.6):

$$\hat{T}(P, P') = p_U(P)\, U(P, P') + [1 - p_U(P)]\, V(P, P').$$

If $\psi^\dagger(P') - \eta_\psi(P') = 0$ for some state P', then, by construction, P' cannot be reached via the V kernel, which is given by Eq. (8.7b). It may however be reachable via the U kernel, Eq. (8.7a), provided that $p_U(P) > 0$ and $h_R(P, P') > 0$. Based on the discussion above, we can informally state the following sufficient condition for the existence of finitely long histories. Let $\mathcal{F}$ be the set of states "outside the system", in the sense outlined above:

$$\mathcal{F} = \left\{ P' : \psi^\dagger(P') = \eta_\psi(P') \right\}.$$

Then the histories of the zero-variance game will eventually terminate if there exists a subset of finite measure of reachable states that are connected via U to $\mathcal{F}$.

Obviously, if the set $\mathcal{F}$ is empty, then no finitely long histories may exist. Even in cases where $\mathcal{F}$ is not empty, it is possible that finitely long histories do not exist if for example $h_R(P, P') = 0$ for $P' \in \mathcal{F}$, or if $p_U(P) = 0$ whenever $P' \in \mathcal{F}$ and $h(P, P') > 0$. However, the *generic* zero-variance game actually generates finitely long histories. This conclusion contradicts several statements made by Hoogenboom (2008). The following section demonstrates that the statement is true with practical examples.

8.1.6 A simple demonstration

Following Mancusi and Zoia (2020), we will now demonstrate that it is possible to implement the zero-variance scheme in the simple, zero-dimensional, point-kinetics model, where we neglect the space, energy and angle dependence of the neutron flux. In this simplified model, the functions ψ, χ, $\psi^\dagger$, and $\chi^\dagger$ are functions of time only. The analogue kernels read

$$\begin{aligned} T(t,t') &= v\Sigma_t \exp\left[-v\Sigma_t(t'-t)\right]\cdot\Theta(t'-t) \\ C_p(t',t'') &= \frac{\Sigma_s+\nu_p\Sigma_f}{\Sigma_t}\cdot\delta(t''-t') \\ C_d(t',t'') &= \frac{\nu_d\Sigma_f}{\Sigma_t}\cdot\lambda\exp\left[-\lambda(t''-t')\right]\cdot\Theta(t''-t'), \end{aligned}$$

where Θ represents the Heaviside function. The adjoint source is taken to be

$$\eta_\psi(t) = \frac{1}{\Sigma_t}\mathbb{1}_{[0,t_f]}(t),$$

with $\mathbb{1}_{[0,t_f]}(t)$ being the indicator function of the $[0,t_f]$ time interval. This choice corresponds to constructing a zero-variance game for the response

$$\begin{aligned} R &= \int \psi(t)\,\eta_\psi(t)\,\mathrm{d}t \\ &= \frac{1}{\Sigma_t}\int_0^{t_f}\psi(t)\,\mathrm{d}t, \end{aligned} \tag{8.9}$$

which is the fluence between $t=0$ and $t=t_f$. The adjoint Boltzmann equation can be solved and yields a closed analytical form for $\chi^\dagger(t)$, which we omit for the sake of conciseness (Mancusi and Zoia 2020).

We consider four estimators for the response R:

- the collision estimator
$$h_{\text{coll}}(t,t') = \frac{\mathbb{1}_{[0,t_f]}(t')}{\Sigma_t}; \tag{8.10}$$
note that this estimator is actually a one-point estimator, because it is independent of t;
- the expectation estimator
$$h_{\text{exp}}(t,t') = \eta_\chi(t); \tag{8.11}$$
this is also a one-point estimator, but contrarily to Eq. (8.10) it only depends on the starting time t and is independent of the final time t';
- the "modified expectation estimator"
$$h_{\text{exp*}}(t,t') = \eta_\chi(t)\frac{\psi^\dagger(t')-\eta_\psi(t')}{\chi^\dagger(t)-\eta_\chi(t)}; \tag{8.12}$$
- the track-length estimator
$$h_{\text{track}}(t,t') = v\cdot\min(t'-t,t_f-t)\cdot\mathbb{1}_{[0,t_f]}(t). \tag{8.13}$$

Each estimator corresponds to a different form of the zero-variance flight kernel $\hat{T}(t,t')$, Eq. (8.5a). We omit the proof that these estimators are partially unbiased (Lux and Koblinger 2018; Mancusi and Zoia 2020).

The collision estimator

For the collision estimator, Eq. (8.10), the flight kernel $\hat{T}_{\text{coll}}(t, t')$ takes the form of a non-homogeneous exponential distribution:

$$\hat{T}_{\text{coll}}(t, t') = v\hat{\Sigma}_t(t') \exp\left[-v \cdot \int_t^{t'} \hat{\Sigma}(u)\mathrm{d}u\right] \cdot \Theta(t' - t),$$

where the modified cross section $\hat{\Sigma}_t$ is given by

$$\hat{\Sigma}_t(t) = \Sigma_t - \frac{1}{v} \cdot \frac{\partial \ln \chi^\dagger(t)}{\partial t}.$$

Given these definitions and the fact that $\chi^\dagger(t) = 0$ for $t \geq t_f$, it is easy to show that the final time t' always satisfies $t < t' < t_f$. In other words, the zero-variance flight kernel can never lead the history outside the $[0, t_f]$ time interval. At each jump, the current time t approaches the final time t_f but never quite reaches it. In a game with Russian roulette, the history will eventually be truncated by the weight cutoff, but without Russian roulette the zero-variance history would be infinitely long. A similar behavior is observed in the zero-variance scheme based on the collision estimator in stationary conditions (Hoogenboom 2008).

In terms of the analysis of Section 8.1.5, there exist states from which no further contribution to the detector is possible ($t' > t_f$). However, these states are not reachable because $U(t, t') = 0$ if $t' > t_f$; the estimator vanishes if the final time t' is outside the detector interval $[0, t_f]$. Therefore, the collision estimator results in infinitely long histories.

The modified expectation estimator

The zero-variance flight kernel for the modified expectation estimator is given by the following expression:

$$\hat{T}_{\text{exp*}}(t, t') = T(t, t') \frac{\psi^\dagger(t') - \eta_\psi(t')}{\chi^\dagger(t) - \eta_\chi(t)}.$$

Comparing with Eq. (8.7b), one should immediately remark that

$$\hat{T}_{\text{exp*}}(t, t') = V(t, t').$$

In other words, the modified expectation estimator can be cast in the form of Eq. (8.6), provided that one sets $p_U(t) = 0$. Therefore, this estimator can never lead particles outside the system (because this is the property that characterizes V). The zero-variance game results in infinitely long histories, just like the collision estimator.

Note however that infinitely long histories are a peculiar property of the collision estimator and the modified expectation estimator. According to the discussion of Section 8.1.5, infinitely long histories can only arise if, roughly speaking, $p_U(P) \cdot U(P, P') = 0$ for any P' outside the system. The collision estimator realizes this by ensuring that the second factor vanishes, while the modified expectation estimator realizes this by suppressing the first one.

The expectation estimator and the track-length estimator

Consider now the zero-variance flight kernels $\hat{T}_{\text{exp}}(t, t')$ and $\hat{T}_{\text{track}}(t, t')$, associated to the expectation estimator (Eq. (8.11)) and track-length estimator (Eq. (8.13)), respectively. They

w_{RR}	collision	mod. expectation	expectation	track
10^{-1}	0.945 91(4)	0.945 99(7)	0.945 90(1)	0.945 896(6)
10^{-2}	0.945 891(4)	0.945 90(1)	0.945 889 8(3)	0.945 890 0(2)
10^{-3}	0.945 891 4(6)	0.945 889(2)	0.945 890 360(4)	0.945 890 361(5)
0	—	—	0.945 890 360 6	0.945 890 360 6
R	0.945 890 360 6			

Table 8.1: Results of calculations for the total particle fluence R (Eq. (8.9)), for different Monte Carlo calculations (differing in the choices of the estimators/kernels), and for different values of the Russian roulette threshold w_{RR}. A threshold of zero corresponds to a calculation without Russian roulette. The uncertainties represent the standard error. The final row (R) contains the value of the response, calculated according to the analytical solution of the point-kinetics equations. The results correspond to the supercritical scenario from Mancusi and Zoia (2020). Adapted from Mancusi and Zoia (2020), with kind permission of the European Physical Journal (EPJ).

can be written in the form of Eq. (8.6), with

$$U_{\text{exp}}(t,t') = T(t,t')$$

for the expectation estimator, and

$$U_{\text{track}}(t,t') = T(t,t')\frac{h_{\text{track}}(t,t')}{\eta_\chi(t)}$$

for the track-length estimator. Since neither of these kernels vanishes for $t' > t_f$, each flight has a finite probability to lead the particle outside the system, thereby ending the history. Russian roulette is not necessary for the zero-variance schemes to terminate.

Numerical results

Table 8.1 shows the results of four different Monte Carlo calculations, each of which was performed using a different set of zero-variance kernels and source distributions, as indicated by the column titles. The observable is the total fluence, defined by Eq. (8.9); the names of the columns also indicate which estimator was used (for example, the collision estimator was used in the calculation with the zero-variance kernels associated to the collision estimator). Results are given for several values of the Russian roulette threshold, in order to highlight the fact that the variance of the result does not quite vanish for finite values of the threshold, but it approaches zero as the threshold approaches zero. The calculation without Russian roulette ($w_{RR} = 0$) is not possible (does not terminate) for the collision and modified expectation estimator, as discussed above, but it is possible for the expectation estimator and the track-length estimator. We could not reliably estimate the uncertainty on the zero-variance calculations without Russian roulette, because under these conditions the uncertainty is essentially determined by numerical round-off errors. More extensive demonstrations are presented in Mancusi and Zoia (2020).

8.2 Weight cancellation

We saw in Sections 3.6 and 3.8 that it is sometimes useful to introduce negative weights when solving an integral equation with the Monte Carlo method. In particular, this remark

applies to the solution of the Boltzmann equation. Even though the kernels involved in the standard forms of the Boltzmann equation (e.g. Eq. (2.49)) are usually positive, neutrons with negative weights can be introduced for the purpose of solving variants of the Boltzmann problem where the solution flips sign, such as in the determination of higher harmonics of the k-eigenvalue equation (T. E. Booth and Gubernatis 2010). In other problems, the equation to solve (and the solution) are complex, and the Monte Carlo algorithm requires complex neutron weights; this happens for instance in the search for **critical buckling** (Yamamoto 2012) or in the study of **power reactor noise** (Yamamoto 2013). "Power reactor noise" denotes the fluctuations in the neutron population induced by periodic perturbations of the reactor state, which may be due for example to mechanical vibrations of pins, assemblies, or even of the whole core. There are also uses of this idea outside the domain of particle transport (Assaraf et al. 2007; G. H. Booth et al. 2009; Spencer et al. 2012).

8.2.1 Negative-weighted delta tracking

Let us consider a specific example of Monte Carlo game for particle transport that uses negative weights. Woodcock's **delta tracking** (Woodcock et al. 1965) is a tracking technique for particles in continuously varying media. In the simplest variant of delta tracking, particle flights are sampled using a constant macroscopic *sampling cross section*, which is required to be larger than or equal to the total macroscopic cross section at any point in the system. Recently, Legrady, Molnar, et al. (2017) proposed **negative-weighted delta tracking** (NWDT), a generalization of delta tracking that relaxes the requirement that the sampling cross section should be a majorant of the total cross section. This comes at the cost of occasionally flipping the sign of the particle weights. The new tracking algorithm was proved and verified to be unbiased in fixed-source problems. Thus, the introduction of particles with negative weights seems relatively harmless at first sight.

A few years ago, in the context of a Ph.D. thesis supervised by me, we tried to apply negative-weighted delta tracking to a k-eigenvalue problem. The physical Boltzmann equation to solve reads (see Section 2.3.2)

$$\hat{\boldsymbol{\Omega}} \cdot \nabla\varphi + \Sigma_t\varphi = \boldsymbol{S}\varphi + \frac{1}{k}\boldsymbol{F}\varphi,$$

where k is the sought eigenvalue. The system we considered was a simple rod model (Belanger, Mancusi, and Zoia 2021).

Our first natural attempt was to attempt to solve the k-eigenvalue problems with a slightly generalized version of power iteration. Specifically:

- Russian roulette needs to be adapted to neutrons with negative weight. We apply roulette to neutrons using the magnitude of the weight, $|w|$; neutrons that survive have their weight reset to $\text{sign}(w) = w/|w|$.
- The sampling and normalization of the fission source need to be adapted. The number of fission neutrons generated at each collision site is taken to be

$$n_f = \left\lfloor |w| \frac{\nu\Sigma_f}{\Sigma_t} \cdot \frac{1}{k_{\text{eff}}^{(g-1)}} + \xi \right\rfloor,$$

  where $k_{\text{eff}}^{(g-1)}$ is the estimate of the value of k_{eff} obtained at the previous generation, and ξ is a random number from the $\mathcal{U}([0,1[)$ distribution. This formula is commonly

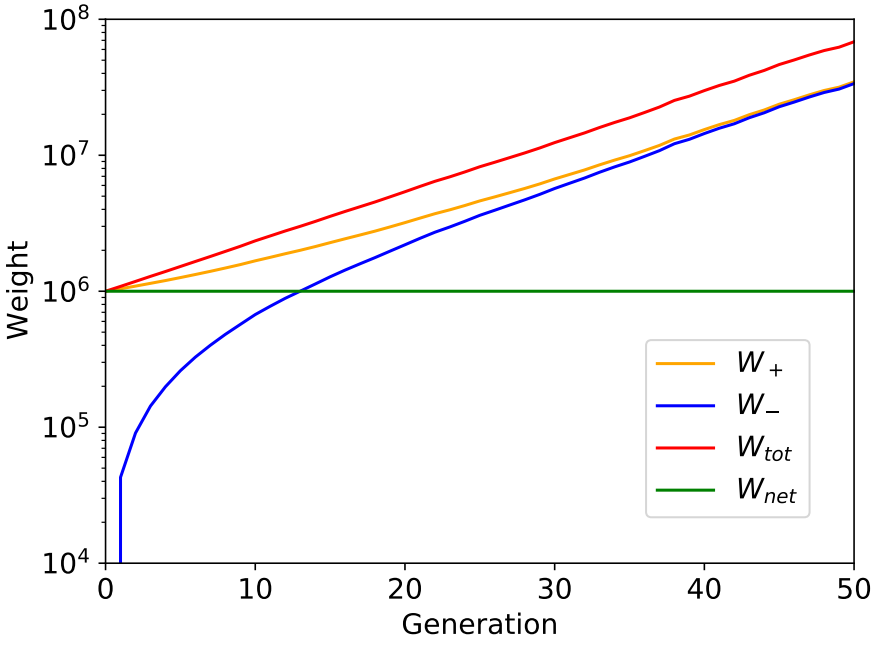

Figure 8.1: Weight of neutrons with positive (W_+) and negative weight (W_-), as a function of the generation in power iteration. The total weight ($W_{\text{tot}} = W_+ + W_-$) and the net weight ($W_{\text{next}} = W_+ - W_-$) are also shown. The system is a rod populated with 10^6 neutrons. Adapted from Belanger, Mancusi, and Zoia (2021), with permission.

used in industrial Monte Carlo codes (with positive weights), except for the fact that w is usually written instead of $|w|$.

- Fission neutrons are generated with a weight of $\text{sign}(w)$ (in Monte Carlo codes without negative neutrons, they are given a weight of 1).
- Finally, at the end of the generation, the weights of all the fission neutrons are renormalized in such a way that their sum is equal to the initial source weight. Let the **positive weight** W_+ be

$$W_+ = \sum_i w_i \Theta(w_i),$$

where Θ is the Heaviside function. Similarly, let the **negative weight** W_- be

$$W_- = -\sum_i w_i \Theta(-w_i).$$

Note that both W_+ and W_- are positive. The **net weight** is given by

$$W_{\text{net}} = W_+ - W_- = \sum_i w_i,$$

while the **total weight** is given by

$$W_{\text{tot}} = W_+ - W_- = \sum_i |w_i|.$$

The renormalization procedure ensures that the net weight is constant.

Figure 8.1 shows the behavior of the amount of positive and negative weight present in the fission source at the beginning of generation, as a function of the generation. The negative weight starts at zero (no negative neutrons are present in the source), but it quickly starts growing exponentially. Likewise, the positive weight starts at the initial value of 10^6 and grows exponentially. The net weight, which is the difference between the positive and negative weights, stays constant; this is to be expected, because of the renormalization of the fission source. However, the total weight grows exponentially. The result of renormalization is that the number of neutrons to transport is proportional to the *total* weight, and so are the computational cost and the memory footprint of each generation. Clearly, the simulation of Fig. 8.1 is not sustainable.

8.2.2 The failure of power iteration

It is possible to model the power iteration with negative-weighted delta tracking as a pair of coupled Boltzmann equations, which we write in integro-differential form:

$$\hat{\boldsymbol{\Omega}} \cdot \nabla \varphi_+ + \Sigma_{\text{smp}} \varphi_+ = \boldsymbol{S}\varphi_+ + \frac{1}{k}\boldsymbol{F}\varphi_+ + \Delta(\Sigma_{\text{smp}} - \Sigma_t)\,\varphi_+ + \Delta(\Sigma_t - \Sigma_{\text{smp}})\,\varphi_- \quad \text{(8.14a)}$$

$$\hat{\boldsymbol{\Omega}} \cdot \nabla \varphi_- + \Sigma_{\text{smp}} \varphi_- = \boldsymbol{S}\varphi_- + \frac{1}{k}\boldsymbol{F}\varphi_- + \Delta(\Sigma_{\text{smp}} - \Sigma_t)\,\varphi_- + \Delta(\Sigma_t - \Sigma_{\text{smp}})\,\varphi_+. \quad \text{(8.14b)}$$

Here Σ_{smp} is the sampling cross section, φ_+ and φ_- respectively represent the fluxes of positive and negative neutrons (in what follows, we will use "positive/negative neutrons" as a shorthand for "neutrons with positive/negative weights"), the function Δ is defined as

$$\Delta(x) = x\,\Theta(x),$$

and Θ represents the Heaviside function. The "physical" flux is represented by the difference between the flux of positive and negative neutrons:

$$\varphi = \varphi_+ - \varphi_-.$$

By taking the difference of Eqs. (8.14a) and (8.14b) one obtains an equation for φ alone:

$$\hat{\boldsymbol{\Omega}} \cdot \nabla \varphi + \Sigma_t \varphi = \boldsymbol{S}\varphi + \frac{1}{k}\boldsymbol{F}\varphi. \quad \text{(8.15)}$$

This is the physical Boltzmann equation that we are trying to solve with Monte Carlo. However, consider now the sum of Eqs. (8.14a) and (8.14b), which yields

$$\hat{\boldsymbol{\Omega}} \cdot \nabla \eta + \Sigma_{t,\eta} \eta = \boldsymbol{S}\eta + \frac{1}{k}\boldsymbol{F}\eta. \quad \text{(8.16)}$$

Here we have introduced $\eta = \varphi_+ + \varphi_-$ and

$$\Sigma_{t,\eta}\eta = \Sigma_{\text{smp}} - |\Sigma_{\text{smp}} - \Sigma_t|.$$

Equation (8.16) has the same form as the physical k-eigenvalue equation, Eq. (8.15), except that Σ_t is replaced by $\Sigma_{t,\eta}$. It is easy to show that

$$\Sigma_{t,\eta} \leq \Sigma_t.$$

Therefore, the capture cross section associated with Eq. (8.16) is smaller than the physical capture cross section:

$$\begin{aligned}\Sigma_{c,\eta} &= \Sigma_{t,\eta} - \Sigma_s - \Sigma_f \\ &\leq \Sigma_t - \Sigma_s - \Sigma_f \\ &= \Sigma_c.\end{aligned}$$

So, on physical grounds, we can conclude that the dominant eigenvalue of Eq. (8.16) is higher than k_{eff}, which is the dominant eigenvalue of the physical equation. Since the power iteration always converges to the dominant eigenvalue, the Monte Carlo simulation of Eq. (8.16) will *not* converge to the physical eigenvalue.

What is the form of the eigenfunctions of Eq. (8.14)? It is easy to observe that Eq. (8.14) is symmetric under the exchange between φ_+ and φ_-; therefore, any eigenpair $\varphi_\pm$ must be either symmetric or antisymmetric under the exchange. Indeed, the antisymmetric eigenpairs ($\varphi_+ = -\varphi_-$) are given by $\varphi_\pm = \pm\varphi$, where φ is a solution of the physical Boltzmann equation, Eq. (8.15). The symmetric eigenpairs ($\varphi_+ = \varphi_-$) are given by $\varphi_\pm = \eta$, corresponding to the solution of the "unphysical" Boltzmann equation, Eq. (8.16). Therefore, the dominant unphysical eigenmode is represented by equal amounts of positive and negative weight.

8.2.3 Strategies for weight cancellation

This remark suggests that it should be possible to remove the unphysical eigenmodes by combining and "cancelling" positive and negative neutrons. Clearly, two neutrons located at the same phase-space point P, with weights of equal magnitude but opposing signs, do not contribute anything to the simulation on average, and can be safely eliminated. Applying weight cancellation to transport problems, however, is difficult because neutrons practically never occupy the very same point in phase space. In order to achieve cancellation, it is necessary to devise a way to combine neutrons that are "close by" in phase space, in some sense.

There are a few ways to achieve this goal. Arguably the simplest strategy is the following. Consider the neutrons that comprise the fission source. We cluster them based on their proximity, for example using a mesh superimposed on the geometry, or using the cells of the Monte Carlo geometry as cancellation regions. We compute the net weight for each region, and we assign it to all the neutrons within that region (Zhang et al. 2016). This is a form of **approximate regional weight cancellation**; it achieves some form of cancellation "at a distance", but it is not an exact algorithm. The mesh discretization biases the evaluation of the neutron weights. Making the mesh finer will help reduce the bias, but only up to a certain point. First, note that the fission source contains neutrons with different energies and directions; in principle, these dimensions should also be discretized. Second, for a given number of neutrons in the fission source, the efficiency of approximate regional cancellation decreases as the mesh becomes finer, because each region will contain fewer neutrons to cancel.

It is interesting to ask whether there exist weight cancellation algorithms that do not introduce any bias. One such algorithm was proposed by T. E. Booth and Gubernatis (2010). It is also a form of regional cancellation, in that it discretizes the geometry in regions. The central idea is to remove a fraction of weight from each neutron and "spread" it uniformly over the region the neutron belongs to, as we will discuss in more detail below. Cancellation

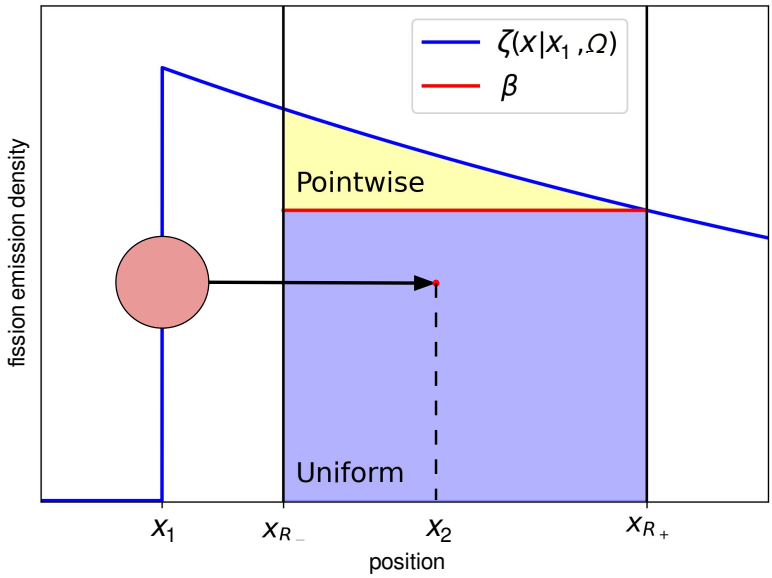

Figure 8.2: Schematic representation of the one-dimensional regional cancellation algorithm by T. E. Booth and Gubernatis (2010). The yellow and lavender shadings respectively represent the pointwise part and the uniform part of the fission density. Adapted from Belanger, Mancusi, and Zoia (2021), with permission.

is achieved by combining the uniform weight portions of different neutrons and converting the resulting net weight to new fission neutrons. The main limitation of Booth and Gubernatis' algorithm is that it is limited to very simple one-dimensional problems (a single-speed rod model).

Let us assume that a neutron with energy E_1 flies from $\boldsymbol{r}_1$ with direction $\hat{\boldsymbol{\Omega}}_1$ to $\boldsymbol{r}_2$, and undergoes a collision there. Let R denote the cancellation region that $\boldsymbol{r}_2$ belongs to, and assume for the moment that $\boldsymbol{r}_1$ does not belong to R. In the rod model, if $\boldsymbol{r}_1$ is outside R and $\boldsymbol{r}_2$ is inside R, then all the points in R are reachable with a single flight starting at $\boldsymbol{r}_1$ with direction $\hat{\boldsymbol{\Omega}}_1$. Figure 8.2 illustrates this idea in the simple case of a uniform system. The neutron starting at x_1 enters the region $R = [x_{R_-}, x_{R_+}]$ and undergoes a collision at x_2, but any point in R could have been sampled as the collision site. This is highlighted by the *fission density* $\zeta(x|x_1, \hat{\boldsymbol{\Omega}})$, which represents the expected number of fission neutrons emitted after a flight from x_1 to x_2 and a collision at x_2; note that the fission density does not vanish anywhere in the region.

We follow T. E. Booth and Gubernatis (2010) here. The fission density is proportional to the weight of the neutron, w. We decide to represent the latter as the sum of a pointwise component located at x_2 and a uniform component distributed over R. Somewhat surprisingly, the relative weight of the two contributions is actually a free parameter of the model. Specifically, if we denote our free parameter as β, then the amount of weight that is uniformly spread over R is given by

$$w_u = w \cdot \frac{\beta}{\zeta(x_2|x_1, \hat{\boldsymbol{\Omega}})}, \tag{8.17}$$

while the pointwise weight (located at x_2) is given by

$$w_p = w - w_u = w \cdot \frac{\zeta(x_2|x_1, \hat{\mathbf{\Omega}}) - \beta}{\zeta(x_2|x_1, \hat{\mathbf{\Omega}})}. \tag{8.18}$$

Since we want to maximize the efficiency of cancellation, we want the value of β to be as large as possible. The most natural choice it to take β equal to the minimum of $\zeta(x|x_1, \hat{\mathbf{\Omega}})$ over R:

$$\beta = \min_{x \in R} \zeta(x|x_1, \hat{\mathbf{\Omega}}).$$

This corresponds to the choice made in Fig. 8.2. However, this is by no means the only possible choice. By construction, weight is conserved for any value of β. For values of β larger than zero but smaller than the minimum, the qualitative behavior is the same but, for a given $\boldsymbol{r}_1$ and $\boldsymbol{r}_2$, one obtains a smaller uniform weight, which degrades the efficiency of cancellation. For values of β larger than the minimum, there are positions in R where $w_u > w$, and therefore $w_p < 0$. Thus, depending on the choice of β, the cancellation algorithm can generate (additional) negative weight. This is not necessarily a problem, as we will see below.

Booth and Gubernatis' original formulation of the algorithm is essentially heuristic: the unbiasedness of the algorithm is not rigorously proven; no criterion for the choice of the free parameter β is given; finally, and perhaps most importantly, it is far from clear how the rod-model algorithm can be generalized to more than one dimension and beyond one-speed models, let alone to continuous energy. In particular, in two dimensions or higher, it is not true anymore that any point of the cancellation region containing $\boldsymbol{r}_2$ is reachable with a single flight from $\boldsymbol{r}_1$; the only reachable points are those on the half-line connecting $\boldsymbol{r}_1$ to $\boldsymbol{r}_2$. Thus, the neutron weight cannot be trivially spread over the whole cancellation region.

8.2.4 Exact regional cancellation in three dimensions

Drawing inspiration from this seminal work, we developed an exact regional weight cancellation algorithm for transport in three dimensions (but the principle of the algorithm easily generalizes to any number of dimensions) and to multi-group energy treatment (a further generalization to continuous energy is possible, but there are a few nettlesome details that need to be addressed). The key insight to generalizing the algorithm to three-dimensional problems is twofold. First, we generalize cancellation regions to phase space; this means that in general we also need to discretize the directions and the energy. Second, suppose a neutron undergoes a collision at $P_0 = (\boldsymbol{r}_0, \hat{\mathbf{\Omega}}_0, E_0)$, is emitted from the collision at $P_1 = (\boldsymbol{r}_1, \hat{\mathbf{\Omega}}_1, E_1)$ and undergoes a second collision at $P_2 = (\boldsymbol{r}_2, \hat{\mathbf{\Omega}}_2, E_2)$, with $\boldsymbol{r}_2 \in R$ (note also that $\boldsymbol{r}_0 = \boldsymbol{r}_1$, $\hat{\mathbf{\Omega}}_1 = \hat{\mathbf{\Omega}}_2$ and $E_1 = E_2$). In three dimensions, the endpoints of all possible flights starting from P_1 do not cover the whole cancellation region; however, if one considers all possible exit directions $\hat{\mathbf{\Omega}}_1$ for neutrons of energy E_1 exiting the collisions at P_0, it is possible that the endpoints of all the possible flights *do* cover the cancellation region. This means that, instead of considering the expected fission density in R due to a flight starting at P_1, we actually need to consider the expected fission density in R due to a collision happening at P_0. The idea is schematically illustrated in Fig. 8.3.

In three dimensions, the uniform and pointwise weights are still given by Eqs. (8.17) and (8.18), but the fission density function ζ is conditioned to a collision happening at P_0,

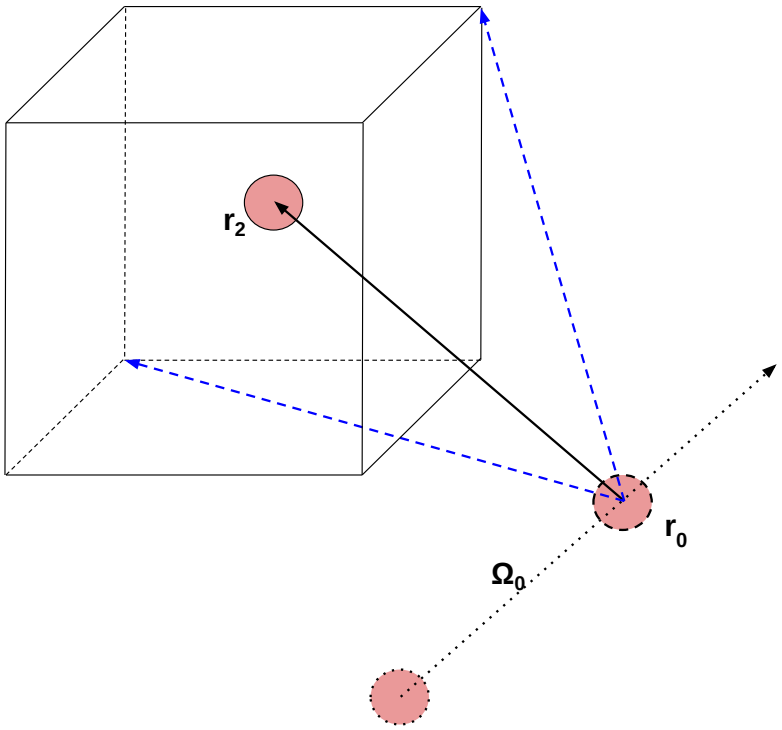

Figure 8.3: Schematic representation of the three-dimensional exact regional cancellation algorithm. Adapted from Belanger, Mancusi, and Zoia (2021), with permission.

instead of a flight starting at P_1. In practice, for simulations based on negative-weighted delta-tracking, the shape of the expected fission density is rather simple:

$$\zeta(P_2|P_0,E_1) = \Sigma_f(P_2)\exp\left(-\Sigma_m|\boldsymbol{r}_2-\boldsymbol{r}_0|\right)\frac{f(\hat{\boldsymbol{\Omega}}_1|\boldsymbol{r}_0,\hat{\boldsymbol{\Omega}}_0,E_0\to E_1)}{|\boldsymbol{r}_2-\boldsymbol{r}_0|^2},$$

where $\hat{\boldsymbol{\Omega}}_1 = \frac{\boldsymbol{r}_2-\boldsymbol{r}_0}{|\boldsymbol{r}_2-\boldsymbol{r}_0|}$, and the scattering kernel $f(\hat{\boldsymbol{\Omega}}_1|\boldsymbol{r}_0,\hat{\boldsymbol{\Omega}}_0,E_0\to E_1)$ is the conditional distribution for the direction $\hat{\boldsymbol{\Omega}}_1$ after the collision, given that the collision takes place at $\boldsymbol{r}_0$ with incident direction $\hat{\boldsymbol{\Omega}}_0$, incident energy E_0 *and outgoing energy* E_1. Note that the definition of the scattering kernel is a bit unusual because it is also conditioned to a given outgoing energy. With this definition, the regional cancellation algorithm is rather simple. When a particle undergoes a collision in R, its weight is split into a uniform part and a point-wise part:

$$\begin{aligned} w_u &= w\cdot\frac{\beta}{\zeta(P_2|P_0,E_1)} \\ w_p &= w-w_u = w\cdot\frac{\zeta(P_2|P_0,E_1)-\beta}{\zeta(P_2|P_0,E_1)}, \end{aligned}$$

which are fully analogous to Eqs. (8.17) and (8.18).

In Belanger, Mancusi, and Zoia (2021), we demonstrated the feasibility of three-dimensional exact cancellation in a multi-group benchmark (E. E. Lewis et al. 2001). Our exact regional cancellation algorithm was proved to successfully halt the growth of the number of neutrons and their total weight, without introducing any bias in the resulting observables.

8.2.5 Optimization of weight cancellation

In a subsequent paper (Belanger, Mancusi, and Zoia 2022a), we provided a clearer theoretical framework to discuss all the questions related to exact regional cancellation. Booth-Gubernatis regional cancellation can be modelled as a higher-order next-event estimator for the fission density with the following form:

$$\vartheta_R(P_2|P_0,R,Q) = \frac{\beta}{V_R\zeta(P_2|P_0)} + \left(1 - \frac{\beta}{\zeta(P_2|P_0)}\right)\delta(Q-P_2); \tag{8.19}$$

here Q is a generic point within the cancellation region R, $\beta(P_0)$ is a free parameter, V_R is the phase-space volume of R, and we have omitted the intermediate energy E_1 from the arguments of the expected fission density ζ, for the sake of conciseness. Equation (8.19) is a next-next event estimator. In the paper, we actually discuss the possibility to use even next-next-next-event estimators by considering the expected fission *emission* density instead of the fission density. This choice may present some practical advantages, but it is not mandatory.

Establishing a theoretical framework for exact regional cancellation gives several insights. First, we have sufficient conditions under which the estimator ϑ_R is unbiased. Specifically, Eq. (8.19) is unbiased if β is a function of P_0 only. In other words, the choice of the cancellation parameter is allowed to depend on the particle and on the phase-space coordinates before the last collision, but it is not allowed to depend on the coordinates of the final point.

Moreover, the shape of the estimator makes it possible to optimize the choice of the cancellation parameter. Specifically, let us suppose that K particles undergo collisions at points $P_{0,k}$ and land at points $P_{2,k}$ in cancellation region R ($k = 1,\dots,K$). Let $w_{k,p}$ and $w_{k,u}$ respectively be the pointwise and uniform part of the weight of the k-th particle. The *total weight* after cancellation (i.e. after combining the uniform parts of all the weights) is given by

$$\begin{aligned}\Gamma_1(P_{0,1},\dots,P_{0,K};P_{2,1},\dots,P_{2,K}) &= \sum_{k=1}^{K}|w_{k,p}| + |\sum_{k=1}^{K} w_{k,u}| \\ &= \sum_{k=1}^{K}\left|\frac{\zeta_k-\beta_k}{\zeta_k}w_k\right| + \left|\sum_{k=1}^{K}\frac{\beta_k}{\zeta_k}w_k\right|.\end{aligned} \tag{8.20}$$

Here β_k is the value of the cancellation parameter and $\zeta_k = \zeta(P_{2,k}|P_{0,k})$ is the value of the expected fission (emission) density for the k-th particle. Ideally, we would like to choose the values of the β_k parameters so that Γ_1 is minimized. Note however that we cannot simply minimize Eq. (8.20) with respect to β_k, because the resulting optimal parameter values would depend on $P_{2,k}$, which is not allowed if we require an unbiased estimator. Moreover, Γ_1 is somewhat tricky to minimize analytically because it is not differentiable with respect to β_k.

For these reasons, we instead consider the squared weight after cancellation:

$$\Gamma_2(P_{0,1},\dots,P_{0,K};P_{2,1},\dots,P_{2,K}) = \sum_{k=1}^{K}\left(\frac{\zeta_k-\beta_k}{\zeta_k}w_k\right)^2 + \left(\sum_{k=1}^{K}\frac{\beta_k}{\zeta_k}w_k\right)^2, \tag{8.21}$$

This quantity is differentiable with respect to β_k, but it still depends on $P_{2,k}$. We can eliminate these coordinates by averaging over them according to their natural distribution, which is

$$\mathcal{P}(P_{2,1},\ldots,P_{2,K}|P_{0,1},\ldots,P_{0,K}) = \frac{\prod_{k=1}^{K}\zeta_k}{\prod_{k=1}^{K}\int_R \zeta_k \,\mathrm{d}P_{2,k}}.$$

This yields the following function to minimize with respect to β_k:

$$\langle\Gamma_2\rangle(P_{0,1},\ldots,P_{0,K}) = \frac{\int_R \Gamma_2(P_{0,1},\ldots,P_{0,K};P_{2,1},\ldots,P_{2,K})\prod_{k=1}^{K}\zeta_k \,\mathrm{d}P_{2,k}}{\int_R \prod_{k=1}^{K}\zeta_k \,\mathrm{d}P_{2,k}}.$$

Straightforward calculations show that the minimum is given by

$$\beta_k = \langle\zeta_k\rangle\, c_k \left(1 - \frac{S}{w_k}\right), \tag{8.22}$$

where we have introduced the average fission density and average inverse of the fission density for the k-th particle

$$\langle\zeta_k\rangle = \frac{\int_R \zeta(P_{0,k},P)\,\mathrm{d}P}{\int_R \mathrm{d}P} \tag{8.23}$$

$$\left\langle\zeta_k^{-1}\right\rangle = \frac{\int_R \zeta(P_{0,k},P)^{-1}\,\mathrm{d}P}{\int_R \mathrm{d}P}, \tag{8.24}$$

as well as the following quantities

$$c_k = \left(2\langle\zeta_k\rangle\left\langle\zeta_k^{-1}\right\rangle - 1\right)^{-1}$$

$$S = \frac{\sum_{k=1}^{K} c_k w_k}{1 + \sum_{k=1}^{K} c_k}.$$

In order to use the optimal parameter values given by Eq. (8.22), it is necessary to evaluate the average fission density and average inverse of the fission density, Eqs. (8.23) and (8.24). For homogeneous cancellation regions of simple shapes and simple scattering distribution laws (e.g. isotropic), it is conceivable that the integrals in Eqs. (8.23) and (8.24) could be analytically evaluated. In general, however, the integrals need to be evaluated numerically; note that an inaccurate evaluation will only affect the efficiency of cancellation, but the method will remain unbiased.

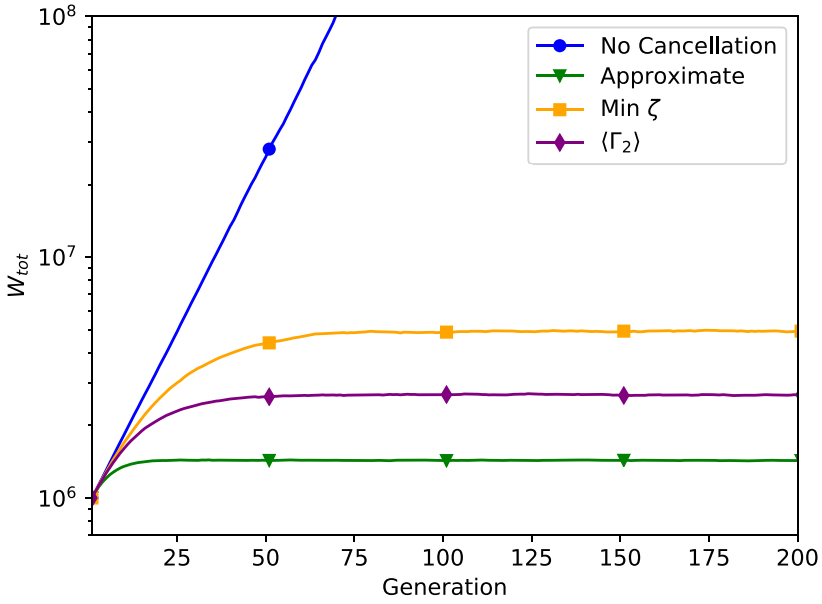

Figure 8.4: Amount of total weight in the modified C5G7 benchmark, as a function of generation, for different cancellation methods, including no cancellation and approximate cancellation. Adapted from Belanger, Mancusi, and Zoia (2022a), with permission.

In our paper, we used pseudo-random and quasi-random sequences to estimate the integrals. Figure 8.4 shows the evolution of the amount of total weight in the modified C5G7 benchmark with negative-weighted delta tracking, as a function of generation, for different cancellation methods. As discussed above, the total weight grows exponentially in the calculation without weight cancellation. We can also choose β_k to be the minimum of the expected fission density for the k-th particle:

$$\beta_k = \min_{P \in R} \zeta(P_{0,k}, P).$$

This yields the yellow curve in Fig. 8.4. This is sufficient to suppress the exponential growth, as promised. The optimal choice of the cancellation parameter, Eq. (8.22), yields the purple curve. The saturation level of this calculation is lower than the yellow curve, which implies that cancellation is indeed more efficient. This is remarkable because the optimal choice sometimes must occasionally result in additional negative pointwise weight being generated at the fission site. In spite of this, the overall efficiency of cancellation is increased. Finally, the green curve shows the result of using approximate regional cancellation à la Zhang et al. (2016), as discussed in Section 8.2.3 above. One remarks that approximate cancellation is even more effective than the optimal exact cancellation algorithm in moderating the increase in total particle weight. Of course, this comes at the price of introducing a bias in the calculation, although we were admittedly unable to highlight the presence of the bias in a complex calculation such as the C5G7 benchmark.

References

The work presented in this chapter is based on the following publications:

Belanger, H., D. Mancusi, and A. Zoia (2021). *Exact Weight Cancellation in Monte Carlo Eigenvalue Transport Problems*. In: *Phys. Rev. E* 104.1, p. 015306. DOI: 10/gk7tnk.

— (2022a). *Unbiasedness and Optimization of Regional Weight Cancellation*. In: *Phys. Rev. E* 106.2, p. 025302. DOI: 10.1103/PhysRevE.106.025302.

Mancusi, D. and A. Zoia (2020). *Zero-Variance Schemes for Kinetic Monte Carlo Simulations*. In: *Eur. Phys. J. Plus* 135.5 (6), p. 401. DOI: 10.1140/epjp/s13360-020-00387-8.

The content of Section 8.2 is drawn from the Ph.D. thesis of my student Hunter Belanger (Belanger 2022).

Conclusions and perspectives

I wish to conclude this manuscript by expressing my view for the future development of my research career. I can see several productive research directions, which I will detail below.

9.1 Towards multi-physics Monte Carlo simulations for reactor cores

I mentioned in Section 8.1 that zero-variance games can provide valuable guidance for the development of efficient variance-reduction schemes. As explained in Chapter 7, the computational cost of dynamic Monte Carlo calculations is still orders of magnitude too large for widespread adoption of this technique, e.g. in safety calculations. It is useful in this context to draw parallels with and inspiration from the recent developments in fixed-source, stationary calculations. About twenty-five years ago Wagner and Haghighat (1998) suggested using a deterministic solver to calculate the adjoint flux for the detector, and use it as an importance map for Monte Carlo calculations. This method, known as Consistent Adjoint-Driven Importance Sampling (CADIS), was immediately shown to yield very promising efficiency gains. It took a few years for the community to build software that simplified the application of CADIS to existing Monte Carlo problems (Mosher et al. 2013); once this obstacle was removed, CADIS quickly superseded all previous variance-reduction techniques in industrial applications (Munk and Slaybaugh 2019).

It is likely that dynamic Monte Carlo calculations will tread along a similar path. As of today, we know the rules of the optimal kinetic Monte Carlo game; we also know how to write deterministic solvers for the time-dependent adjoint Boltzmann equation. We need to put the pieces together and democratize the use of time-dependent CADIS-based Monte Carlo in kinetic simulations. Eventually, the physical feedback mechanisms will also have to be factored in the calculation of the importance map, in order to maximize the efficiency of dynamic simulations.

Are zero-variance games the final say in matters of variance reduction? Vigilant Readers may have noticed that zero-variance games suffer from an(other) important conceptual limitation: in a given calculation, only *one* estimator can be optimized at a time. Indeed, the zero-variance game depends not only on the observable that we optimize for, but even more specifically on the estimator that we select (Eq. (8.5)). Estimators other than the zero-variance one, in general, have a finite variance. This is true even in stationary conditions. In coupled dynamic calculations for reactor physics, the Monte Carlo particle transport code is used as a solver for e.g. power deposition (for the case of a coupling with thermal-hydraulics)

or reaction rates (for depletion). The outputs are generally discretized in space (on a mesh or on a set of volumes), and sometimes in energy. Clearly, the typical use case is far from concerning a single observable.

In practice, one can still use zero-variance games to guide the construction of efficient Monte Carlo simulations. Taking inspiration again from stationary calculations, there exist generalizations of the CADIS method that tackle the problem of "distributing" the CADIS acceleration over several observables. In one such method, called Forward-Weighted CADIS (FW-CADIS, Peplow et al. 2007), the objective is to obtain roughly the same variance for the estimation of a neutron flux in all cells of a mesh covering the simulation domain (Munk and Slaybaugh 2019). This is done by taking the adjoint source to be inversely proportional to the (direct) neutron flux, which is estimated in a preliminary deterministic calculation[1]. A similar approach is likely to work in kinetic and dynamic calculations, too.

9.2 Extending weight cancellation

In Section 8.2 I discussed our recent advances on the development of weight cancellation techniques. These methods stemmed out of the need to control the growth of particle population in criticality simulations involving negative-weighted delta tracking. In a few very recent publications (Belanger, Mancusi, Rouchon, et al. 2023; Belanger, Mancusi, and Zoia 2022b), we showed that weight cancellation can yield enormous gains in the efficiency of simulations for power reactor noise (R. Sanchez 2015; Yamamoto 2013). It is my feeling that we are only beginning to understand the potential of these techniques.

On the one hand, regionalized weight cancellation techniques are still primitive. The efficiency of cancellation depends on the choice of the mesh. In Belanger, Mancusi, and Zoia (2021), we heuristically found that there is an optimum size for the cells of the cancellation mesh; however, the optimal size depends non-linearly on the net weight circulating in the system. This makes it somewhat difficult to build an optimal or nearly optimal mesh without a preliminary empirical study. Moreover, in its current implementation, regionalized cancellation is restricted to happen at fission events, which are a very limited subset of the events that occur in the lifetime of a neutron. I cannot see any reason why the formalism of regionalized cancellation cannot be applied to any type of collision. Cancelling particle weights at every collision step would largely increase the efficiency of exact regional cancellation, and possibly bring it to levels of efficiency comparable to those of approximate regional cancellation (Zhang et al. 2016). Finally, other weight cancellation techniques need to be explored. For example, in the context of fermion Monte Carlo, Arnow et al. (1982) proposed to perform pairwise cancellation of particle weights by considering transitions to common intermediate states. This algorithm is applicable to neutron transport, too, but a naïve implementation has the disadvantage of scaling quadratically with the number of particles present in the system (T. E. Booth 2003). The quadratic cost can be avoided by limiting cancellation to particles that are sufficiently close together. In short, I am confident that there are still large improvements to bring to the methodology of cancellation.

On the other hand, there are many applications of viable weight cancellation techniques. As mentioned above, the first one that we have explored is the simulation of power reactor noise. The noise transport problem is a fixed-source problem that is characterized by the

[1] As far as I am aware, there are only heuristic explanations for the fact that FW-CADIS yields uniform variance (and indeed, the theory may very well indicate that the expected variance is not exactly uniform).

fact that the source term and some of the cross sections involved are complex. This in turn implies that the solutions are complex. In Monte Carlo, complex solutions require the use of particles with complex weights. The real and imaginary part of the particle weights do not have a fixed sign; particles with both signs are present in the simulation. Hence, weight cancellation is beneficial to the efficiency of noise simulations, because it makes it possible to combine particle weights of opposite sign, thereby reducing the total amount of weight to transport; this reduces the computational cost *and* the variance of the calculation at the same time (Belanger, Mancusi, Rouchon, et al. 2023).

Another application of cancellation is the calculation of higher-order eigenmodes (beyond the fundamental state) of the Boltzmann k-eigenvalue equation. This is actually one of the original motivations for the development of cancellation techniques (T. E. Booth and Gubernatis 2010; Zhang et al. 2016). Higher-order eigenfunctions do not have a fixed sign, contrary to the fundamental mode. Thus, the Monte Carlo simulation of higher eigenmodes requires the use of particles with positive and negative weights. As for noise, weight cancellation can boost the efficiency of the simulation. In some algorithms, cancellation is actually required for the algorithm to converge to the correct solution (T. E. Booth and Gubernatis 2010).

More broadly, I expect weight cancellation to be generally useful in all situations where particle weights can take opposite signs. This is the case of other problems in transport theory, such as the search for critical buckling (Yamamoto 2012). Even more generally, weight cancellation is actually useful in all situations where the distribution of particle weights is liable to have a large dispersion. For Monte Carlo simulations with positive particle weights, the dispersion of the weight distribution is typically controlled using Russian roulette and splitting. However, it is not always straightforward to provide a good value for the *reference weight*, i.e. the weight that particles are assigned after roulette or splitting. This happens for example in variance-reduction calculations using modified flight and collision kernels. In contrast, weight cancellation does not require the definition of a reference weight. The typical particle weight after cancellation is dynamically determined by the weights of the incoming particles.

Finally, it should be possible to generalize weight cancellation to other types of Monte Carlo simulations, beyond particle transport. One possibility that comes to my mind in particular is its use in Monte Carlo simulations of Lévy flights (Lévy 1954; Mandelbrot 1982), which are commonly used in models across the fields of biology, ecology, geophysics, and other. Lévy flights are characterized by the fact that the flight distances follow a power law; this should be contrasted with the exponential flights that are characteristic of neutron transport. For exponential flights, the mean free path gives the order of magnitude of the size of the cells of the optimal cancellation mesh. Lévy flights do not have a typical length scale (they are actually scale-invariant); since the flight lengths have a heavy-tailed distribution, I expect regional cancellation methods to be less sensitive to the coarseness of the cancellation mesh, compared to exponential flights.

9.3 Fluctuations, feedbacks and stochastic processes

In the *zero-power regime*, i.e. at low reactor power, where relatively few neutrons circulate in the core, the Boltzmann equation is not a good model for the prediction of the behavior of the neutron population. More accurately, the Boltzmann equation describes the mean value of

the neutron population in phase space, but in the zero-power regime the relative fluctuations in the population size are comparable to the mean values. The theory of stochastic processes provides the tools to reason about the statistical behavior of the neutron population (Pál and Pázsit 2006; M. M. R. Williams 1974).

In Monte Carlo simulations for nuclear reactor cores, the number of particles is always far smaller than the number of particles present in the real core, by several orders of magnitude[2]. A reactor core containing a number of neutrons of the order of a Monte Carlo calculation would be operating close to the zero-power regime. In this sense, Monte Carlo calculation *always* effectively operate in the zero-power regime, even when simulating a reactor at full power, in the sense that the relative fluctuations are rarely negligible. This is particularly important in the presence of physical feedback mechanisms, such as thermal-hydraulics or depletion. Indeed, feedback mechanisms act on the neutron population, but their intensity depends on the size of the population itself; thus, the system with feedback is non-linear. The physics is further complicated by the fact that feedbacks mostly act on the neutron population, but variations of the latter are somewhat ballasted by the presence of precursors, which introduce other characteristic time scales.

In non-linear conditions, random fluctuations in the population have another unwanted consequence: they introduce a statistical bias in the population mean; this follows from Jensen's inequality (Rudin 2013). The bias is small if fluctuations are small; therefore, the bias will typically be unmeasurable in a real reactor at full power, and the reactor will operate very close to the "deterministic" point. In contrast, in a Monte Carlo calculation, the bias is much larger and may become observable under suitable conditions. This is an intrinsic limitation of the application of the Monte Carlo method to the treatment of non-linear feedback mechanisms.

In an industrial calculation with non-linear feedbacks, it is definitely desirable to quantify the bias and keep it under control. One way to approach this problem is to use stochastic processes to model fluctuations in Monte Carlo codes. The aim of this approach is to be predictive about the fluctuations and biases expected in Monte Carlo calculations, and use these tools to formulate recommendations for their use. The first step towards this goal is the characterization of fluctuations and correlations in static and dynamic calculations, which is one of the recent endeavors that I have undertaken with one of my Ph.D. students (Bonnet et al. 2022). Further steps involve the extension of the formalism to accommodate physical feedback effects, and the formulation of suitable criteria to at least detect the presence of a sizeable bias.

[2] In a typical commercial PWR at full power, the total number of neutrons that circulate at any given time is of the order of 10^{15}.

Bibliography

Aichelin, J. (1991). *"Quantum" Molecular Dynamics—a Dynamical Microscopic n-Body Approach to Investigate Fragment Formation and the Nuclear Equation of State in Heavy Ion Collisions*. In: *Phys. Rep.* 202.5, pp. 233–360. DOI: 10.1016/0370-1573(91)90094-3 (cit. on pp. 94, 101).

Allison, J., K. Amako, J. Apostolakis, et al. (2016). *Recent Developments in Geant4*. In: *Nucl. Instrum. Meth. Phys. Res. A* 835, pp. 186–225. DOI: 10/f88zjr (cit. on p. 64).

Alvarez-Pol, H., J. Benlliure, E. Casarejos, et al. (2010). *Production of New Neutron-Rich Isotopes of Heavy Elements in Fragmentation Reactions of ^{238}U Projectiles at 1A GeV*. In: *Phys. Rev. C* 82.4, p. 41602. DOI: 10/d23qv7 (cit. on p. 91).

Andreo, P. and A. Brahme (1984). *Restricted Energy-Loss Straggling and Multiple Scattering of Electrons in Mixed Monte Carlo Procedures*. In: *Radiat. Res.* 100.1, pp. 16–29. DOI: 10/dcrpt9 (cit. on pp. 34, 35).

Arfken, G. B., H. J. Weber, and F. E. Harris (2012). *Mathematical Methods for Physicists: A Comprehensive Guide*. 7e édition. Amsterdam ; Boston: Academic Press Inc. 1220 pp. (cit. on p. 43).

Arnow, D. M. et al. (1982). *Green's Function Monte Carlo for Few Fermion Problems*. In: *J. Chem. Phys.* 77.11, pp. 5562–5572. DOI: 10.1063/1.443762 (cit. on p. 144).

Assaraf, R., M. Caffarel, and A. Khelif (2007). *The Fermion Monte Carlo Revisited*. In: *J. Phys. A: Math. Theor.* 40.6, p. 1181. DOI: 10.1088/1751-8113/40/6/001 (cit. on p. 131).

Audirac, L., A. Obertelli, P. Doornenbal, et al. (2013). *Evaporation-Cost Dependence in Heavy-Ion Fragmentation*. In: *Phys. Rev. C* 88.4, p. 41602. DOI: 10/gg89jg (cit. on pp. 101, 103).

Bass, R. (1974). *Fusion of Heavy Nuclei in a Classical Model*. In: *Nucl. Phys. A* 231.1, pp. 45–63. DOI: 10/fqqp86 (cit. on p. 95).

Bateman, H. (1908). *The Solution of a System of Differential Equations Occurring in the Theory of Radio-Active Transformations*. In: *Proc. Camb. Philos. Soc.* 15, pp. 423–427 (cit. on p. 37).

Batzel, R. E., D. R. Miller, and G. T. Seaborg (1951). *The High Energy Spallation Products of Copper*. In: *Phys. Rev.* 84.4, pp. 671–683. DOI: 10.1103/PhysRev.84.671 (cit. on p. 66).

Belanger, H. (2022). *Development of Numerical Methods for Neutronics in Continuous Media*. PhD thesis. Université Paris-Saclay. 207 pp. (cit. on p. 141).

Belanger, H., D. Mancusi, A. Rouchon, et al. (2023). *Variance Reduction and Noise Source Sampling Techniques for Monte Carlo Simulations of Neutron Noise Induced by Mechanical Vibrations*. In: *Nucl. Sci. Eng.* 197.4, pp. 534–557. DOI: 10.1080/00295639.2022.2126719 (cit. on pp. 144, 145).

Belanger, H., D. Mancusi, and A. Zoia (2021). *Exact Weight Cancellation in Monte Carlo Eigenvalue Transport Problems*. In: *Phys. Rev. E* 104.1, p. 015306. DOI: 10/gk7tnk (cit. on pp. 131, 132, 135, 137, 144).

— (2022a). *Unbiasedness and Optimization of Regional Weight Cancellation*. In: *Phys. Rev. E* 106.2, p. 025302. DOI: 10.1103/PhysRevE.106.025302 (cit. on pp. 138, 140).

— (2022b). *Variance Reduction Techniques for Monte Carlo Neutron Noise Simulations*. In: *Proc. Int. Conf. Phys. React. - Physor 2022*. Proceedings of the International Conference on Physics of Reactors - Physor 2022 (cit. on p. 144).

Bell, G. I. and S. Glasstone (1970). *Nuclear Reactor Theory*. New York: Van Nostrand Reinhold Company (cit. on pp. 11, 21, 29, 39).

Benlliure, J., M. Fernández-Ordóñez, L. Audouin, et al. (2008). *Production of Medium-Mass Neutron-Rich Nuclei in Reactions Induced by ^{136}Xe Projectiles at 1 AGeV on a Beryllium Target*. In: *Phys. Rev. C* 78.5, p. 54605. DOI: 10/cpn9m9 (cit. on p. 91).

Benlliure, J., A. Grewe, et al. (1998). *Calculated Nuclide Production Yields in Relativistic Collisions of Fissile Nuclei*. In: *Nucl. Phys. A* 628.3, pp. 458–478. DOI: 10/bt35q8 (cit. on p. 76).

Benlliure, J., T. Kurtukian-Nieto, L. Audouin, et al. (2007). *Production of Heavy Neutron-Rich Nuclei "South" of Lead*. In: *Eur. Phys. J. Spec. Top.* 150.1, pp. 309–310. DOI: 10/b9r2nv (cit. on p. 91).

Berger, M. J. et al. (1963). *Monte Carlo Calculation of the Penetration and Diffusion of Fast Charged Particles*. In: *Methods in Computational Physics*. Ed. by Alder B., Fernbach S. and Rotenberg M. Vol. 1. Academic Press, pp. 135–215 (cit. on pp. 34, 35).

Bertrand, F. E. and R. W. Peelle (1973). *Complete Hydrogen and Helium Particle Spectra from 30- to 60-MeV Proton Bombardment of Nuclei with A=12 to 209 and Comparison with the Intranuclear Cascade Model*. In: *Phys. Rev. C* 8.3, pp. 1045–1064. DOI: 10.1103/PhysRevC.8.1045 (cit. on p. 82).

Betzler, B. R., B. C. Kiedrowski, and W. R. Martin (2012). *Calculating Alpha Eigenvalues in a Continuous-Energy Infinite Medium with Monte Carlo*. technical report LA-UR-12-24472, 1050477. Los Alamos, NM, United States: Los Alamos National Laboratory, p. 20. DOI: 10.2172/1050477 (cit. on p. 19).

Bjørnholm, S. and J. E. Lynn (1980). *The Double-Humped Fission Barrier*. In: *Rev. Mod. Phys.* 52.4, pp. 725–931. DOI: 10.1103/RevModPhys.52.725 (cit. on p. 75).

Blank, B., S. Andriamonje, R. Del Moral, et al. (1994). *Production Cross Sections and the Particle Stability of Proton-Rich Nuclei from ^{58}Ni Fragmentation*. In: *Phys. Rev. C* 50.5, pp. 2398–2407. DOI: 10/dv3bv2 (cit. on p. 91).

Blunck, O. and S. Leisegang (1950). *Zum Energieverlust schneller Elektronen in dünnen Schichten*. In: *Z. Physik* 128.4, pp. 500–505. DOI: 10/cbr7mr (cit. on p. 34).

Bohr, N. and J. A. Wheeler (1939). *The Mechanism of Nuclear Fission*. In: *Phys. Rev.* 56.5, pp. 426–450. DOI: 10/cwr279 (cit. on p. 74).

Bohr, N. (1936). *Neutron Capture and Nuclear Constitution*. In: *Nature* 137.3461, pp. 344–348. DOI: 10.1038/137344a0 (cit. on p. 65).

— (1937). *Transmutations of Atomic Nuclei*. In: *Science* 86.2225, pp. 161–165. DOI: 10.1126/science.86.2225.161 (cit. on p. 65).

Boltzmann, L. (1872). *Weitere Studien über das Wärmegleichgewicht unter Gasmolekülen*. In: *Sitz-Ber Akad Wiss Wien II* 66, pp. 275–370. DOI: 10.1007/978-3-322-84986-1_3 (cit. on p. 35).

Bonnet, T., D. Mancusi, and A. Zoia (2022). *Space and Time Correlations for Diffusion Models with Prompt and Delayed Birth-and-Death Events*. In: *Phys. Rev. E* 105.6, p. 064105. DOI: 10.1103/PhysRevE.105.064105 (cit. on p. 146).

Booth, G. H., A. J. W. Thom, and A. Alavi (2009). *Fermion Monte Carlo without Fixed Nodes: A Game of Life, Death, and Annihilation in Slater Determinant Space*. In: *J. Chem. Phys.* 131.5, p. 054106. DOI: 10/d3828h (cit. on p. 131).

Booth, T. E. (1989). *Zero-Variance Solutions for Linear Monte Carlo*. In: *Nucl. Sci. Eng.* 102.4, pp. 332–340. DOI: 10.13182/NSE89-A23646 (cit. on p. 124).

— (2003). *Computing the Higher K-Eigenfunctions by Monte Carlo Power Iteration: A Conjecture*. In: *Nucl. Sci. Eng.* 143.3, pp. 291–300. DOI: 10.13182/NSE02-10TN (cit. on p. 144).

Booth, T. E. and J. E. Gubernatis (2010). *Exact Regional Monte Carlo Weight Cancellation for Second Eigenfunction Calculations*. In: *Nucl. Sci. Eng.* 165.3, pp. 283–291. DOI: 10/gh6d94 (cit. on pp. 131, 134, 135, 145).

Botvina, A. et al. (1987). *Statistical Simulation of the Break-up of Highly Excited Nuclei*. In: *Nucl. Phys. A* 475.4, pp. 663–686. DOI: 10.1016/0375-9474(87)90232-6 (cit. on p. 91).

Boudard, A., J. Cugnon, J.-C. David, et al. (2013). *New Potentialities of the Liège Intranuclear Cascade (INCL) Model for Reactions Induced by Nucleons and Light Charged Particles*. In: *Phys. Rev. C* 87.1, p. 14606. DOI: 10/gg89jj (cit. on pp. 69, 70, 72, 81, 84, 87–90).

Boudard, A., J. Cugnon, S. Leray, et al. (2002). *Intranuclear Cascade Model for a Comprehensive Description of Spallation Reaction Data*. In: *Phys. Rev. C* 66.4, p. 44615. DOI: 10/bpjc4h (cit. on pp. 81, 82, 86, 93, 105).

— (2004). *A New Model for Production of Fast Light Clusters in Spallation Reactions*. In: *Nucl. Phys. A* 740.1–2, pp. 195–210 (cit. on p. 86).

Brandan, M. E. and G. R. Satchler (1997). *The Interaction between Light Heavy-Ions and What It Tells Us*. In: *Phys. Rep.* 285.4, pp. 143–243. DOI: 10.1016/S0370-1573(96)00048-8 (cit. on p. 83).

Brobeck, W. M. et al. (1947). *Initial Performance of the 184-Inch Cyclotron of the University of California*. In: *Phys. Rev.* 71.7, pp. 449–450. DOI: 10.1103/PhysRev.71.449 (cit. on p. 65).

Brown, D. et al. (2010). *Photonuclear Physics and Data Evaluations*. technical report LLNL-TR-455702. Livermore, CA, United States: Lawrence Livermore National Laboratory. DOI: 10.2172/1121396 (cit. on p. 38).

Brown, D. A. et al. (2018). *ENDF/B-VIII.0: The 8th Major Release of the Nuclear Reaction Data Library with CIELO-project Cross Sections, New Standards and Thermal Scattering Data*. In: *Nucl. Data Sheets*. Special Issue on Nuclear Reaction Data 148, pp. 1–142. DOI: 10/gc79sf (cit. on pp. 12, 17, 31, 36, 38, 61).

Brown, F. B. (2009). *A Review of Best Practices for Monte Carlo Criticality Calculations*. LA-UR-09-03136; LA-UR-09-3136. Los Alamos, NM, United States: Los Alamos National Laboratory (cit. on p. 54).

Brun, E. et al. (2015). *TRIPOLI-4®, CEA, EDF and AREVA Reference Monte Carlo Code*. In: *Ann. Nucl. Energy* 82, pp. 151–160. DOI: 10/f7kr95 (cit. on pp. 112, 115).

Bunakov, V. E. and G. V. Matvejev (1985). *The Physical and Mathematical Foundations of the Intranuclear Cascade Model Algorithm*. In: *Z. Physik A* 322.3, pp. 511–521. DOI: 10.1007/BF01412089 (cit. on pp. 67, 68, 81).

Businaro, U. L. and S. Gallone (1955a). *On the Interpretation of Fission Asymmetry According to the Liquid Drop Nuclear Model*. In: *Nuovo Cim.* 1.4, pp. 629–643. DOI: 10.1007/BF02855221 (cit. on p. 86).

— (1955b). *Saddle Shapes, Threshold Energies and Fission Asymmetry on the Liquid Drop Model*. In: *Nuovo Cim.* 1.6, pp. 1277–1279. DOI: 10.1007/BF02731434 (cit. on p. 86).

Carter, L. L. and E. D. Cashwell (1975). *Particle Transport Simulation with the Monte Carlo Method: Prepared for the Division of Military Application, U.S. Energy Research and Development Administration*. ERDA Critical Review Series. Oak Ridge, TN, USA; Springfield, VA, USA: Technical Information Center, Office of Public Affairs, U.S. Energy Research and Development Administration. 115 pp. (cit. on p. 40).

Charity, R. J. (2010). *Systematic Description of Evaporation Spectra for Light and Heavy Compound Nuclei*. In: *Phys. Rev. C* 82.1, p. 14610. DOI: 10/fqwd7v (cit. on p. 78).

Charity, R. J., K. X. Jing, et al. (1990). *Sources of Complex Fragment Emission in Lanthanum-Induced Reactions at E/A = 14.7 and 18.0 MeV*. In: *Nucl. Phys. A* 511.1, pp. 59–91. DOI: 10/b4xs37 (cit. on p. 78).

Charity, R. J., M. A. McMahan, et al. (1988). *Systematics of Complex Fragment Emission in Niobium-Induced Reactions*. In: *Nucl. Phys. A* 483.2, pp. 371–405. DOI: 10/cq6px8 (cit. on pp. 78, 84, 91, 102).

Cowley, A. A. et al. (1996). *Inclusive (p,α) Reactions on ^{27}Al, ^{59}Co, and ^{197}Au at Incident Energies of 120, 160, and 200 MeV*. In: *Phys. Rev. C* 54.2, pp. 778–783. DOI: 10.1103/PhysRevC.54.778 (cit. on p. 82).

Cugnon, J. (1980). *Monte Carlo Calculation of High-Energy Heavy-Ion Interactions*. In: *Phys. Rev. C* 22.5, pp. 1885–1896. DOI: 10/d5sk2w (cit. on p. 81).

— (1982). *Intranuclear Cascade Model. A Review*. In: *Nucl. Phys. A* 387.1, pp. 191–203. DOI: 10.1016/0375-9474(82)90200-7 (cit. on p. 81).

— (1987). *Proton-Nucleus Interaction at High Energy*. In: *Nucl. Phys. A* 462.4, pp. 751–780. DOI: 10.1016/0375-9474(87)90575-6 (cit. on p. 81).

— (1992). *Antideuteron Annihilation on Nuclei*. In: *Nucl. Phys. A* 542.4, pp. 559–578. DOI: 10.1016/0375-9474(92)90257-K (cit. on p. 81).

— (2012). *A Short Introduction to Spallation Reactions: Theoretical Tools: Foundations and Domain of Validity*. In: *Few-Body Syst.* 53.1-2, pp. 143–149. DOI: 10.1007/s00601-011-0249-2 (cit. on pp. 67, 69, 71).

Cugnon, J., P. Deneye, and J. Vandermeulen (1989). *Multipion Dynamics Following Antiproton Annihilation on Nuclei*. In: *Nucl. Phys. A* 500.3, pp. 701–730. DOI: 10.1016/0375-9474(89)90236-4 (cit. on p. 81).

— (1990). *Hypernucleus Formation after Antiproton Annihilation on Nuclei*. In: *Nucl. Phys. A* 513.3, pp. 636–652. DOI: 10.1016/0375-9474(90)90402-8 (cit. on p. 81).

Cugnon, J. and R. M. Lombard (1984). *Kaon Production in High Energy Nucleus-Nucleus Collisions*. In: *Phys. Lett. B* 134.6, pp. 392–396. DOI: 10.1016/0370-2693(84)91368-6 (cit. on p. 81).

Cugnon, J., T. Mizutani, and J. Vandermeulen (1981). *Equilibration in Relativistic Nuclear Collisions. A Monte Carlo Calculation*. In: *Nucl. Phys. A* 352.3, pp. 505–534. DOI: 10.1016/0375-9474(81)90427-9 (cit. on p. 81).

Cugnon, J., C. Volant, and S. Vuillier (1997). *Improved Intranuclear Cascade Model for Nucleon-Nucleus Interactions*. In: *Nucl. Phys. A* 620.4, pp. 475–509. DOI: 10.1016/S0375-9474(97)00186-3 (cit. on p. 81).

David, J. .-C. (2015). *Spallation Reactions: A Successful Interplay between Modeling and Applications*. In: *Eur. Phys. J. A* 51.6, p. 68. DOI: 10.1140/epja/i2015-15068-1 (cit. on pp. 91, 103).

De Vries, H., C. W. De Jager, and C. De Vries (1987). *Nuclear Charge-Density-Distribution Parameters from Elastic Electron Scattering*. In: *At. Data Nucl. Data Tables* 36.3, pp. 495–536. DOI: 10/b2dvkf (cit. on p. 82).

De Witt Huberts, P. K. A. (1990). *Proton Spectral Functions and Momentum Distributions in Nuclei from High-Resolution (e,e'p) Experiments*. In: *J. Phys. G Nucl. Part. Phys.* 16.4, p. 507. DOI: 10/cqmjbw (cit. on p. 92).

Duderstadt, J. J. and W. R. Martin (1979). *Transport Theory*. New York: Wiley. 613 pp. (cit. on pp. 20, 29).

Dudouet, J., D. Cussol, et al. (2014). *Benchmarking Geant4 Nuclear Models for Hadron Therapy with 95 MeV/Nucleon Carbon Ions*. In: *Phys. Rev. C* 89.5, p. 054616. DOI: 10.1103/PhysRevC.89.054616 (cit. on pp. 98, 99).

Dudouet, J., D. Juliani, M. Labalme, et al. (2013a). *Comparison of Two Analysis Methods for Nuclear Reaction Measurements of ^{12}C + ^{12}C Interactions at 95 MeV/u for Hadron Therapy*. In: *Nucl. Instrum. Meth. Phys. Res. A* 715, pp. 98–104. DOI: 10/gg89jp (cit. on p. 98).

— (2013b). *Double-Differential Fragmentation Cross-Section Measurements of 95 MeV/Nucleon ^{12}C Beams on Thin Targets for Hadron Therapy*. In: *Phys. Rev. C* 88.2, p. 24606. DOI: 10/gg89jn (cit. on pp. 98, 99).

Durante, M. (2002). *Radiation Protection in Space*. In: *Riv. Nuovo Cim.* 25.8, pp. 1–70 (cit. on p. 91).

Fabjan, C. W. and F. Gianotti (2003). *Calorimetry for Particle Physics*. In: *Rev. Mod. Phys.* 75.4, pp. 1243–1286. DOI: 10/b83x26 (cit. on p. 63).

Faucher, M. (2019). *Coupling between Monte Carlo Neutron Transport and Thermal-Hydraulics for the Simulation of Transients Due to Reactivity Insertions*. Paris, France: Université Paris-Saclay. 192 pp. (cit. on pp. 110, 115, 120).

Faucher, M., D. Mancusi, and A. Zoia (2018). *New Kinetic Simulation Capabilities for Tripoli-4®: Methods and Applications*. In: *Ann. Nucl. Energy* 120, pp. 74–88. DOI: 10.1016/j.anucene.2018.05.030 (cit. on pp. 110–112, 115).

— (2019). *Variance-Reduction Methods for Monte Carlo Kinetic Simulations*. In: International Conference on Mathematics and Computational Methods Applied to Nuclear Science and Engineering, M&C 2019, pp. 130–139 (cit. on pp. 112, 113).

— (2021). *Multi-Physics Transient Simulations with TRIPOLI-4®*. In: *EPJ Web Conf.* International Conference on Physics of Reactors (PHYSOR2020): Transition to a Scalable Nuclear Future. Vol. 247. EDP Sciences, p. 07019 (cit. on pp. 115, 117).

Ferraro, D., M. Faucher, et al. (2019). *Serpent and Tripoli-4® Transient Calculations Comparisons for Several Reactivity Insertion Scenarios in a 3D PWR Minicore Benchmark*. In: International Conference on Mathematics and Computational Methods Applied to Nuclear Science and Engineering, M&C 2019, pp. 1734–1743 (cit. on pp. 115–117).

Ferraro, D., M. García, et al. (2020). *Serpent/SUBCHANFLOW Pin-by-Pin Coupled Transient Calculations for the SPERT-IIIE Hot Full Power Tests*. In: *Ann. Nucl. Energy* 142, p. 107387. DOI: 10.1016/j.anucene.2020.107387 (cit. on pp. 115, 118).

Ferreres-Solé, S. and T. Sjöstrand (2018). *The Space–Time Structure of Hadronization in the Lund Model*. In: *Eur. Phys. J. C* 78.11, p. 983. DOI: 10.1140/epjc/s10052-018-6459-8 (cit. on p. 71).

Folger, G., V. N. Ivanchenko, and J. P. Wellisch (2004). *The Binary Cascade*. In: *Eur. Phys. J. A* 21.3, pp. 407–417. DOI: 10.1140/epja/i2003-10219-7 (cit. on pp. 71, 96).

Frenkel, I. (1936). In: *Sov. Phys.* 9, p. 533 (cit. on p. 65).

Friedman, E. and A. Gal (2007). *In-Medium Nuclear Interactions of Low-Energy Hadrons*. In: *Phys. Rep.* 452.4–5, pp. 89–153. DOI: 10/cgxs7g (cit. on p. 105).

Furihata, S. (2000). *Statistical Analysis of Light Fragment Production from Medium Energy Proton-Induced Reactions*. In: *Nucl. Instrum. Meth. Phys. Res. B* 171.3, pp. 251–258. DOI: 10/d3bhds (cit. on p. 77).

Galin, J. et al. (1974). *Limitation to Complete Fusion during a Collision between Two Complex Nuclei*. In: *Phys. Rev. C* 9.3, pp. 1018–1024. DOI: 10/bkph7t (cit. on p. 95).

Geant4 Physics Reference Manual (2022). URL: https://geant4-userdoc.web.cern.ch/UsersGuides/PhysicsReferenceManual/html/hadronic/LowEnergyNeutron/index.html#low-energy-neutrons (visited on 07/04/2022) (cit. on p. 64).

Goldberger, M. L. (1948). *The Interaction of High Energy Neutrons and Heavy Nuclei*. In: *Phys. Rev.* 74.10, pp. 1269–1277. DOI: 10.1103/PhysRev.74.1269 (cit. on p. 67).

Goldberger, M. L. and K. M. Watson (1964). *Collision Theory*. Courier Corporation. 930 pp. (cit. on p. 67).

Goudsmit, S. and J. L. Saunderson (1940). *Multiple Scattering of Electrons*. In: *Phys. Rev.* 57.1, pp. 24–29. DOI: 10/ddw75m (cit. on p. 34).

Griffin, J. J. (1966). *Statistical Model of Intermediate Structure*. In: *Phys. Rev. Lett.* 17.9, pp. 478–481. DOI: 10/fnq2wh (cit. on p. 71).

Guertin, A. et al. (2005). *Neutron and Light-Charged-Particle Productions in Proton-Induced Reactions on ^{208}Pb at 62.9 MeV*. In: *Eur. Phys. J. A* 23.1, pp. 49–60. DOI: 10.1140/epja/i2004-10073-1 (cit. on pp. 82, 90).

Handbook for Calculations of Nuclear Reaction Data Reference Input Parameter Library (1998). IAEA-TECDOC-1034. Vienna: International Atomic Energy Agency (cit. on p. 75).

Hauser, W. and H. Feshbach (1952). *The Inelastic Scattering of Neutrons*. In: *Phys. Rev.* 87.2, pp. 366–373. DOI: 10/bzn3s2 (cit. on p. 76).

Heilbronn, L. et al. (2007). *Secondary Neutron-Production Cross Sections from Heavy-Ion Interactions between 230 and 600 MeV/Nucleon*. In: *Nucl. Sci. Eng.* 157.2, p. 142. DOI: 10/gg89jz (cit. on p. 97).

Herbach, C. .-M. et al. (2006). *Charged-Particle Evaporation and Pre-Equilibrium Emission in 1.2 GeV Proton-Induced Spallation Reactions*. In: *Nucl. Phys. A* 765.3, pp. 426–463. DOI: 10.1016/j.nuclphysa.2005.10.014 (cit. on pp. 82, 88).

Hoogenboom, J. E. (2008). *Zero-Variance Monte Carlo Schemes Revisited*. In: *Nucl. Sci. Eng.* 160.1, pp. 1–22. DOI: 10.13182/NSE160-01 (cit. on pp. 124, 127, 129).

IAEA Benchmark of Spallation Models (2022). URL: http://www-nds.iaea.org/spallations (visited on 06/10/2022) (cit. on p. 70).

Ignatyuk, A. V., G. N. Smirenkin, and A. S. Tishin (1975). *Phenomenological description of energy dependence of the level density parameter*. In: *Yad. Fiz.* 21.3, pp. 485–490 (cit. on p. 75).

Imke, U. and V. H. Sanchez (2012). *Validation of the Subchannel Code SUBCHANFLOW Using the NUPEC PWR Tests (PSBT)*. In: *Sci. Technol. Nucl. Install.* 2012, p. 465059. DOI: 10/gb8c6t (cit. on p. 115).

Ivanchenko, V. N. et al. (2010). *Geant4 Models for Simulation of Multiple Scattering*. In: *J. Phys. Conf. Ser.* 219.3, p. 32045. DOI: 10/fr88kd (cit. on p. 34).

Iwata, Y. et al. (2001). *Double-Differential Cross Sections for the Neutron Production from Heavy-Ion Reactions at Energies E/A=290–600 MeV*. In: *Phys. Rev. C* 64.5, p. 54609. DOI: 10/d28gpz (cit. on p. 96).

Jacob, N. P. and S. S. Markowitz (1975). *Cross Sections above 0.3 GeV for (p, 2p) Reactions of ^{48}Ti and ^{74}Ge*. In: *Phys. Rev. C* 11.2, pp. 541–545. DOI: 10/b744jh (cit. on p. 101).

Kaitaniemi, P. et al. (2011). *INCL Intra-Nuclear Cascade and ABLA de-Excitation Models in Geant4*. In: *Prog. Nucl. Sci. Technol.* 2.0, pp. 788–793. DOI: 10.15669/pnst.2.788 (cit. on pp. 91, 95).

Kaplan, E. L. (1958). *Monte Carlo Methods for Equilibrium Solutions in Neutron Multiplication*. University of California Lawrence Radiation Laboratory. 114 pp. (cit. on p. 109).

Kelić, A., M. V. Ricciardi, and K.-H. Schmidt (2008). *ABLA07 — Towards a Complete Description of the Decay Channels of a Nuclear System from Spontaneous Fission to Multifragmentation*. In: Joint ICTP-IAEA Advanced Workshop on Model Codes for Spallation Reactions. Trieste, Italy, p. 181 (cit. on pp. 69, 70, 84, 86, 99).

Kemerer, C. F. (1987). *An Empirical Validation of Software Cost Estimation Models*. In: *Commun. ACM* 30.5, pp. 416–429. DOI: 10.1145/22899.22906 (cit. on p. 92).

Koning, A. J. et al. (2019). *TENDL: Complete Nuclear Data Library for Innovative Nuclear Science and Technology*. In: *Nucl. Data Sheets*. Special Issue on Nuclear Reaction Data 155, pp. 1–55. DOI: 10/gjfbgt (cit. on p. 61).

Kraft, G. (1990). *The Radiobiological and Physical Basis for Radiotherapy with Protons and Heavier Ions*. In: *Strahlenther. Onkol.* 166.1, pp. 10–13 (cit. on p. 91).

— (2000). *Tumor Therapy with Heavy Charged Particles*. In: *Prog. Part. Nucl. Phys.* 45 (supplement 2), S473–S544. DOI: 10/fcfbc6 (cit. on p. 91).

Kreyszig, E. (1989). *Introductory Functional Analysis with Applications*. Wiley Classics Library. New York: Wiley. 688 pp. (cit. on p. 29).

Kruglov, K. et al. (2002). *Yields of Neutron-Rich Isotopes around Z = 28 Produced in 30 MeV Proton-Induced Fission of ^{238}U*. In: *Eur. Phys. J. Hadrons Nucl.* 14.3, pp. 365–370. DOI: 10/fdtdgb (cit. on p. 76).

Kurcewicz, J., Z. Liu, M. Pfützner, et al. (2006). *Production Cross-Sections of Protactinium and Thorium Isotopes Produced in Fragmentation of ^{238}U at 1 AGeV*. In: *Nucl. Phys. A* 767, pp. 1–12. DOI: 10/c4vhk9 (cit. on p. 91).

Landau, L. D. (1944). *On the Energy Loss of Fast Particles by Ionization*. In: *J. Phys.* 8, pp. 201–205 (cit. on p. 34).

Larsen, E. W. (1979). *The Spectrum of the Multigroup Neutron Transport Operator for Bounded Spatial Domains*. In: *J. Math. Phys.* 20.8, pp. 1776–1782. DOI: 10/b9bxsn (cit. on p. 20).

Larsen, E. W. and P. F. Zweifel (1974). *On the Spectrum of the Linear Transport Operator*. In: *J. Math. Phys.* 15.11, pp. 1987–1997. DOI: 10.1063/1.1666570 (cit. on p. 20).

Legrady, D., B. Molnar, et al. (2017). *Woodcock Tracking with Arbitrary Sampling Cross Section Using Negative Weights*. In: *Ann. Nucl. Energy* 102, pp. 116–123. DOI: 10/f9wb8q (cit. on p. 131).

Legrady, D. and J. E. Hoogenboom (2008). *Scouting the Feasibility of Monte Carlo Reactor Dynamics Simulations*. In: PHYSOR'08: International Conference on the Physics of Reactors. Interlaken, Switzerland (cit. on pp. 109, 110).

Leppänen, J. et al. (2015). *The Serpent Monte Carlo Code: Status, Development and Applications in 2013*. In: *Annals of Nuclear Energy*. Joint International Conference on Supercomputing in Nuclear Applications and Monte Carlo 2013, SNA + MC 2013. Pluri- and

Trans-disciplinarity, Towards New Modeling and Numerical Simulation Paradigms 82, pp. 142–150. DOI: 10/f7kqrr (cit. on p. 115).

Leray, S. et al. (2002). *Spallation Neutron Production by 0.8, 1.2, and 1.6 GeV Protons on Various Targets*. In: *Phys. Rev. C* 65.4, p. 44621. DOI: 10/db4tnb (cit. on pp. 69, 70).

Leray, S. et al. (2011). *Results from the IAEA Benchmark of Spallation Models*. In: *J. Korean Phys. Soc.* 59.23, pp. 791–796. DOI: 10/bxc3qw (cit. on pp. 69–71).

Letourneau, A. et al. (2002). *Composite-Particle Emission in the Reaction p+Au at 2.5 GeV*. In: *Nucl. Phys. A* 712.1, pp. 133–166. DOI: 10.1016/S0375-9474(02)01133-8 (cit. on p. 82).

Lévy, P. (1954). *Théorie de l'addition Des Variables Aléatoires*. Gauthier-Villars (cit. on p. 145).

Lewis, E. E. et al. (2001). *Benchmark Specification for Deterministic 2-D/3-D MOX Fuel Assembly Transport Calculations without Spatial Homogenization (C5G7 MOX)*. In: *NEA/NSC* 280 (cit. on p. 137).

Lewis, H. W. (1950). *Multiple Scattering in an Infinite Medium*. In: *Phys. Rev.* 78.5, pp. 526–529. DOI: 10/cdkr5w (cit. on p. 34).

Lux, I. and L. Koblinger (2018). *Monte Carlo Particle Transport Methods: Neutron and Photon Calculations*. 1st ed. CRC Press. DOI: 10.1201/9781351074834 (cit. on pp. 23, 40, 44, 45, 47, 122–124, 128).

Machleidt, R. and I. Slaus (2001). *The Nucleon-Nucleon Interaction*. In: *J. Phys. G: Nucl. Part. Phys.* 27.5, R69–R108. DOI: 10/cb49bg (cit. on p. 36).

Mancusi, D., A. Boudard, J. Cugnon, et al. (2014). *Extension of the Liège Intranuclear-Cascade Model to Reactions Induced by Light Nuclei*. In: *Phys. Rev. C* 90.5, p. 54602. DOI: 10/gg89jt (cit. on pp. 81, 92, 93, 96–100).

Mancusi, D., R. J. Charity, and J. Cugnon (2010). *Unified Description of Fission in Fusion and Spallation Reactions*. In: *Phys. Rev. C* 82.4, p. 44610. DOI: 10/dbvzss (cit. on pp. 91, 102).

Mancusi, D. (2023). *Fredholm*. Version v0.1. DOI: 10.5281/zenodo.8009653 (cit. on p. 57).

Mancusi, D., A. Boudard, J. Carbonell, et al. (2015). *Improving the Description of Proton-Induced One-Nucleon Removal in Intranuclear-Cascade Models*. In: *Phys. Rev. C* 91.3, p. 034602. DOI: 10.1103/PhysRevC.91.034602 (cit. on pp. 81, 101, 102, 104–107).

Mancusi, D., M. Faucher, and A. Zoia (2022). *Monte Carlo Simulations of the SPERT III E-core Transient Experiments*. In: *Eur. Phys. J. Plus* 137.1, p. 127. DOI: 10/gn42qs (cit. on pp. 115, 116, 118, 119).

Mancusi, D., K. Niita, et al. (2009). *Stability of Nuclei in Peripheral Collisions in the JAERI Quantum Molecular Dynamics Model*. In: *Phys. Rev. C* 79.1, p. 014614. DOI: 10.1103/PhysRevC.79.014614 (cit. on p. 96).

Mancusi, D. and A. Zoia (2020). *Zero-Variance Schemes for Kinetic Monte Carlo Simulations*. In: *Eur. Phys. J. Plus* 135.5 (6), p. 401. DOI: 10.1140/epjp/s13360-020-00387-8 (cit. on pp. 122, 124, 125, 128, 130).

Mandelbrot, B. B. (1982). *The Fractal Geometry of Nature*. San Francisco: W.H. Freeman. 460 pp. (cit. on p. 145).

Mashnik, S. G., K. K. Gudima, R. E. Prael, et al. (2008). *CEM03.03 and LAQGSM03.03 Event Generators for the MCNP6, MCNPX, and MARS15 Transport Codes*. In: Joint ICTP-IAEA Advanced Workshop on Model Codes for Spallation Reactions, p. 51 (cit. on pp. 71, 81, 102).

Mashnik, S. G., L. M. Kerby, et al. (2014). *Production of Energetic Light Fragments in Spallation Reactions*. In: *EPJ Web Conf.* INPC 2013 – International Nuclear Physics Conference. Vol. 66. EDP Sciences, p. 3059. DOI: 10/gg89jw (cit. on p. 99).

Metropolis, N., R. Bivins, M. Storm, J. M. Miller, et al. (1958). *Monte Carlo Calculations on Intranuclear Cascades. II. High-Energy Studies and Pion Processes*. In: *Phys. Rev.* 110.1, pp. 204–219. DOI: 10.1103/PhysRev.110.204 (cit. on p. 67).

Metropolis, N., R. Bivins, M. Storm, A. Turkevich, et al. (1958). *Monte Carlo Calculations on Intranuclear Cascades. I. Low-Energy Studies*. In: *Phys. Rev.* 110.1, pp. 185–203. DOI: 10.1103/PhysRev.110.185 (cit. on p. 67).

Miao, J., B. Forget, and K. Smith (2018). *Predicting Correlation Coefficients for Monte Carlo Eigenvalue Simulations with Multitype Branching Process*. In: *Ann. Nucl. Energy* 112, pp. 307–321. DOI: 10.1016/j.anucene.2017.10.014 (cit. on p. 54).

Molière, G. (1948). *Theorie Der Streuung Schneller Geladener Teilchen II: Mehrfach- Und Vielfachstreuung*. In: *Z. Für Naturforschung* 3.a, pp. 78–97. DOI: 10/gg89j8 (cit. on p. 34).

Moretto, L. G. (1975). *Statistical Emission of Large Fragments: A General Theoretical Approach*. In: *Nucl. Phys. A* 247.2, pp. 211–230. DOI: 10/bw6g3z (cit. on p. 77).

Moretto, L. G. and G. J. Wozniak (1988). *The Role of the Compound Nucleus in Complex Fragment Emission at Low and Intermediate Energies*. In: *Prog. Part. Nucl. Phys.* 21, pp. 401–457. DOI: 10.1016/0146-6410(88)90036-1 (cit. on p. 77).

Morrissey, D. J. and B. M. Sherrill (1998). *Radioactive Nuclear Beam Facilities Based on Projectile Fragmentation*. In: *Philos. T. Roy. Soc. A* 356.1744, pp. 1985–2006. DOI: 10/fpxk4z (cit. on p. 91).

Mosher, S. W. et al. (2013). *ADVANTG—an Automated Variance Reduction Parameter Generator*. ORNL/TM-2013/416 Rev. Oak Ridge, TN, United States: Oak Ridge National Laboratory, p. 105 (cit. on p. 143).

Munk, M. and R. N. Slaybaugh (2019). *Review of Hybrid Methods for Deep-Penetration Neutron Transport*. In: *Nucl. Sci. Eng.* 193.10, pp. 1055–1089. DOI: 10.1080/00295639.2019.1586273 (cit. on pp. 124, 143, 144).

Newton, R. G. (1966). *Scattering Theory of Waves and Particles*. International Series in Pure and Applied Physics. New York: McGraw-Hill. 681 pp. (cit. on p. 11).

Niita, K., S. Chiba, et al. (1995). *Analysis of the (N,xN') Reactions by Quantum Molecular Dynamics plus Statistical Decay Model*. In: *Phys. Rev. C* 52.5, pp. 2620–2635. DOI: 10/cc78wc (cit. on pp. 96, 101).

Niita, K., T. Sato, et al. (2006). *PHITS—a Particle and Heavy Ion Transport Code System*. In: *Radiat. Meas.* Space Radiation Transport, Shielding, and Risk Assessment Models 41.9, pp. 1080–1090. DOI: 10.1016/j.radmeas.2006.07.013 (cit. on p. 71).

Nix, J. R. and W. J. Swiatecki (1965). *Studies in the Liquid-Drop Theory of Nuclear Fission*. In: *Nucl. Phys.* 71.1, pp. 1–94. DOI: 10.1016/0029-5582(65)90038-6 (cit. on p. 77).

O'connor, P. R. and G. T. Seaborg (1948). *High Energy Spallation and Fission Products of Uranium*. In: *Phys. Rev.* 74.9, pp. 1189–1190. DOI: 10.1103/PhysRev.74.1189 (cit. on p. 66).

Pál, L. and I. Pázsit (2006). *Neutron Fluctuations in a Multiplying Medium Randomly Varying in Time*. In: *Phys. Scr.* 74.1, pp. 62–70. DOI: 10/dcd36m (cit. on p. 146).

Paul, H. and J. Sacher (1989). *Fitted Empirical Reference Cross Sections for K-shell Ionization by Protons*. In: *At. Data Nucl. Data Tables* 42.1, pp. 105–156. DOI: 10/cmqd53 (cit. on p. 32).

Pedoux, S. and J. Cugnon (2011). *Extension of the Liège Intranuclear Cascade Model at Incident Energies between 2 and 12 GeV. Aspects of Pion Production*. In: *Nucl. Phys. A* 866.1, pp. 16–36. DOI: 10.1016/j.nuclphysa.2011.07.004 (cit. on pp. 71, 81).

Peplow, D. E., E. D. Blakeman, and J. C. Wagner (2007). *Advanced Variance Reduction Strategies for Optimizing Mesh Tallies in MAVRIC*. In: American Nuclear Society 2007 Winter Meeting: "Making the Renaissance Real". Washington, DC (cit. on p. 144).

Perkins, S., D. Cullen, and S. Seltzer (1991). *Tables and Graphs of Electron-Interaction Cross Sections from 10 eV to 100 GeV Derived from the LLNL Evaluated Electron Data Library (EEDL), Z = 1–100*. technical report UCRL-50400-Vol.31, 5691165. Livermore, CA, United States: Lawrence Livermore National Laboratory. DOI: 10.2172/5691165 (cit. on pp. 31, 32).

PISA Collaboration, A. Bubak, et al. (2007). *Non-Equilibrium Emission of Complex Fragments from p+Au Collisions at 2.5 GeV Proton Beam Energy*. In: *Phys. Rev. C* 76.1, p. 014618. DOI: 10.1103/PhysRevC.76.014618 (cit. on pp. 82, 83).

PISA Collaboration, A. Budzanowski, et al. (2008). *Competition of Coalescence and "Fireball" Processes in Nonequilibrium Emission of Light Charged Particles from p+Au Collisions*. In: *Phys. Rev. C* 78.2, p. 024603. DOI: 10.1103/PhysRevC.78.024603 (cit. on pp. 82, 83, 87).

— (2009). *Variation of Nonequilibrium Processes in the p+Ni System with Beam Energy*. In: *Phys. Rev. C* 80.5, p. 054604. DOI: 10.1103/PhysRevC.80.054604 (cit. on pp. 82, 83).

Plompen, A. J. M. et al. (2020). *The Joint Evaluated Fission and Fusion Nuclear Data Library, JEFF-3.3*. In: *Eur. Phys. J. A* 56.7, p. 181. DOI: 10/gg9gtm (cit. on pp. 17, 31, 38).

Polyanin, A. D. and A. V. Manzhirov (2008). *Handbook of Integral Equations*. 2nd ed. Handbooks of Mathematical Equations. Boca Raton: Chapman & Hall/CRC. 1108 pp. (cit. on p. 54).

Prinja, A. K. and E. W. Larsen (2010). *General Principles of Neutron Transport*. In: *Handbook of Nuclear Engineering*. Ed. by D. G. Cacuci. Boston, MA: Springer US, pp. 427–542. DOI: 10.1007/978-0-387-98149-9_5 (cit. on p. 29).

Quesada, J. M. et al. (2011). *Recent Developments in Pre-Equilibrium and De-excitation Models in Geant4*. In: *Prog. Nucl. Sci. Technol.* 2, pp. 936–941. DOI: 10/gg89kb (cit. on p. 96).

Ravn, H. L. (1998). *Radioactive Ion-Beam Projects Based on the Two-Accelerator or ISOL Principle*. In: *Philos. T. Roy. Soc. A* 356.1744, pp. 1955–1984. DOI: 10/cmhb52 (cit. on p. 91).

Remler, E. A. and A. P. Sathe (1975). *Quasi-Classical Scattering Theory and Bound State Production Processes*. In: *Ann. Phys.* 91.2, pp. 295–324. DOI: 10/cdq2z5 (cit. on p. 101).

Rodríguez-Sánchez, J. L. et al. (2017). *Improvement of One-Nucleon Removal and Total Reaction Cross Sections in the Liège Intranuclear-Cascade Model Using Hartree-Fock-Bogoliubov Calculations*. In: *Phys. Rev. C* 96.5, p. 054602. DOI: 10.1103/PhysRevC.96.054602 (cit. on pp. 101, 107).

Rudin, W. (2013). *Real and Complex Analysis*. 3. ed., internat. ed. McGraw-Hill International Editions Mathematics Series. New York: McGraw-Hill. 416 pp. (cit. on pp. 29, 146).

Rutherford, E. (1905). *Radio-Activity*. Cambridge: University Press (cit. on p. 37).

Salvat, F. (2015). *PENELOPE-2014: A Code System for Monte Carlo Simulation of Electron and Photon Transport*. In: vol. 3. NEA/NSC/DOC (cit. on p. 35).

Sanchez, R. (2015). *Some Comments in Neutron Noise Theory*. In: *Ann. Nucl. Energy* 86, pp. 88–98. DOI: 10/f7zjpt (cit. on p. 144).

Sanchez-Espinoza, V. H. et al. (2021). *The McSAFE Project — High-performance Monte Carlo Based Methods for Safety Demonstration: From Proof of Concept to Industry Applications*. In: *EPJ Web Conf.* PHYSOR2020 – International Conference on Physics of Reactors: Transition to a Scalable Nuclear Future. Vol. 247. EDP Sciences, p. 06004. DOI: 10/gmnwbw (cit. on p. 115).

Schmidt, K.-H., A. Kelić, and M. V. Ricciardi (2008). *Experimental Evidence for the Separability of Compound-Nucleus and Fragment Properties in Fission*. In: *EPL* 83.3, p. 32001. DOI: 10.1209/0295-5075/83/32001 (cit. on p. 76).

Schneider, D. O. and D. V. Cormack (1959). *Monte Carlo Calculations of Electron Energy Loss*. In: *Radiat. Res.* 11.3, pp. 418–429. DOI: 10/ccfgtr (cit. on p. 34).

Serber, R. (1947). *Nuclear Reactions at High Energies*. In: *Phys. Rev.* 72.11, pp. 1114–1115. DOI: 10/btv7vw (cit. on pp. 66, 82).

Serber, R. and R. P. Crease (1998). *Peace & War: Reminiscences of a Life on the Frontiers of Science*. The George B. Pegram Lecture Series. New York: Columbia University Press. 241 pp. (cit. on p. 66).

Sierk, A. J. (1986). *Macroscopic Model of Rotating Nuclei*. In: *Phys. Rev. C* 33.6, pp. 2039–2053. DOI: 10/bsgdc9 (cit. on p. 75).

Sjenitzer, B. L. and J. E. Hoogenboom (2013). *Dynamic Monte Carlo Method for Nuclear Reactor Kinetics Calculations*. In: *Nucl. Sci. Eng.* 175.1, pp. 94–107. DOI: 10.13182/NSE12-44 (cit. on pp. 109, 110).

Sjenitzer, B. L. (2013). *The Dynamic Monte Carlo Method for Transient Analysis of Nuclear Reactors*. S.l.: Delft University of Technology, Netherlands (cit. on pp. 109, 110).

Soppera, N., M. Bossant, and E. Dupont (2014). *JANIS 4: An Improved Version of the NEA Java-based Nuclear Data Information System*. In: *Nucl. Data Sheets* 120, pp. 294–296. DOI: 10.1016/j.nds.2014.07.071 (cit. on p. 61).

Sorge, H., H. Stöcker, and W. Greiner (1989). *Poincaré Invariant Hamiltonian Dynamics: Modelling Multi-Hadronic Interactions in a Phase Space Approach*. In: *Ann. Phys.* 192.2, pp. 266–306. DOI: 10/cbjq7p (cit. on p. 101).

Spanier, J. and E. M. Gelbard (2008). *Monte Carlo Principles and Neutron Transport Problems*. Dover ed. Mineola, NY, United States: Dover Publications. 244 pp. (cit. on pp. 40, 41, 44, 55, 63).

Spencer, J. S., N. S. Blunt, and W. M. C. Foulkes (2012). *The Sign Problem and Population Dynamics in the Full Configuration Interaction Quantum Monte Carlo Method*. In: *J. Chem. Phys.* 136.5, p. 054110. DOI: 10/ghkfqp (cit. on p. 131).

Stolz, A., T. Faestermann, J. Friese, et al. (2002). *Projectile Fragmentation of ^{112}Sn at E_{lab}=1A GeV*. In: *Phys. Rev. C* 65.6, p. 64603. DOI: 10/fht64n (cit. on p. 91).

Świątecki, W. J. (1983). *Note on Nuclear Disintegration Widths*. In: *Aust. J. Phys.* 36.5, pp. 641–648. DOI: 10/gg89kf (cit. on p. 77).

Swinhoe, M. et al. (1991). *A Review of Passive Neutron Coincidence Measurements in the Euratom Safeguards Directorate*. technical report. Commission of the European Communities (CEC), pp. 391–395 (cit. on p. 63).

Thomas, K., R. Davies, and A. J. Sierk (1985). *Conditional Saddle-Point Configurations*. In: *Phys. Rev. C* 31.3, pp. 915–922. DOI: 10.1103/PhysRevC.31.915 (cit. on p. 78).

Toneev, V. D. and K. K. Gudima (1983). *Particle Emission in Light and Heavy Ion Reactions*. In: *Nucl. Phys. A* 400.1, pp. 173–189. DOI: 10/b36b5x (cit. on p. 84).

Uffink, J. and G. Valente (2015). *Lanford's Theorem and the Emergence of Irreversibility*. In: *Found. Phys.* 45.4, pp. 404–438. DOI: 10/f65vjx (cit. on p. 35).

Urbàn, L. (2002). *Multiple Scattering Model in GEANT4*. CERN-OPEN-2002-070. CERN, p. 14 (cit. on p. 34).

Vavilov, P. V. (1957). *Ionization Losses of High-Energy Heavy Particles*. In: *Sov. Phys JETP* 5 (cit. on p. 34).

Wagner, J. C. and A. Haghighat (1998). *Automated Variance Reduction of Monte Carlo Shielding Calculations Using the Discrete Ordinates Adjoint Function*. In: *Nucl. Sci. Eng.* 128.2, pp. 186–208. DOI: 10.13182/NSE98-2 (cit. on pp. 124, 143).

Wang, M. et al. (2017). *The AME2016 Atomic Mass Evaluation (II). Tables, Graphs and References*. In: *Chinese Phys. C* 41.3, p. 030003. DOI: 10.1088/1674-1137/41/3/030003 (cit. on p. 61).

Weber, M., C. Donzaud, J. Dufour, et al. (1994). *Longitudinal Momenta and Production Cross-Sections of Isotopes Formed by Fragmentation of a 500 A×MeV ^{86}Kr Beam*. In: *Nucl. Phys. A* 578.3–4, pp. 659–672. DOI: 10/fhn5m7 (cit. on pp. 99, 100).

Weisskopf, V. F. (1937). *Statistics and Nuclear Reactions*. In: *Phys. Rev.* 52.4, pp. 295–303. DOI: 10/brfjg9 (cit. on p. 72).

Weisskopf, V. F. and D. H. Ewing (1940). *On the Yield of Nuclear Reactions with Heavy Elements*. In: *Phys. Rev.* 57.6, pp. 472–485. DOI: 10/cdtc92 (cit. on p. 72).

Wigner, E. (1938). *The Transition State Method*. In: *Trans. Faraday Soc.* 34, p. 29. DOI: 10.1039/tf9383400029 (cit. on p. 74).

Williams, E. J. and J. Chadwick (1939). *Concerning the Scattering of Fast Electrons and of Cosmic-Ray Particles*. In: *Proc. R. Soc. Lond. Ser. Math. Phys. Sci.* 169.939, pp. 531–572. DOI: 10/bcqnkz (cit. on p. 34).

Williams, M. M. R. (1974). *Random Processes in Nuclear Reactors*. 1st ed. Oxford ; New York: Pergamon Press. 243 pp. (cit. on p. 146).

Woodcock, E. et al. (1965). *Techniques Used in the GEM Code for Monte Carlo Neutronics Calculations in Reactors and Other Systems of Complex Geometry*. In: Applications of Computing Methods to Reactor Problems. Vol. 557. 2 (cit. on pp. 126, 131).

Wright, D. H. and M. H. Kelsey (2015). *The Geant4 Bertini Cascade*. In: *Nucl. Instrum. Meth. Phys. Res. A* 804, pp. 175–188. DOI: 10.1016/j.nima.2015.09.058 (cit. on pp. 71, 84, 96, 102).

Wu, T. Y. and T. Ohmura (1962). *Quantum Theory of Scattering*. Prentice-Hall International Series In Physics. Englewood Cliffs, NJ, United States: Prentice-Hall, Inc. (cit. on p. 11).

Yamamoto, T. (2012). *Monte Carlo Algorithm for Buckling Search and Neutron Leakage-Corrected Calculations*. In: *Ann. Nucl. Energy* 47, pp. 14–20. DOI: 10.1016/j.anucene.2012.04.017 (cit. on pp. 131, 145).

— (2013). *Monte Carlo Method with Complex-Valued Weights for Frequency Domain Analyses of Neutron Noise*. In: *Ann. Nucl. Energy* 58, pp. 72–79. DOI: 10.1016/j.anucene.2013.03.002 (cit. on pp. 131, 144).

Yariv, Y., Th. Aoust, et al. (2007). *Intra-Nuclear Cascade Models at Low Energy?* In: International Conference on Nuclear Data for Science and Technology. Nice, France: EDP Sciences, p. 296. DOI: 10.1051/ndata:07738 (cit. on p. 71).

Yariv, Y. and Z. Fraenkel (1979). *Intranuclear Cascade Calculation of High-Energy Heavy-Ion Interactions*. In: *Phys. Rev. C* 20.6, pp. 2227–2243. DOI: 10/bmrpgz (cit. on pp. 72, 81, 82, 91, 102).

— (1981). *Intranuclear Cascade Calculation of High Energy Heavy Ion Collisions: Effect of Interactions between Cascade Particles*. In: *Phys. Rev. C* 24.2, pp. 488–494. DOI: 10/b3jhtz (cit. on pp. 72, 81, 82, 91).

Zenihiro, J., H. Sakaguchi, T. Murakami, et al. (2010). *Neutron Density Distributions of ^{204,206,208}Pb Deduced via Proton Elastic Scattering at E_p=295 MeV*. In: *Phys. Rev. C* 82.4, p. 44611. DOI: 10/d64mzk (cit. on p. 104).

Zhang, P., H. Lee, and D. Lee (2016). *A General Solution Strategy of Modified Power Method for Higher Mode Solutions*. In: *J. Comput. Phys.* 305, pp. 387–402. DOI: 10/f736ps (cit. on pp. 134, 140, 144, 145).

Zheng-Ming, L. and A. Brahme (1993). *An Overview of the Transport Theory of Charged Particles*. In: *Radiat. Phys. Chem.* 41.4-5, pp. 673–703. DOI: 10.1016/0969-806X(93)90318-O (cit. on pp. 33, 35).